

NASA Contractor Report 198370

NASA-CR-198370  
19960008875

# Interfacial Effects on the Thermal and Mechanical Properties of Graphite/Copper Composites

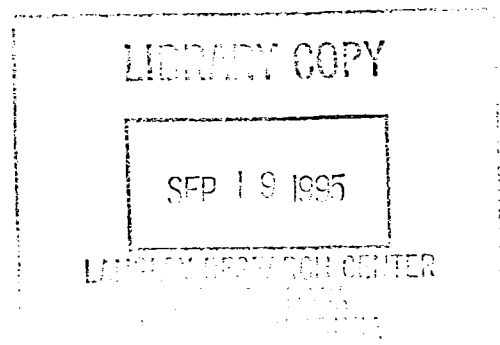
Sandra Marie DeVincent  
*Case Western Reserve University*  
*Cleveland, Ohio*

August 1995

Prepared for  
Lewis Research Center  
Under Cooperative Agreement NCC3-94



National Aeronautics and  
Space Administration







3 1176 01422 7574

**INTERFACIAL EFFECTS ON THE THERMAL AND MECHANICAL PROPERTIES  
OF GRAPHITE/COPPER COMPOSITES**

by

**SANDRA MARIE DeVINCENT**

**Submitted in partial fulfillment of the requirements  
for the degree of Doctor of Philosophy**

**Thesis Advisor: Gary M. Michal**

**Department of Materials Science and Engineering  
CASE WESTERN RESERVE UNIVERSITY**

**January 1994**

# INTERFACIAL EFFECTS ON THE THERMAL AND MECHANICAL PROPERTIES OF GRAPHITE/COPPER COMPOSITES

Abstract

by

SANDRA MARIE DeVINCENT\*

Graphite surfaces are not wet by pure copper. This lack of wetting has been responsible for a debonding phenomenon that has been found in continuous graphite fiber reinforced copper matrix composites subjected to elevated temperatures. By suitably alloying copper, its ability to wet graphite surfaces can be enhanced. Information obtained during sessile drop testing has led to the development of a copper-chromium alloy that suitably wets graphite.

Unidirectionally reinforced graphite/copper composites have been fabricated using a pressure infiltration casting procedure. P100 pitch-based fibers have been used to reinforce copper and copper-chromium alloys. X-ray radiography and optical microscopy have been used to assess the fiber distribution in the cast composites. Scanning electron microscopy and Auger electron spectroscopy analyses were conducted to study the distribution and continuity of the chromium carbide reaction phase that forms at the fiber/matrix interface in the alloyed matrix composites. The effects of the chromium in the copper matrix on the mechanical and thermal properties of P100Gr/Cu composites have been evaluated through tensile testing, three-point bend testing, thermal cycling and thermal conductivity calculations.

---

\*NASA Resident Research Associate at Lewis Research Center.



The addition of chromium has resulted in an increased shear modulus and essentially zero thermal expansion in the P100Gr/Cu-xCr composites through enhanced fiber/matrix bonding. The composites have longitudinal tensile strengths in excess of 700 MPa with elastic moduli of 393 GPa. After 100 hr at 760°C, 84% of the as-cast strength is retained in the alloyed matrix composites. The elastic moduli are unchanged by the thermal exposure.

It has been found that problems with spreading of the fiber tows strongly affect the long transverse tensile properties and the short transverse thermal conductivity of the P100Gr/Cu-xCr composites. The long transverse tensile strength is limited by rows of touching fibers which are paths of easy crack propagation under low tensile loads. The short transverse thermal conductivity is dictated by the fiber/matrix interface. Conduction across this interface has been estimated to be two orders of magnitude lower than that across the composite. This is due to the mechanical, and not chemical, nature of the Gr/Cu bond.



## Acknowledgements

Few accomplishments are achieved without the guidance and support of others. Many helping hands were extended to me during the course of this dissertation. At the NASA Lewis Research Center, I would like to recognize the assistance of Jeannie Taylor, Tony Kapucinski, Mike Miller, Todd Leonhardt, Joe Wagner, Bill Armstrong, Bill Karpinski and Ron Philips. I would also like to acknowledge Dr. Anita Garg for the TEM analysis. Special thanks are owed to Dr. David Ellis, Dr. Robert Miner and Dr. Hugh Gray for their support, both technically and financially.

I would like to recognize Dennis Keller, RealWorld Quality Systems, Inc., for his assistance with the statistical analysis of the longitudinal tensile data.

At Case Western Reserve University, I owe much appreciation to Ranjan Kejriwal, Chris Tuma and Dick Howe for their assistance with the three-point bending set-up and testing. I would also like to express my sincere gratitude to Dr. Wayne Jennings, in the Center for Surface Analysis of Materials, at CWRU, for his assistance with the Auger electron spectroscopy.

I would like to thank the members of my examination committee, Dr. John Lewandowski, Dr. Wendell Williams and Dr. Gary Chottiner, for their support and patience. Sincere thanks for constant interest, enthusiasm and assistance are extended to my advisor, Dr. Gary Michal. During my years at CWRU I have written many papers and done much travelling with him, in addition to having taken a handful of his courses. He is a wonderful teacher. I have learned much from him.

Finally, this research has been supported by the NASA Lewis Research Center in Cleveland, Ohio, through a NASA Graduate Student Researchers Program Fellowship under Grant no. 50-632.

## Table of Contents

Abstract.....	ii
Acknowledgements .....	v
Table of Contents .....	vi
List of Figures .....	xi
List of Tables .....	xvii
<b>1 INTRODUCTION .....</b>	<b>1</b>
<b>1.1 Graphite Fiber Reinforced/Copper Matrix Composites .....</b>	<b>1</b>
1.1.1 Application .....	1
1.1.2 Research and Development.....	3
1.1.2.1 Previous Work .....	3
1.1.2.2 Process Development .....	9
1.1.2.3 Engineering the Interface.....	10
1.1.3 Overview.....	12
<b>2 BACKGROUND .....</b>	<b>14</b>
<b>2.1 Pitch-Based Carbon Fibers .....</b>	<b>14</b>
2.1.1 Processing of Mesophase Pitch Fibers.....	14
2.1.2 Effect of Graphite Structure on Graphite Properties .....	16
2.1.3 Microstructure of Pitch-Based Graphite Fibers .....	18
2.1.4 Effect of Microstructure on Fiber Tensile Properties .....	18
2.1.5 P100 Graphite Fibers.....	21
2.1.5.1 Microstructure and Morphology.....	21
2.1.5.2 Mechanical and Thermal Properties.....	22

2.2	Oxygen-Free High Conductivity Copper.....	25
2.2.1	Processing.....	25
2.2.2	Physical Properties.....	27
2.2.3	Mechanical Properties.....	31
2.2.4	Effect of Impurities and Alloying Elements.....	35
2.3	Liquid Metal Infiltration.....	35
2.3.1	Wetting of Reinforcement by Matrix.....	38
2.3.2	Introduction of Engineered Interface.....	38
2.4	Interfacial Reactions.....	39
2.4.1	Thermodynamics of $\text{Cr}_3\text{C}_2$ Formation.....	39
2.4.2.	Kinetics of $\text{Cr}_3\text{C}_2$ Formation.....	41
2.4.3	Implications for Gr/Cu Composites.....	46
2.5	Failure of Fiber Reinforced Composites.....	47
2.6	Deflection of Straight Beams.....	48
2.7	Thermal Properties.....	51
2.7.1	Heat Capacity.....	51
2.7.2	Thermal Expansion.....	52
2.7.2.1	Expansion Coefficient of Composite Materials.....	53
2.7.2.2	Microstresses.....	54
2.7.3	Heat Conduction.....	54
2.7.4	Thermal Conduction Processes.....	55
2.7.4.1	Thermal Resistivity.....	58
2.7.4.2	Umklapp Process.....	58
2.7.5	Electrical Conductivity.....	59
2.7.6	Thermal Conductivity of Metals.....	60

	2.7.7	Conductivity of Composite Materials.....	62
3		EXPERIMENTAL PROCEDURES .....	65
	3.1	Pressure Infiltration Casting.....	65
	3.1.1	Procedure .....	65
	3.1.2	Materials.....	67
	3.1.3	X-Ray Inspection.....	67
	3.1.4	Plate Machining .....	67
	3.2	Optical Metallography .....	72
	3.3	Scanning Electron Microscopy .....	72
	3.4	Auger Electron Spectroscopy.....	73
	3.5	Transmission Electron Microscopy.....	73
	3.6	Tensile Testing .....	73
	3.6.1	Specimen Design.....	73
	3.6.2	Heat Treatment.....	74
	3.6.3	Test Method .....	74
	3.6.4	Fractography .....	79
	3.6.5	Statistical Analysis.....	79
	3.7	Three-Point Bend Testing .....	80
	3.7.1	Test Method .....	80
	3.7.2	Data Analysis.....	80
	3.8	Thermal Expansion.....	82
	3.9	Thermal Conductivity .....	83
	3.9.1	Specific Heat Measurements.....	83
	3.9.2	Thermal Diffusivity Measurements.....	84
	3.9.3	Thermal Conductivity Calculations .....	84

4	RESULTS.....	85
4.1	X-Ray Inspection .....	85
4.2	Optical Metallography .....	85
4.3	Scanning Electron Microscopy.....	93
4.4	Auger Electron Spectroscopy.....	93
4.5	Transmission Electron Microscopy.....	102
4.6	Tensile Properties .....	102
4.6.1	Longitudinal Tensile Properties.....	102
4.6.2	Long Transverse Tensile Properties.....	110
4.6.3	Fractography .....	110
4.7	Three-Point Bend Properties .....	113
4.8	Thermal Expansion.....	113
4.8.1	Long Transverse Behavior.....	113
4.8.2	Longitudinal Behavior.....	113
4.8.3	Cycling Response Variability.....	118
4.9	Thermal Conductivity .....	129
4.9.1	Heat Capacity .....	131
4.9.2	Thermal Diffusivity .....	131
4.9.3	Thermal Conductivity .....	132
5	DISCUSSION.....	136
5.1	Casting Quality .....	136
5.1.1	Density Variations.....	136
5.1.2	Fiber Distribution.....	137
5.2	Interfacial Reaction Layer Characterization.....	142
5.2.1	Identification of Reaction Layer Phase.....	142

5.2.2	Reaction Layer Continuity .....	142
5.2.3	Fiber/Matrix Adhesion .....	143
5.3	Tensile Properties .....	143
5.4	Bend Properties .....	145
5.5	Thermal Expansion Behavior.....	147
5.6	Thermal Conductivity .....	149
6	CONCLUSIONS .....	156
	REFERENCES .....	159
Appendix I	Statistical Analyses .....	164
Appendix II	Mechanical Properties.....	165



## List of Figures

Figure 1.1	Generic space power system radiator concepts [1] .....	2
Figure 1.2	Comparison of thermal conductivity of Gr/Cu composites with competitive materials [5] .....	6
Figure 1.3	Comparison of specific thermal conductivity of Gr/Cu composites with competitive materials [5] .....	6
Figure 1.4	Comparison of transverse specific thermal conductivity of Gr/Cu composites with competitive materials [5].....	7
Figure 1.5	Comparison of the dynamic modulus of elasticity of Gr/Cu composites to unreinforced OFHC copper [5].....	7
Figure 1.6	Debonding at the interface in hot pressed P100Gr/Cu composite [1] .....	8
Figure 2.1	Schematic of the melt spinning process [20] .....	15
Figure 2.2	Structure of graphite and its approximate orientation in carbon fibers [21].....	17
Figure 2.3	Microstructures of pitch-based carbon fibers [21].....	19
Figure 2.4	Transverse microstructure of graphite fibers [25] .....	20
Figure 2.5	(a) Transverse schematic of an oriented core filament. Three regions: C for chaotic, G for girdle, and T for transitional regions are separated by thick dotted lines and defined on the basis of variations in the nature of layering, which is represented by fine lines. (b) SEM image of fractures P100 fibers. The fibers in the lower right reveal well developed equatorial girdles. In other fibers, the texture is less regular.....	23
Figure 2.6	(a) Fracture surface of P100 graphite fiber revealing orientation of graphene sheets. (b) Higher magnification.....	24
Figure 2.7	OFHC copper production process [36].....	26
Figure 2.8	Elevated temperature electrical conductivity of OFHC copper [37].....	29
Figure 2.9	Elevated temperature electrical resistivity of annealed OFHC copper [33] .....	29
Figure 2.10	Elevated temperature thermal conductivity of annealed OFHC copper [33] .....	30
Figure 2.11	Thermal linear expansion of copper [38].....	30
Figure 2.12	Elevated temperature specific heat of copper [40].....	32
Figure 2.13	Elevated temperature dynamic modulus of elasticity [41] .....	32

Figure 2.14	Effect of annealing on tensile properties of hard drawn copper rod [42] .....	33
Figure 2.15	Effect of annealing on grain size of OFHC copper strip cold rolled 50% [43] .....	33
Figure 2.16	Increase of electrical resistivity of copper with admixtures of various elements [44] .....	34
Figure 2.17	Infiltration of contact area between two fibers by a non-wetting metal [47] .....	37
Figure 2.18	Sessile drop configuration [16] .....	37
Figure 2.19	Cu-Cr phase diagram [52] .....	40
Figure 2.20	Cr-Cr <sub>3</sub> C <sub>2</sub> phase diagram [54] .....	40
Figure 2.21	Simplified sessile drop geometry indicating boundary conditions for determining rate of diffusion of Cr out of liquid Cu [51] .....	42
Figure 2.22	Flux of Cr out of liquid Cu sessile drop at 1130°C. Flux through bottom surface, impermeable top and sides [51] .....	45
Figure 2.23	Reaction layer thickness as a function of time at 1130°C. Controlling growth mechanisms: diffusion of Cr out of liquid Cu and diffusion of C through solid Cr <sub>3</sub> C <sub>2</sub> [51] .....	45
Figure 2.24	Comparison of anisotropic and isotropic shear factors for the deflection of straight beams [63] .....	49
Figure 2.25	Transient heat flow through a cube element [64] .....	56
Figure 2.26	Electrical resistivity as a function of temperature for annealed, dilute, random and binary solid solutions [67] .....	61
Figure 2.27	Parallel slab (laminate) arrangement of two phases [64] .....	63
Figure 3.1	Conceptual schematic of pressure infiltration casting process [68] .....	66
Figure 3.2	P100 graphite fiber orientation in composite plates .....	68
Figure 3.3	Plate machining design indicating all test specimens .....	69
Figure 3.4	Machining specifications for additional long transverse tensile specimens .....	70
Figure 3.5	Long transverse and longitudinal tensile specimen designs .....	75
Figure 3.6	Three-point bend loading configuration .....	81
Figure 4.1	X-ray radiograph of P100Gr/Cu plate Cu-B1P1 with corresponding density measurements .....	86

Figure 4.2	X-ray radiograph of P100Gr/Cu-0.3Cr plate 0.3Cr-B1P2 with corresponding density measurements .....	87
Figure 4.3	X-ray radiograph of P100Gr/Cu-0.7Cr plate 0.7Cr-B1P2 with corresponding density measurements .....	88
Figure 4.4	Short transverse optical micrographs of P100Gr/Cu plates Cu-B1P1 and Cu-B1P4 .....	90
Figure 4.5	Short transverse optical micrographs of P100Gr/Cu-0.3Cr plates 0.3Cr-B1P2 and 0.3Cr-B1P3 .....	91
Figure 4.6	Short transverse optical micrographs of P100Gr/Cu-0.7Cr plates 0.7Cr-B1P2 and 0.7Cr-B1P1 .....	92
Figure 4.7	SEM micrograph of 0.3Cr-B1P3 specimen, etched 45 s, showing small amounts of reaction phase .....	94
Figure 4.8	Higher magnification SEM micrograph of 0.3Cr-B1P3 specimen, etched 45 s, area indicated on Figure 4.7 .....	94
Figure 4.9	SEM micrograph of 0.3Cr-B1P3 specimen, etched 45 s, showing small amounts of reaction phase .....	95
Figure 4.10	SEM micrograph of 0.3Cr-B1P3 specimen, etched 45 s, showing continuous reaction phase in matrix-rich region .....	95
Figure 4.11	SEM micrograph of 0.7Cr-B1P1 specimen, etched 45 s, showing continuous reaction phase in matrix-rich regions .....	96
Figure 4.12	SEM micrograph of 0.7Cr-B1P1 specimen, etched 45 s, showing areas of both continuous and discontinuous reaction phase .....	96
Figure 4.13	SEM micrograph of 0.7Cr-B1P1 specimen, etched 45 s, showing continuous reaction phase of 0.2-0.3 $\mu\text{m}$ thickness .....	97
Figure 4.14	Higher magnification SEM micrograph of 0.7Cr-B1P1 specimen, etched 45 s, area indicated in Figure 4.13 .....	97
Figure 4.15	SEM micrograph of 0.7Cr-B1P1 specimen, etched 45 s, showing areas where P100 fibers are covered by particles of reaction phase .....	98
Figure 4.16	Higher magnification SEM micrograph of 0.7Cr-B1P1 specimen, etched 45 s, area indicated in Figure 4.15 .....	98
Figure 4.17	AES micrograph of 0.7Cr-B1P2 P100Gr/Cu-0.7Cr specimen indicating area of elemental Cr analysis .....	99
Figure 4.18	AES elemental Cr map of 0.7Cr-B1P2 P100Gr/Cu-0.7Cr specimen showing Cr segregation to the fiber surface .....	99

Figure 4.19	AES micrograph of 0.7Cr-B1P2 P100Gr/Cu-0.7Cr specimen indicating areas of elemental Cr map and line scan analysis .....	100
Figure 4.20	AES elemental Cr map of 0.7Cr-B1P2 P100Gr/Cu-0.7Cr specimen showing Cr segregation to the fiber surface.....	100
Figure 4.21	AES line scan for Cu, C, Cr and O taken over the 0.7Cr-B1P2 P100Gr/Cu-0.7Cr interfacial region as indicated in Figure 4.19 .....	101
Figure 4.22	TEM micrograph of reaction phase. Layer is measured to be 1700-2400 Å in thickness.....	103
Figure 4.23	Selected area diffraction pattern taken in a region containing Cu matrix and reaction phase. Reaction phase identified to be $\text{Cr}_3\text{C}_2$ .....	103
Figure 4.24	Shear failure of P100Gr/Cu-xCr composite longitudinal tensile specimen .....	104
Figure 4.25	Stress-strain curve of P100Gr/Cu longitudinal tensile specimen (Cu-B1P1-N) .....	105
Figure 4.26	As-cast P100Gr/Cu-xCr longitudinal tensile strength: 0°TS (MPa) .....	106
Figure 4.27	As-cast P100Gr/Cu-xCr longitudinal elastic modulus: E (GPa).....	107
Figure 4.28	Heat treated (760°C) P100Gr/Cu-xCr longitudinal tensile properties: 0°TS (MPa)....	108
Figure 4.29	Average as-cast and heat treated (760°C) P100Gr/Cu-xCr longitudinal tensile properties: 0°TS (MPa), E (GPa).....	109
Figure 4.30	As-cast P100gr/Cu-xCr long transverse tensile strength: 0°TS (MPa) .....	111
Figure 4.31	SEM micrograph of P100Gr/Cu-0.7Cr long transverse tensile fracture (0.7Cr-B1P1-E) showing separation of P100 fibers from matrix (complete debonding).....	112
Figure 4.32	SEM micrograph of P100Gr/Cu-0.7Cr long transverse tensile fracture (0.7Cr-B1P1-E) showing small particles of reaction phase.....	112
Figure 4.33	Load vs. displacement in three-point bending for P100Gr/Cu-0.3Cr composite .....	114
Figure 4.34	Slope vs. span length for three-point bending of P100Gr/Cu composite.....	115
Figure 4.35	Slope vs. span length for three-point bending of P100Gr/Cu-0.3Cr composite.....	116
Figure 4.36	Slope vs. span length for three-point bending of P100Gr/Cu-0.7Cr composite.....	117
Figure 4.37	Long transverse thermal expansion behaviors of P100Gr/Cu-xCr composites as compared to those of Cu and pyrolytic Gr .....	119
Figure 4.38	Longitudinal thermal expansion behavior of P100Gr/Cu composite as compared to those of Cu and P100 Gr fiber.....	120
Figure 4.39	Longitudinal thermal expansion behavior of P100Gr/Cu-0.3Cr.....	121

Figure 4.40	Longitudinal thermal expansion behavior of P100Gr/Cu-0.7Cr.....	122
Figure 4.41	Comparison of the initial longitudinal thermal cycle of the P100Gr/Cu-xCr composites with varying matrix compositions .....	123
Figure 4.42	P100Gr/Cu (B1) longitudinal thermal expansion .....	124
Figure 4.43	P100Gr/Cu (B1) long transverse thermal expansion.....	124
Figure 4.44	P100Gr/Cu (B2) longitudinal thermal expansion .....	125
Figure 4.45	P100Gr/Cu (B2) long transverse thermal expansion.....	125
Figure 4.46	P100Gr/Cu-0.3Cr (B1) longitudinal thermal expansion .....	126
Figure 4.47	P100Gr/Cu-0.3Cr (B1) long transverse thermal expansion.....	126
Figure 4.48	P100Gr/Cu-0.3Cr (B2) longitudinal thermal expansion .....	127
Figure 4.49	P100Gr/Cu-0.3Cr (B2) long transverse thermal expansion.....	127
Figure 4.50	P100Gr/Cu-0.7Cr (B1) longitudinal thermal expansion .....	128
Figure 4.51	P100Gr/Cu-0.7Cr (B1) long transverse thermal expansion.....	128
Figure 4.52	Short transverse specific heat of P100Gr/Cu-xCr composites.....	133
Figure 4.53	Short transverse thermal diffusivity of P100Gr/Cu-xCr composites .....	134
Figure 4.54	Short transverse thermal conductivity of P100Gr/Cu-xCr composites.....	135
Figure 5.1	Ideally close-packed bundle of fibers of radius $r$ .....	138
Figure 5.2	P100 2K fiber tow packing configurations: (a) parallel arrays, no strain, (b) close-packed, no strain, (c) close-packed, strain due to wrapping .....	140
Figure 5.3	Proposed laminate construction: 20% Cu - 80% P100Gr/Cu composite. Plate average of 56% P100 fiber $\Rightarrow$ P100Gr/Cu composite phase of 70% fiber .....	141
Figure 5.4	P100Gr/Cu-xCr transverse (90°) loading configurations showing path of crack propagation.....	146
Figure 5.5	Short transverse thermal conductivity of P100Gr/Cu-xCr composites.....	151
Figure 5.6	Calculated effective transverse thermal conductivity of the P100 fibers + "interface"..	151
Figure 5.7	Orientation of P100 fibers in P100Gr/Cu-xCr composite with respect to direction of heat flow.....	152

Figure 5.8	Calculated transverse thermal conductivity of the "interface" ( $k_{Gr} = 2.6 \text{ W/cm-K}$ ) ....	153
Figure 5.9	Calculated transverse thermal conductivity of the "interface" ( $k_{Gr} = 1.3 \text{ W/cm-K}$ ) ....	153
Figure 5.10	Comparison of short transverse thermal conductivity of individual components .....	155
Figure 5.11	Parallel slab illustration of P100Gr/Cu-xCr composite components .....	155

## List of Tables

Table 2.1	Physical properties of Thornel P100 fibers [31] .....	22
Table 2.2	Composition and property limits of OFHC copper [33] .....	27
Table 2.3	Physical properties of OFHC copper.....	28
Table 2.4	Room temperature mechanical properties of OFHC copper sheet [33, 35] .....	35
Table 3.1	P100Gr/Cu-xCr composite plate identification and descriptions.....	71
Table 3.2	Long transverse tensile test matrix.....	76
Table 3.3	Longitudinal tensile test matrix - P100Gr/Cu.....	77
Table 3.4	Longitudinal tensile test matrix - P100Gr/Cu-0.3Cr.....	78
Table 3.5	Longitudinal tensile test matrix - P100Gr/Cu-0.7Cr.....	79
Table 3.6	Thermal expansion test matrix.....	82
Table 3.7	Thermal conductivity measurement specimens.....	83
Table 4.1	Plate-to-plate and batch-to-batch variations (S = standard deviation) .....	89
Table 4.2	Thermal expansion test specimen summary .....	129
Table 4.3	Data used for thermal conductivity calculations .....	130





## 1 INTRODUCTION

### 1.1 Graphite Fiber Reinforced/Copper Matrix Composites

#### 1.1.1 Application

The increasing size and complexity of space-based hardware will lead to higher power consumption demands for future spacecraft and satellites. Although several types of advanced power systems are under consideration, they all have a heat source and a power conversion system. The power conversion systems require high temperature operation and an efficient, minimum-mass heat rejection radiator system.

Several designs for space power radiators exist. Figure 1.1 illustrates a generic continuous fin radiator concept and a generic separate fin concept [1]. Excess heat from the power conversion system is sent to the radiator along a titanium heat pipe which is brazed directly to a radiator panel or fin. The panel both radiates heat directly and conducts the heat to a cooler area of the panel surface for radiation into space. The operating temperatures of the radiators depend on the type of heat source employed [2]. Space power systems with solar heat sources have an operating temperature range of 300 to 600 K (27 to 327°C). Power systems with nuclear heat sources have operating temperatures as high as 1000 K (727°C). Current designs call for beryllium, niobium or titanium alloys as radiator panel materials. However, each of these materials has drawbacks. Beryllium is lightweight and has a high modulus, but has safety, cost and handling problems. Niobium and titanium alloys have good high temperature properties, but are poor thermal conductors.

Compared with conventional metals, metal matrix composites containing high modulus graphite fiber reinforcement can provide both weight savings and greater strength and stiffness [3]. These composites are especially attractive for thermal management systems. Ultra high modulus pitch-based graphite fibers, with an elastic modulus of 758 GPa (110 Msi) or greater, have recently been developed. These fibers have thermal conductivities, along the axis of the fiber, better than that

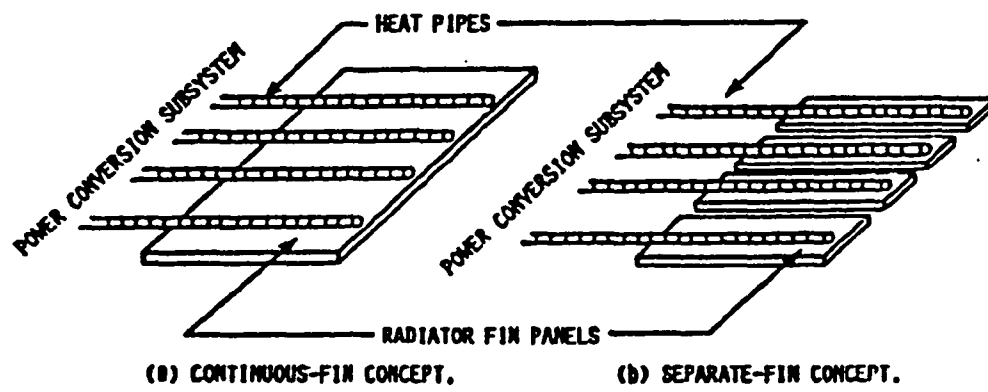


Figure 1.1. Generic space power system radiator concepts [1].

of copper. They also possess a similar density to and greater elastic modulus than beryllium. Using these ultra-high modulus fibers to reinforce a copper matrix offers potential to produce lightweight, high modulus, high thermal conductivity composite materials for space radiator applications. A preliminary design analysis study [4] has estimated that a graphite/copper (Gr/Cu) composite radiator could offer the same performance as a beryllium panel with a mass savings of up to 9 percent for an SP-100 radiator.

### 1.1.2 Research and Development

#### 1.1.2.1 Previous Work

An exploratory study was conducted to determine the feasibility of Gr/Cu composites for space power radiator applications [1]. This study evaluated a limited amount of vendor-supplied and NASA Lewis fabricated Gr/Cu composites. The focus of the investigation included the key factors involved in the design of space power radiator panels. Specific thermal conductivity and specific modulus of elasticity were investigated over a wide range of temperatures.

The Gr/Cu composites tested in this study were fabricated using unidirectionally oriented pitch-based P100 graphite fibers produced by Amoco Performance Products. The P100 fiber is supplied in tows, each containing approximately 2000 individual fibers of about 10  $\mu\text{m}$  in diameter. The P100 tow had a nominal modulus of elasticity of 690 GPa, an ultimate tensile strength of 2070 MPa and a density of 2.15  $\text{kg/m}^3$ . Gr/Cu experimental panels were purchased from DWA Composite Specialties. Panels were also fabricated at NASA Lewis Research Center by hot pressing copper coated P100 graphite fibers supplied by American Cyanamid Corporation.

The longitudinal thermal conductivities of the materials tested at temperatures up to 1100K (827°C) are shown in Figure 1.2. The unreinforced OFHC (oxygen free, high conductivity) copper and the NASA fabricated Gr/Cu composite were tested by the laser-flash method. The unreinforced copper lost about 10% of its room temperature thermal conductivity at 1100K. This reduction appears to be linear with temperature. Also indicated on this plot are handbook values for beryllium,

which has approximately one-third of the thermal conductivity of unreinforced OFHC copper over this temperature range.

The NASA fabricated 67 volume percent (v/o) composite panel exhibits similar thermal conductivity to unreinforced copper over the entire temperature range investigated. The composite lost about 20% of its room temperature thermal conductivity by 1100K. Most of this loss occurred at temperatures below 600K (327°C). Above 600K, the reduction paralleled that of the unreinforced copper.

Longitudinal thermal conductivity of the DWA 38 v/o Gr/Cu-Ti composite, measured by the steady-state comparative-rod technique, is less than half that of the NASA fabricated composite. Although the composites contain different volume fractions of fibers, the thermal conductivity properties can still be compared. Because the thermal conductivity of P100 graphite, along the fiber axis, is about the same as that of copper, the longitudinal thermal conductivity of the P100 Gr/Cu composites should be independent of fiber content. Deviations can therefore be attributed to matrix effects. The low thermal conductivity of the DWA supplied composite is most likely due to the titanium addition. Although this addition increased the strength of the matrix and improved the fiber/matrix interfacial bond, it substantially reduced the thermal conductivity of the copper matrix. The DWA composite showed a similar rate of reduction with temperature as both the NASA fabricated composite and the unreinforced copper.

While Gr/Cu composites exhibit excellent thermal conductivity in the longitudinal direction (parallel to the fibers), the thermal conductivity in the short-transverse direction (through-the-thickness) is considerably lower. In this orientation, the NASA fabricated composite has a thermal conductivity of only 60 W/mK at room temperature. This is about one-seventh that in the longitudinal direction.

The density dependent, specific thermal conductivity is one of the most important design considerations for space power radiator systems. The longitudinal specific thermal conductivity of

the Gr/Cu composites is plotted as a function of temperature in Figure 1.3. The values for copper and beryllium are included for comparison. The results for the composite, in the longitudinal direction, are significantly better than those for copper over the temperature range considered, and are better than those for beryllium at higher temperatures. These data indicate that Gr/Cu composites offer good potential for high specific thermal conductivity applications at elevated temperatures, as long as the heat can be conducted in the direction of the reinforcing fibers.

As indicated in Figures 1.2 and 1.3, the short transverse thermal conductivity of the Gr/Cu composites is much lower than the longitudinal. While this may appear discouraging, it must be noted that space power radiator systems operate at temperatures above the maximum service temperatures of copper and beryllium. The primary competition at elevated temperatures is titanium and niobium alloys. Figure 1.4 compares the short transverse specific thermal conductivity of the composite to Ti-6Al-4V and Nb-1Zr alloys. The plot shows that the NASA fabricated composite has better short-transverse specific thermal conductivity properties than the niobium alloys over the entire temperature range, and the titanium alloys at temperatures up to 700K (427°C). This temperature approaches the upper service temperature limit for titanium alloys. Because the titanium alloys do not have sufficient strength at these temperatures, Gr/Cu composites have better properties than both of these alloys at all usable temperatures.

Another important design criterion for space power radiator systems is modulus of elasticity. The specific modulus is even more critical because the vibrational frequency of a space power radiator is proportional to the square root of the modulus/density ratio. Dynamic modulus of elasticity, in the longitudinal direction, of P100 Gr/Cu composites was measured over a range of temperatures. Sonic flexural resonance techniques were employed. The results for the NASA fabricated and DWA supplied composites are given in Figure 1.5, along with data for unreinforced copper. The two composites showed essentially no loss of modulus at temperatures up to 650K (377°C). Unreinforced copper, on the other hand, lost almost 10% of its room temperature modulus by 500K (227°C).

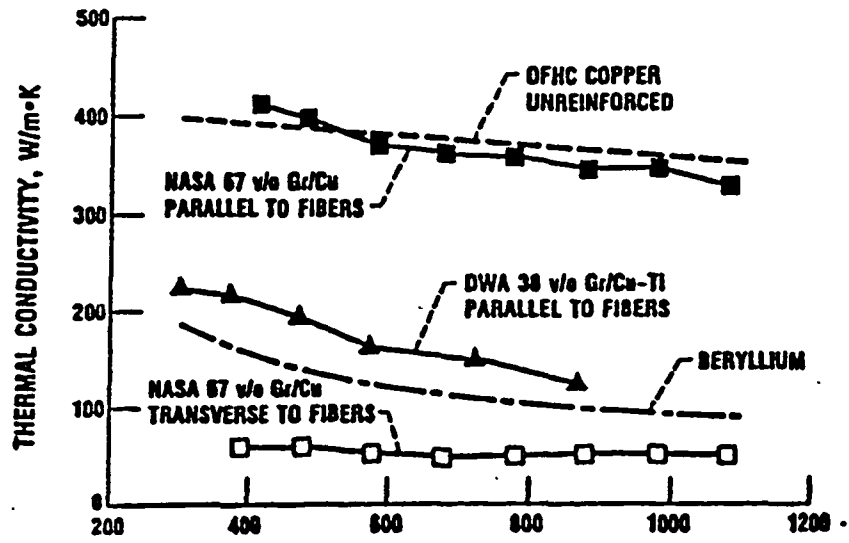


Figure 1.2. Comparison of thermal conductivity of Gr/Cu composites with competitive materials [5].

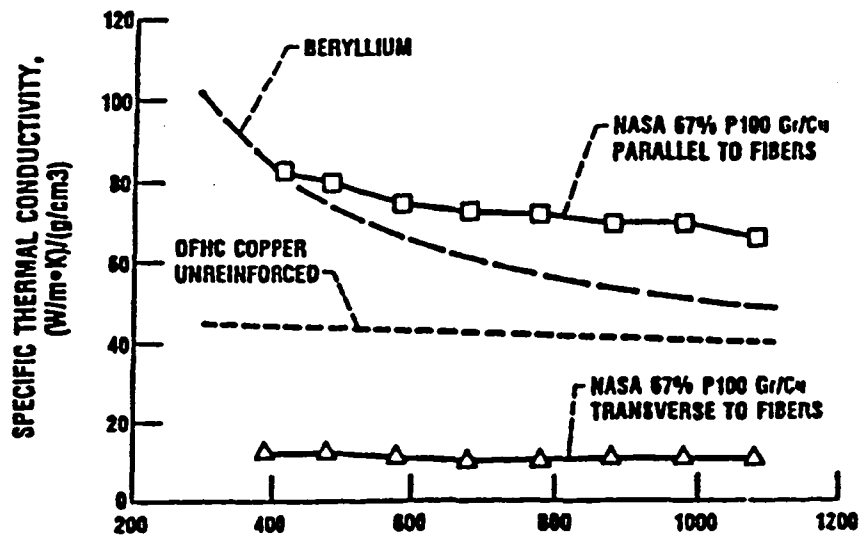


Figure 1.3. Comparison of specific thermal conductivity of Gr/Cu composites with competitive materials [5].

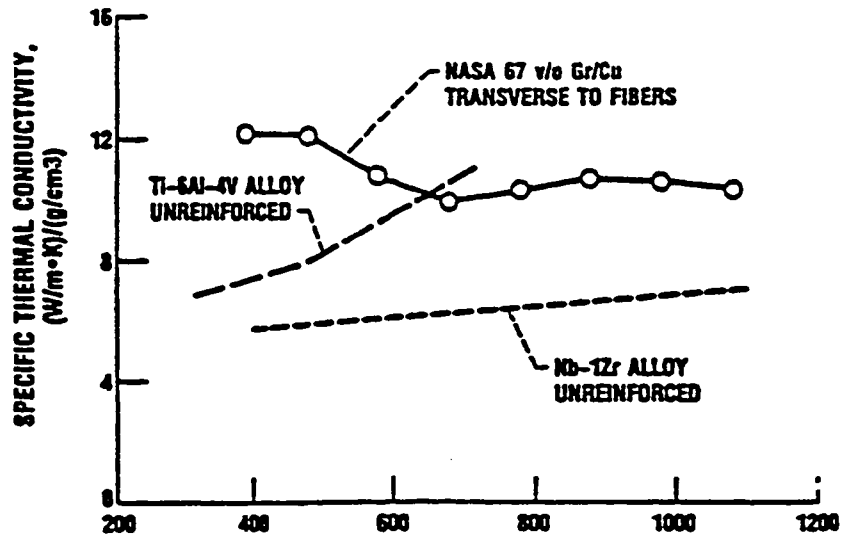


Figure 1.4. Comparison of transverse specific thermal conductivity of Gr/Cu composites with competitive materials [5].

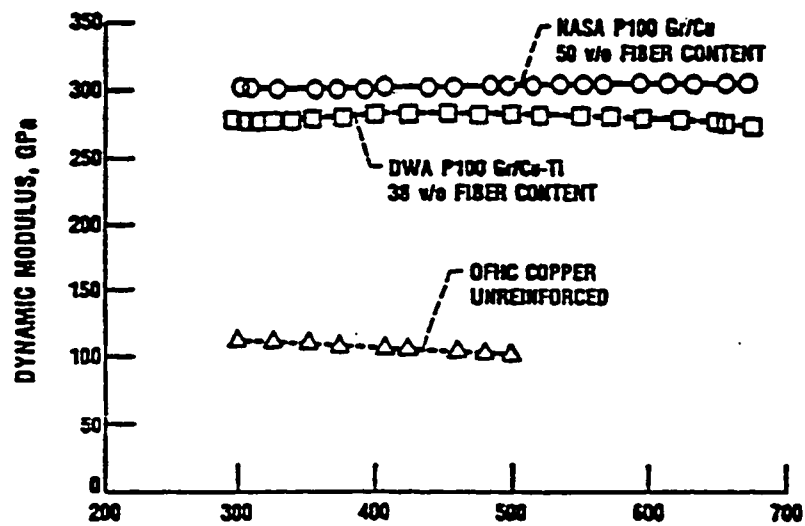


Figure 1.5. Comparison of the dynamic modulus of elasticity of Gr/Cu composites to unreinforced OFHC copper [5].

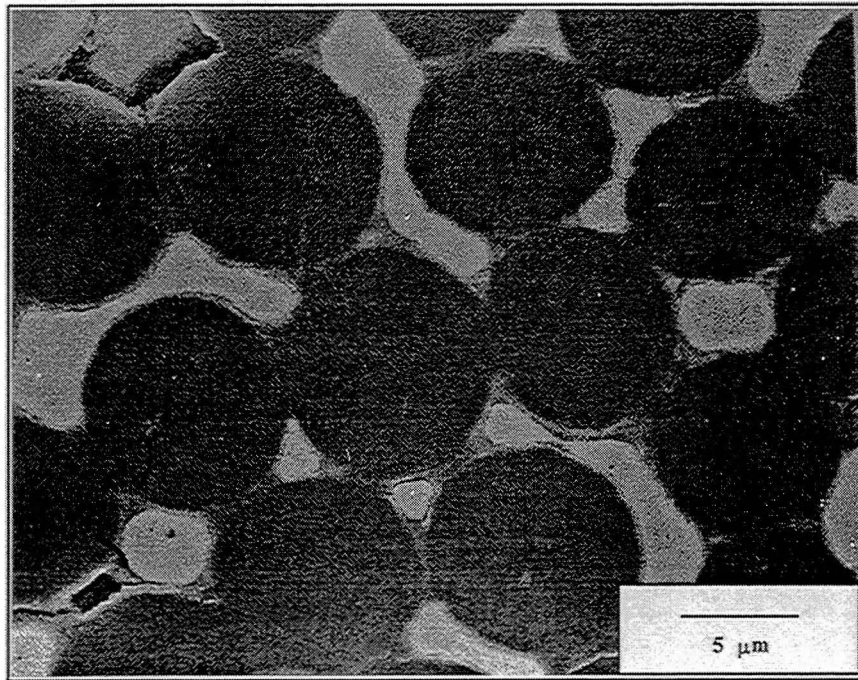


Figure 1.6. Debonding at the interface in hot pressed P100Gr/Cu composite [1].



From a design viewpoint, the retention of modulus at elevated temperatures is desired because the structural stiffness of the composite can be maintained during operation. The high modulus/density ratio allows the design of a structure such that the fundamental frequency can be safely above the natural frequency of the space platform, thus eliminating problems associated with unexpected resonances. Although the properties of Gr/Cu composites were shown to be promising, a debonding phenomenon was found to occur after exposure to elevated temperatures, as shown in Figure 1.6. The lack of wetting of the fiber reinforcement by the copper matrix left the long term stability of these composites in question.

#### 1.1.2.2 Process Development

Powder metallurgy processing techniques have been utilized to produce Gr/Cu composites containing 5 wt% Ni and 0.2-4 wt% Cr in the copper matrix [6]. The method involves the incorporation of 20 vol% P55 graphite fibers in a foam made from an aqueous suspension of fine powders. The composite was consolidated by hot pressing. A uniform fiber distribution was achieved with little fiber contact or porosity. Subsequent exposure to high temperatures, however, resulted in interface decohesion with the formation of cavities around the fibers by coalescence of the decohered areas. A composite sample exposed to 900°C for 1 hr showed substantial cavity formation, which led to macroscopic swelling of the sample and porosity on the order of 12.5%. The authors suggest that the cavity formation was due to thermal expansion stresses, which when high enough, can cause the opening of voids by decohesion at the interface. Investigation of the fracture surfaces revealed extensive fiber pullout, indicative of low interfacial adhesion. Improvements in interfacial adhesion were obtained by the introduction of chromium to the Cu-5Ni matrix. This was due to the formation of a carbide layer at the fiber/matrix interface. While the formation of a reaction phase at the interface showed some improvement in properties, fiber damage was observed because of the large thickness of the phase (up to 10  $\mu\text{m}$ ). Cracking of the fibers and interface cracks limit the performance of these powder metallurgy processed Gr/Cu composites.

Pressure infiltration casting techniques were first utilized to produce Gr/Cu composites only a few years ago [7]. These cast composites were produced by PCast Equipment Corporation using both high stiffness and high strength graphite fibers. During the early stages of development of cast Gr/Cu composites, many problems were identified. The initial castings revealed a nonuniform fiber distribution, difficulty separating the fibers within a tow, void formation and shrinkage porosity, and incomplete infiltration. Poor pressure control, solidification rate control and mold design were identified as possible causes for these problems.

During the course of this dissertation, process parameters were identified to produce sound Gr/Cu castings with fair fiber distributions. These criteria are most easily met for composite systems having high volume fractions ( $>50\%$ ) of large diameter ( $>7\text{ }\mu\text{m}$ ) fiber reinforcement. Many problems still exist for the fabrication of  $<7\text{ }\mu\text{m}$  diameter fiber reinforced composites [8].

#### 1.1.2.3 Engineering the Interface

Research conducted in the area of improving Gr/Cu interfacial bonding has fallen into two focus areas: 1. alloying the Cu matrix, and 2. coating the Gr fibers. Enhanced wetting of the Gr fibers by the matrix has supplied the impetus for these approaches. Improved bonding is expected through chemical reactions at the Gr/Cu interface.

The alloyed matrix and fiber coating processes have both advantages and disadvantages associated with them. By the addition of a second element to the Cu matrix, increased wetting and bonding of the matrix to the Gr fibers can be achieved. This better bonding increases the ability for load transfer to the fibers. This results in improved mechanical properties and stable thermal cycling behavior of the Gr/Cu composites [8]. On the other hand, the addition of an alloying element decreases the thermal conductivity of the Cu matrix [9]. This is primarily due to residual solute present in the Cu matrix after diffusion to and chemical reaction with the Gr fibers. This will decrease the short-transverse (perpendicular to the fibers) thermal conductivity.

By coating the Gr fibers prior to composite fabrication, the location of the addition can be controlled. This will result in minimal decrease in matrix thermal conductivity and therefore in better short-transverse thermal conductivity. The coating process, however, adds an extra handling step and expense. There is also concern of degradation of the fibers due to extensive chemical reaction with the coating.

Prior to this investigation, limited work had been conducted in the area of Gr/Cu interfaces. Perhaps the most widely referenced study has been that of Mortimer and Nicholas [10, 11, 12]. They have reported that small additions of Cr reduce the contact angle formed, during sessile drop studies, by Cu molten on HX30 Gr and vitreous carbon in studies conducted in vacuum. Through metallographic examination, they found the presence of reaction products at the interfaces of the Gr/Cu-Cr alloy samples. Four types of reaction products were identified: continuous layers of uniform thickness, discontinuous layers of nearly uniform thickness, flaky layers partly detached from the carbon substrate and interfacial areas containing many small particles. The reaction product of a Cu-1at%Cr alloy was continuous, and quantitatively determined to be  $\text{Cr}_3\text{C}_2$ .

For sessile drop experiments conducted under conditions where a continuous reaction layer forms, the appropriate form of the Young-Dupre equation is as follows [10]:

$$\gamma_{SV_{\text{carbide}}} = \gamma_{LV_{\text{alloy}}} \cos \theta_{\text{carbide/alloy}} + \gamma_{SL_{\text{carbide/alloy}}} \quad (1.1)$$

where  $\gamma_{SV_{\text{carbide}}}$  is the carbide/vapor interfacial energy,  $\gamma_{LV_{\text{alloy}}}$  is the alloy/vapor interfacial energy,  $\theta_{\text{carbide/alloy}}$  is the contact angle between the carbide and the alloy and  $\gamma_{SL_{\text{carbide/alloy}}}$  is the carbide/alloy interfacial energy. The values for  $\gamma_{LV_{\text{alloy}}}$  for Cu-Cr alloys are not known, but are assumed to be less than or equal to that of the interfacial energy of pure Cu and its vapor,  $\gamma_{LV_{\text{Cu}}}$ . The value for  $\gamma_{LV_{\text{Cu}}}$  has been determined as a function of temperature [13].

Mortimer and Nicholas [12] and Ramqvist [14] have conducted sessile drop tests of Cu on  $\text{Cr}_3\text{C}_2$  substrates. Both investigations measured a wetting angle of 45 to 50°. This contrasts with nonwetting angles of approximately 140° observed for pure Cu sessile drops on graphite substrates [10]. From their studies, Mortimer and Nicholas estimated the interfacial energy of  $\text{Cr}_3\text{C}_2$  to its vapor to be 975 to 1070 mJ/m<sup>2</sup> [11, 12].

Nogi et al. [15] have conducted similar sessile drop experiments in an Ar-5H<sub>2</sub> atmosphere with Cu alloys on single crystal Gr substrates. They also concluded that Gr is wet by Cu-Cr alloys when the Cr content is high enough to create a continuous reaction layer at the interface.

In a more recent study [16], sessile drop tests were conducted on twelve Cu-based alloys to determine if the wetting of Gr by liquid Cu can be improved through alloying additions. Of the alloys studied, additions of Fe, La, Mn, Nb, Si, Ta and Ti did not wet H-490 Gr at the alloying levels examined. The additions of Hf, Y and Zr decreased the wetting angles, but did not reduce the angles to much below 111° at the alloying levels investigated. The additions of Cr and V at approximately the level of 1 at% were able to enhance the wetting behavior such that wetting angles of 45°, or less, were produced. However, because of the difficulties of dissolving V in liquid Cu, a temperature of 1530°C was needed to achieve that degree of wetting. This renders the Cu-V alloy systems impractical for fabrication processes.

The Gr/Cu interfacial energy is affected by alloying additions that change the contact angle of the system. The addition of greater than 1 at% Cr results in a  $\text{Cr}_3\text{C}_2$ /Cu interfacial energy as low as 10 mJ/m<sup>2</sup>. Although additions of about 1 at% of either Cr and V lower the contact angle to 45°, Cr is more effective in lowering the interfacial energy of the system per at% addition.

### 1.1.3 Overview

This study has determined the effects of the presence of the  $\text{Cr}_3\text{C}_2$  reaction layer phase on the thermal and mechanical properties of pressure infiltration cast Gr/Cu composites. Through metallographic and microscopic investigations, the presence and continuity of the reaction phase at

the fiber/matrix interface have been assessed. The influence of the alloyed matrix, copper-chromium, on the room temperature tensile, three-point bend, thermal expansion and thermal conductivity properties of unidirectionally reinforced Gr/Cu composites has been quantified. Explanation for the behavioral trends have been given with reference to the nature of the bond at the fiber/matrix interface.

## 2 BACKGROUND

### 2.1 Pitch-Based Carbon Fibers

Mesophase pitch-based carbon fibers have been recognized as strategic materials for the near future because of their high performance-to-weight ratio [17], particularly for use in space environments [18]. Since 1980, ultrahigh modulus pitch-based fibers have been developed for use in aircraft and spacecraft structures [19]. The important properties of these fibers include high mechanical stiffness, tensile strength, thermal stability, thermal conductivity (along the fiber axis), low coefficient of thermal expansion and electrical conductivity.

#### 2.1.1 Processing of Mesophase Pitch Fibers

The production of high modulus pitch-based carbon fibers was first developed by Singer of Union Carbide in 1970 [19]. The basic idea was to advance the pitch raw material to a mesophase, or liquid crystal pitch, which was capable of orientation through flow and shear. The mesophase pitch could then be melt spun and drawn into fine filaments. The result was molecular constituents that were highly oriented and retained that orientation throughout all subsequent processing. This process was commercialized by Union Carbide in 1974-75 with the introduction of Thornel P-55 (pitch-based fiber,  $E = 55$  Msi). Ultrahigh modulus fibers (elastic moduli of 690-830 GPa) were later developed and commercially produced in 1980-82.

The production of mesophase pitch-based fibers begins with the conversion of a coal-tar or petroleum pitch feed stock into a liquid crystalline or mesophase state through thermal treatment. This highly ordered, deformable liquid is then extruded in a melt spinning process to form a precursor fiber. Stretching of the precursor fiber is not necessary due to the high degree of molecular orientation that is gained in the pitch filament during melt spinning. After spinning, the pitch-based fiber is thermoset and then carbonized. Figure 2.1 details a typical melt spinning process and the process variables which must be controlled [20]. Generally the precursor is melted in an extruder

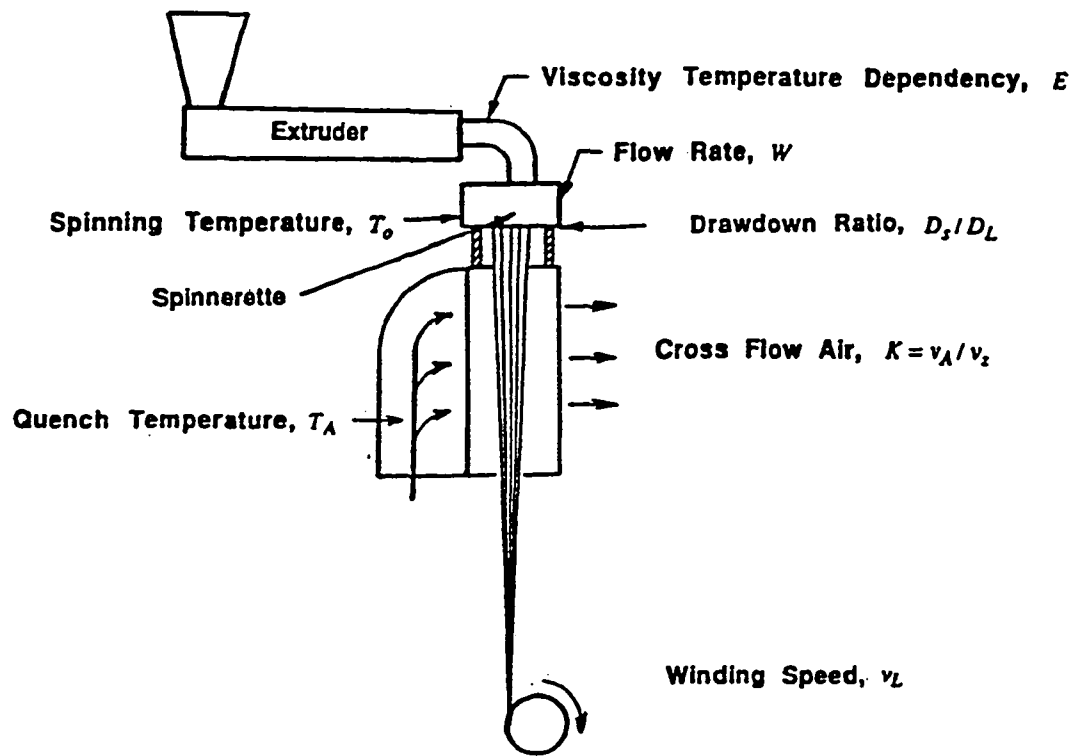


Figure 2.1. Schematic of the melt spinning process [20].

which then pumps the melt into a spin pack which contains a filter for removing small particles from the melt. Once it has passed through the filter, the melt exits the bottom of the spin pack through a spinnerette, cools and forms a filament. An air quench is often used. The solidified fiber is then wound onto a spinning spool.

### 2.1.2 Effect of Graphite Structure on Fiber Properties

Carbon fibers are composed of 99.9% pure carbon, most of which is arranged into graphite crystallites. These crystallites tend to organize into layers, and the mechanical properties of carbon fibers are a result of this structure. Figure 2.2 shows the layer plane structure and the corresponding dimensions of graphite [21]. The orientation of the crystallites within the carbon fibers is also shown. Within the layers, covalent bonds link the carbon atoms in the crystallographic *a*-direction [22]. These anisotropic, nonpolar  $\sigma$ -bonds, created by the  $sp^2$  hybridization of the electron orbitals in the carbon layers, make the graphite structure extremely strong in the *a*-direction. As a result, the theoretical tensile modulus and ultimate tensile strength of graphite along its axis are very high, approximately 1000 GPa and 100 GPa, respectively [23]. Conversely, the weak van der Waals bonding that exists between atoms in adjoining planes makes the mechanical properties in the *c*-direction quite low. The theoretical modulus, normal to the *a*-direction, is only 35 GPa [21]. This results in a high degree of anisotropy in most properties including thermal and electrical conductivity.

As shown in Figure 2.2, the structure of the graphite crystallites in carbon fibers is not perfect. The layer planes are slightly offset, creating what is referred to as turbostratic graphite [24]. A small increase in the interlayer spacing, 3.37-3.45 Å compared to 3.35 Å found in a perfect crystal, accompanies this offset. The orientation of the graphite layers is nearly parallel to the fiber axis. The strong covalent bonding within these layer planes accounts for the longitudinal properties in carbon fibers.

At present, commercial pitch-based carbon fiber is available with a tensile modulus which is 85% of the theoretical maximum. The tensile strength, however, is only 5% of that theoretically



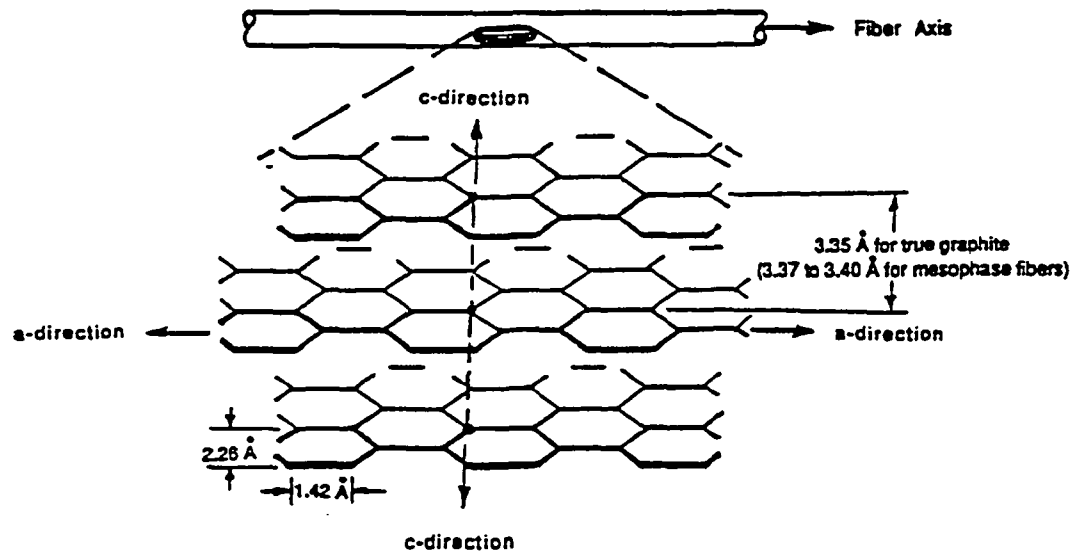


Figure 2.2. Structure of graphite and its approximate orientation in carbon fibers [21].

possible. The strength of a fiber is essentially limited by the number and size of flaws in the structure. These will range from the local misalignment of atomic planes to the inclusion of foreign particles and voids.

### 2.1.3 Microstructure of Pitch-Based Graphite Fibers

Unlike other varieties of carbon fibers, the pitch-based fibers exhibit a variety of microstructures. These varieties, as shown in Figure 2.3, are obtained by varying the spinning conditions of the liquid crystalline precursor [21]. Commercial mesophase pitch-based fibers commonly exhibit either radial, flat-layer or random microstructures. Each type of microstructure, except for random, can be considered a collection of large flat sheets, extending down the fiber axis, arranged in some geometric fashion across the fiber cross section.

Other terminology, including some combinations of microstructures, has been proposed to describe the configuration of graphite basal planes in the transverse plane of the fiber. Idealized orientations include circumferential, radial and random. Figure 2.4 contains schematic illustrations of five possible microstructures for graphite fibers. Most fibers are found to exhibit more than one type of morphology in their cross section and will contain both orthotropic and isotropic configurations. Typically, pitch-based fibers reveal a radial alignment of the basal planes [25].

### 2.1.4 Effect of Microstructure on Fiber Tensile Properties

The theoretical Young's modulus of graphite is estimated to be 1000 GPa. A well established correlation exists between preferred orientation and Young's modulus - the more highly oriented the layer planes in the carbon fiber, the higher the elastic modulus. Because the energy required to align the layer planes in a graphitizing material such as a carbon fiber from mesophase pitch is not that great, very high moduli can be obtained [26, 27].

The theoretical tensile strength of a solid is more difficult to estimate than the modulus. The Orowan-Polanyi expression [28]:

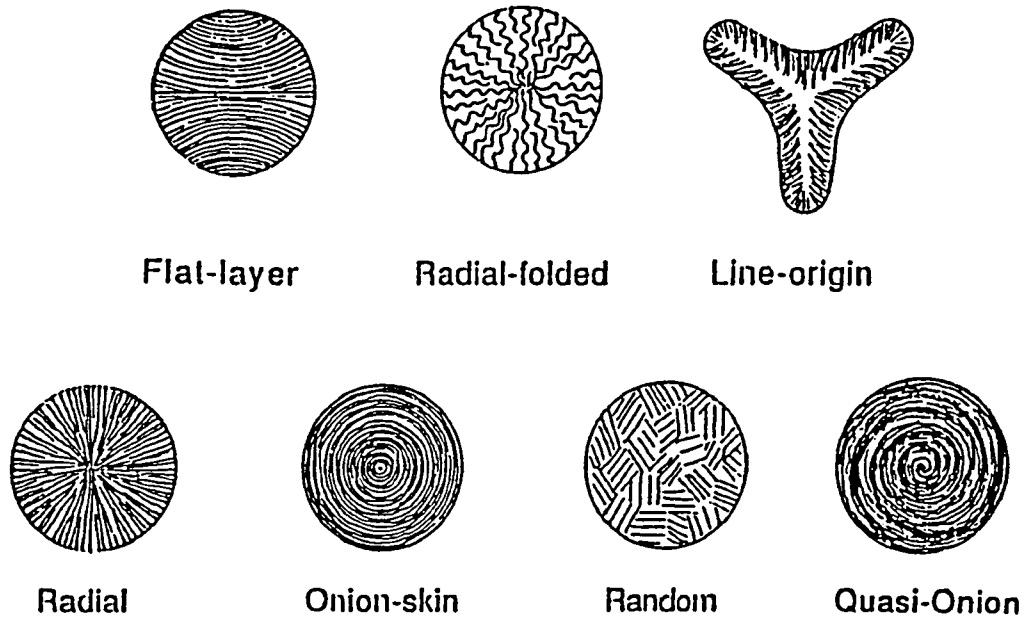
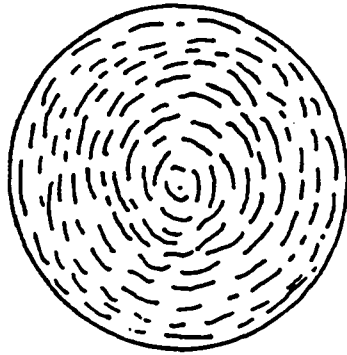
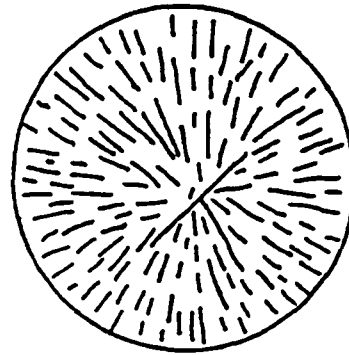


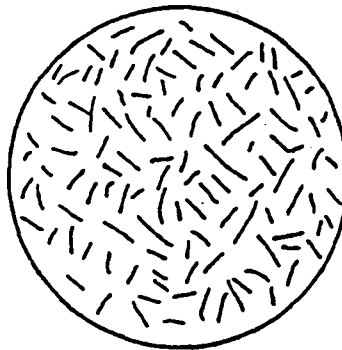
Figure 2.3. Microstructures of pitch-based carbon fibers [21].



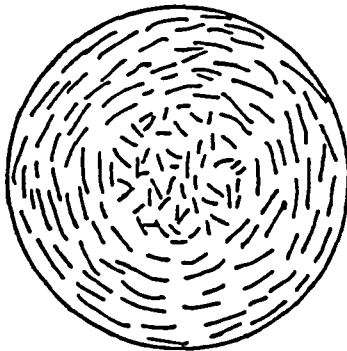
**(a) Circumferentially Orthotropic**



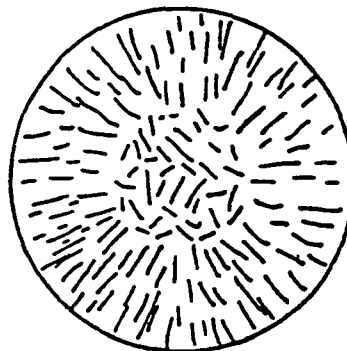
**(b) Radially Orthotropic**



**(c) Transversely Isotropic**



**(d) Circumferentially Orthotropic  
with Transversely Isotropic Core**



**(e) Radially Orthotropic  
with Transversely Isotropic Core**

Figure 2.4. Transverse microstructure of graphite fibers [25].

$$\sigma_t = \left( \frac{E \gamma_a}{a} \right)^{1/2} \quad (2.1)$$

relates the theoretical strength ( $\sigma_t$ ) to Young's modulus ( $E$ ), the surface energy ( $\gamma_a$ ) and the interplanar spacing of the planes perpendicular to the tensile axis. The ratio of theoretical strength to Young's modulus ( $\sigma_t/E$ ) varies, but is in the range 0.1-0.2 for many materials. For a perfect graphite, with a theoretical modulus of 1000 GPa, a theoretical strength of 100 GPa might be expected. However, because of defects, the practical strength is always an order of magnitude lower. In brittle solids, the defects are small cracks which act as stress concentrators. The cracks will grow under the action of a stress,  $\sigma$ , if they are greater than a critical size,  $C$ , as determined by the Griffith relationship:

$$\sigma^2 = \frac{2E \gamma_a}{\pi C} \quad (2.2)$$

The more perfect the crystal structure of a carbon fiber, the more brittle and difficult it is to handle [26].

The critical crack length estimated for mesophase pitch-based fibers is 130 nm [21]. This is a factor of ten larger than the crystallite thickness. The high modulus Thornel fibers, produced by Amoco Performance Products, Inc., have been found to have a high degree of three-dimensional order, and therefore, a medium for crack propagation. It has also been suggested that in these high modulus fibers cracks will propagate outside the initiating crystallite in order for the fibers to fail, explaining the low tensile strengths observed [29]. The ultrahigh modulus is a direct result of the almost perfect orientation of the closely spaced layer planes.

## 2.1.5 P100 Graphite Fibers

### 2.1.5.1 Microstructure and Morphology

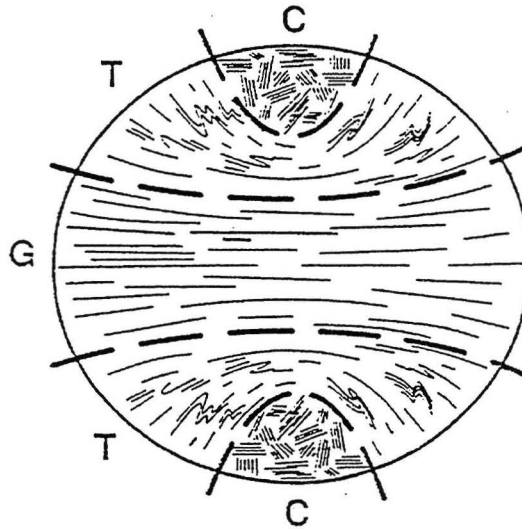
P100 graphite fibers, purchased from Amoco Performance Products, Inc., have been examined using SEM [30]. The fractured fibers studied exhibited both a random core and an oriented core morphology; appreciable variation in morphology was found to occur within a single fiber batch. The oriented core structure consists of an equatorial girdle that crosses the fiber diameter. The orientation of graphene sheet layering is basically continuous in this region. Two polar zones of chaotic structure where layering is markedly discontinuous, and two transitional zones, are also found. An idealized sketch of this structure and a corresponding SEM image are given in Figure 2.5. The fibers in the lower right reveal well developed equatorial girdles. In other fibers, the texture is less regular. Higher magnification views of fractured fibers are shown in Figure 2.6.

#### 2.1.5.2 Mechanical and Thermal Properties

The physical properties of P100 graphite fibers are included in Table 2.1.

Table 2.1. Physical properties of Thornel P100 fibers [31].

Property	S.I. Units	U.S. Customary Units
Tensile Strength	2.37 GPa	350 ksi
Tensile Modulus	758 GPa	110 Msi
Density	2.15 kg/m <sup>3</sup>	0.078 lb/in <sup>3</sup>
Filament Diameter	10 mm	10 <sup>-3</sup> in
Elongation at Break	0.32 %	0.32 %
Elastic Recovery	100 %	100 %
Carbon Assay	99+ %	99+ %
Surface Area	0.4 m <sup>2</sup> /g	2.82 x 10 <sup>4</sup> in <sup>2</sup> /lb
Longitudinal Thermal Conductivity	1.24 cal/cm-s-°C 520 W/m-K	300 btu/ft-hr-°F
Electrical Resistivity	2.5 mohm-m	7.05 ohms
Longitudinal CTE at 21°C (70°F)	-1.45 ppm/K	-0.8 ppm/°F



(a) Transverse schematic of an oriented core filament. Three regions: *C* for chaotic, *G* for girdle, and *T* for transitional. Regions are separated by thick dotted lines and defined on the basis of variations in the nature of layering, which is represented by fine lines [30].

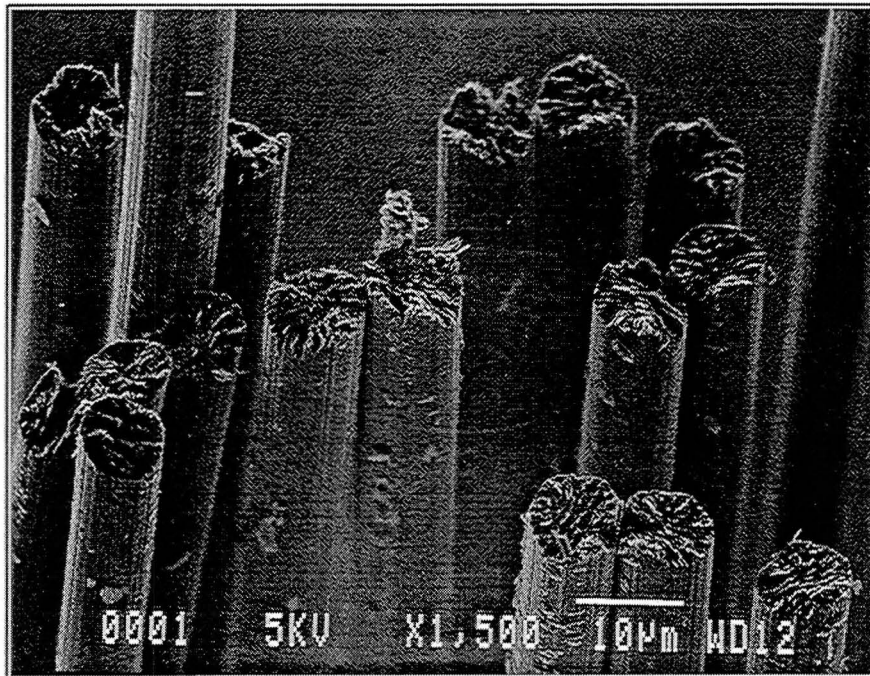
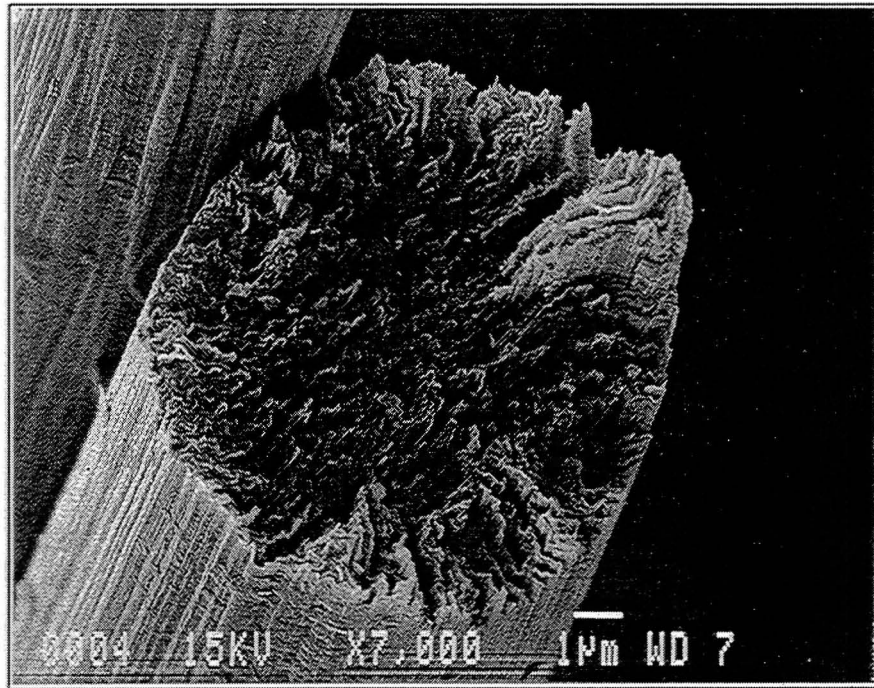


Figure 2.5. (b) SEM image of fractured P100 fibers. The fibers in the lower right reveal well developed equatorial girdles. In other fibers, the texture is less regular. (Photo courtesy of S. Farmer and P. Dickerson, NASA LeRC)



(a) Fracture surface of P100 graphite fiber revealing orientation of graphene sheets.

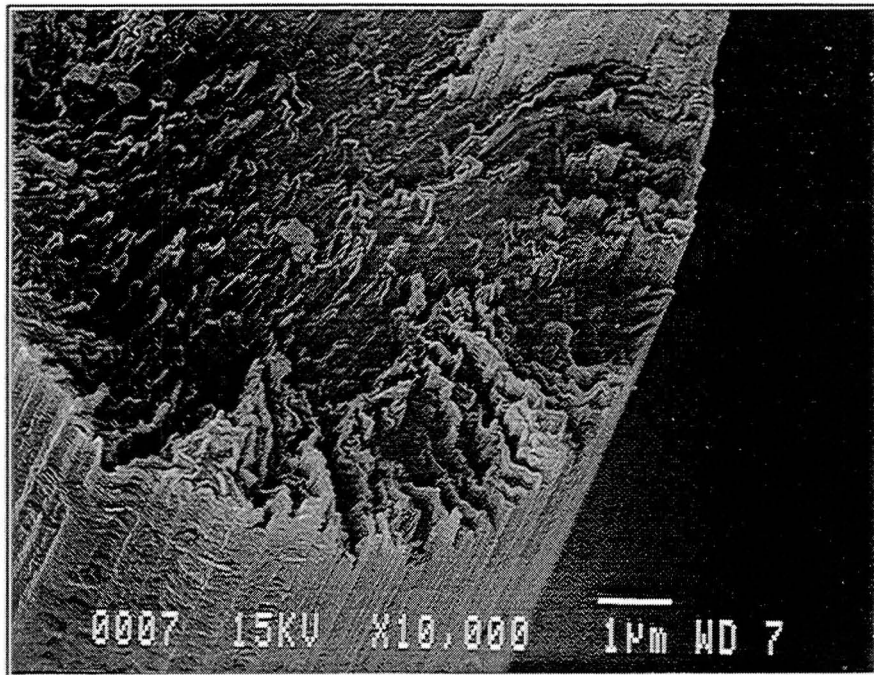


Figure 2.6. (b) Higher magnification.  
(Photos courtesy of S. Farmer and P. Dickerson, NASA LeRC)



Pitch-based graphite fibers have been found to maintain their mechanical properties at high temperatures. A slight increase in tensile modulus and strength has been observed when P100 fibers were tested at temperatures up to 1300°C [32]. The longitudinal thermal conductivity of P100 fibers is higher than that of pure Cu (392 W/m-K).

## 2.2 Oxygen-Free High Conductivity Copper [33-36]

Oxygen-free high conductivity (OFHC) copper is produced by the melting and forming of select refinery cathodes into continuous cast shapes. It is melted and cast under strictly controlled conditions which yield a consistently homogeneous product, virtually free of oxygen. No deoxidizing elements are used in the production of OFHC copper. Therefore, there are no residual deoxidants in the finished product.

Due to the low impurity content, OFHC copper has a unique combination of properties. It has high ductility and toughness, which results in excellent hot and cold workability. Because it is free from deoxidizing agents and impurities, OFHC copper has high electrical and thermal conductivities. Virtually free from oxygen, it is immune to embrittlement when maintained at high temperatures under reducing conditions. OFHC copper is also dimensionally stable when heated in hydrogen and exhibits low volatility under high vacuum. It is readily joined by welding or brazing. OFHC copper, like many other coppers, has excellent corrosion resistance.

### 2.2.1 Processing

The majority of copper is producing by continuous or semicontinuous casting. During the production of OFHC copper, a positive pressure of gas is maintained to protect the metal from oxygen during melting, casting and solidification. Present fabrication methods used for OFHC copper utilize highly automated production lines consisting of a cathode preheating furnace, a charging machine, a melting furnace, a holding furnace and a semicontinuous casting machine. An example production line is illustrated in Figure 2.7.

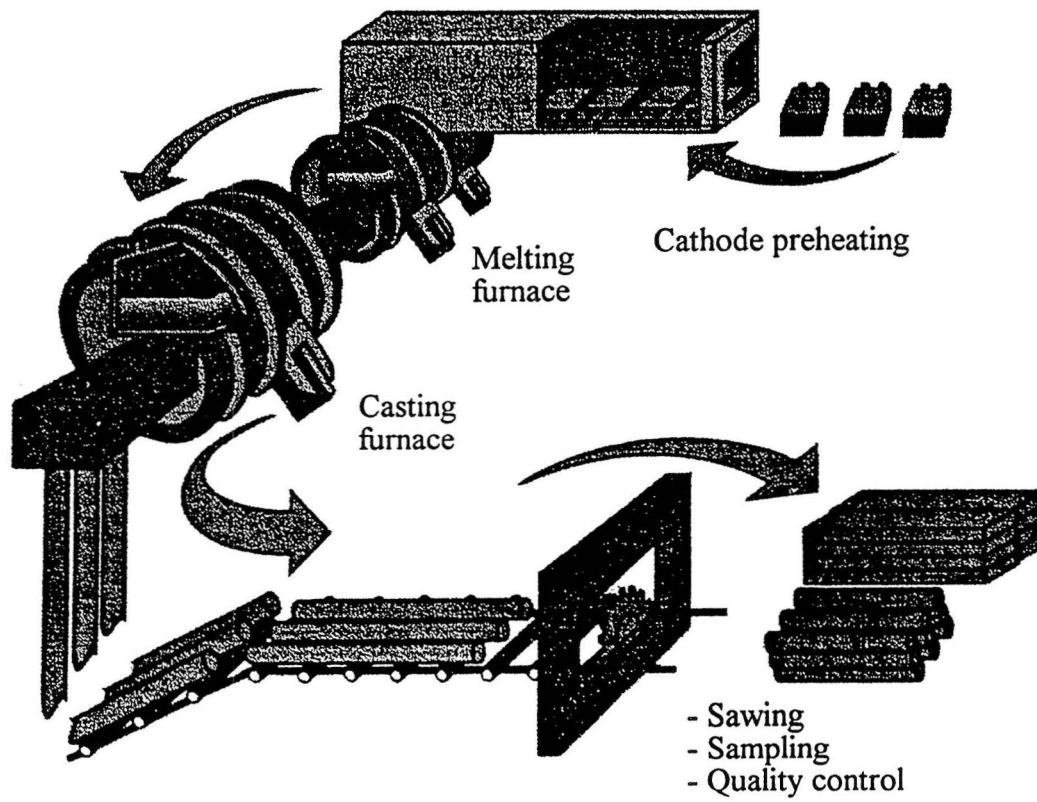


Figure 2.7. OFHC copper production process [36].

Cathodes are preheated in a controlled atmosphere to remove surface moisture and impurities. Reducing substances protect the preheating, charging, melting, melt transfer, holding and casting operations. The atmospheric conditions in the various equipment components are strictly monitored and controlled. Each casting is made under controlled casting speed, cooling rate and protection gas conditions. The absence of oxygen ensures the homogeneity of the castings. Guaranteed properties of OFHC copper are quantified in Table 2.2.

Table 2.2. Composition and property limits of OFHC copper [33].

Certified Grade OFHC Brand Copper Copper No. 101 ASTM B 170 Grade 1		Regular Grade OFHC Brand Copper Copper No. 102 ASTM B 170 Grade 2	
Composition			
Copper	99.99% min.	Copper + silver	99.95% min.
Bismuth	10 ppm max.		
Cadmium	1 ppm max.		
Lead	10 ppm max.		
Mercury	1 ppm max.		
Oxygen	10 ppm max.		
Phosphorus	3 ppm max.		
Selenium	10 ppm max.		
Sulfur	18 ppm max.		
Tellurium	10 ppm max.		
Zinc	1 ppm max.		
Other *	40 ppm total max.		
* Antimony, arsenic, bismuth, manganese, selenium, tellurium, tin			
Electrical Resistivity, maximum			
1.71 $\mu\text{ohm-cm}$ at 20°C (68°F)		1.724 $\mu\text{ohm-cm}$ at 20°C (68°F)	
Electrical Conductivity, minimum			
101.0% IACS		100.0% IACS	

### 2.2.2 Physical Properties

Nominal physical property values for OFHC copper are given in Table 2.3. The individual properties are detailed below.

Table 2.3. Physical properties of OFHC copper [33].

Property	S.I. Units	U.S. Customary Units
Melting Point	1083°C	1981°F
Electrical Resistivity*	1.71 mohm-cm at 20°C	10.3 ohms at 68°F
Electrical Conductivity†	0.586 Mohm-cm at 20°C	101% IACS at 68°F
Thermal Conductivity	0.934 cal/cm-s-°C at 20°C 391.7 W/m-K	226 btu/ft-hr-°F at 68°F
Coef. of Thermal Expansion	17.0 x 10 <sup>-6</sup> /°C (20-100°C) 17.3 x 10 <sup>-6</sup> /°C (20-200°C) 17.7 x 10 <sup>-6</sup> /°C (20-300°C)	9.4 x 10 <sup>-6</sup> /°F (68-212°F) 9.6 x 10 <sup>-6</sup> /°F (68-392°F) 9.8 x 10 <sup>-6</sup> /°F (68-572°F)
Specific Heat (Heat Capacity)	0.092 cal/g°C at 20°C	0.092 btu/lb/°F at 68°F
Density	8.94 g/cm <sup>3</sup> at 20°C	0.323 lb/in <sup>3</sup> at 68°F
Specific Gravity	8.94	8.94
Modulus of Elasticity (Tension)	117 MPa	17 Msi
Modulus of Rigidity	44 MPa	6.4 Msi

\* Maximum resistivity of annealed Certified Grade OFHC copper.

† Minimum conductivity of annealed Certified Grade OFHC copper.

Electrical Conductivity and Resistivity. The electrical conductivity of OFHC copper decreases with increasing temperature as shown in Figure 2.8. In a similar manner, the effects of increasing temperature can be expressed as a function of the electrical resistivity as shown in Figure 2.9. At very low temperatures, the electrical conductivity of copper increases as the temperature approaches absolute zero. While copper does not become superconductive, at -269°C the resistivity of the material corresponds to an electrical conductivity of approximately 600% IACS.

Thermal Conductivity. Like the electrical conductivity, the thermal conductivity decreases with increasing temperature as indicated in Figure 2.10. The ratio of the thermal conductivity to the electrical conductivity is directly proportional to the temperature. The value of the constant of proportionality is independent of the metal. This is further described in Section 2.7.6.

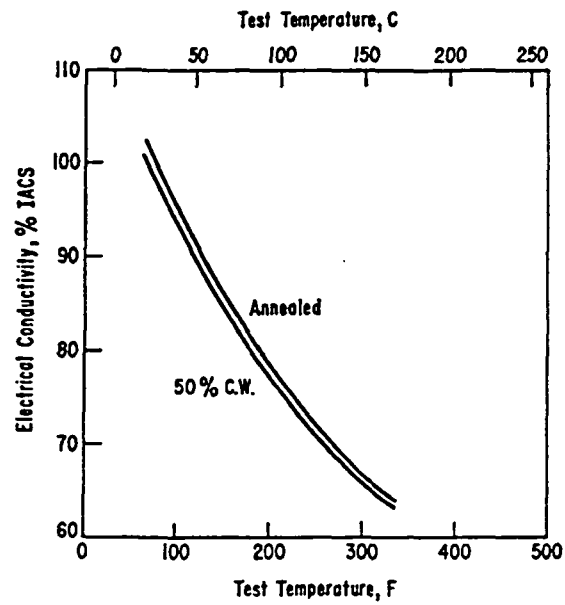


Figure 2.8. Elevated temperature electrical conductivity of OFHC copper [37].

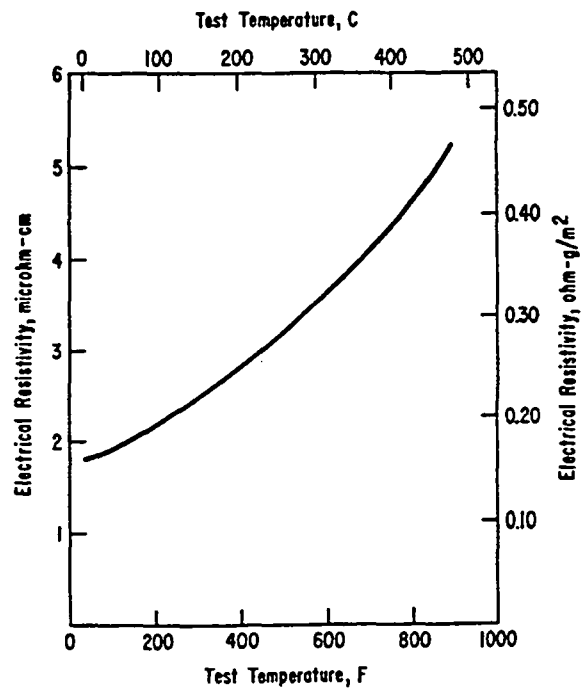


Figure 2.9. Elevated temperature electrical resistivity of annealed OFHC copper [33].

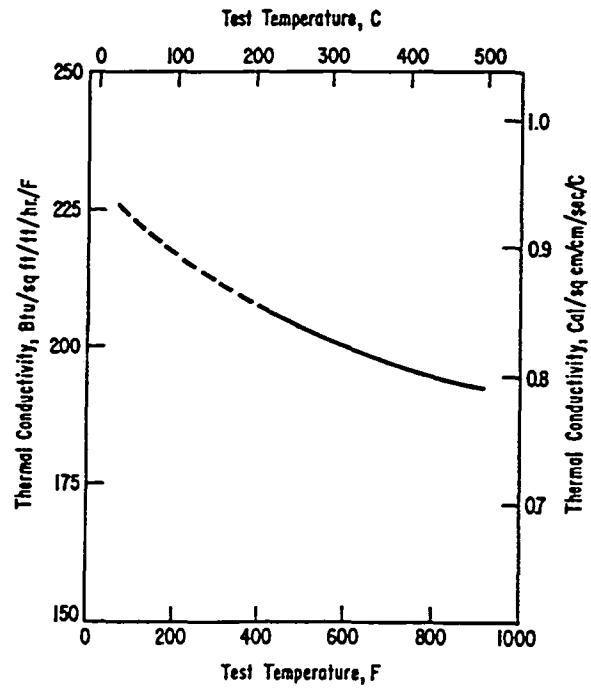


Figure 2.10. Elevated temperature thermal conductivity of annealed OFHC copper [33].

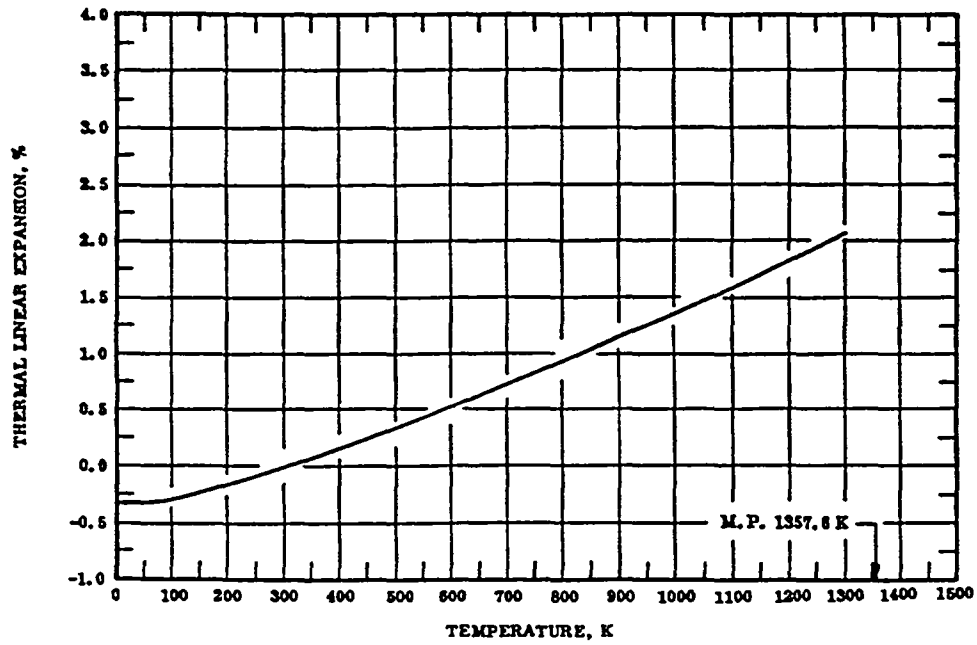


Figure 2.11. Thermal linear expansion of copper [38].

Thermal Expansion. The effect of temperature on the thermal expansion of copper is given by the following set of equations [38]:

$$\begin{aligned}\Delta L / L_0 &= -0.281 + 1.073 \times 10^{-3}(T - 100) + 2.904 \times 10^{-6}(T - 100)^2 - 4.548 \times 10^{-9}(T - 100)^3 \\ &\quad (100 < T < 293\text{K}) \\ \Delta L / L_0 &= 1.685 \times 10^{-3}(T - 293) + 2.702 \times 10^{-7}(T - 293)^2 + 1.149 \times 10^{-10}(T - 293)^3 \\ &\quad (293 < T < 1300\text{ K})\end{aligned}\tag{2.3}$$

where  $\Delta L$  is the change in length and  $L_0$  is the original length of the specimen. A graphical representation is shown in Figure 2.11. The total expansion of copper from 0 K to the melting point has been measured to be 2.78% [39].

Specific Heat. Figure 2.12 shows the effect of temperature on the specific heat of copper. There is a linear increase in specific heat from room temperature to the melting point.

### 2.2.3 Mechanical Properties

The room temperature mechanical properties of copper are listed in Table 2.4. The elastic modulus of copper, in both tension and compression, is 117 GPa (17 Msi). The modulus decreases with increasing temperature. Figure 2.13 shows this decrease on the dynamic modulus, which is usually slightly higher than the static modulus. The mechanical properties vary with annealing temperature as shown in Figure 2.14. As shown, the tensile strength and yield strength significantly decrease above 300°C and reach minimum values at about 700°C. The ductility, as measured by both elongation and reduction in area, reaches a maximum at approximately 530°C, and then decreases as the temperature increases. This is due to grain growth at high temperatures as illustrated in Figure 2.15.

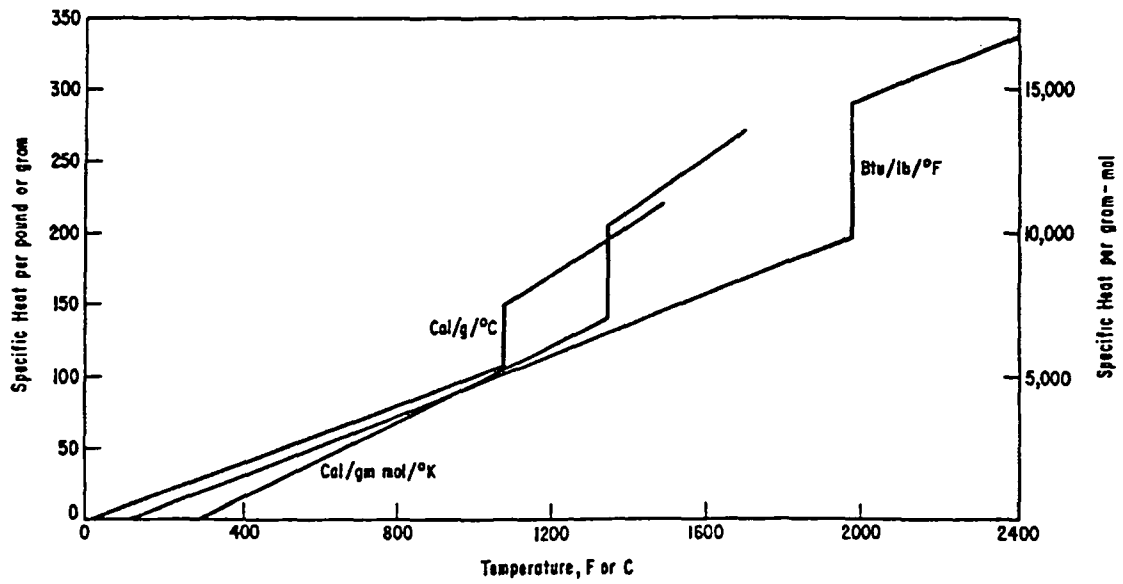


Figure 2.12. Elevated temperature specific heat of copper [40].

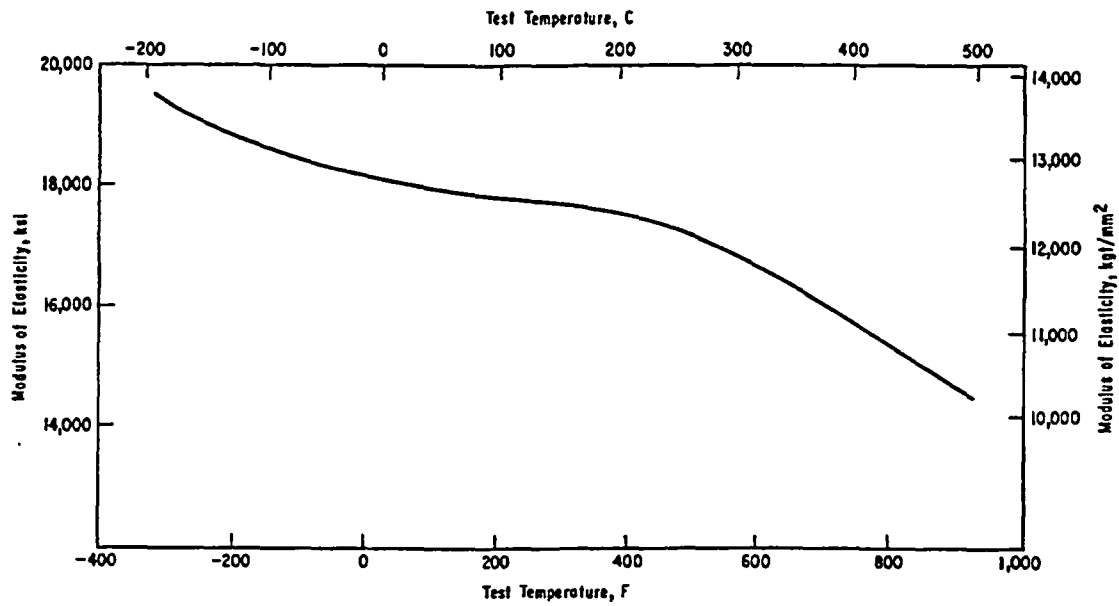


Figure 2.13. Elevated temperature dynamic modulus of elasticity of OFHC copper [41].



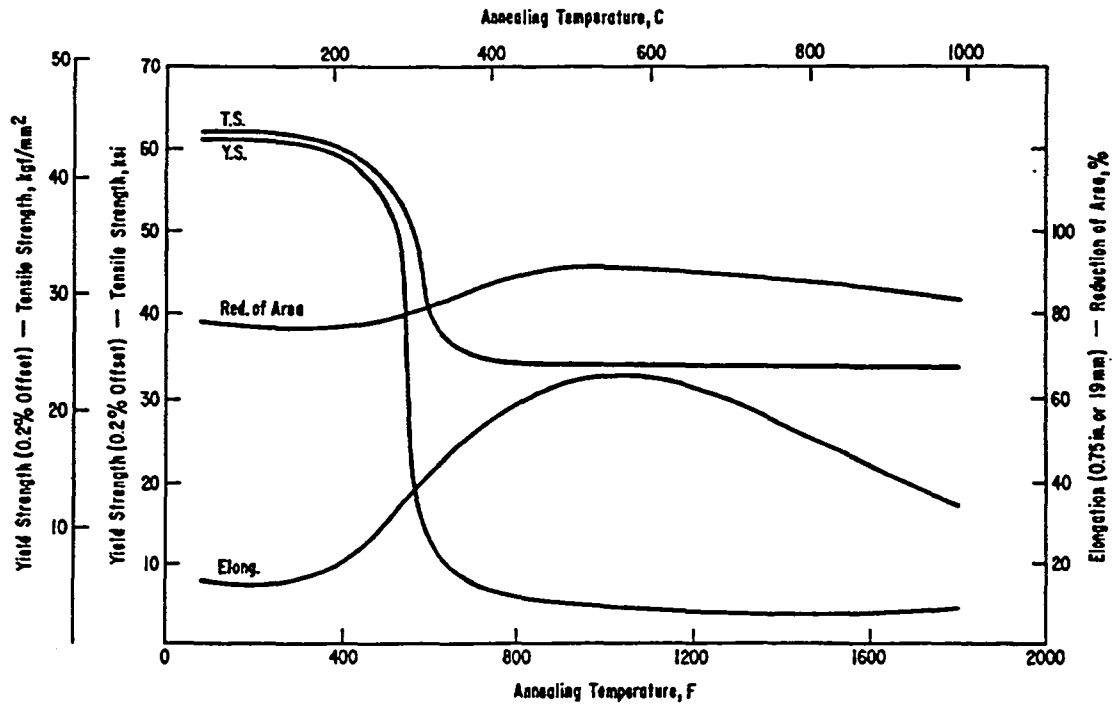


Figure 2.14. Effect of annealing on tensile properties of hard drawn OFHC copper rod [42].

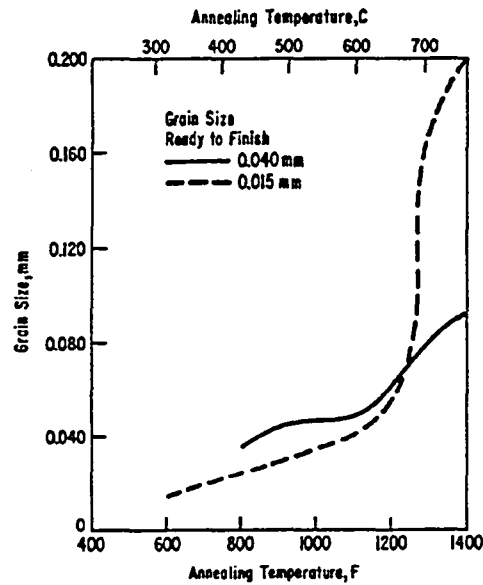


Figure 2.15. Effect of annealing on grain size of OFHC copper strip cold rolled 50% [43].

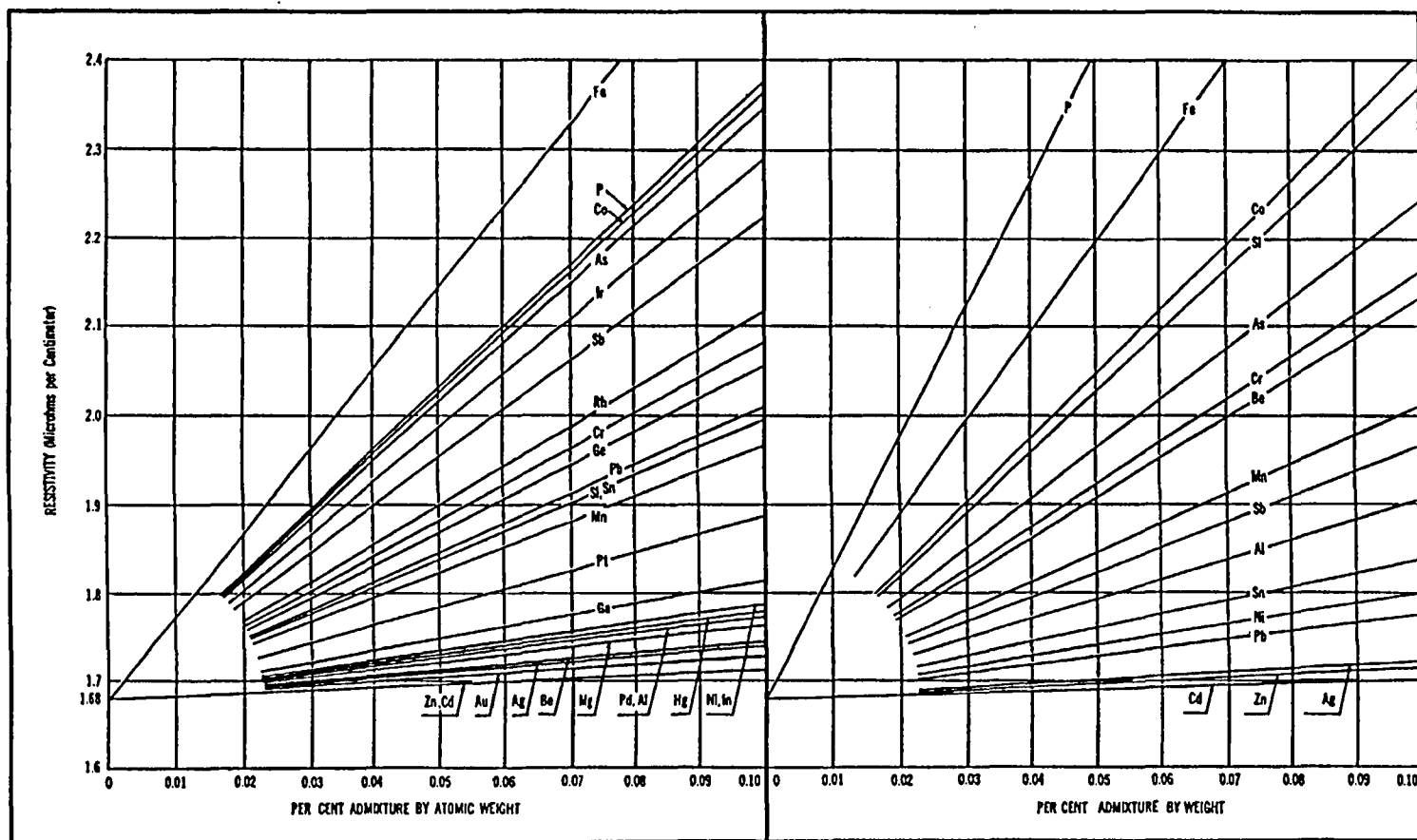


Figure 2.16. Increase of electrical resistivity of copper with admixtures of various elements [44].

Table 2.4. Room temperature mechanical properties of OFHC copper sheet [33, 35].

Temper	UTS MPa (ksi)	E GPa (Msi)	Elongation (%)	Shear Strength MPa (ksi)
hardened	345 (50)	117 (17)	6	193 (28)
annealed*	234 (34)	117 (17)	45	159 (23)

\* 0.025 mm grain size.

#### 2.2.4 Effect of Impurities and Alloying Elements

Alloying additions to OFHC copper are often needed to improve strength and hardness. Many electrical and electronic applications require adequate mechanical strength and hardness, along with high electrical and thermal conductivity. Typically, however, alloying elements that increase strength also reduce conductivity.

The influence of various alloying elements on the electrical resistivity of copper is shown in Figure 2.16. Additions in both atomic percent and weight percent are given. To utilize the graph for determining the resistivity of OFHC copper plus a certain alloying element, consider the line representing the element of interest. Locating the intersection of this line and the vertical line corresponding to the percent alloying addition, yields a value for the resistivity on the y-axis. For example, the addition of 0.08 at% chromium to OFHC copper results in a measured resistivity of 2.0 mohm-cm. This corresponds to a drop to 86.3% IACS.

### 2.3 Liquid Metal Infiltration

Of the many methods available for producing metal matrix composites, infiltration casting processes are some of the most economical. Liquid metal infiltration processes offer a considerable advantage in the production of intricate parts, where the full benefits of continuous fibers may be realized [45]. However, the advantages of liquid metal infiltration cannot be achieved without improvements in the infiltration behavior and the fiber/matrix bonding. Problems associated with

continuous fiber reinforced composites produced by melt infiltration include: (1) failure of the melt to penetrate narrow gaps between adjacent fibers, (2) intermetallic or reaction phase formation at fiber/matrix interfaces, and (3) inhomogeneous distribution of fibers in the composite [46]. In continuously reinforced composites, the defects between touching fibers may be caused by interfacial and meniscus forces which inhibit full melt penetration in the contact zone. Driving the liquid metal into these spaces between the reinforcing fibers is a complex process, dependent on several physical phenomena which often make the application of pressure on the metal matrix a necessity [47]. There is a pressure differential due to the capillary forces at the liquid metal front during infiltration of the reinforcement. This pressure differential dictates whether infiltration will occur spontaneously, as in wetting systems, or will require the application of pressure, as in nonwetting systems. Figure 2.17 illustrates the contact point between two fibers. The pressure required to infiltrate the contact area is [47]:

$$P = \frac{\gamma_{LV} \sin\left(\theta - \alpha - \frac{\pi}{2}\right)}{R \sin \alpha \tan \frac{\alpha}{2}} \quad (2.4)$$

where  $\gamma_{LV}$  = liquid/vapor interfacial energy  
 $\theta$  = is the contact angle  
 $\alpha$  = meniscus radius.

As  $\alpha$  approaches zero, the pressure becomes infinitely large. (Realistically, if the pressure became infinitely large, it is likely that the fibers would be physically moved about and no longer be in contact.) For a given infiltration pressure, defects at the contact area of two fibers will be approximately equal to  $2R \sin \alpha$ . If two fibers touch over a length  $L$ , the defect will be just as long parallel to the fiber axis. The size of these defects can be decreased by increasing the infiltration

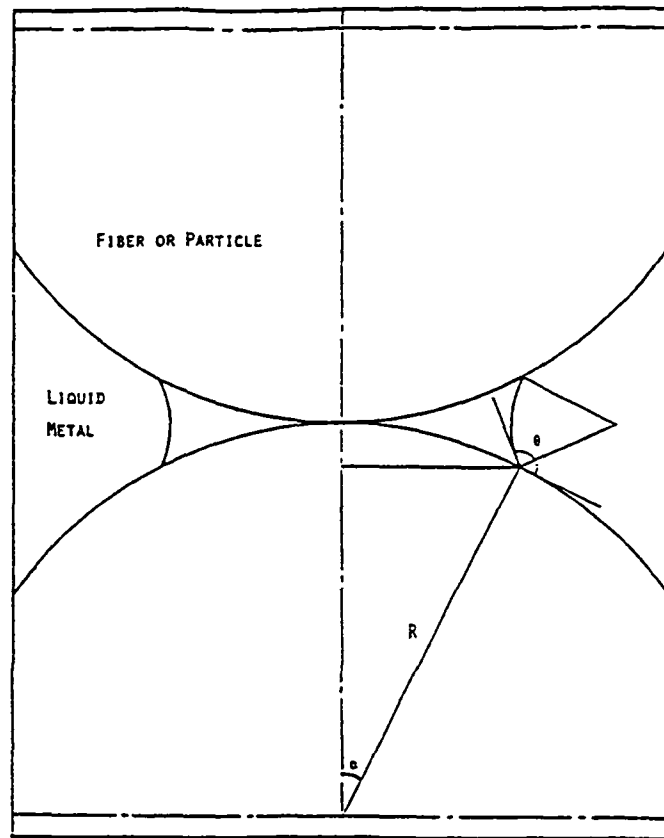
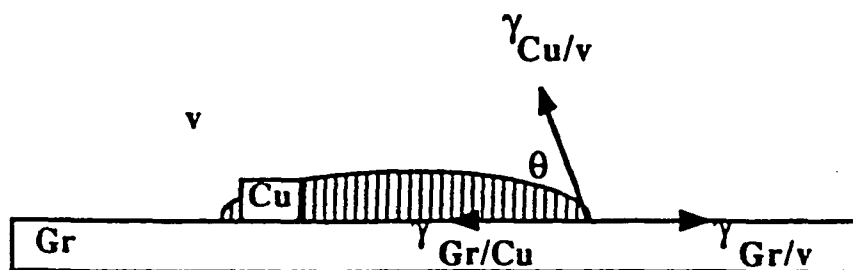


Figure 2.17. Infiltration of contact area between two fibers by a nonwetting metal [47].



2.18. Sessile drop configuration, defining the contact angle [16].

pressure. These defects can be eliminated only by either suppressing fiber contacts, or by promoting fiber wetting in these areas.

### 2.3.1. Wetting of Reinforcement by Matrix

Wetting is favored by the formation of strong chemical bonds at the fiber/matrix interface [48]. The wettability of a solid by a liquid is indicated by the contact angle  $\theta$  shown in Figure 2.18. The angle is related to the three surface tensions by Young's Equation [49]:

$$\gamma_{LV} \cos \theta = \gamma_{SV} - \gamma_{SL} \quad (5)$$

Wetting is characteristic of a contact angle of  $\theta < 90^\circ$ . Good wetting often results in good bond strength in the final composite. Often, the formation of these bonds is accompanied by mutual dissolution and/or reaction of the two bulk phases. This can be quite detrimental to the composite if a substantial portion of the reinforcement is reacted in the creation of the chemical bonds. It is necessary, therefore, to reach a compromise between the contradictory requirements of good wetting and absence of excessive reaction.

### 2.3.2 Introduction of Engineered Interface

One of the primary advantages of liquid metal infiltration is the ability to introduce an engineered interface. This can be achieved through coating the reinforcement or alloying the matrix. The reaction of alloying additions with the reinforcing fibers during infiltration can create interfacial phases that enhance both wetting and bond strength, provided the reaction is not excessive and damaging to the fibers.

The creation of an interfacial reaction layer is a two step process [50]. The first stage involves the reaction of the alloying addition (or matrix in some cases) with the fiber to chemically create the phase. In the case of carbon fibers, this is a carbide phase. The second stage consists of diffusion controlled growth of the new reaction phase. Often the diffusion times involved are

sufficiently small for most of the reaction to occur with subsequent layer growth while the matrix is molten [50]. Estimates of the diffusion distance of Cr in molten Cu are included in the following section.

## 2.4 Interfacial Reactions

Investigation of the wetting of characteristics observed in the Gr/Cu-Cr system [16] entailed an extensive analysis of the reaction layer formation at the interface. A model which describes the creation and growth of the reaction phase has been developed [51]. Consideration of the thermodynamics of the system allowed for the identification of the most stable chromium carbide phase to form under the test conditions. The kinetics of reaction layer formation were modelled in terms of bulk diffusion mechanisms.

### 2.4.1 Thermodynamics of $\text{Cr}_3\text{C}_2$ Formation

To start a thermodynamic assessment of the most stable chromium carbide phase, the activity of Cr in the liquid Cu sessile drop was determined. As indicated by x-ray diffraction results, the reaction layer phase that forms at the Gr/Cu-Cr alloy interface is  $\text{Cr}_3\text{C}_2$ . This result is consistent with thermodynamic considerations of the most stable reaction layer phase. From the Cu-Cr phase diagram shown in Figure 2.19 [52], at 1130°C the Cr liquid-solid transition occurs at  $X_{\text{Cr}} = 0.02$ , a composition of 2 at%. Assuming Henrian behavior, the activity coefficient of Cr in liquid Cu is found to be approximately 50. For example, formation of  $\text{Cr}_3\text{C}_2$  in a Cu-1.22at%Cr alloy is considered. The activity of Cr in liquid Cu is 0.61 for this alloy composition at 1130°C. Taking the activity of C in the graphite substrate as unity, and that the chromium carbide phases form as pure substances, the free energy of formation for each potentially stable carbide phase can be determined [53]. The  $\text{Cr}_3\text{C}_2$  phase is observed to be the most stable. This is in agreement with the phase diagram given in Figure 2.20 [54]. Using the same thermochemical data regarding the formation of  $\text{Cr}_3\text{C}_2$ , the minimum Cr

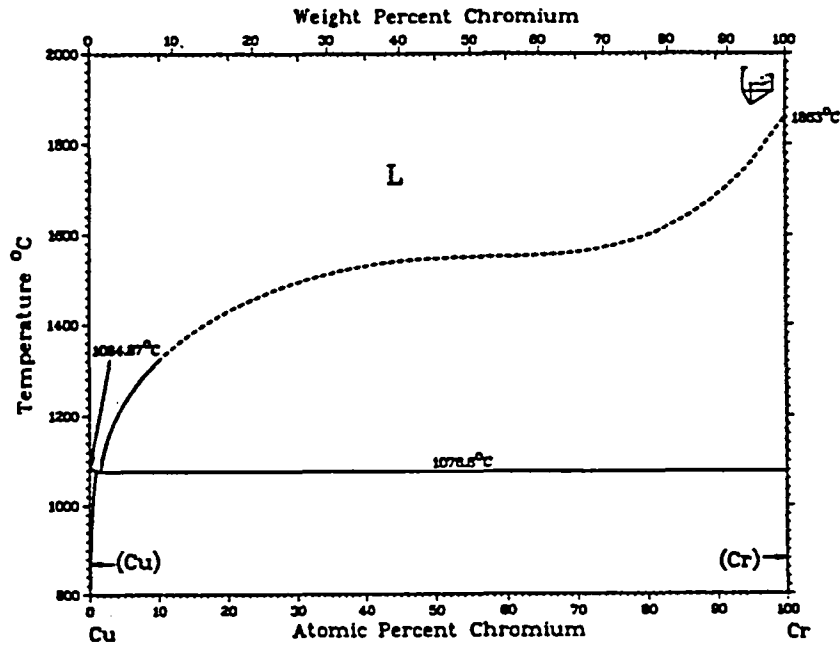
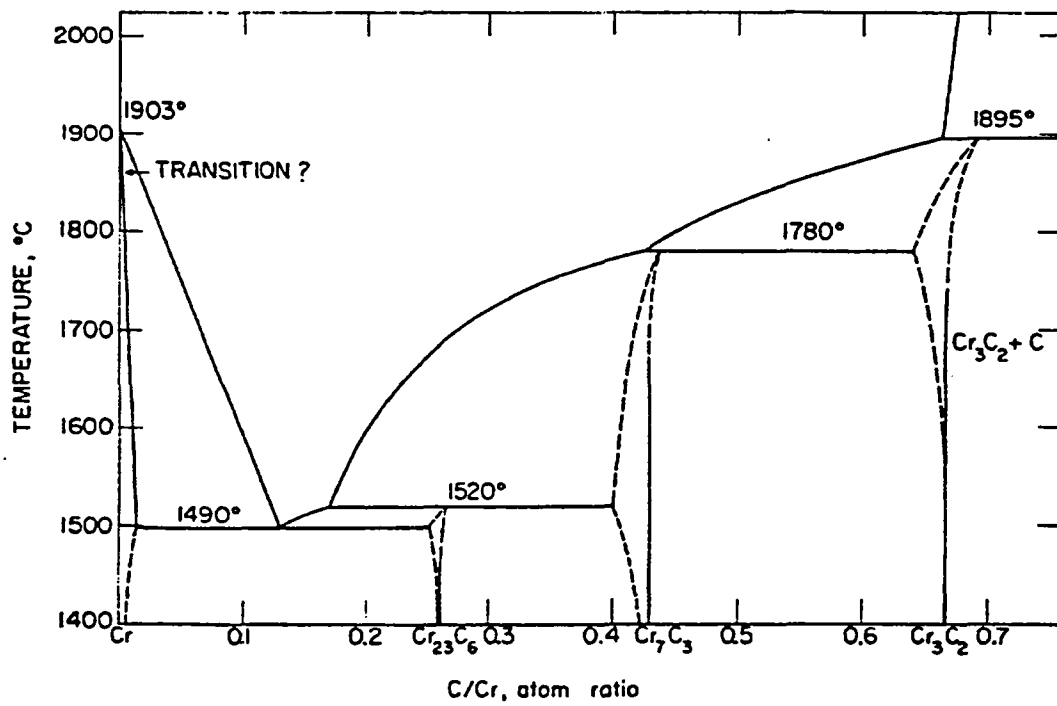


Figure 2.19. Cu-Cr phase diagram [52].

Figure 2.20. Cr-Cr<sub>3</sub>C<sub>2</sub> phase diagram [54].



concentration in liquid Cu at 1130°C, at which  $\text{Cr}_3\text{C}_2$  can form, was also calculated. The Cr level can be reduced to 0.078 at% before equilibrium is achieved.

Mass balance calculations verify the feasibility of forming a reaction layer of 10  $\mu\text{m}$  thickness with the Cu-1.22at%Cr alloy. Using a radius of 9.5 mm and a thickness of 2.0 mm, the volume of the Cu-Cr sessile drop was calculated to be 570  $\text{mm}^3$ . The volume of a reaction layer of 10  $\mu\text{m}$  thickness is 2.9  $\text{mm}^3$ . Using a density of 6.68  $\text{g/cm}^3$  for  $\text{Cr}_3\text{C}_2$ , and assuming that the Cr level in the sessile drop can be reduced to 0.078 at% before the formation of  $\text{Cr}_3\text{C}_2$  becomes thermodynamically unfavorable, a potential carbide layer volume of 8.2  $\text{mm}^3$  can form from the Cu-1.22at%Cr alloy. Based on a mass balance analysis, a carbide layer approximately 2.8 times thicker than that observed could have formed.

#### 2.4.2 Kinetics of $\text{Cr}_3\text{C}_2$ Formation

The preceding discussion indicates that sufficient Cr was available in the liquid Cu sessile drops to form reaction layers consisting of  $\text{Cr}_3\text{C}_2$  that were greater than 10  $\mu\text{m}$  in thickness. The fact that layers thicker than 10  $\mu\text{m}$  were not observed indicates that kinetic factors were influencing the reaction layer growth. Several possible mass transport mechanisms could be controlling the final thicknesses of the reaction layers that were observed.

The first kinetic factor to be explored is the rate of diffusion of Cr out of the liquid Cu. This process can be modelled using the simplified sessile drop geometry shown in Figure 2.21. The following equation defines the time dependent concentration of Cr in the cylindrical volume shown in the figure, assuming solute can only exit the volume through the bottom interface [55]:

$$c(z,t) = c_e + (c_0 - c_e) \sum_{n=1}^{\infty} \frac{2 \left( \frac{k}{D} \right) \cos \alpha_n z}{\left\{ \left[ \alpha_n^2 + \left( \frac{k}{D} \right)^2 \right] z_0 + \left( \frac{k}{D} \right) \right\} \cos \alpha_n z_0} \exp(-D \alpha_n^2 t) \quad (2.5)$$

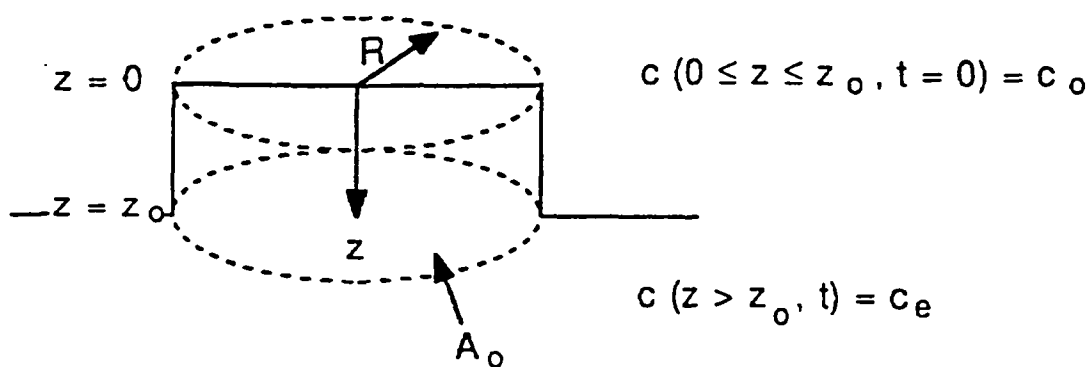


Figure 2.21 Simplified sessile drop geometry indicating boundary conditions for determining rate of diffusion of Cr out of liquid Cu [51].

where  $c_e$  = concentration of Cr in equilibrium with  $\text{Cr}_3\text{C}_2$  (0.078 at%)  
 $c_0$  = initial concentration of Cr in the sessile drop (1.22 at%)  
 $D$  = diffusion coefficient of Cr in liquid Cu at 1130°C [56] ( $3 \times 10^{-6} \text{ cm}^2/\text{s}$ )  
 $k$  = interfacial mass coefficient between the sessile drop and the  $\text{Cr}_3\text{C}_2$  reaction layer  
 $t$  = time

and  $\alpha_n$  is defined by the roots of the following transcendental equation [55]:

$$z_0 \alpha_n \tan z_0 \alpha_n = \left( \frac{k}{D} \right) z_0 \quad (2.6)$$

The total flux of Cr out of the bottom interface of the sessile drop,  $J$ , can be determined using the following equations:

$$J_{total} = \int_0^t -A_0 D \frac{dc}{dz} \Big|_{z=z_0} dt \quad (2.7a)$$

$$J = A_0 (c_0 - c_e) \sum_{n=1}^{\infty} \frac{2 \left( \frac{k}{D} \right) \cos \alpha_n z}{\left\{ \left[ \alpha_n^2 + \left( \frac{k}{D} \right)^2 \right] z_0 + \left( \frac{k}{D} \right) \right\} \cos \alpha_n z_0} \left[ 1 - \exp(-D \alpha_n^2 t) \right] \quad (2.7b)$$

The total flux of Cr that can exit through the bottom interface of the sessile drop of the Cu-1.22at%Cr alloy is plotted as a function of time in Figure 2.22 for several possible values of the interfacial mass transfer coefficient. The figure shows that for interfacial mass coefficient values greater than  $1.5 \times 10^{-4} \text{ cm/s}$ , interfacial transport is not greatly influencing the rate of Cr exiting the sessile drop. Under

such conditions, more than half of the total available Cr level of  $7.4 \times 10^{-4}$  moles in the sessile drop could exit in 3600 s, the duration of the sessile drop tests conducted.

A second kinetic factor to be explored is the rate of C diffusion through the solid  $\text{Cr}_3\text{C}_2$  layer at  $1130^\circ\text{C}$ . This process leads to a model for parabolic growth of the  $\text{Cr}_3\text{C}_2$  layer. The following equation defines the thickness of the reaction layer,  $h$ , as a function of time,  $t$  [57]:

$$h = \sqrt{\frac{2(c_1 - c_2)Dt}{c_2}} \quad (2.8)$$

where  $c_1$  = concentration of C in the  $\text{Cr}_3\text{C}_2$  at the graphite interface  
 $c_2$  = concentration of C in the  $\text{Cr}_3\text{C}_2$  at the sessile drop interface  
 $D$  = diffusion coefficient for C in solid  $\text{Cr}_3\text{C}_2$  at  $1130^\circ\text{C}$  [53].

The concentration variation for C across the  $\text{Cr}_3\text{C}_2$  layer at  $1130^\circ\text{C}$  is known to be very small based upon the phase diagram shown in Figure 2.20 [54]. For the sake of calculation, a value for  $(c_1 - c_2)/c_2$  of 0.01 was assumed. The diffusion coefficient for C in  $\text{Cr}_3\text{C}_2$  is not known, but the activation energy for the diffusion coefficient has been determined to be 45 kcal/mole [53]. Using Equation 2.8 and a known reaction layer thickness of 10 mm in 3600 s, values of  $D_0 = 0.14 \text{ cm}^2/\text{s}$  and  $D = 1.3 \times 10^{-8} \text{ cm}^2/\text{s}$  at  $1130^\circ\text{C}$  were determined.

Using Equation 2.8, the thickness of the  $\text{Cr}_3\text{C}_2$  reaction layer was determined as a function of time and plotted in Figure 2.23. For comparison, the thickness of the reaction layer that could be produced by the total flux of Cr out of the the liquid Cu sessile drop, shown in Figure 2.22, is also plotted in Figure 2.23. In this latter case, a value for the interfacial mass transfer coefficient of  $1.5 \times 10^{-3} \text{ cm/s}$  was used. Only for the first 100 s of growth, up to a reaction layer thickness of approximately 1.6  $\mu\text{m}$ , is diffusion of Cr out of the sessile drop controlling the rate of growth of the

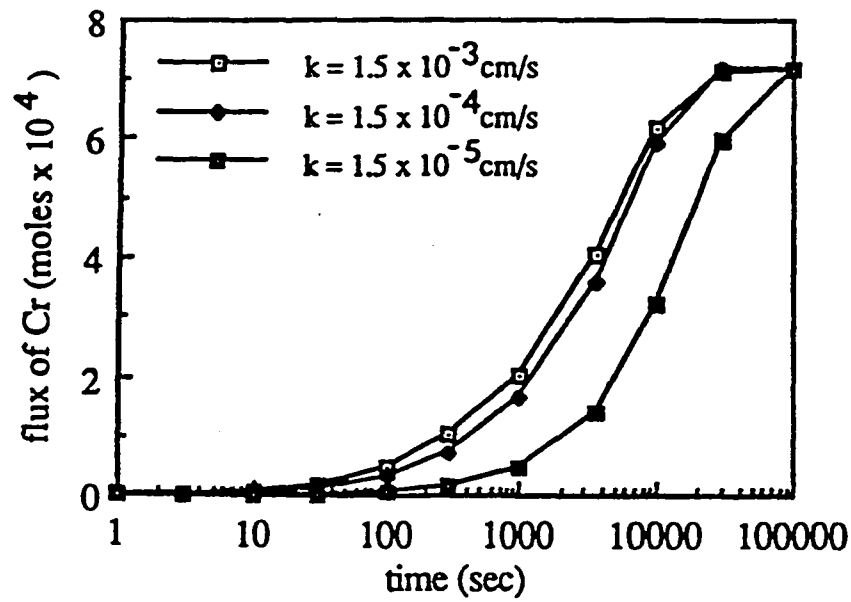


Figure 2.22. Flux of Cr out of liquid Cu sessile drop at 1130°C. Flux through bottom surface, impermeable top and sides [51].

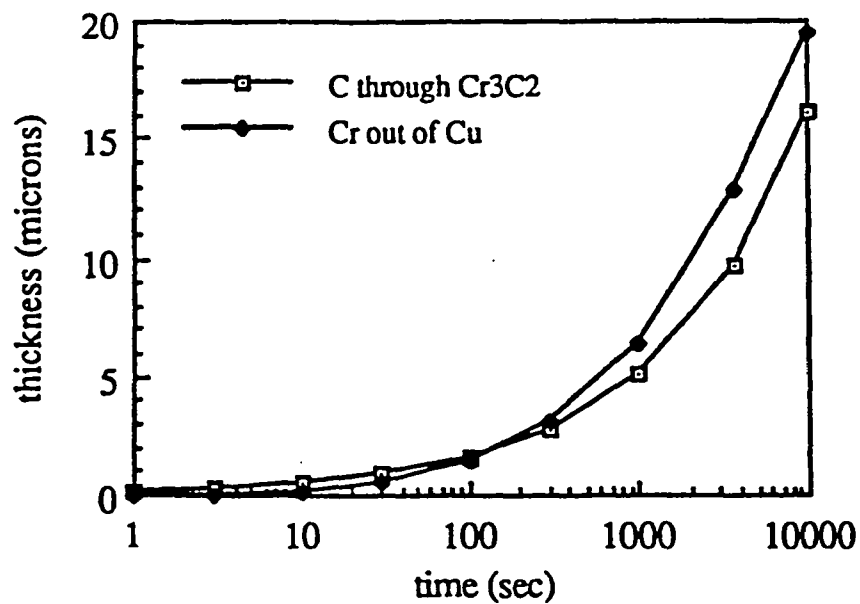


Figure 2.23. Reaction layer thickness as a function of time at 1130°C. Controlling growth mechanisms: diffusion of Cr out of liquid Cu and diffusion of C through solid  $\text{Cr}_3\text{C}_2$  [51].

reaction layer. From that point onward, diffusion of C through the  $\text{Cr}_3\text{C}_2$  layer controls the rate of growth.

#### 2.4.3 Implications for Gr/Cu Composites

Many favorable properties of Gr fibers are attributed to their surface finish. Because of this, considerable concern has been noted of the possibility of severe degradation of Gr fibers from gross reaction layer formation [10, 11, 12]. Severe damage to the fiber surface could lead to degradation of the overall composite properties. Having observed reaction layers with thicknesses up to 10  $\mu\text{m}$ , for the sessile drop configuration, it is necessary to calculate the thickness of the reaction layer expected in an actual composite. The amount of the Gr fiber that will be consumed by the reaction can also be estimated.

The thickness of  $\text{Cr}_3\text{C}_2$  reaction layer that can form in realistic Gr/Cu composites is much reduced compared with that which forms in the sessile drop tests because of the greatly increased Gr surface area per volume of Cu-Cr alloy. The following expression gives the Gr surface area per unit volume of composite,  $S_V$ :

$$S_V = \frac{2V_V}{r} \quad (2.9)$$

where  $V_V$  = volume fraction of Gr fibers in the composite  
 $r$  = radius of Gr fibers.

For a volume fraction of 0.5, 5  $\mu\text{m}$  radius Gr fibers, the Gr surface area/volume is 200  $\text{mm}^2/\text{mm}^3$ . For a Cu-1.22at%Cr alloy matrix there is only enough Cr available to form a  $\text{Cr}_3\text{C}_2$  reaction layer about the Gr fibers 36 nm thick. If a leaner alloy with 0.12at%Cr were used as the matrix, the maximum reaction layer thickness would be reduced to 1.5 nm.

The atomic volumes of C in Gr and Cr in Cu are approximately 8.8 and 12  $\text{\AA}^3$ , respectively [59]. This implies that a distance equal to about one third of the  $\text{Cr}_3\text{C}_2$  reaction layer formed would

be lost from the surface of the Gr fibers. The molecular volume of  $\text{Cr}_3\text{C}_2$  based upon a density of  $6.68 \text{ g/cm}^3$  is approximately  $44.7 \text{ \AA}^3$ . There is a reduction in volume of 16.5% when C in Gr and Cr in Cu combine to form  $\text{Cr}_3\text{C}_2$ . If the reaction layer forms when the Cu-Cr alloy matrix is in the solid state, the fibers and the matrix would be put in a state of residual tension by the formation of the  $\text{Cr}_3\text{C}_2$ .

## 2.5 Fracture of Fiber Reinforced Composites

Composite materials often fracture by either debonding or matrix cracking. When a reinforcing fiber fractures within its matrix under tensile loading, two possible modes of failure of the composite specimen can take place [60]. The first is pull-out of the fiber or debonding (adhesive failure). In this case, a cylindrical crack grows along the fiber/matrix interface away from the fiber break. Eventually, the fiber is pulled out of the matrix. The second is growth of a circular crack initiated at the fiber outwards into the matrix (cohesive failure). This will lead to rupture of the specimen. Generally, two factors determine which mode of failure is dominant: the relative value of the fracture energy of adhesion between the fiber and the matrix  $G_a$ , and the fracture energy of the matrix itself  $G_c$ . If adhesion is relatively weak, the crack will propagate along the interface as a debond. If adhesion is strong, a perpendicular crack will grow outwards into the matrix.

In order for debonding to occur, the strain energy release rate must reach a critical value [61]. In some cases, stable crack growth will occur, for which the load must be increased for further crack growth. In other cases, crack growth is unstable, leading to catastrophic failure. As a fiber is debonded from its matrix, frictional resistance to pull-out increases and the force necessary to propagate the debond increases continuously with increasing debond length.

For the case of matrix cracking, catastrophic growth of an initial crack occurs when critical conditions are reached [61]. The stress required to propagate the crack decreases with increasing crack radius.

In tensile failure of composite materials, some combination of the two fracture mechanisms is often found [60]. In general, the composites fail when the energy release rate of the system reaches a critical value. After a fiber breaks within the matrix, either debonding or matrix cracking is possible. Due to the high stress concentration at the break, a relatively small force is needed to initiate either fracture mode. Usually, a small matrix crack will form first. For fibers having small diameters as compared to the size of the surrounding matrix, the new crack will propagate along the fiber/matrix interface. For larger diameter fibers (compared to the size of surrounding matrix), the crack will propagate outward until the sample fractures, or until the crack reaches a neighboring fiber. The mode of failure depends upon the relative magnitude of the force required to propagate the crack under either condition.

## 2.6 Deflection of Straight Beams

The deflection of straight beams, elastically stressed, and having constant cross sections throughout their length is given by the formula [62]:

$$\delta = \frac{k_b PL}{EI} + \frac{k_s PL}{GA} \quad (2.10)$$

where  $\delta$  = deflection  
 $P$  = total beam load acting perpendicular to the neutral axis  
 $L$  = beam span  
 $I$  = beam moment of inertia  
 $A$  = modified beam area  
 $E$  = beam elastic modulus  
 $G$  = beam shear modulus

The constants,  $k_b$  and  $k_s$ , are dependent upon beam loading and the locations of the point whose deflection is to be calculated. The first term on the right hand side of Equation 2.10 gives the bending deflection and the second term the shear deflection. The constant associated with the shear deflection,  $k_s$ , is defined for isotropic and anisotropic solids as follows [63]:



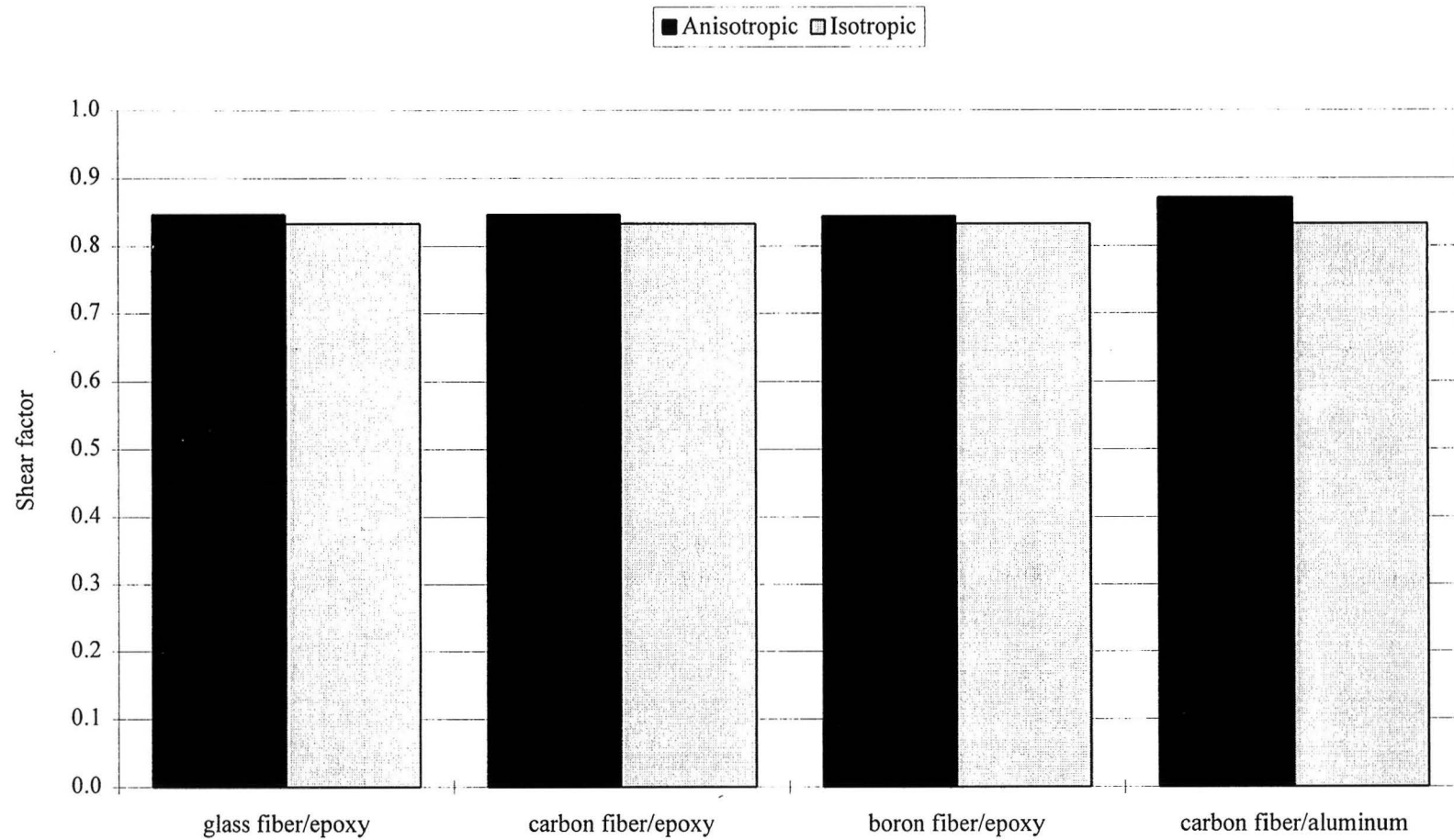


Figure 2.24. Comparison of anisotropic and isotropic shear factors for the deflection of straight beams [63].

$$k_{isotropic} = \frac{5}{6} = 0.83 \quad (2.11a)$$

$$k_{anisotropic} = \left( \frac{5 E_{11}}{6 E_{11} - \nu_{12} G_{12}} \right) \quad (2.11b)$$

A comparison of the two shear factors has shown that there is little difference between the isotropic and the anisotropic values for  $k_s$ . The results of the analysis are shown in Figure 2.24. It is therefore, justifiable to use the simpler analysis and substitute in for the isotropic shear factor. For a simply supported rectangular beam with loading and deflection concentrated at the midspan, incorporating values for  $k_b$ ,  $k_s$ ,  $I$  and  $A$  into the above equation yields the following:

$$\delta = \frac{1}{4} \frac{PL^3}{Eb^3} + \frac{3}{10} \frac{PL}{Gbh} \quad (2.12)$$

where  $b$  is the specimen thickness,  $h$  is the specimen width, and  $E$  and  $G$  are the elastic and shear moduli in the longitudinal direction of the composite, respectively. Dividing  $\delta$  by  $P$ , and separating out the constants, leaves Equation 2.12 in the following form:

$$\frac{\delta}{P} = \frac{1}{4Eb^3} L^3 + \frac{3}{10Gbh} L \quad (2.13)$$

Using the above equation, of the form  $y = mL^3 + nL$ , allows for direct calculation of the elastic and shear moduli when the slopes for a given series of load-displacement curves are known.

## 2.7 Thermal Properties

The thermal properties of interest include the heat capacity, coefficient of thermal expansion and thermal conductivity. The heat capacity and thermal conductivity determine the rate of temperature change in a material during heat treatment in fabrication and in use. They are fundamental in determining the resistance to thermal stresses. Many of the difficulties associated with the production and use of materials, composites and coatings result from dimensional changes with temperature.

### 2.7.1 Heat Capacity

Heat capacity is a measure of the energy required to raise the temperature of a material, or increase in energy content per degree of temperature rise. The energy needed to raise the temperature of a material from its minimum energy state (at absolute zero) goes into: (1) vibrational energy by which atoms vibrate around their lattice positions with an amplitude and frequency that depend on temperature; (2) rotational energy for molecules in gases, liquids and crystals having rotational degrees of freedom; (3) raising the energy level of electrons in the structure; and (4) changing atomic positions. Each of these changes corresponds to an increase in internal energy and is accompanied by an increase in configurational entropy. Heat capacity is usually measured at constant pressure, but theoretical calculations are often reported at constant volume [64]:

$$c_p = \left( \frac{\partial Q}{\partial T} \right)_p = \left( \frac{\partial H}{\partial T} \right)_p \quad \text{cal/mole}^\circ\text{C} \quad (2.14)$$

$$c_v = \left( \frac{\partial Q}{\partial T} \right)_v = \left( \frac{\partial E}{\partial T} \right)_v \quad \text{cal/mole}^\circ\text{C} \quad (2.15)$$

$$c_p - c_v = \frac{\alpha^2 V_0 T}{\beta} \quad (2.16)$$

where  $Q$  = heat exchange  
 $E$  = internal energy  
 $H$  = enthalpy  
 $\alpha$  = volume thermal expansion coefficient,  $\alpha = -dv/vdT$   
 $\beta$  = compressibility,  $\beta = -dv/vdp$   
 $V_0$  = molar volume.

Often, heat capacity data are presented as the specific heat capacity (cal/g°C). For condensed phases, there is only a small difference between  $c_p$  and  $c_v$  for most applications. This difference may, however, become significant at high temperatures.

### 2.7.2 Thermal Expansion

The specific volume of most crystals increases with increasing temperature. This increase is determined primarily by the increased amplitude of atomic vibrations about a mean position. The change in volume due to lattice vibrations is closely related to the increase in energy content. As the lattice energy increases, the increased amplitude of vibration between equivalent energy positions results in an increased atomic separation corresponding to lattice expansion. At a given temperature, the coefficient of thermal expansion (CTE) is defined as:

$$\alpha = \frac{1}{l_0} \frac{dl}{dT} \quad (2.17)$$

and the coefficient of volume expansion is:

$$\alpha_v = \frac{1}{V_0} \frac{dV}{dT} \quad (2.18)$$

where  $l_0$  and  $V_0$  are the original specimen length and volume, respectively. For an isotropic solid,  $\alpha_v = 3\alpha$ . Generally, these values are a function of temperature. Because the change in volume due to slightly anharmonic lattice vibrations is closely related to the increase in energy content, thermal expansion increases with temperature, as does heat capacity.

For cubic crystals, the thermal expansion coefficients along different crystallographic axes are equal. The corresponding changes in dimension are symmetrical. For nonisometric crystals, however, the thermal expansion varies along different crystallographic axes. Graphite, due to its layered crystalline structure, exhibits highly anisotropic expansion. The expansion is much lower in the plane of the layer (CTE =  $1 \times 10^{-6}/^{\circ}\text{C}$ ) than normal to it (CTE =  $27 \times 10^{-6}/^{\circ}\text{C}$ ). In strongly anisometric crystals, the expansion coefficient in one direction may be negative, as is the case for graphite along the a-axis, and the resulting volume expansion quite low. The negative coefficient of thermal expansion observed in graphite (crystals) below  $400^{\circ}\text{C}$  is primarily due to in-plane vibrations [65].

#### 2.7.2.1 Expansion Coefficient of Composite Materials

The coefficient of thermal expansion for a composite material can be calculated based upon a model. Assuming no cracks develop, the contraction of each grain is the same as the overall contraction and all microstresses are pure hydrostatic tension and compression (interfacial shear is negligible), the coefficient of volume expansion for a composite material is given by [64]:

$$\alpha_c = \frac{\alpha_1 K_1 f_1 / \rho_1 + \alpha_2 K_2 f_2 / \rho_2 + \dots}{K_1 f_1 / \rho_1 + K_2 f_2 / \rho_2 + \dots} \quad (2.19)$$

where  $\alpha_i$  is the CTE,  $K = E / 3(1 - 2\mu)$  is the bulk modulus,  $f_i$  is the weight fraction,  $\rho_i$  is the density, of phase  $i$ . An alternative model takes into account shear effects at the boundaries between grains or phases. Considering the displacement of the individual components and applying continuity relations at the interfaces, the overall expansion coefficient can be expressed as follows:

$$\alpha_c = \alpha_1 + V_2 (\alpha_2 - \alpha_1) \frac{K_1 (3K_2 + 4G_1)^2 + (K_2 - K_1) (16G_1^2 + 12G_1 K_2)}{(4G_1 + 3K_2) [4V_2 G_1 (K_2 - K_1) + 3K_1 K_2 + 4G_1 K_1]} \quad (2.20)$$

where  $V_i$  is the volume and  $G_i$  is the shear modulus, of phase  $i$ .

### 2.7.2.2 Microstresses

Stresses that develop as a result of large differences between thermal expansion coefficients of two phases of a composite, or in different crystallographic directions, may be sufficient to cause microcracks in the composite material. The effect of heating and reheating can result in increased cracking on cooling or annealing of cracks already present. The opening and closing of such cracks can lead to observed hysteresis behavior in thermal property measurements due to the large stresses that develop. This type of hysteresis occurs particularly in materials where the CTE largely varies in different directions, or in composites where the CTE mismatch is quite high.

Microstresses can also develop in materials that are restrained from expansion by being held in a fixed support or by being attached to a material of different expansion coefficient. If a solid body is completely restrained from expanding, the stress in the part is described by [64]:

$$\sigma = \frac{E\alpha\Delta T}{1-\mu} \quad (2.21)$$

where  $E$  is the Young's modulus,  $\Delta T$  is the temperature change and  $\mu$  is Poisson's ratio.

### 2.7.3 Heat Conduction

The basic equation describing the rate of heat transfer through a material under a particular temperature gradient is as follows:

$$\frac{dQ}{d\theta} = -kA \frac{dT}{dx} \quad (2.22)$$

where  $dQ$  is the amount of heat flowing normal to an area  $A$  in time  $d\theta$ . The heat flow is proportional to the temperature gradient,  $-dT/dx$ . The proportionality constant,  $k$ , is the thermal conductivity, a material constant.

To apply Equation 2.22 under steady state conditions in which the heat flux ( $q = dQ/d\theta$ ) and the temperature at each point are independent of time, requires an integration for the shape under consideration. For heat flux through a flat slab, Equation 2.22 is:

$$q = -kA \frac{T_2 - T_1}{x_2 - x_1} \quad (2.23)$$

For radial heat flow out through a cylinder of length,  $l$ , inner diameter,  $D_1$ , and outer diameter,  $D_2$ :

$$q = -k(2\pi l) \frac{T_2 - T_1}{\ln D_2 - \ln D_1} \quad (2.24)$$

The ratio of thermal conductivity to heat capacity,  $k/\rho c_p$ , is the thermal diffusivity, in units of length<sup>2</sup>/time. The rate of change of temperature of a volume element  $dx dy dz$  is illustrated in Figure 2.25 and given as:

$$\frac{dT}{d\theta} = \frac{d\left(\frac{k}{\rho c_p} \frac{dT}{dx}\right)}{dx} \quad (2.25)$$

#### 2.7.4 Thermal Conduction Processes

Under the influence of a temperature gradient, the conduction process for heat-energy transfer depends on the energy concentration present per unit volume, its velocity of movement and its rate of dissipation with the surroundings. In order to predict the resulting thermal conductivity, each of these

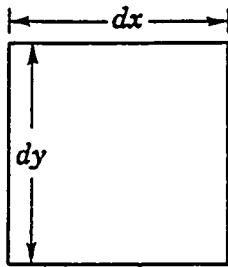


Diagram of a cube element with dimensions  $dx$  and  $dy$ . Heat flow  $Q_{in}$  enters from the left and  $Q_{out}$  exits to the right. The element is a square with width  $dx$  and height  $dy$ .

$$Q_{in} = -k_x (dy \, dz) \left( \frac{dT}{dx} \right) d\theta$$

$$Q_{out} = -(dy \, dz) \left[ k_x \frac{dT}{dx} + \frac{d \left( k_x \frac{dT}{dx} \right)}{dx} dx \right] d\theta$$

$$Q_{in} - Q_{out} = (dx \, dy \, dz) \frac{d \left( k_x \frac{dT}{dx} \right)}{dx} d\theta$$

$$= (dx \, dy \, dz) \left( \rho c \frac{dT}{d\theta} \right) d\theta$$

Figure 2.25. Transient heat flow through a cube element [64].



factors must be considered. The thermal conductivity coefficient  $k$  of a solid is defined with respect to steady-state heat flow along a rod with temperature gradient  $dT / dx$  as [66]:

$$j = -k \frac{dT}{dx} \quad (2.26)$$

where  $j$  is the flux of thermal energy, or the energy transmitted across unit area per unit time.

The thermal energy transfer process is a random process due to collisions of electrons and phonons as the energy travels through a sample. Because the energy is not propagated directly through the sample without deflection, the expression for the thermal conductivity depends on the temperature gradient in the material and the mean free path. The behavior of electrons and phonons in a solid can be described in terms of that of particles or molecules of a gas. From the kinetic theory of gases, the thermal conductivity is approximated as:

$$k = \frac{1}{3} cvl \quad (2.27)$$

where  $c$  is the heat capacity per unit volume,  $v$  is the average particle velocity and  $l$  is the mean free path of the particle between collisions [66]. The flux of particles in the  $x$  direction is  $\frac{1}{2} n |v_x|$ , where  $n$  is the concentration of molecules and  $v_x$  is the average particle velocity. A particle moving from a region at local temperature  $T + \Delta T$  to a region at local temperature  $T$  will give up energy  $c\Delta T$ , where  $c$  is the heat capacity of the particle. The temperature difference between the ends of the free path of the particle is given by:

$$\Delta T = \frac{dT}{dx} l_x = \frac{dT}{dx} v_x \tau \quad (2.28)$$

where  $\tau$  is the average time between collisions. The net flux of energy is therefore:

$$j = -n v_x^2 c \tau \frac{dT}{dx} = -\frac{1}{3} n v^2 c \tau \frac{dT}{dx} \quad (2.29)$$

If, as in the case of phonons in a solid,  $v$  is constant, Equation 2.29 can be written as:

$$j = -\frac{1}{3} c v l \frac{dT}{dx} \quad (2.30)$$

with  $l \equiv v\tau$  and  $c \equiv n c$ . Thus  $k = \frac{1}{3} c v l$ .

#### 2.7.4.1 Thermal Resistivity

The phonon mean free path  $l$  is determined primarily by two processes: (1) geometrical scattering and (2) scattering by other phonons. If the forces between atoms were purely harmonic, there would be no mechanism for collisions between different phonons. In this case, the mean free path would be limited solely by phonon collisions with crystal boundaries, and by lattice imperfections. There is a coupling between different phonons which limits the mean free path with anharmonic lattice imperfections. At high temperatures the total number of excited phonons is proportional to  $T$ . The collision frequency of a given phonon is proportional to the number of phonons with which it can collide. The effect of anharmonic coupling on thermal resistivity predicts, therefore, that  $l \propto 1/T$  at high temperatures as further described below.

#### 2.7.4.2 Umklapp Processes

The major process which limits the thermal conductivity of any given material is phonon-phonon scattering involving a reciprocal lattice vector, called the umklapp process. The important three-phonon collision processes that cause thermal resistivity are of the form [66]:

$$\mathbf{K}_1 + \mathbf{K}_2 = \mathbf{K}_3 + \mathbf{G} \quad (2.31)$$

where  $\mathbf{K}_1$  and  $\mathbf{K}_2$  are the wave vectors of two individual phonons absorbed in the collision process,  $\mathbf{K}_3$  is the wave vector of the emitted phonon and  $\mathbf{G}$  is the reciprocal lattice vector. There are various cases of wave interaction processes in crystals for which the total wave vector change is not zero, and may be a reciprocal lattice vector. These processes are likely to occur in periodic lattices.

Other important factors limiting the mean free path are geometrical effects. These include scattering by crystal boundaries, the distribution of isotopic masses in natural chemical elements, chemical impurities, lattice imperfections and amorphous structures.

#### 2.7.5 Electrical Conductivity

The electrical conductivity is determined from Ohm's Law as [66, 67]:

$$\sigma = \frac{ne^2\tau}{m} \quad (2.32)$$

where  $n$  = number of electrons per unit volume  
 $e$  = electron charge  
 $\tau$  = time between collisions of conduction electrons  
 $m$  = electron mass.

The electrical resistivity is defined as the reciprocal of the conductivity and is given by [66]:

$$\rho = \frac{m}{ne^2\tau} \quad (2.33)$$

The mean free path of a conduction electron is defined as  $l = v\tau$ . For pure Cu,  $v = 1.57 \times 10^8 \text{ cm/s}$ .

The mean free path, therefore, is  $l \approx 3 \times 10^{-6} \text{ cm}$  at room temperature.

The electrical resistivity of most metals is governed by collisions of the conduction electrons with lattice phonons at room temperature (300 K), and by collisions with impurity atoms and mechanical imperfections in the lattice at liquid helium temperature (4 K) [66]. The rates of these collisions are often independent and the net resistivity is:

$$\rho = \rho_i + \rho_L \quad (2.34)$$

where  $\rho_i$  is the resistivity due to the presence of impurities and  $\rho_L$  is the resistivity due to the scatter of the electron waves by phonons in the lattice. Frequently,  $\rho_i$  is independent of temperature and  $\rho_L$  is independent of the number of defects (when the total concentration is low). Matthiessen's Rule, given as Equation 2.34, expresses this empirical observation as illustrated in Figure 2.26. The Debye temperature,  $\theta_D$ , is the temperature at which the atoms have an approximately constant rate of change of energy of oscillation with temperature.

Matthiessen showed, in 1862, that the slopes of the curves of resistivity versus temperature of well-annealed, very dilute, solid-solution alloys containing approximately 3 at% or less of alloying elements were essentially equal to those of the annealed, pure base element [67]. The intercepts of the curves are primarily affected by alloy or impurity content. The residual resistivities,  $\rho_i$  at 0 K, shift the curves and account for the differences in the resistivities of the various dilute alloys at a given temperature.

#### 2.7.6 Thermal Conductivity of Metals

In pure metals, free electrons are the major heat carriers and therefore the electronic contribution to the thermal conductivity is dominant at all temperatures [66]. In impure metals and disordered alloys the electron mean free path is lowered by collisions with impurities. In these cases, the phonon contribution to the thermal conductivity may be comparable to the electronic contribution.

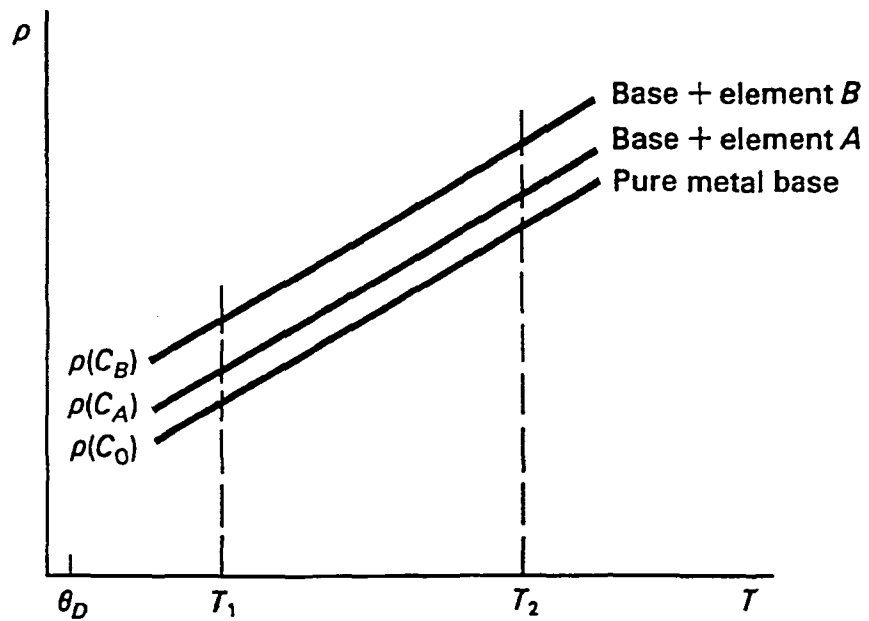


Figure 2.26. Electrical resistivity as a function of temperature for annealed, dilute, random and binary solid solutions [67].

For pure metals, the thermal conductivity,  $k$ , and the electrical conductivity,  $\sigma$ , are related by the Wiedemann-Franz law as follows [68]:

$$\frac{k}{\sigma T} = L = \text{constant} \quad (2.35)$$

The Lorenz number,  $L$ , is approximately  $22 \text{ to } 29 \times 10^{-9} \text{ volts}^2 / \text{K}^2$  for pure metals at  $0^\circ\text{C}$  and changes very little above  $0^\circ\text{C}$ . While the equation is not suitable for nonmetals in which the concentration of free electrons is very low, it can be used for semi-metals, such as graphite, where the electrical conductivity in the  $a$ -direction is very high.

#### 2.7.7 Conductivity of Composite Materials

The resulting conductivity of two phase or composite materials depends on the arrangement of the individual components and the microstructure of the material. An idealized phase arrangement can be considered as shown in Figure 2.26. This parallel slab arrangement is typical of laminate composites. For the simple geometry, if heat flow is parallel to the plane of the slabs, they behave like a parallel electrical circuit. Each slab has the same thermal gradient, and most of the heat flow is through the better conductor. In this case, the composite thermal conductivity is given by [64, 69]:

$$k_c = V_1 k_1 + V_2 k_2 \quad (2.36)$$

where  $V_1$  and  $V_2$  are the volume fractions, and  $k_1$  and  $k_2$  are the thermal conductivities of each component. Under these conditions, where the heat flow is parallel to the plane of the slabs, if  $k_1 \gg k_2$ ,  $k_c \approx V_1 k_1$ . In contrast, for heat flow perpendicular to the plane of the slabs, they are similar to an electrical series circuit. The heat flow through each slab is the same, but the temperature gradients are different. The composite thermal conductivity is now given by [64]:

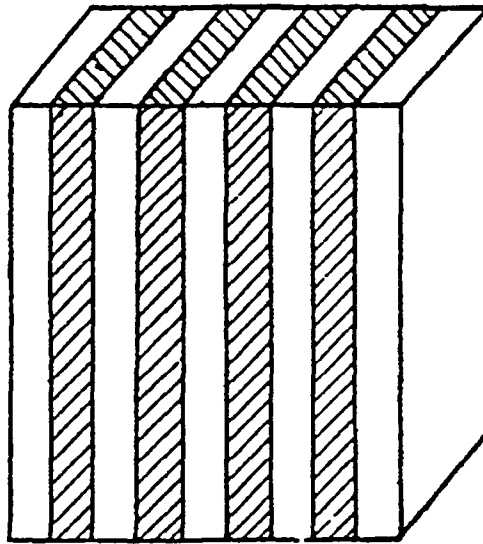


Figure 2.27. Parallel slab (laminate) arrangement of two phases [64].

$$\frac{1}{k_c} = \frac{V_1}{k_1} + \frac{V_2}{k_2}$$

or

(2.37)

$$k_c = \frac{k_1 k_2}{V_1 k_2 + V_2 k_1}$$

In this case, the heat conduction is dominated by the weaker conductor, and if  $k_1 > k_2$ ,  $k_c = k_2 / V_2$ .



### 3 EXPERIMENTAL PROCEDURES

#### 3.1 Pressure Infiltration Casting

During the past several years, the method of pressure infiltration casting (PIC) has been developed for the production of continuous fiber composites [70]. The PIC technique, developed by PCast Equipment Corporation, involves using pressure to assist the infiltration of a liquid metal into a mold containing the fiber reinforcement. The PIC process has been employed to fabricate P100Gr/Cu composites.

##### 3.1.1 Procedure

The casting process is conducted within a single pressure vessel which contains the mold, the preform, the mold furnace, the melt, the melt furnace and means for controlling the solidification. The preform and melt are first evacuated through the mold in order to remove trapped air from the vessel. Once the desired operating temperatures are obtained, the mold is connected to the melt. This connection isolates the vacuum in the mold. The vessel is then pressurized which causes an application of force on the outside of the mold, pushing the two halves of the mold together. The melt is forced into the mold to isostatically infiltrate the preform and all details of the mold cavity. Due to friction between the metal and the mold, the pressure applied to the metal outside of the mold is always greater than the pressure transmitted to the metal inside the mold. By controlling the pressurization rate, the pressure difference between the inside and the outside of the mold can be controlled. Lower strength, less expensive molds can be used when this pressure difference is minimized. The solidification controls allow changes to be made in the solidification rate and direction. In turn, controlling solidification rate and direction allows tailoring of the final microstructure which includes variation in the extent of fiber/matrix interaction. The process sequence is illustrated in Figure 3.1.

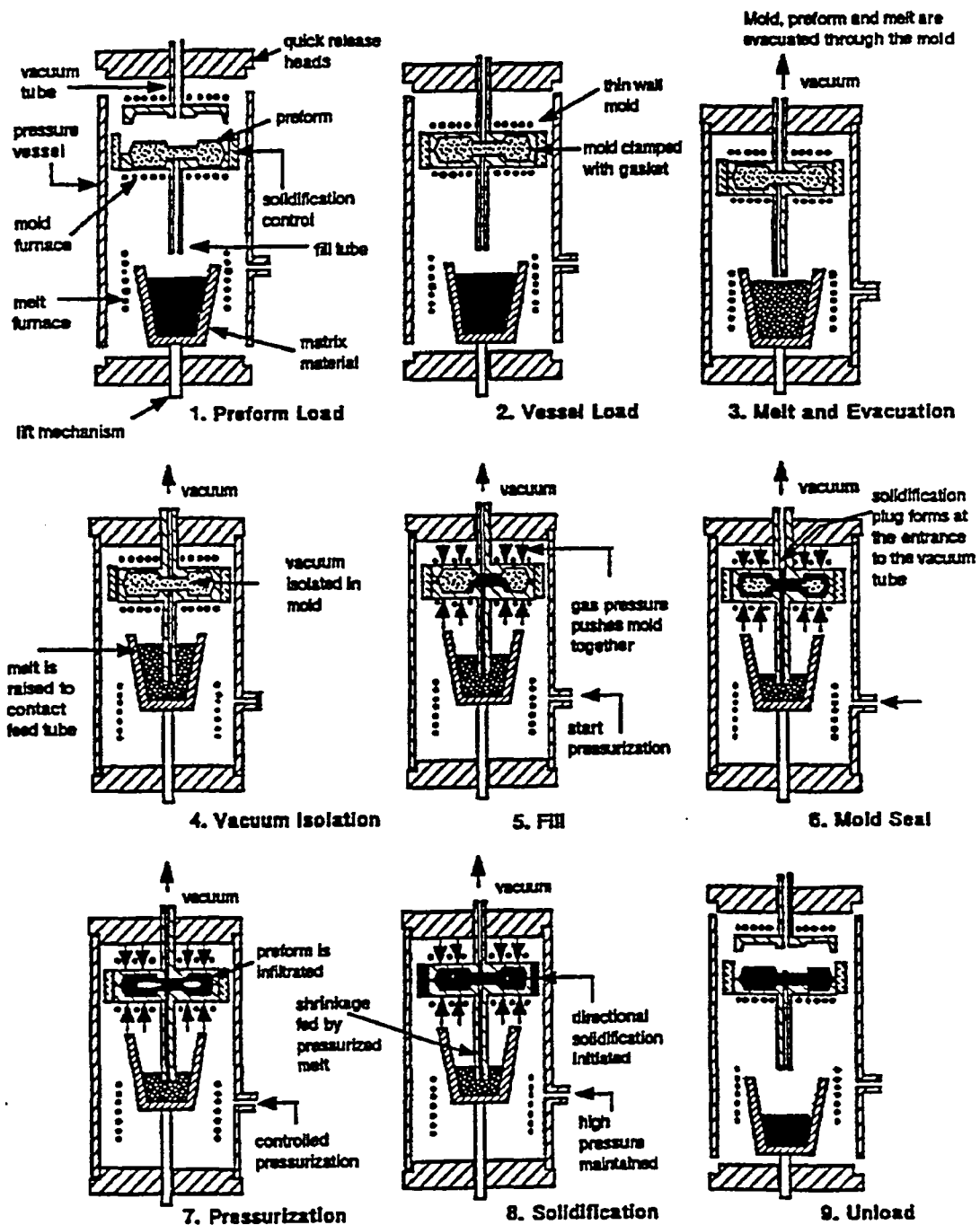


Figure 3.1. Conceptual schematic of pressure infiltration casting process [70].

### 3.1.2 Materials

Unidirectionally reinforced Gr/Cu composites were cast at PCast Equipment Corporation, under contract to NASA Lewis Research Center. Plates approximately 7.5 x 15.2 x 0.15 cm (3 x 6 x 0.060 in) in size were produced. Three matrices were used: (1.) OFHC Cu, (2.) OFHC Cu with 0.3 wt% Cr and (3.) OFHC Cu with 0.7 wt% Cr. The reinforcement consisted of high conductivity, high stiffness, pitch-based P100 graphite fibers purchased from Amoco Performance Products, Inc. The unsized P100 fibers were obtained in 2K tows (2000 fibers per tow). A total of 470 tows were wrapped through each mold to produce plates containing nominally 60 v/o fiber. The fiber was aligned parallel to the 15.2 cm dimension of each plate as shown in Figure 3.2. The density of the P100Gr/Cu composites was anticipated to be about 4.9 g/cm<sup>3</sup> based upon calculations assuming the plates contained 60 v/o graphite fiber. A complete inventory of plates received is given in Table 3.1. In total, twenty plates were cast: eight P100Gr/Cu, eight P100Gr/Cu-0.3Cr and four P100Gr/Cu-0.7Cr. The plates were cast in batches of four. The plate identification system is as follows: Cu-B1P1 = Cu matrix-batch 1 plate 1; 0.7Cr-B1P3 = Cu-0.7Cr matrix-batch 1 plate 3.

### 3.1.3 X-ray Inspection

Each plate was x-rayed through its thickness. The presence of surface cracks and density variations was revealed by changes in the transmitted x-ray intensity as recorded by film placed on the underside of each plate.

### 3.1.4 Plate Machining

Specimens for microscopic analyses and mechanical and thermal testing were wire electrical discharge machined (EDMed) from the various plates. The machining design used for sixteen of the twenty plates is given in Figure 3.3. This design was employed to minimize plate scrap and to allow for the investigation of variations in fiber distribution across the plate through tensile testing. From the four remaining plates, specimens were machined from Cu-B2P4 and 0.3Cr-B2P3 for additional long transverse tensile testing. The machining specifications for those plates are shown in Figure 3.4.

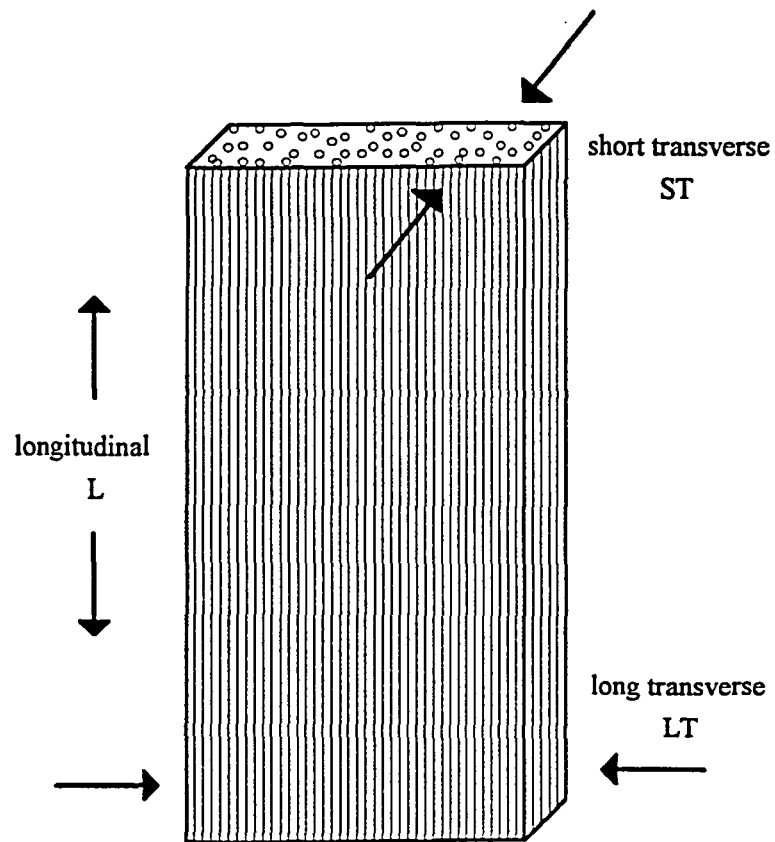


Figure 3.2. P100 graphite fiber orientation in composite plates.

TOP

BOTTOM

	transverse tensile	transverse tensile	transverse tensile	transverse tensile	transverse tensile	thermal diffusivity F	longitudinal tensile		M
						thermal diffusivity G	longitudinal tensile		N
						T-thermal expansion H	longitudinal tensile		O
							longitudinal tensile		P
						I met lab	longitudinal tensile		Q
						J met lab			
						specific heat (K)	L-thermal expansion	L	SCRAP

Figure 3.3. Plate machining design indicating all test specimens.

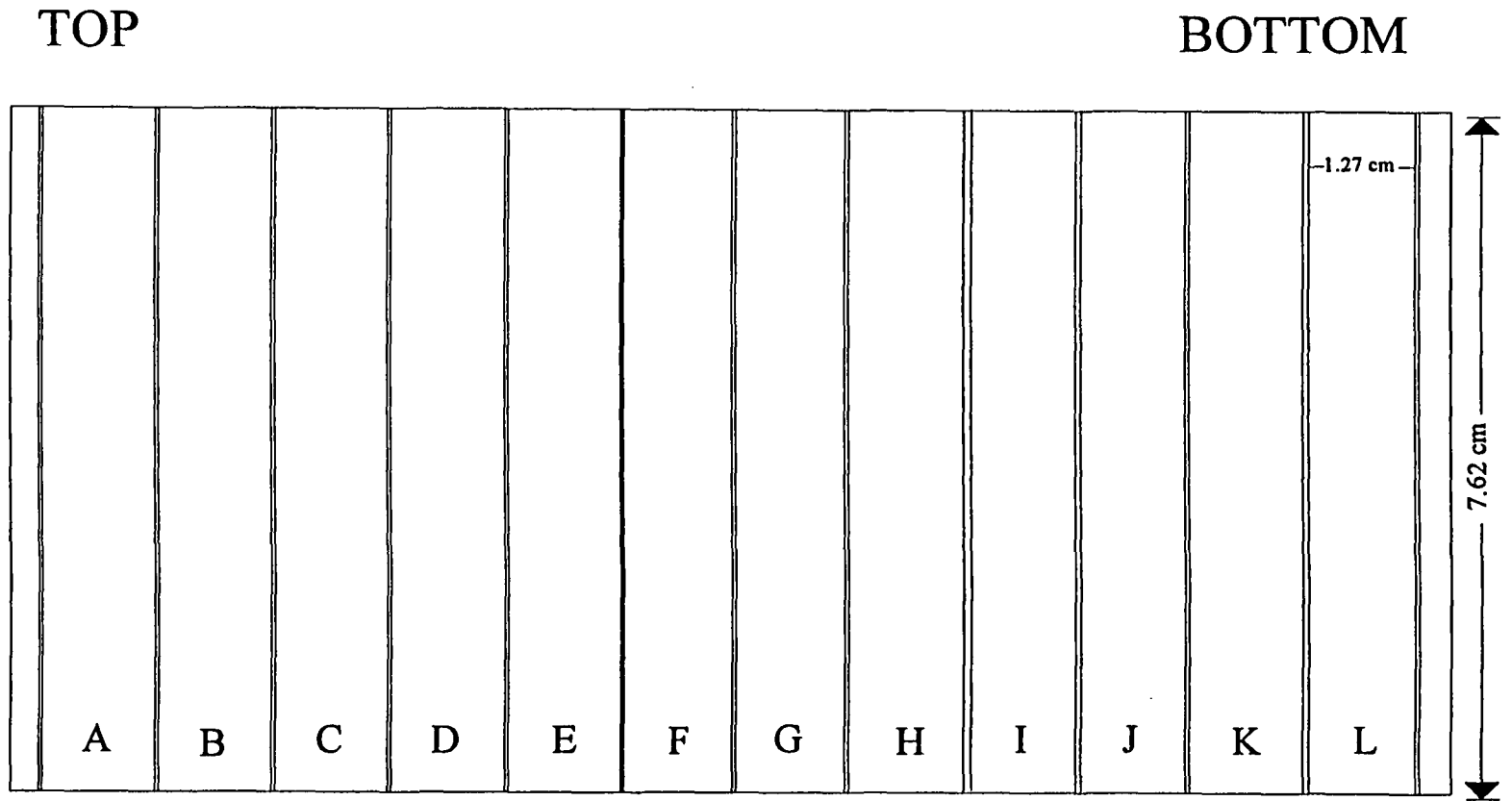


Figure 3.4. Machining specifications for additional long transverse tensile specimens.

Table 3.1. P100Gr/Cu-xCr composite plate identification and descriptions.

	Batch No.	Plate I.D.	Matrix	T <sub>mold</sub> , °C	T <sub>melt</sub> , °C	P <sub>max</sub> , MPa
Cu-B1P1 Cu-B1P2 Cu-B1P3 Cu-B1P4	747	TOA1 TIA2 TIA3 TOA4	Cu	1044	1183	9.10
Cu-B2P1 Cu-B2P2 Cu-B2P3 Cu-B2P4	763	OT1 IT1 IT2 OT2	Cu	1024	1161	9.12
0.3Cr-B1P1 0.3Cr-B1P2 0.3Cr-B1P3 0.3Cr-B1P4	750	OT1A IT2A IT3A OT4A	Cu-0.3Cr	1033	1153	9.10
0.3Cr-B2P1 0.3Cr-B2P2 0.3Cr-B2P3 0.3Cr-B2P4	770	OT1 IT2 IT3 OT4	Cu-0.3Cr	1036	1183	9.14
0.7Cr-B1P1 0.7Cr-B1P2 0.7Cr-B1P3 0.7Cr-B1P4	766	OT1 IT2 IT3 OT4	Cu-0.7Cr	1013	1186	9.02

After machining, the specimens were cleaned with an impregnated metal polishing pad to remove surface oxides. Each specimen was then weighed using an electronic analytical balance (0.1 mg accuracy) and the three dimensions measured using a digital micrometer. The %P100 fiber reinforcement in each composite specimen was calculated using the following equation:

$$\%P100 = \frac{\rho_m - \rho_c}{\rho_m - \rho_f} \cdot 100 \quad (3.1)$$

where  $\rho_c$ ,  $\rho_f$  and  $\rho_m$  are the densities of the composite specimen, P100 fiber and Cu matrix, respectively. The presence of voids and interfacial carbides was not taken into account in calculating

$\rho_c$ . The overall plate densities and %P100 were calculated as weighted averages, taking the volume of each specimen into account.

### 3.2 Optical Metallography

Optical micrographs were obtained for the sixteen plates used for the majority of the mechanical and thermal property evaluations. Investigation in the short transverse orientation allowed for the evaluation of the homogeneity of the composites and the quality of the castings. Fiber distribution, i.e. presence of fiber clusters, incomplete infiltration and Cu channelling (areas containing no fiber reinforcement), was investigated. The presence and continuity of the interfacial reaction layers which formed in the P100Gr/Cu-0.3Cr and P100Gr/Cu-0.7Cr composites were also assessed.

The metallographic specimens were mounted in epoxy and taken to a final polish using 0.5  $\mu\text{m}$  diamond paste. The final polishing step was performed using a DP-Plus long nap, synthetic cloth with an ethyl glycol lubricant. The specimens were polished on a Buehler Vibromet polisher for a period of 4-6 hours. Each specimen was studied using a Reichert MeF3 A optical microscope with a capable magnification range of 8X to 2250X.

Select metallographic specimens were etched to enhance the visibility of the reaction layer which formed at the fiber/matrix interface. A standard Cu etch composed of 2 g  $\text{K}_2\text{Cr}_2\text{O}_4$  + 100 ml  $\text{H}_2\text{O}$  + 8 ml  $\text{H}_2\text{SO}_4$  + 4 drops HCl was used. Etching time was approximately 45 s.

### 3.3 Scanning Electron Microscopy

A Joel 840-A scanning electron microscope (SEM) was used to perform additional analyses on the etched metallographic specimens to further investigate the reaction layer and any damage to the fiber surfaces. Using a Kevex system, energy dispersive spectroscopy (EDS) analyses were conducted to identify the constituents of the reaction layer phase.



### 3.4 Auger Electron Spectroscopy

Polished composite cross-sections were prepared for characterization using a PHI 660 SAM Auger electron spectroscopy (AES) system, with a beam current of 200 nAmps (10 kV) and a beam diameter estimated to be several thousand angstroms. The composite surface was sputtered to remove 1000 Å. A Cr elemental map was obtained from an area containing fibers near a matrix rich region, to verify the SEM observation that the Cr segregates to the fiber surface to form a reaction phase. An additional map was taken from a high magnification area containing a single fiber. Line scans of Cu, Cr, C and O were taken across the interfacial region. This was done to further indicate any segregation of the alloying addition to the interface.

### 3.5 Transmission Electron Microscopy

Transmission electron microscopy (TEM) investigation of the Gr/Cu interface was conducted on the P100Gr/Cu-0.7Cr composite using a Philips 400 microscope. Specimens were prepared by sectioning the plates normal to the fiber axis. Several such sections were held together with epoxy to produce a width of greater than 3 mm. Discs ultrasonically machined from the piece were dimpled and ion beam milled to perforation. The reaction layer was studied and identified using a combination of imaging and selected area diffraction (SAD) methods.

### 3.6 Tensile Testing

#### 3.6.1 Specimen Design

Long transverse and longitudinal tensile specimens were tested from each composite plate. A total of five specimens were obtained from each plate for testing of both reinforcement directions. The tensile tests were conducted on specimens 7.62 x 1.27 x 0.15 cm (3 x 0.5 x 0.060 in) in size. Tapered steel tabs were affixed to the ends of the specimens using a two part epoxy adhesive with a

shear strength of 6.9 Mpa (1000 psi), resulting in a total sample length of 10.2 cm (4 in). With the hope of ensuring composite fractures in the gage length of the extensometer, a 1.59 cm (0.63 in) reduced section of 0.79 cm (0.313 in) thickness was introduced into the longitudinal specimens. The design specifications for both the long transverse and longitudinal tensile test specimens are given in Figure 3.5.

Aluminum specimens were tested prior to each set of tensile tests to monitor errors due to machine variability.

### 3.6.2 Heat Treatment

Longitudinal tensile specimens were heat treated prior to testing. The heat treatment was conducted in a furnace with an argon atmosphere at 760°C (1400°F) for 1, 3, 10, 30 and 100 hr lengths of time. The Gr/Cu specimens were sealed individually in FeCrAlY bags which were back-filled with argon. The bags were then placed inside another FeCrAlY bag containing titanium sponge pellets, back-filled with argon and sealed. This was done to prevent oxidation of the composite specimens. The specimen filled bags were placed in the furnace at temperature. They were removed and air cooled after the specified duration.

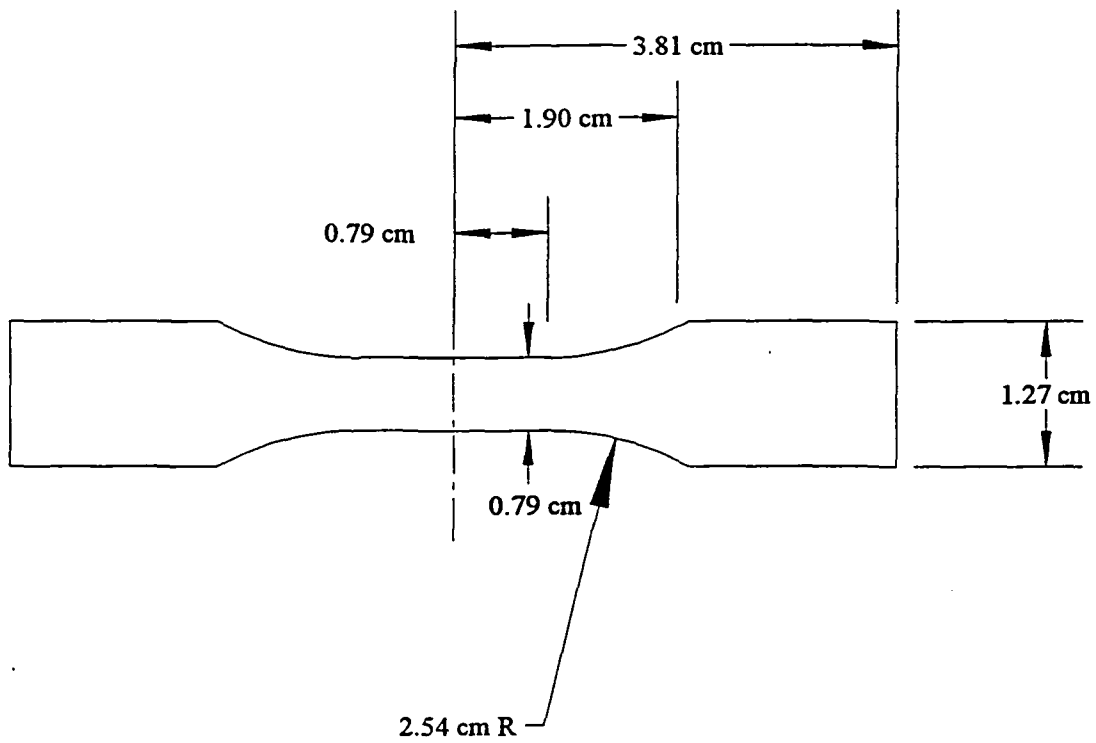
### 3.6.3 Test Method

Room temperature tensile tests were performed in an Instron® load frame equipped with MTS® hydraulic grips. A grip pressure of 20 MPa (3 ksi) was used for the longitudinal tensile specimens to minimize slipping between the specimen tabs and the grips. An extensometer having a 1.27 cm (0.5 in) gage length was used for accurate measurement of the elongation. The machine crosshead was loaded at a constant rate of  $2.12 \times 10^{-4}$  cm/s (0.005 in/min). Load and elongation were recorded by a computer and subsequently converted to stress-strain curves. Linear regression techniques were used to determine the elastic moduli of the specimens.

The long transverse test specimens were tested in the as-cast condition. The matrix of test specimens is given in Table 3.2. The unbalanced nature of the testing design is attributed to the



(a) long transverse



(b) longitudinal

Figure 3.5. Long transverse and longitudinal tensile specimen designs.

difficulty in handling and preparing test specimens containing reinforcement in the long transverse direction.

Table 3.2. Long transverse tensile test matrix.

Plate	I.D.	test order	Plate	I.D.	test order	Plate	I.D.	test order
Cu-B1P1	A	10	0.3Cr-B1P1	B	17	0.7Cr-B1P1	B	30
	E	8		E	19		E	9
Cu-B1P2	A	7	0.3Cr-B1P2	A	41	0.7Cr-B1P4	C	35
	B	15		D	20		D	1
	D	45					E	16
Cu-B1P3	C	2	0.3Cr-B1P4	B	23			
	E	21		D	25			
				E	4			
Cu-B1P4	B	36						
	D	5						
	E	26						
Cu-B2P2	E	43	0.3Cr-B2P1	C	11			
				D	3			
Cu-B2P3	A	14	0.3Cr-B2P2	B	24			
	B	6						
	D	42						
Cu-B2P4	A	22	0.3Cr-B2P3	C	33			
	C	39		D	13			
	D	34		G	29			
	E	38		H	27			
	F	44		I	28			
	G	18		J	31			
	I	32		K	40			
	J	37						
	K	12						

The longitudinal test specimens were tested in both the as-cast and heat treated conditions. A "Design of Experiments" approach was used to develop the test matrix to achieve a fully randomized design. The matrix design is shown in Tables 3.3 through 3.5. Test error (machine variation over time) was accounted for by completely randomizing the testing sequence. It is an unbalance design, however, because there was only one batch of P100Gr/Cu-0.7Cr composites.

Table 3.3. Longitudinal tensile test matrix - P100Gr/Cu.

Plate	I.D.	as-cast	1 hr 760°C	3 hr 760°C	10 hr 760°C	30 hr 760°C	100 hr 760°C		test order
Cu-B1P1	M		M						19
	N	N							44
	O								
	P	P						3PB	13
	Q						Q		50
Cu-B1P2	M			M					40
	N		N						9
	O	O							58
	P						P		49
	Q	Q							52
Cu-B1P3	M							3PB	29
	N	N							16
	O				O				7
	P	P							10
	Q					Q			
Cu-B1P4	M	M							24
	N			N					28
	O	O							68
	P					P			65
	Q				Q				2
Cu-B2P2	M	M							45
	N	N							21
	O		O						43
	P			P					62
	Q					Q			14
Cu-B2P3	M						M		15
	N				N				67
	O	O							72
	P							3PB	
	Q	Q							53
TOTAL	30	12	3	3	3	3	3	3	

Table 3.4. Longitudinal tensile test matrix - P100Gr/Cu-0.3Cr.

Plate	I.D.	as-cast	1 hr 760°C	3 hr 760°C	10 hr 760°C	30 hr 760°C	100 hr 760°C		test order
0.3Cr B1P1	M	M							55
	N		N						4
	O								
	P	P						3PB	36
	Q						Q		59
0.3Cr B1P2	M			M					32
	N		N						38
	O	O							69
	P						P		41
	Q	Q							12
0.3Cr B1P3	M							3PB	
	N	N							46
	O				O				56
	P	P							25
	Q					Q			44
0.3Cr B1P4	M	M							66
	N			N					48
	O	O							39
	P					P			47
	Q				Q				33
0.3Cr B2P1	M	M							42
	N	N							64
	O		O						61
	P			P					11
	Q					Q			57
0.3Cr B2P3	M						M		1
	N				N				26
	O	O							70
	P							3PB	
	Q	Q							8
TOTAL	30	12	3	3	3	3	3	3	

Table 3.5. Longitudinal tensile test matrix - P100Gr/Cu-0.7Cr.

Plate	I.D.	as-cast	1 hr 760°C	3 hr 760°C	10 hr 760°C	30 hr 760°C	100 hr 760°C		test order
0.7Cr B1P1	M		M					3PB	54
	N								5
	O	O							6
	P	P							35
0.7Cr B1P2	Q					Q		3PB	
	M	M			N				22
	N		O						71
	O								51
0.7Cr B1P3	P								31
	Q	Q							
	M	N		M					17
	N	O							30
0.7Cr B1P4	O								20
	P					P			3
	Q						Q		18
0.7Cr B1P4	M	M							27
	N	N							23
	O						O		63
	P			P					37
0.7Cr B1P4	Q				Q				60
TOTAL	20	8	2	2	2	2	2	2	

#### 3.6.4 Fractography

SEM analyses were conducted on failed test specimens in order to qualify interfacial adherence and fracture modes. The presence of a reaction layer phase on the fracture surfaces was investigated.

#### 3.6.5 Statistical Analysis

An analysis of variance approach was employed to analyze the longitudinal tensile data. An unbalanced, fully nested analysis of variance (ANOVA) was conducted for each heat treatment time. The effects on the tensile strength of both matrix composition and heat treatment time were determined. Due to the nature of the test matrix design, it was also possible to comment on specimen-to-specimen (within plate), plate-to-plate (within a batch) and batch-to-batch variations.

### 3.7 Three-Point Bend Testing

#### 3.7.1 Test Method

Specimens 7.62 x 1.27 x 0.15 cm (3 x 0.5 x 0.60 in.) in size were tested from the various plates. The tests were conducted in a similar manner to that of ASTM D 2344 [71]. Test specimens were loaded at a constant crosshead speed of 0.01 mm/min. A maximum load of 150 N was employed to ensure loading in the elastic range only. The specimens were then unloaded. The loading configuration is shown in Figure 3.6. A fiber optic probe, with a displacement sensitivity of 0.018 mm/V, was used over a 2 V range to measure the midspan deflections. The optical sensor was mounted inside the support stand and aligned with the specimen's lower surface. The sensor and the three-point bend fixture were mounted on a rigid base plate to eliminate discrepancies due to vibration. During the test, the midpoint deflection and applied load were continuously monitored on a chart recorder and collected by a computer. Three specimens, one from each matrix composition, were run four times at each of the 4.0, 5.0, 5.6 and 7.0 cm span lengths. A pure Cu specimen was tested as a standard.

#### 3.7.2 Data Analysis

Once the data were collected, load vs. deflection curves were generated for each of the tests. Slopes of the linear elastic portions of the curves were obtained taking into account displacements due to Hertzian contact stresses between the specimen and the roller. These slopes were plotted vs. the span length. Curve fitting was done using a statistical software package (RS1). The coefficients obtained were used to calculate the elastic and shear moduli of the composite specimens using the following equation (Equation 2.13):

$$\frac{\delta}{P} = \frac{1}{4Ebh^3}L^3 + \frac{3}{10Gbh}L \quad (3.2)$$



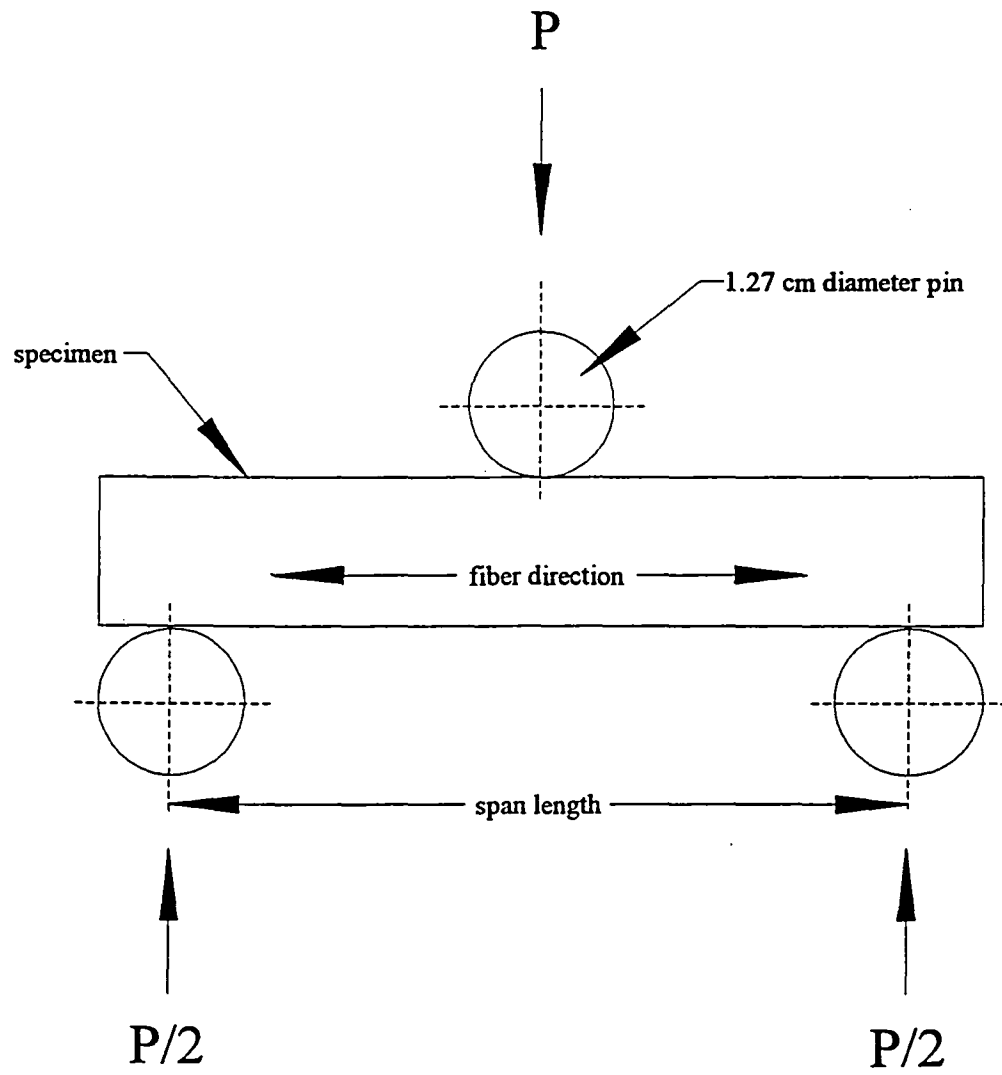


Figure 3.6. Three-point bend loading configuration.

### 3.8 Thermal Expansion

Longitudinal and long transverse thermal expansion specimens were tested from the various cast plates. The longitudinal specimens were approximately 2.54 x 0.98 x 0.17 cm in size. The transverse specimens were 2.54 x 1.27 x 0.17 cm. Each specimen underwent thermal cycling in an argon atmosphere, using a dilatometer. One cycle consisted of heating from 27°C to 827°C and cooling back down to 27°C at a rate of 0.05°C/s (3 °C/min). A total of 32 specimens were tested. One specimen from each matrix composition was tested through multiple cycles. The remaining specimens were tested for one cycle. The entire test matrix is given in Table 3.6. For each cycle, change in length was monitored at a data collection rate of one data point per °C change in temperature. Percent linear change vs. temperature curves were generated from the data. An alumina specimen was tested as a calibration standard.

Table 3.6. Thermal expansion test matrix.

Plate	No. of Cycles	
	Longitudinal	Long Transverse
Cu-B1P1	1	1
Cu-B1P2	1	1
Cu-B1P3	1	1
Cu-B1P4	10	5
Cu-B2P2	1	1
Cu-B2P3	1	1
0.3Cr-B1P1	4	5
0.3Cr-B1P2	1	1
0.3Cr-B1P3	1	1
0.3Cr-B1P4	1	1
0.3Cr-B2P1	1	1
0.3Cr-B2P2	1	1
0.7Cr-B1P1	1	1
0.7Cr-B1P2	1	1
0.7Cr-B1P3	1	1
0.7Cr-B1P4	5	5

### 3.9 Thermal Conductivity

The short transverse thermal conductivities of the P100Gr/Cu-xCr composites were determined using the laser flash technique [72]. This work was conducted under contract to the Thermophysical Properties Research Laboratory (TPRL), Purdue University. In order to calculate thermal conductivities, specific heat and thermal diffusivity measurements were made. The test matrix employed is shown in Table 3.7.

Table 3.7. Thermal conductivity measurement specimens.

Plate	Specimen I.D.	
	Specific Heat	Thermal Diffusivity
Cu-B1P1	K	G
Cu-B2P3	K	G
0.3Cr-B1P4	K	G
0.3Cr-B2P3	K	G
0.7Cr-B1P3	K	G

#### 3.9.1 Specific Heat Measurements

Specific heat was measured using a Perkin-Elmer Model DSC-2 differential scanning calorimeter using sapphire as a reference material. The composite specimens were discs 0.635 cm (0.25 in) in diameter. The sapphire standard and the sample were encapsulated in pans and subjected to the same heat flux. The differential of power required to heat the sample at a same rate as the standard was recorded using a digital data acquisition system. From the mass of the sapphire standard and the pans, the differential power and the known value of the specific heat of sapphire, the specific heat of the sample was computed.

### 3.9.2 Thermal Diffusivity Measurements

Thermal diffusivity was determined using the laser flash technique. In the flash method, the front face of a small 1.27 cm (0.5 in) square sample was subjected to a short laser burst and the resulting rear face temperature rise was recorded. The apparatus consists of a Konrad K2 laser, a high vacuum system including a bell jar with windows for viewing the specimen, a tantalum tube heater surrounding a sample holding assembly, a spring loaded thermocouple or an IR detector, appropriate biasing circuits, amplifiers, A-D converters, crystal clocks and a minicomputer based digital data acquisition system. The computer controls the experiment, collects the data, calculates the results and compares the raw data to the theoretical model [72].

### 3.9.3 Thermal Conductivity Calculations

The thermal conductivity of each composite system was calculated as follows:

$$k(T) = \rho \cdot c_p(T) \cdot \alpha(T) \quad (3.3)$$

where  $k(T)$  = calculated thermal conductivity at temperature  $T$   
 $\rho$  = room temperature bulk density  
 $c_p(T)$  = measured specific heat at temperature  $T$   
 $\alpha(T)$  = measured thermal diffusivity at temperature  $T$ .

## 4 RESULTS

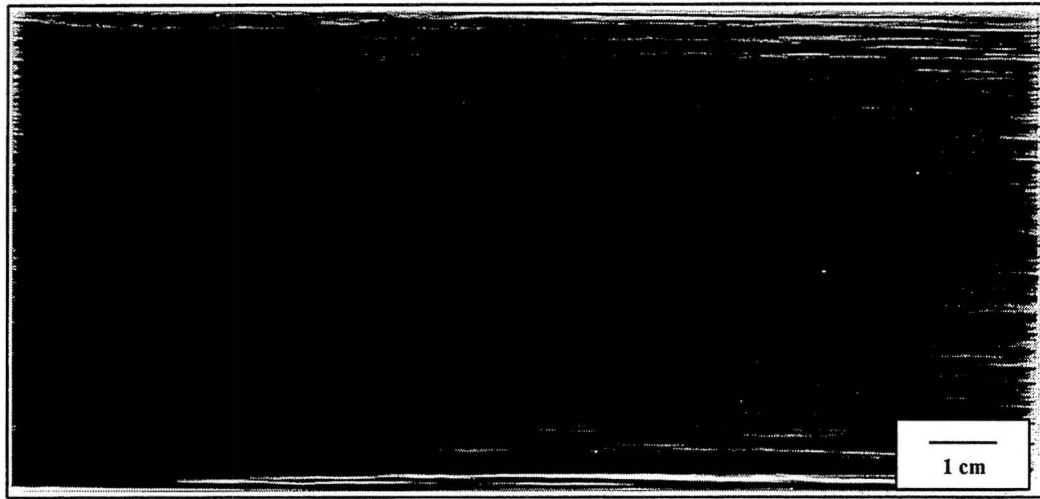
### 4.1 X-Ray Inspection

Select results of the short transverse x-ray inspection for the 20 plates evaluated in this investigation are displayed in Figures 4.1 through 4.3. Listed with the x-ray radiographs are measured densities for the test specimens within each corresponding plate. Specimen-to-specimen, or within plate, variations in density can be observed in the illustrations. The dark areas in the radiographs represent regions with lower than the nominal volume fractions of graphite fibers in the Cu matrix. The white portions of the radiographs contain less of the Cu matrix and conversely a higher volume fraction of the less dense P100 graphite fibers. The continuous nature of the P100 reinforcement is clearly revealed using this inspection technique. Variations in plate thickness and fiber distribution, as well as surface cracks, can be observed.

Variations in plate thickness are most obvious in the P100Gr/Cu-0.7Cr system. Figure 4.3 shows the greatest change in density from top to bottom, the top portion being less dense. Longitudinal surface cracks are evident in approximately one-half of the cast plates. For example, surface cracks are clearly obvious in the P100Gr/Cu-0.3Cr and P100Gr/Cu-0.7Cr plates shown in Figures 4.2 and 4.3. Table 4.1 summarizes the plate-to-plate and batch-to-batch variations in density and percent P100 fiber. Standard deviations were calculated for plate-to-plate (within a batch) and overall variations in volume percent P100 fiber according to the formulas given in Appendix I. The densities were found to range from 4.64-5.20 g/cm<sup>3</sup> with corresponding volume percent fibers of 61-51%.

### 4.2 Optical Metallography

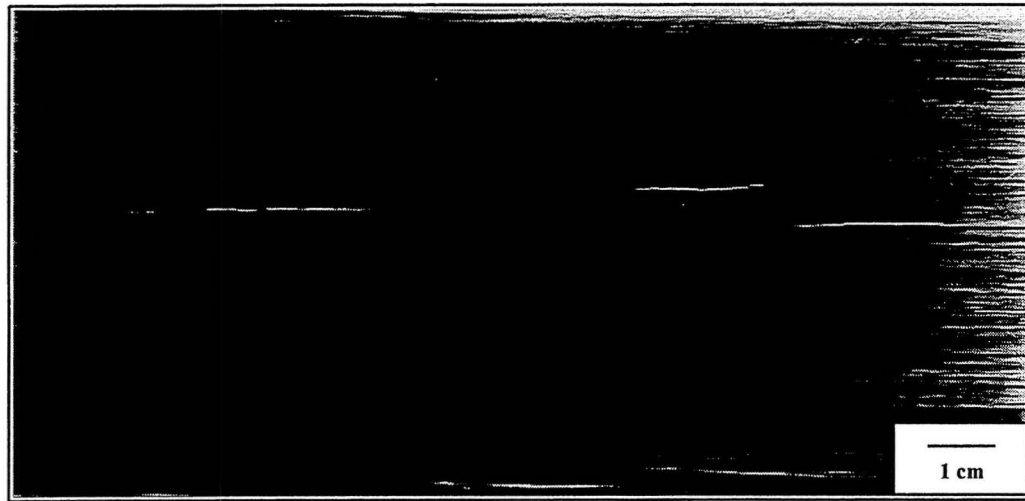
Optical micrographs of sections taken from the short transverse orientation of the various plates tested are shown in Figures 4.4 through 4.6. The low magnification micrographs reveal the



TOP						BOTTOM		
A	B	C	D	E	5.010 57.75	5.052 57.13		M
					F			
					5.062 56.98	5.087 56.62		N
					G			
					5.174 55.33	5.108 56.31		O
					H	5.107 56.32		P
					I			
A	B	C	D	E	J	5.139 55.85		Q
					K			
					5.382 52.26	5.569 49.50	L	SCRAP

measured density (kg/m<sup>3</sup>) - weighted average 5.157  
 calculated P100 fiber v/o (%) - weighted average 55.58

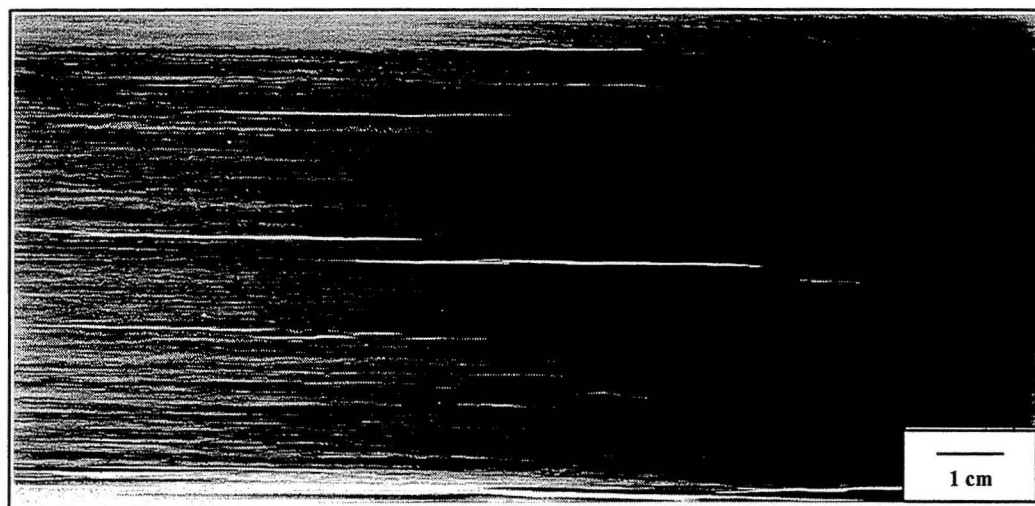
Figure 4.1. X-ray radiograph of P100Gr/Cu plate Cu-B1P1 with corresponding density measurements.



TOP						BOTTOM		
A	B	C	D	E	F	4.968 58.38	4.908 59.26	M
					G	5.067 56.92	4.941 58.78	N
					H	5.116 56.19	4.943 58.74	O
							4.986 58.10	P
					I	5.009 57.77	Q	
					J			
					K	5.129 56.00	5.412 51.82	L

measured density (kg/m<sup>3</sup>) - weighted average 5.070  
 calculated P100 fiber v/o (%) - weighted average 56.87

Figure 4.2. X-ray radiograph of P100Gr/Cu-0.3Cr plate 0.3Cr-B1P2 with corresponding density measurements.



TOP						BOTTOM		
A	B	C	D	E	F	4.460 65.88	4.421 66.45	M
					G	4.730 61.90	4.964 58.43	N
					H	4.756 61.50	4.994 57.99	O
							4.966 58.40	P
					I	4.697 62.38	4.934 58.88	Q
					J	4.768 61.33		
					K	4.623 63.47	5.017 57.66	L
						SCRAP		

measured density (kg/m<sup>3</sup>) - weighted average 4.768  
 calculated P100 fiber v/o (%) - weighted average 61.33

Figure 4.3. X-ray radiograph of P100Gr/Cu-0.7Cr plate 0.7Cr-B1P2 with corresponding density measurements.

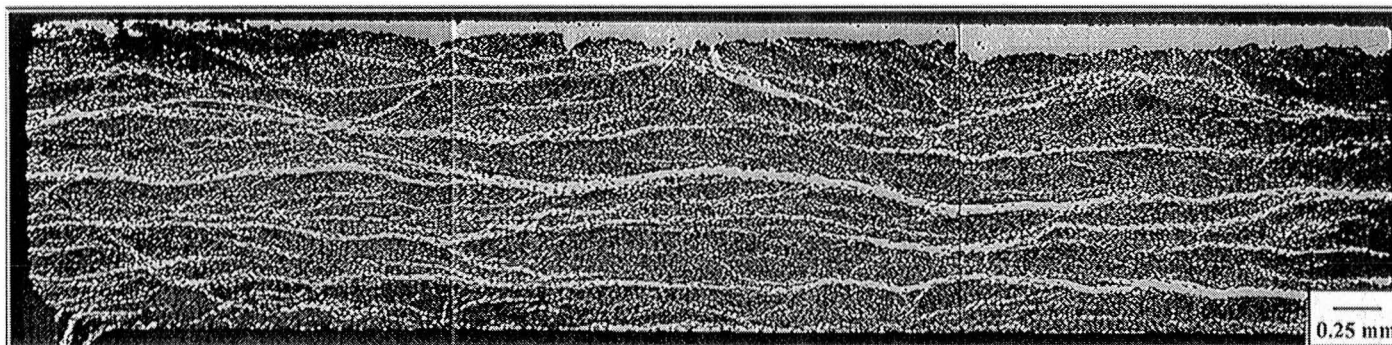


fiber distribution in the through-the-thickness direction of the composites. As in most of the composite plates, some Cu channelling (areas rich in Cu matrix) is evident. It is also possible to see the boundaries of the individual 2K fiber tows. For this particular sampling of micrographs, the P100Gr/Cu-0.7Cr composite had the most homogeneous fiber distribution.

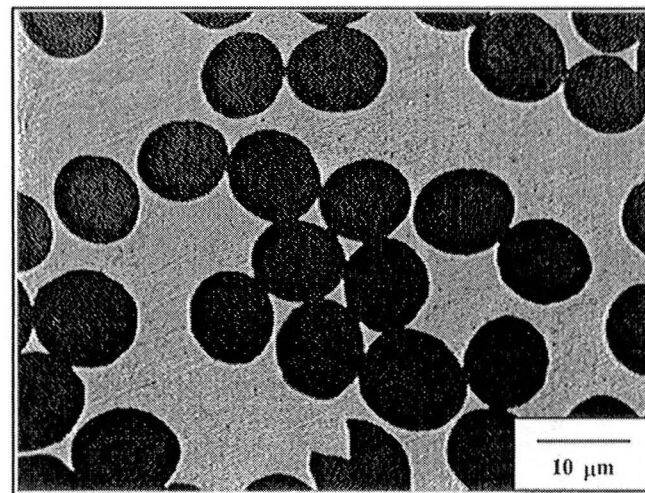
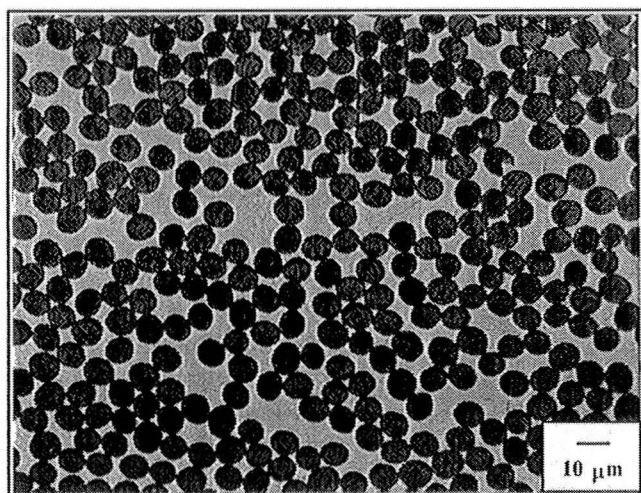
Table 4.1. Plate-to-plate and batch-to-batch variations (S = standard deviation).

Plate	Weighted average		Within batch average Calculated % P100 Gr
	Measured density	Calculated % P100 Gr	
Cu-B1P1	5.157	55.58	56.57 S = 0.78
Cu-B1P2	5.083	56.67	
Cu-B1P3	5.028	57.48	
Cu-B1P4	5.092	56.54	
Cu-B2P1	--	--	57.59 S = 1.41
Cu-B2P2	4.991	58.03	
Cu-B2P3	5.128	56.01	
Cu-B2P4	4.944	58.72	
0.3Cr-B1P1	5.164	55.48	56.20 S = 0.82
0.3Cr-B1P2	5.070	56.87	
0.3Cr-B1P3	5.065	56.95	
0.3Cr-B1P4	5.162	55.51	
0.3Cr-B2P1	4.873	59.78	59.63 S = 0.90
0.3Cr-B2P2	4.828	60.44	
0.3Cr-B2P3	4.948	58.66	
0.3Cr-B2P4	--	--	
0.7Cr-B1P1	5.123	56.08	58.92 S = 2.86
0.7Cr-B1P2	4.768	61.33	
0.7Cr-B1P3	4.761	61.43	
0.7Cr-B1P4	5.071	56.85	
Average over all plates	5.01 S = 0.13	57.69 S = 1.96	

Analysis at higher magnification indicated the presence of a reaction phase at the fiber/matrix interface of the P100Gr/Cu-0.3Cr and P100Gr/Cu-0.7Cr composites. It is evident that the reaction phase formed primarily about the P100 fibers that were surrounded by thicker regions of matrix. Figure 4.6 contains additional micrographs of the P100Gr/Cu-0.7Cr composite (etched 45 s)

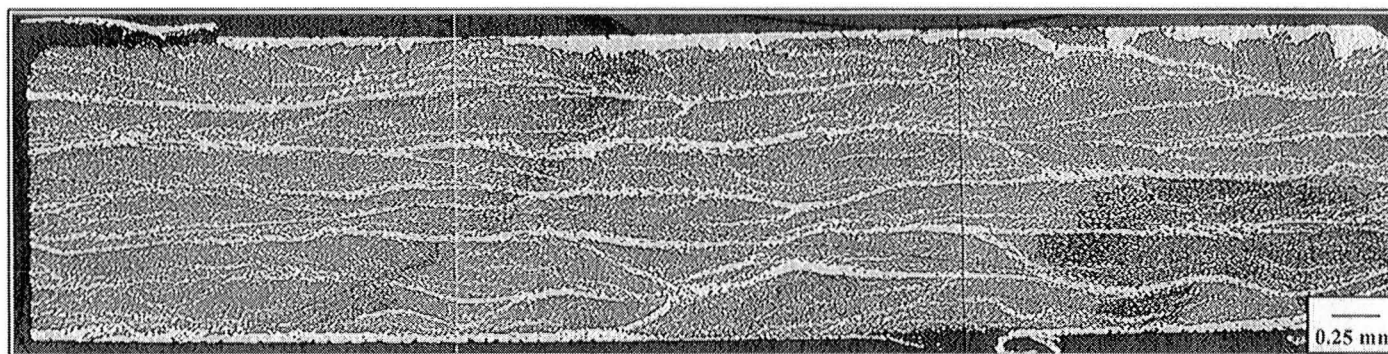


Cu-B1P1

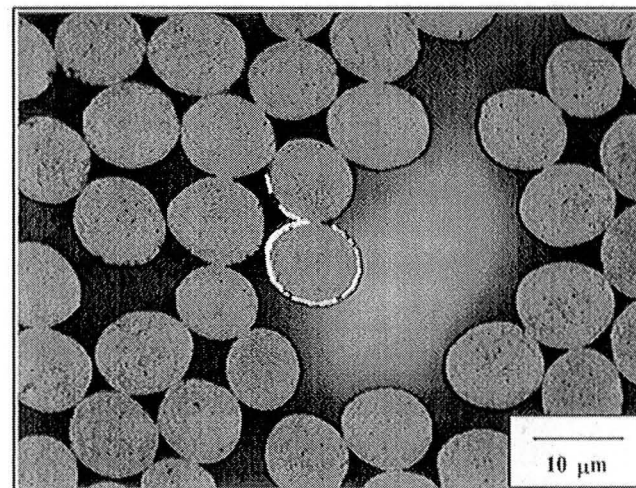
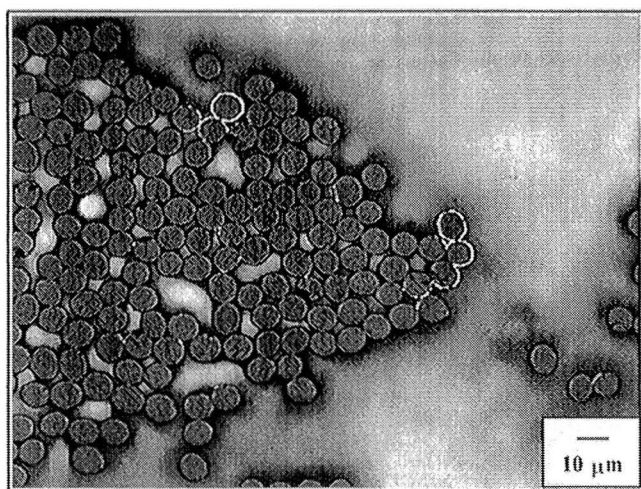


Cu-B1P4

Figure 4.4. Short transverse optical micrographs of P100Gr/Cu plates Cu-B1P1 and Cu-B1P4.

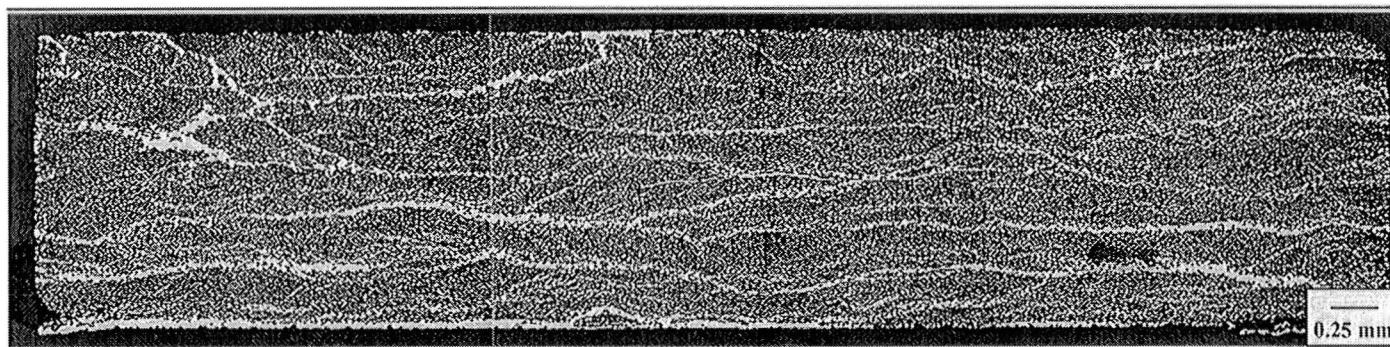


0.3Cr-B1P2

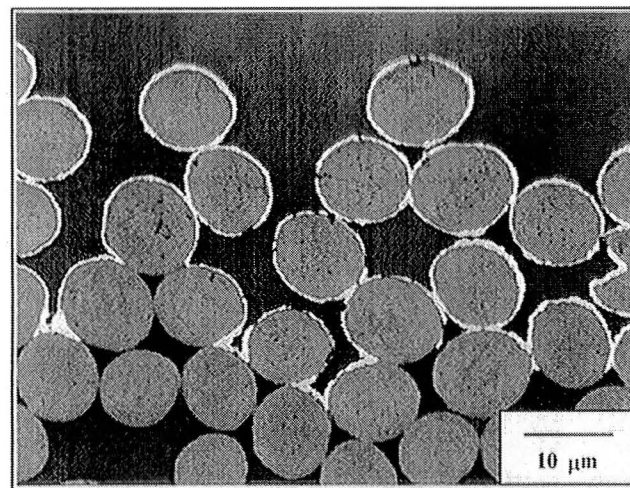
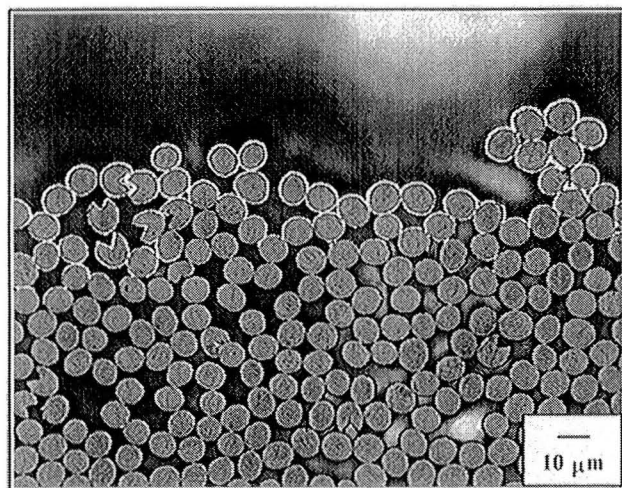


0.3Cr-B1P3

Figure 4.5. Short transverse optical micrographs of P100Gr/Cu-0.3Cr plates 0.3Cr-B1P2 and 0.3Cr-B1P3.



0.7Cr-B1P2



0.7Cr-B1P1

Figure 4.6. Short transverse optical micrographs of P100Gr/Cu-0.7Cr plates 0.7Cr-B1P2 and 0.7Cr-B1P1.

which reveal the reaction layer as the bright phase. This phase formed in a similar manner, but to a lesser degree, in the P100Gr/Cu-0.3Cr system as shown in Figure 4.5.

#### 4.3 Scanning Electron Microscopy

Further investigation of the reaction layer was performed on the SEM. Metallographic specimens of the short transverse orientation from 0.3Cr-B1P3 and 0.7Cr-B1P1 were studied to assess the distribution and continuity of the reaction phase. Figures 4.7 and 4.8 contain micrographs of the P100Gr/Cu-0.3Cr system. Only small amounts of the reaction phase are present. Figures 4.9 and 4.10 were obtained from other locations on the same specimen. As shown, only in matrix rich regions does the reaction phase form in a continuous or semi-continuous manner. Figure 4.11 indicates that the P100Gr/Cu-0.7Cr specimen contains more reaction phase. The majority of this phase, however, forms in matrix-rich areas, while much of the specimen contains little to no reaction phase, as further shown in Figure 4.12. At higher magnification, as can be seen in Figure 4.13, the phase is present in a fairly continuous form and is approximately 0.2-0.3  $\mu\text{m}$  thick. In Figure 4.15, other fiber surfaces are covered only by individual particles of reaction phase. Figures 4.14 and 4.16 contain higher magnification micrographs of the continuous and discontinuous nature of the reaction phase.

#### 4.4 Auger Electron Spectroscopy

Auger electron spectroscopy was used to identify the location of the Cr in the cast composite. An elemental Cr map was obtained for the 0.7Cr-B1P2 specimen. The area of analysis is shown in the AES micrograph in Figure 4.17. The accompanying photo, in Figure 4.18, reveals the Cr located about the fibers near matrix rich regions. Detection of Cr is shown by the white areas of the map. A similar map was obtained for the single fiber shown in Figure 4.19. The Cr is easily seen in the area of the reaction phase as shown in Figure 4.20. An AES line scan for Cu, C, Cr and O was taken



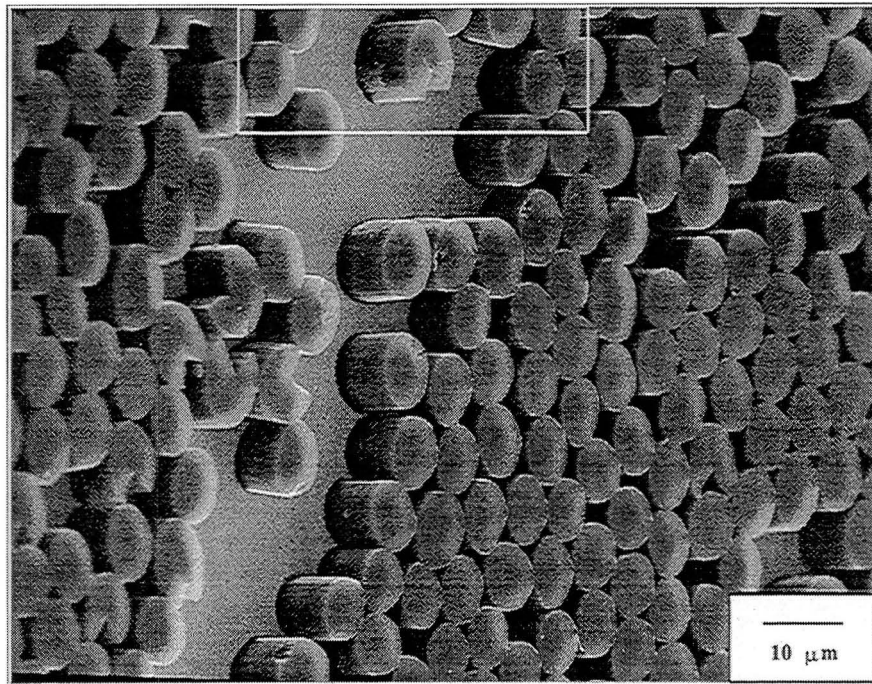


Figure 4.7. SEM micrograph of 0.3Cr-B1P3 specimen, etched 45 s, showing small amounts of reaction phase.

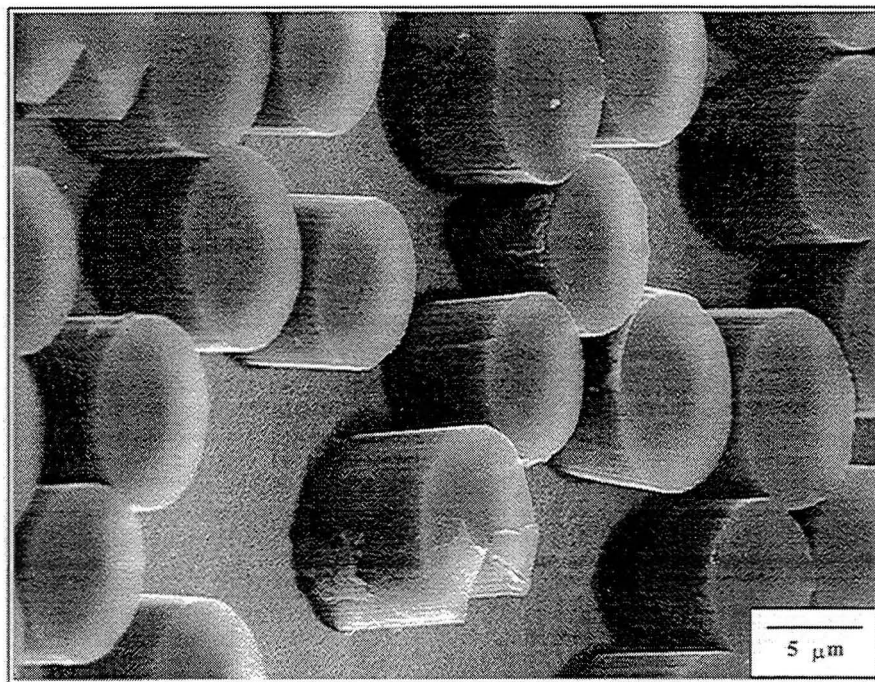


Figure 4.8. Higher magnification SEM micrograph of 0.3Cr-B1P3 specimen, etched 45 s, area indicated in Figure 4.7.

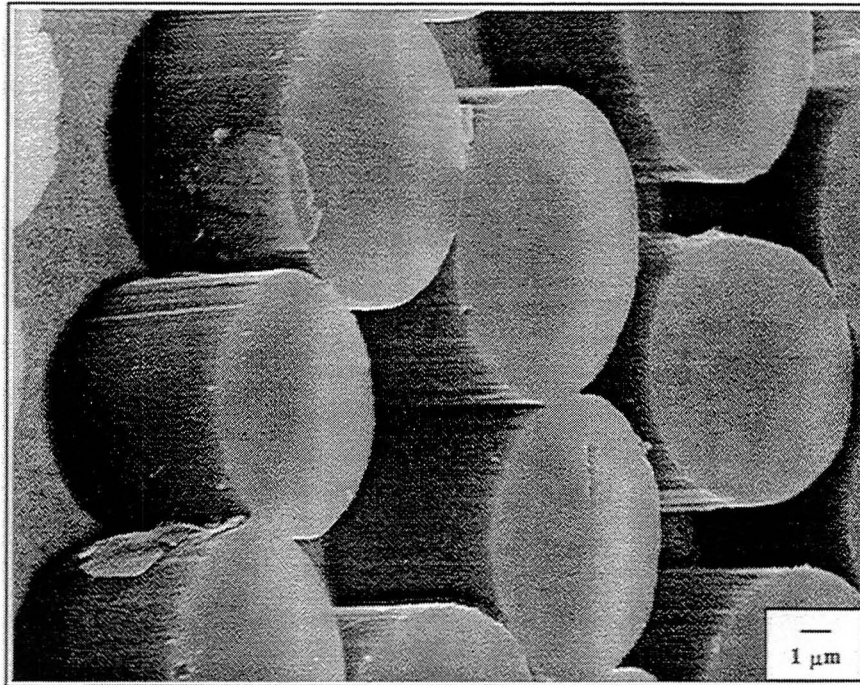


Figure 4.9. SEM micrograph of 0.3Cr-B1P3 specimen, etched 45 s, showing small amounts of reaction phase

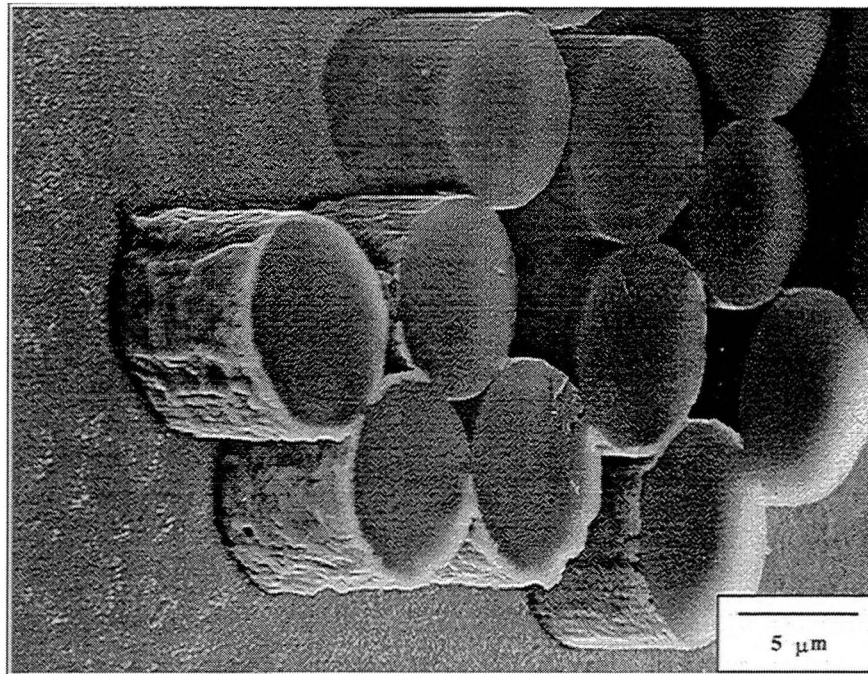


Figure 4.10. SEM micrograph of 0.3Cr-B1P3 specimen, etched 45 s, showing continuous reaction phase in matrix-rich region.

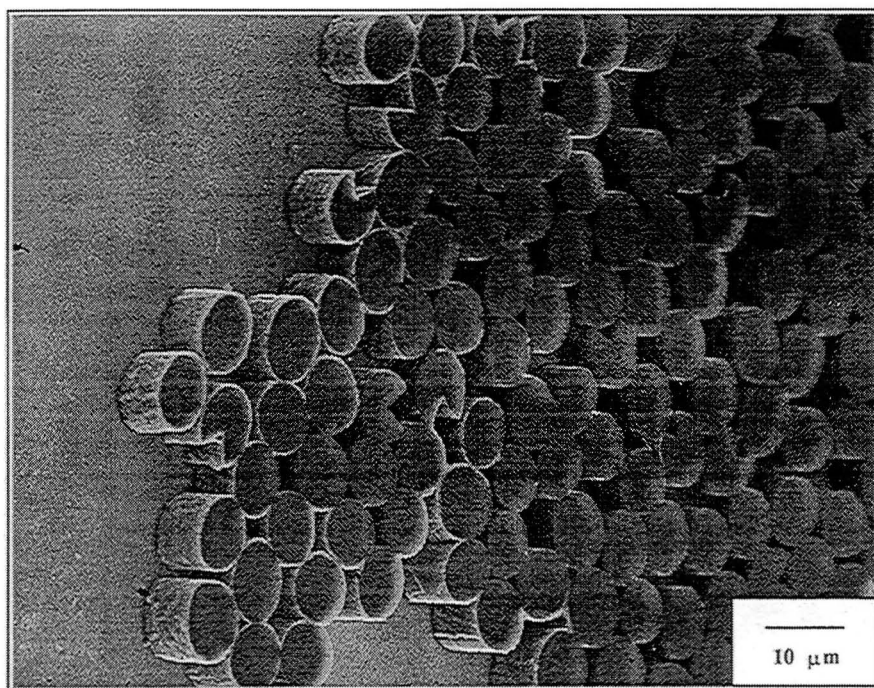


Figure 4.11. SEM micrograph of 0.7Cr-B1P1 specimen, etched 45 s, showing continuous reaction phase in matrix-rich regions.

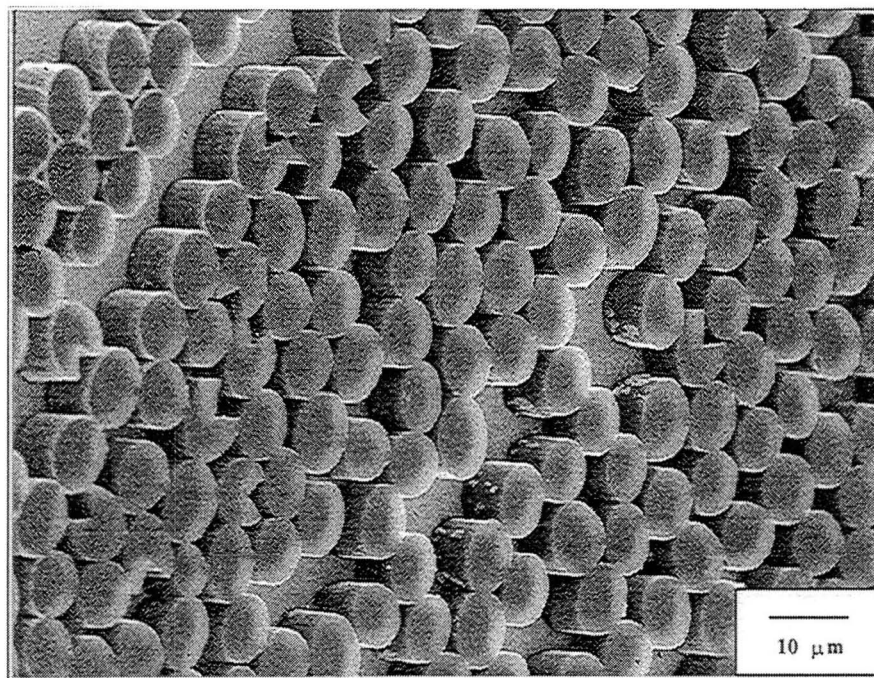


Figure 4.12. SEM micrograph of 0.7Cr-B1P1 specimen, etched 45 s, showing areas of both continuous and discontinuous reaction phase.



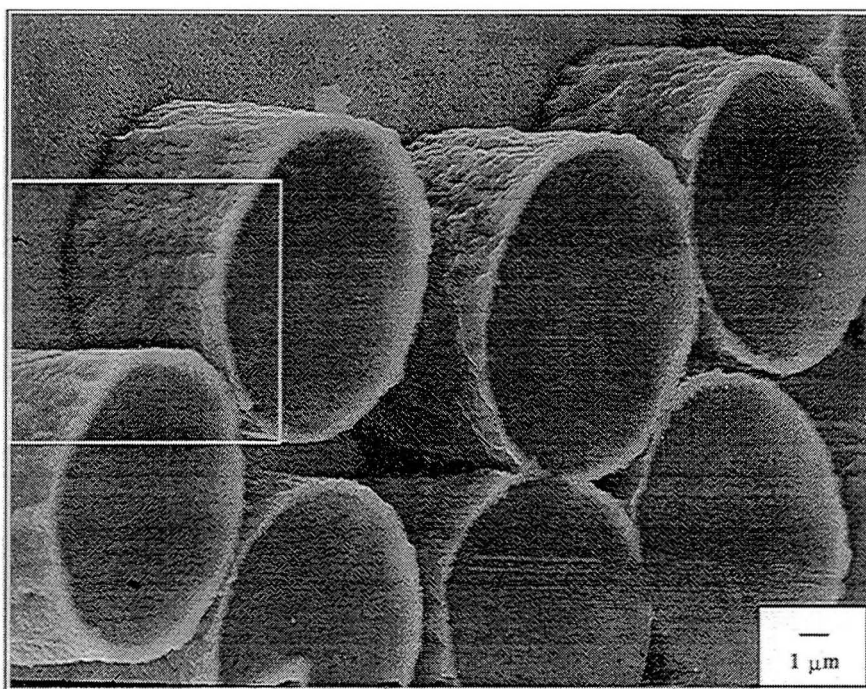


Figure 4.13. SEM micrograph of 0.7Cr-B1P1 specimen, etched 45 s, showing continuous reaction phase of 0.2-0.3  $\mu\text{m}$  thickness.

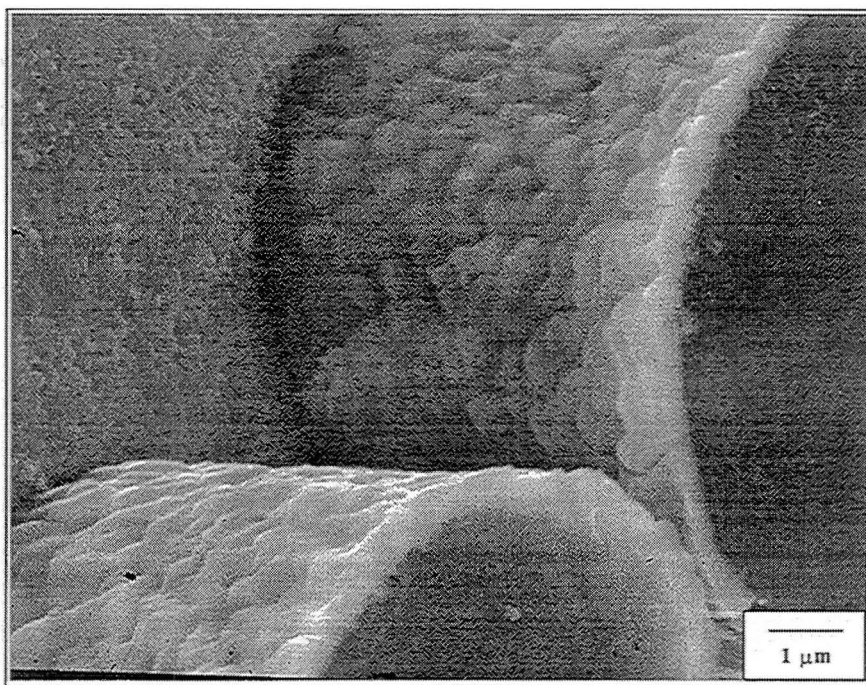


Figure 4.14. Higher magnification SEM micrograph of 0.7Cr-B1P1 specimen, etched 45 s, area indicated in Figure 4.13.

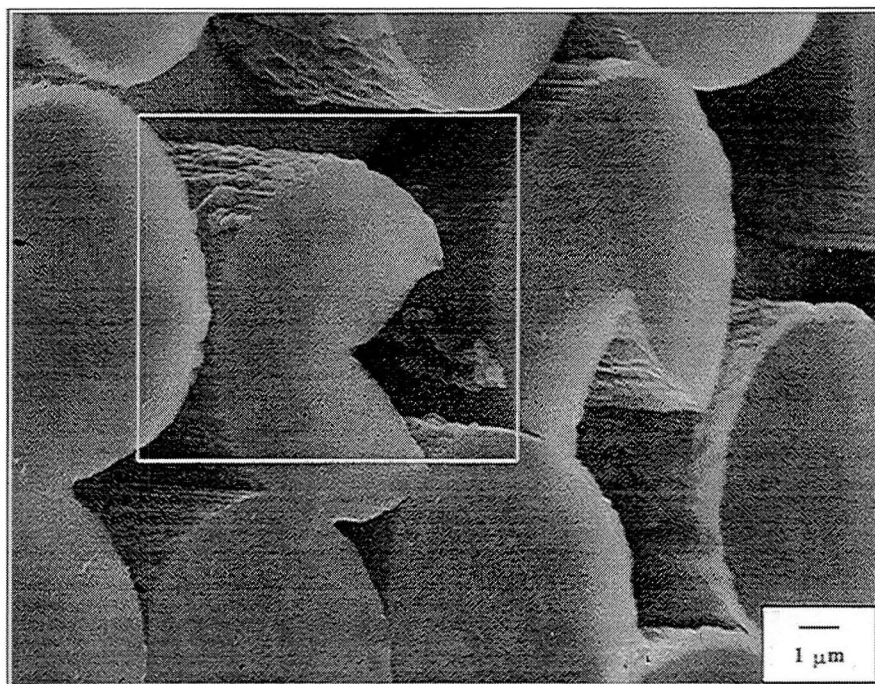


Figure 4.15. SEM micrograph of 0.7Cr-B1P1 specimen, etched 45 s, showing areas where P100 fibers are covered by particles of reaction phase.

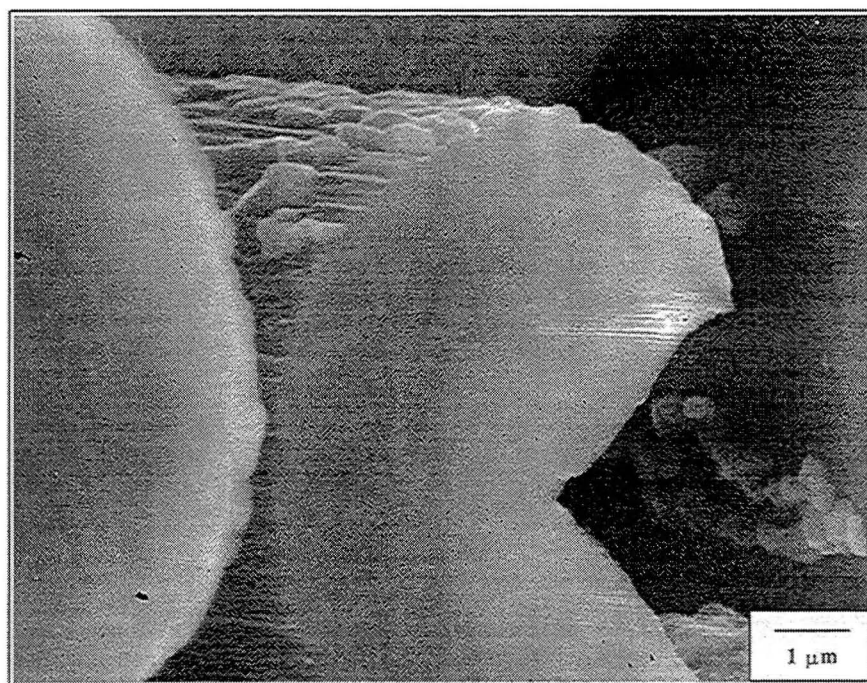


Figure 4.16. Higher magnification SEM micrograph of 0.7Cr-B1P1 specimen, etched 45 s, area indicated in Figure 4.15.

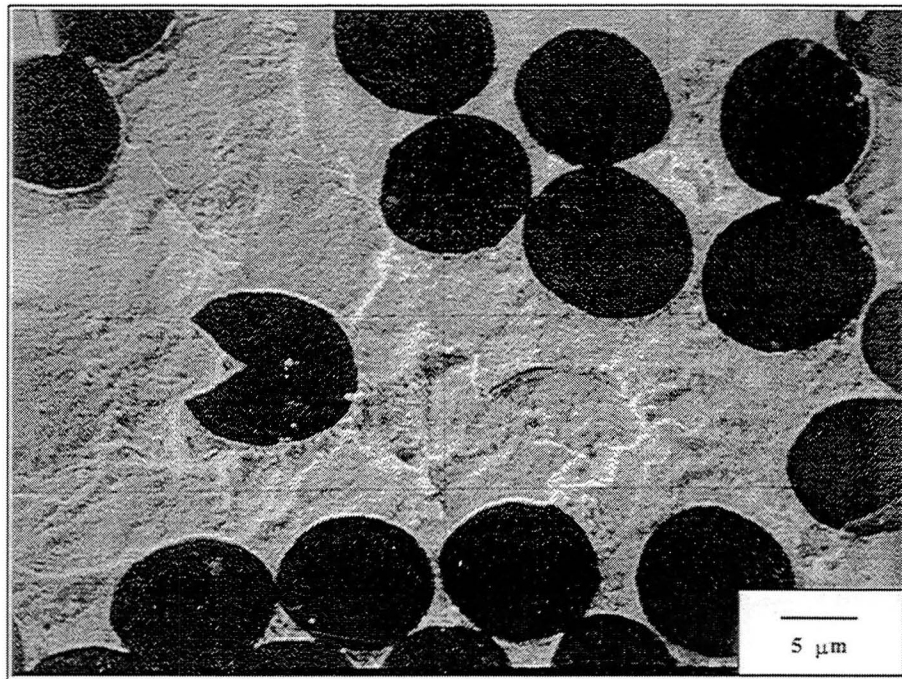


Figure 4.17. AES micrograph of 0.7Cr-B1P2 P100Gr/Cu-0.7Cr specimen indicating area of elemental Cr analysis.

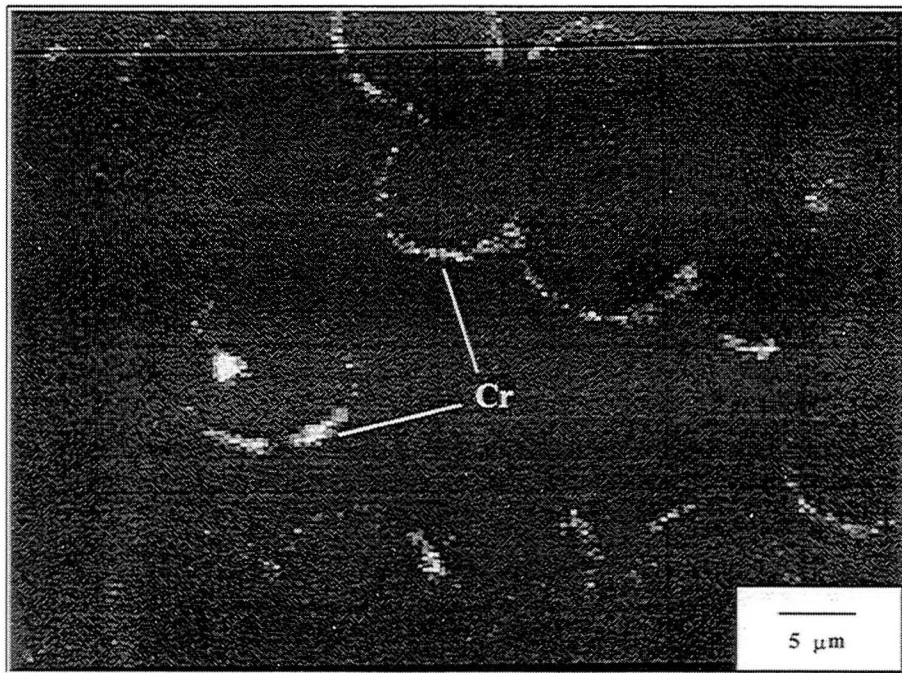


Figure 4.18. AES elemental Cr map of 0.7Cr-B1P2 P100Gr/Cu-0.7Cr specimen showing Cr segregation to the fiber surface.



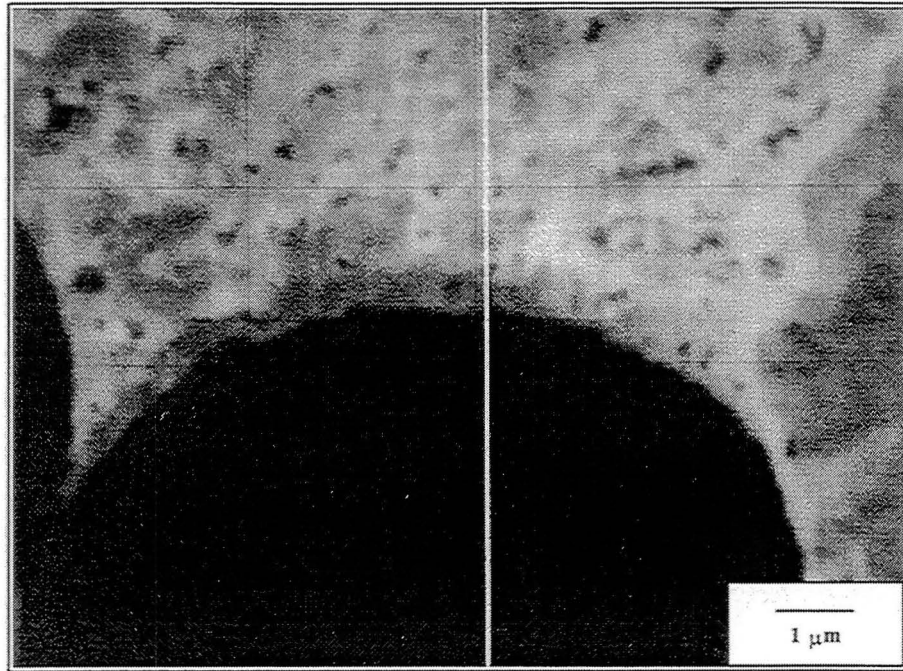


Figure 4.19. AES micrograph of 0.7Cr-B1P2 P100Gr/Cu-0.7Cr specimen indicating areas of elemental Cr map and line scan analyses.

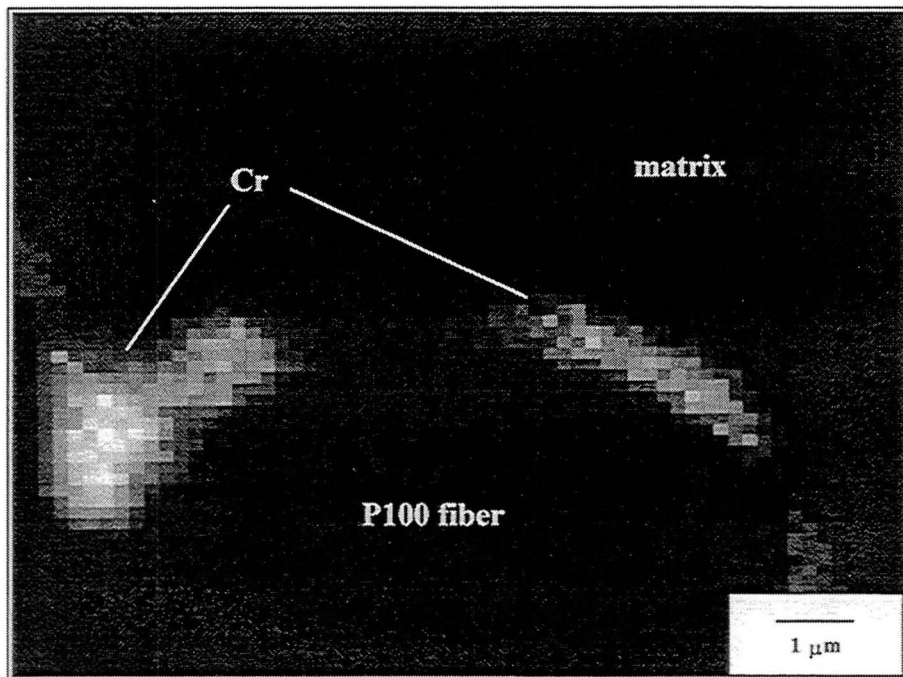


Figure 4.20. AES elemental Cr map 0.7Cr-B1P2 P100Gr/Cu-0.7Cr specimen showing Cr segregation to the fiber surface.

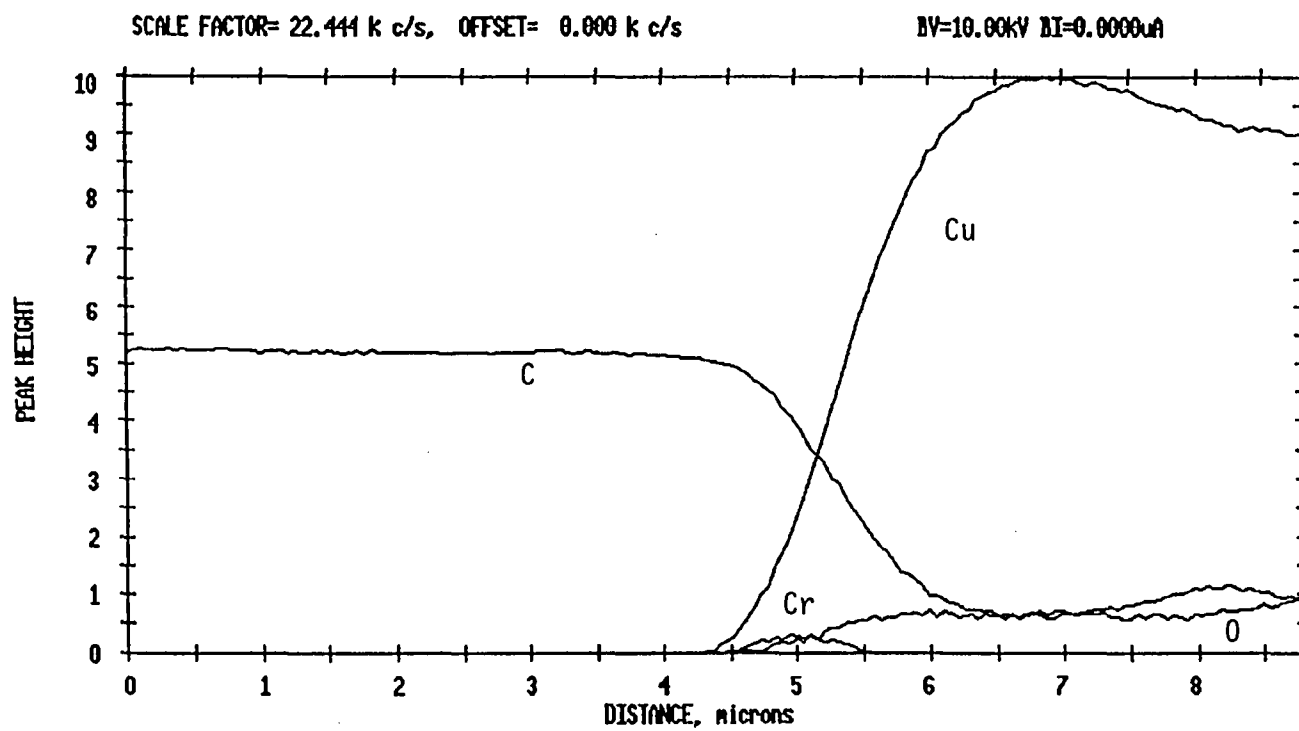


Figure 4.21. AES line scan for Cu, C, Cr and O taken over the 0.7Cr-B1P2 P100Gr/Cu-0.7Cr interfacial region as indicated in Figure 4.19.

across the interfacial region indicated in Figure 4.19. The results are shown in Figure 4.21. The line scan analysis indicates the presence of Cr at the C/Cu interface. The detection of O in the matrix is a result of the heating required to remove the specimen from the metallographic epoxy mount.

#### 4.5 Transmission Electron Microscopy

Identification of the interfacial reaction phase was achieved using the TEM. The bright field micrograph shown in Figure 4.22 indicates that the reaction layer is about 200 nm thick. Low angle grain boundaries in the Cu matrix are also visible in the left portion of this micrograph. The SAD pattern displayed in Figure 4.23 contains superimposed diffraction patterns from the reaction phase and the Cu matrix. Based upon this and other patterns the reaction phase has been identified as  $\text{Cr}_3\text{C}_2$ . The  $\text{Cr}_3\text{C}_2$  structure is orthorhombic with  $a=2.82 \text{ \AA}$ ,  $b=5.52 \text{ \AA}$ ,  $c=11.46 \text{ \AA}$  [Storms, 1967]. In Figure 4.23 the Cu zone axis is  $[\bar{1} 13]$ . The interfacial layer zone axis is  $[001]$ . The orientation relationship between the Cu and  $\text{Cr}_3\text{C}_2$  shown in Figure 4.23 is not well defined.

#### 4.6 Tensile Properties

##### 4.6.1 Longitudinal Tensile Properties

Absolute values for the longitudinal tensile strengths could not be determined due to shear failure of the outer Cu layer/composite interface prior to tensile failure. This shearing occurred in the specimen tab area as shown in Figure 4.24. The maximum tensile stress achieved during longitudinal tensile testing is therefore a measurement of the lower bound tensile strength of the composite. Due to the nature of the specimen failure (outside the gage length of the extensometer), some elastic springback was observed in the stress-strain curves. Regression statistics were used to determine the elastic moduli of the tensile specimens. An example stress-strain curve is given in Figure 4.25. Figures 4.26 and 4.27 contain all as-cast longitudinal tensile data that were collected. Strengths as high as 758 MPa (110 ksi), prior to shear failure, were reported. The elastic moduli of the composites

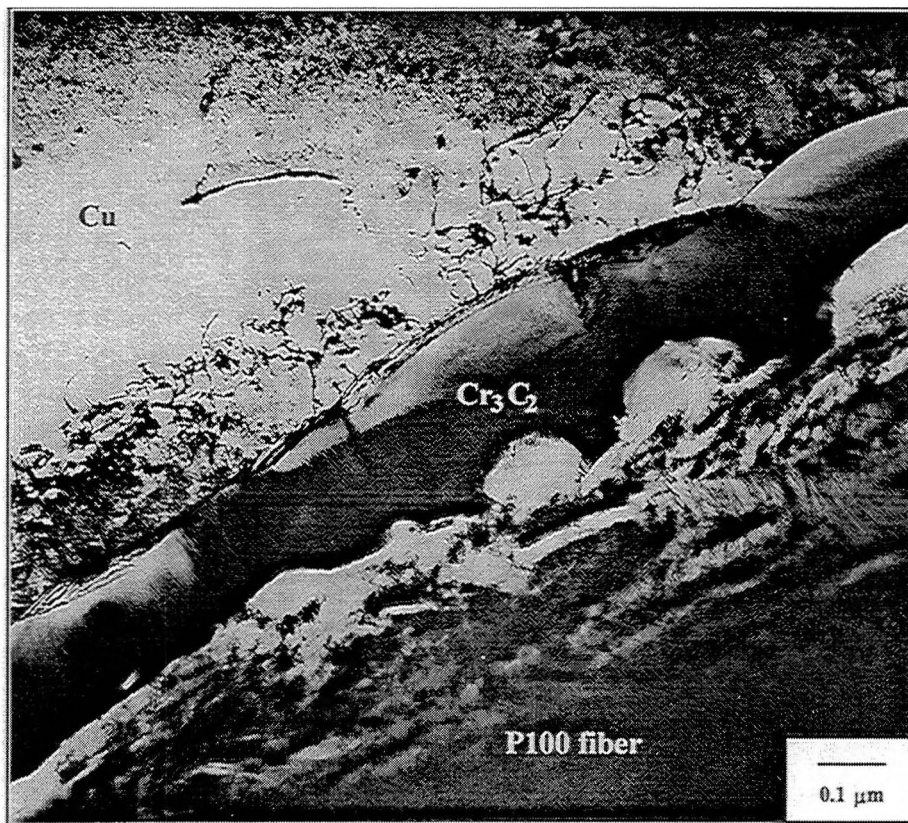


Figure 4.22. TEM micrograph of reaction phase. Layer is measured to be 1700-2400 Å in thickness.

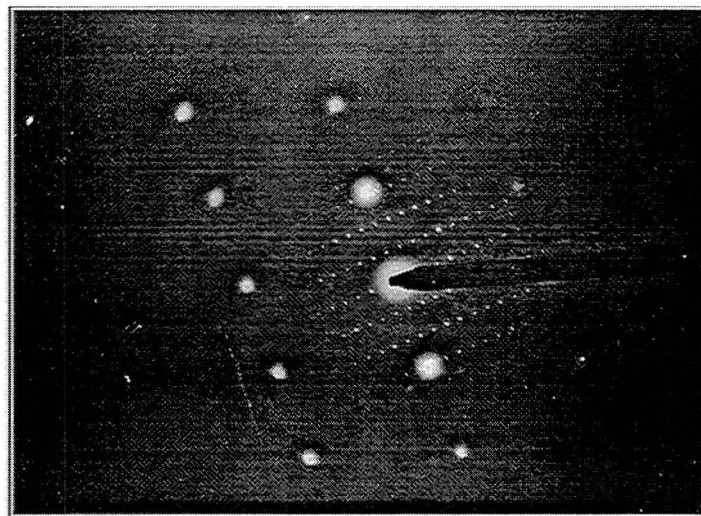


Figure 4.23. Selected area diffraction pattern taken in a region containing Cu matrix and reaction phase. Reaction phase identified to be  $\text{Cr}_3\text{C}_2$ .  
(Photos courtesy of A. Garg, NRC-NASA LeRC)

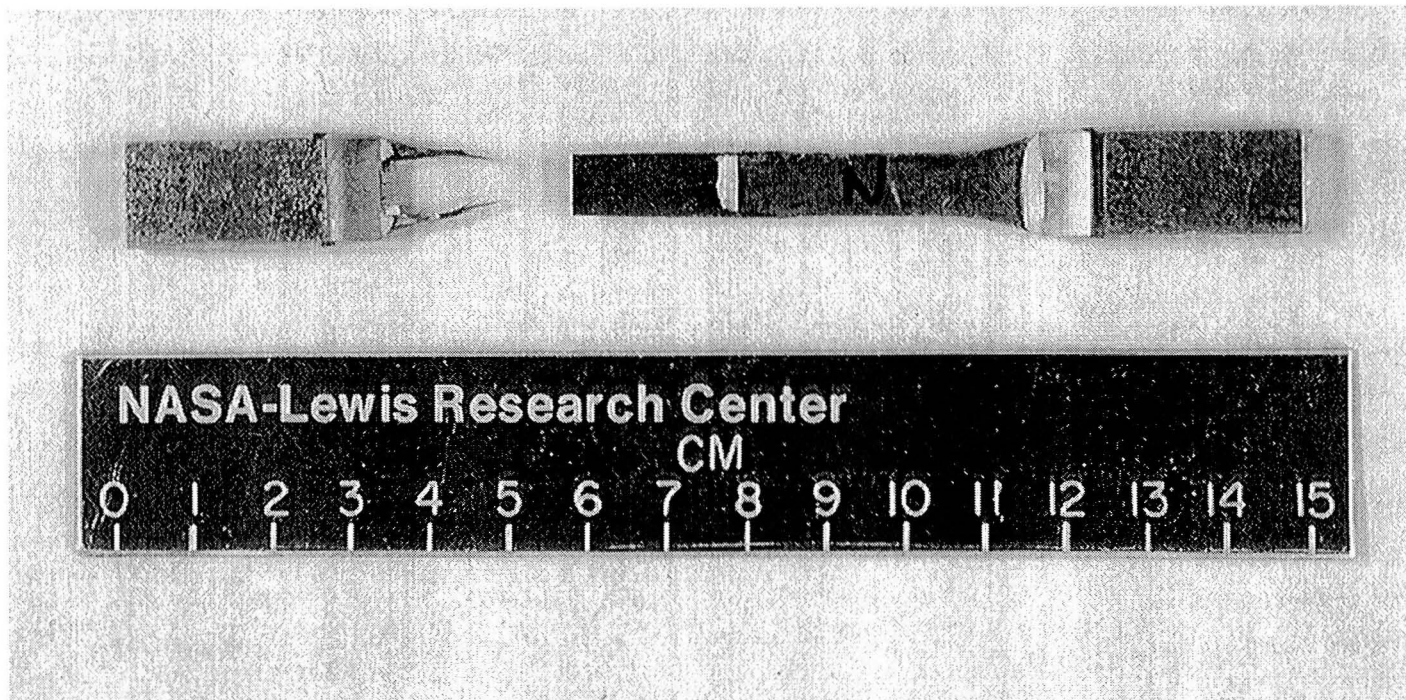


Figure 4.24. Shear failure of P100Gr/Cu-xCr composite longitudinal tensile specimen.



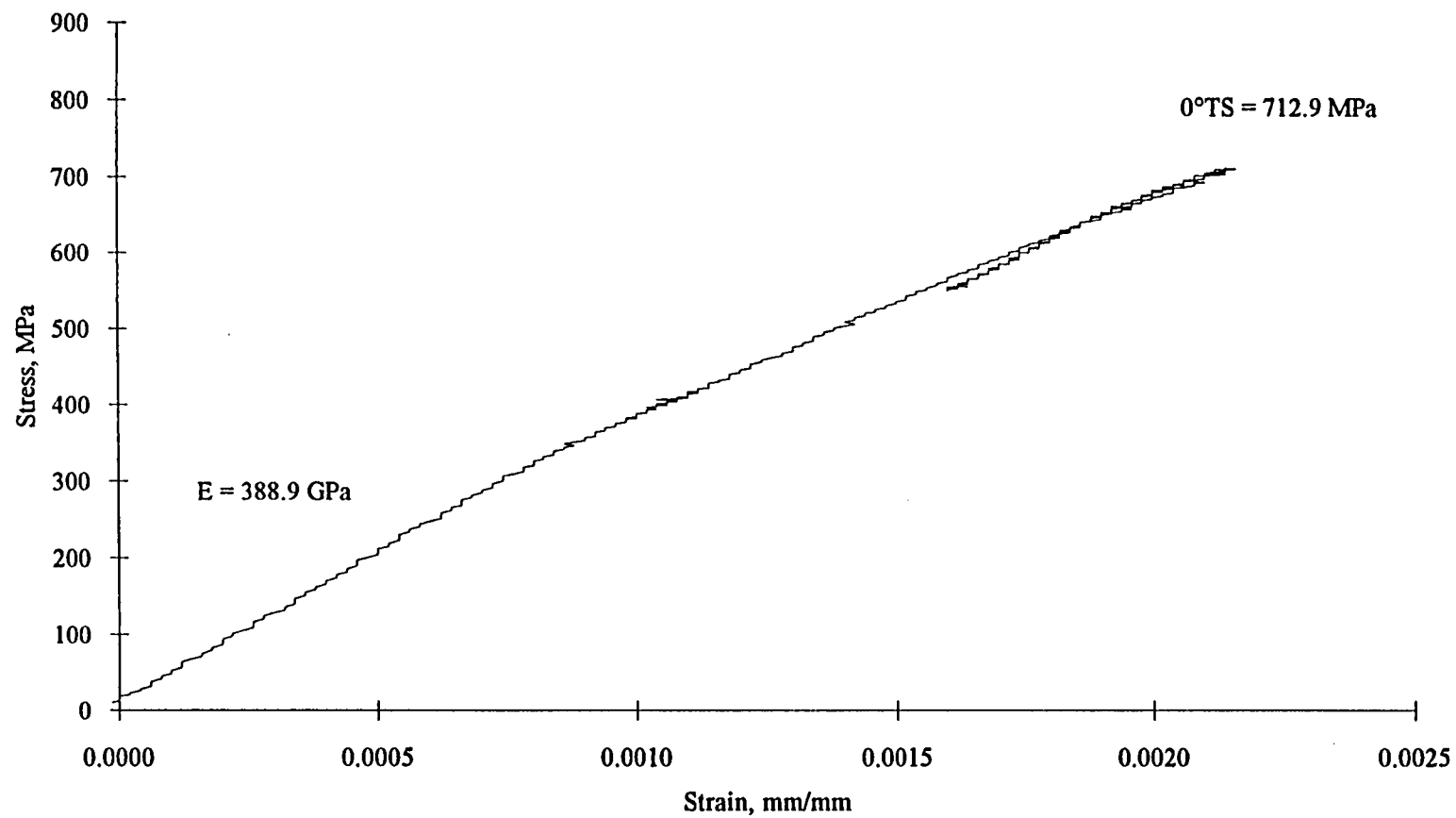


Figure 4.25. Stress-strain curve for P100Gr/Cu longitudinal tensile specimen (Cu-B1P1-N).

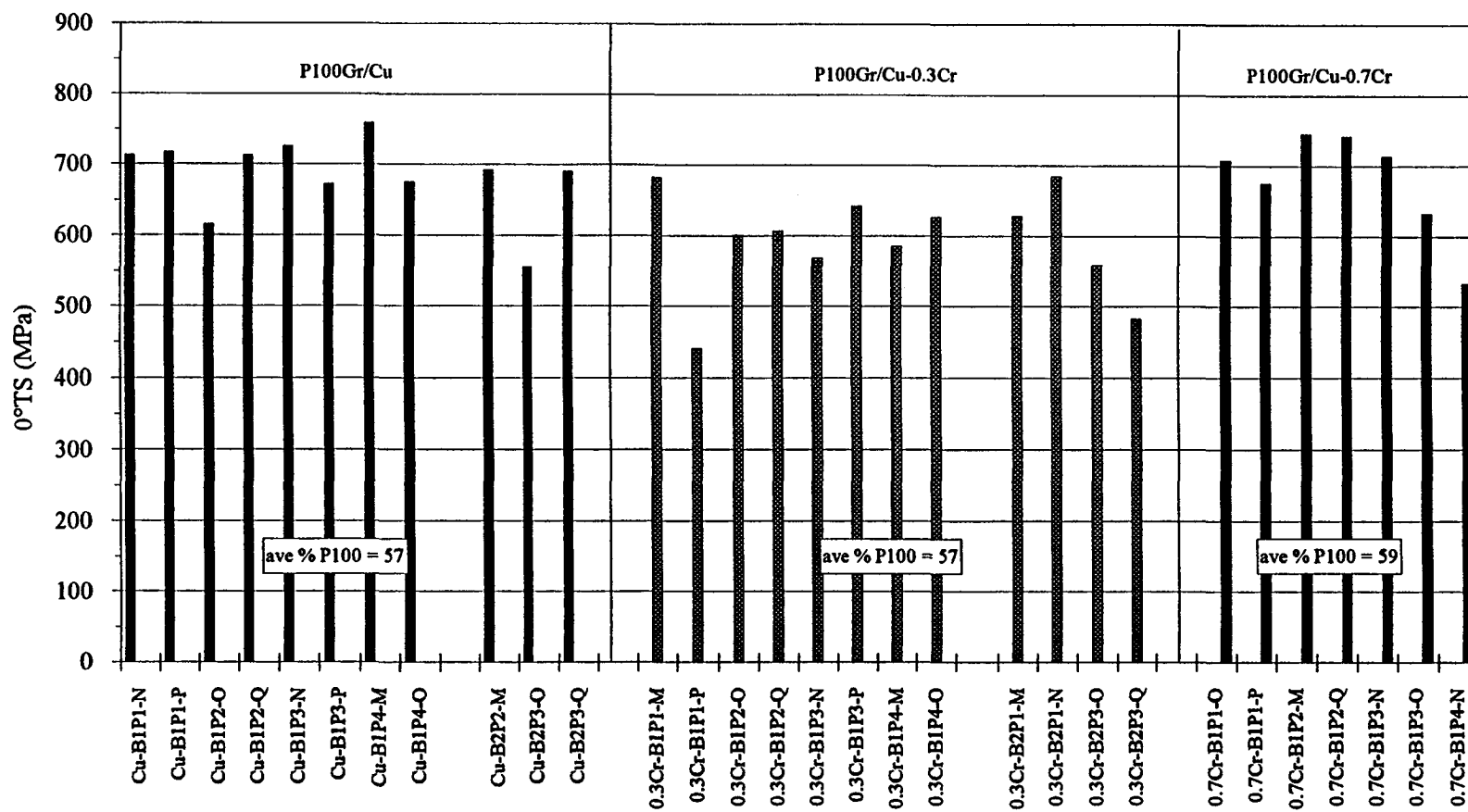


Figure 4.26. As-cast P100Gr/Cu-xCr longitudinal tensile strength: 0°TS (MPa).

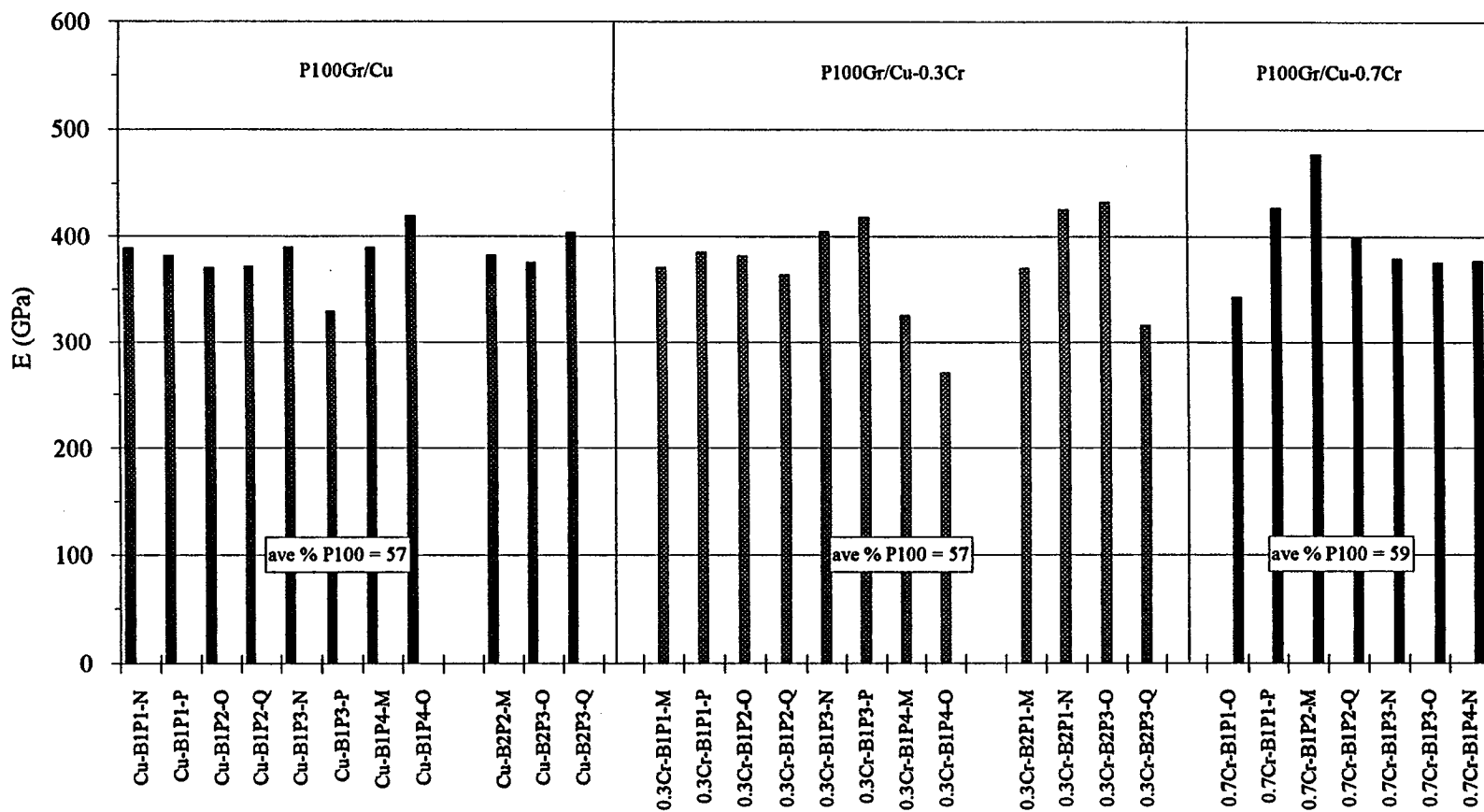


Figure 4.27. As-cast P100Gr/Cu-xCr longitudinal elastic modulus: E (GPa).

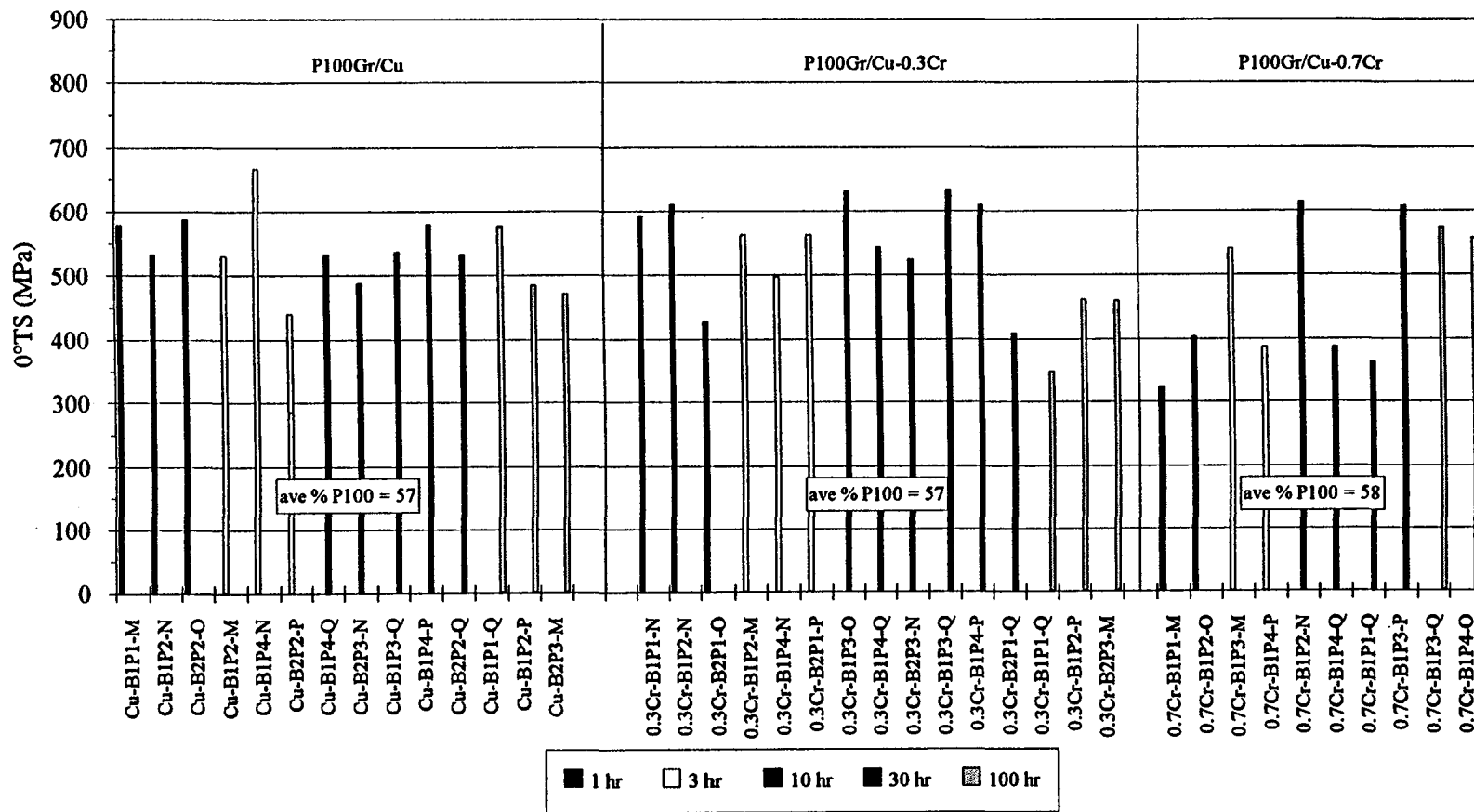


Figure 4.28. Heat treated (760°C) P100Gr/Cu-xCr longitudinal tensile properties: 0°TS (MPa).

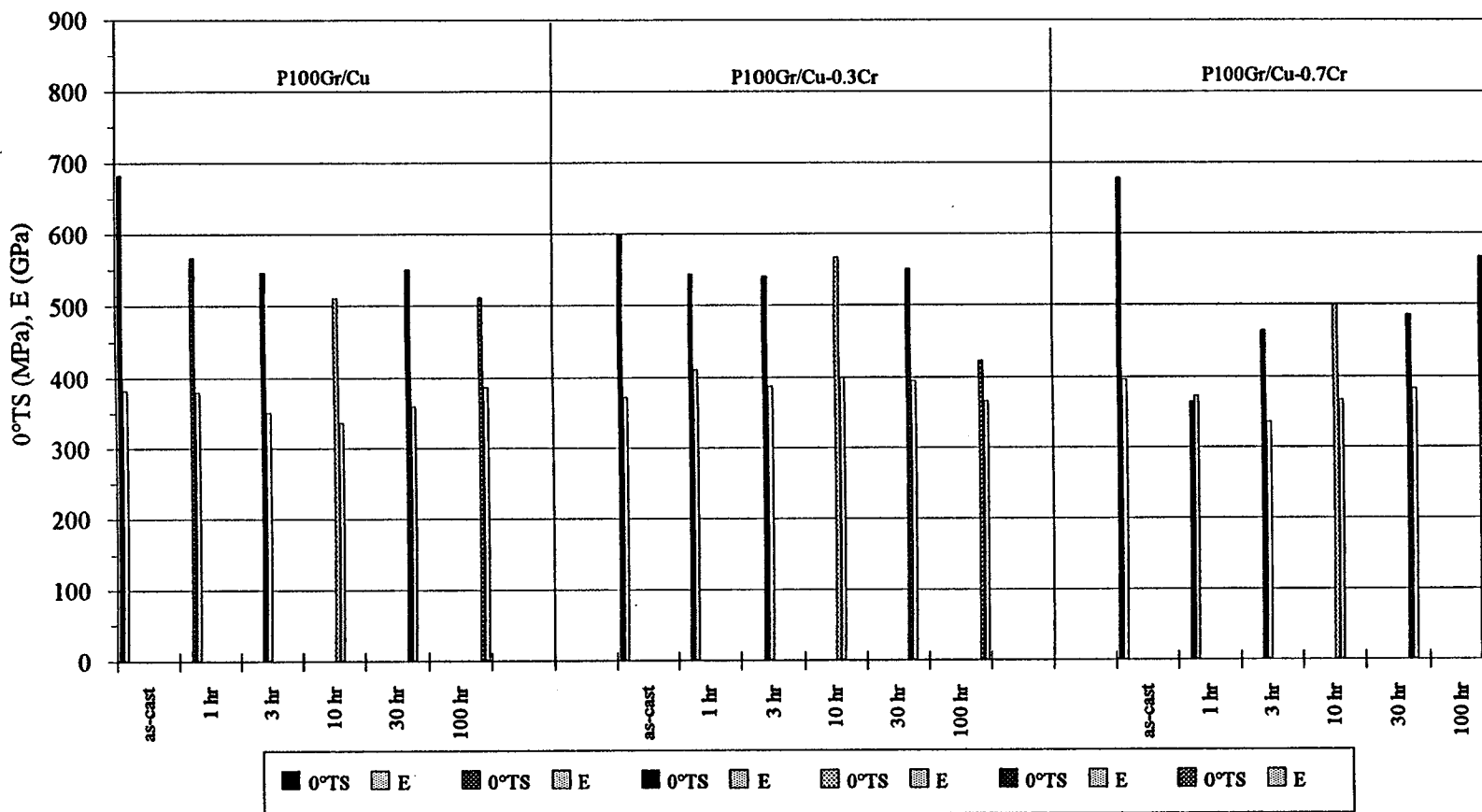


Figure 4.29. Average as-cast and heat treated (760°C) P100Gr/Cu-xCr longitudinal tensile properties: 0°TS (MPa), E (GPa).

were as high as 475 MPa (69 Msi) and approximately 393 MPa (57 Msi) on average. The strength and modulus data obtained for the heat treated specimens are included in Figure 4.28. Figure 4.29 compares the average values of strengths and moduli over all heat treatment times. It is apparent by this comparison that while the as-cast elastic moduli are retained after a 100 hr heat treatment prior to testing, the tensile strengths drop somewhat. The largest drop occurs after only 1 hr at 760°C. The P100Gr/Cu retains 75% of its as-cast tensile strength after 100 hr and the P100Gr/Cu-0.3Cr retains 71%. The P100Gr/Cu-0.7Cr system retains the greatest percentage of its 676 MPa as-cast strength at 84%. The strength of the P100Gr/Cu-0.7Cr system after 100 hr at 760°C is 565 MPa.

Some variability in the raw data is apparent, however, the tensile strengths obtained are not a function of volume fraction P100 reinforcement, in the range investigated (52-61%). The actual data are given in Appendix II.

#### 4.6.2 Long Transverse Tensile Properties

The long transverse tensile strengths of the P100Gr/Cu-xCr composites are plotted in Figure 4.30. Strengths reported to be less than 2 MPa were obtained from specimens having surface cracks in the gage section. Comparing the averages of the highest five strengths from each composition results in the following: P100Gr/Cu = 9.9 MPa, P100Gr/Cu-0.3Cr = 13.6 MPa and P100Gr/Cu-0.7Cr = 13.1 MPa. Reconsidering the data, the alloyed matrix composites have higher long transverse tensile strengths than the pure Cu matrix composites. Elastic moduli were calculated for a small number of specimens. The values were in the range of 12.8-28.7 GPa.

#### 4.6.3 Fractography

Fracture surfaces of long transverse tensile specimens were studied in the SEM. The fracture surfaces revealed separation of the fibers from the matrix with few fiber fractures evident. While the fracture appearances of all the composite compositions were similar, the alloyed matrix composite specimens showed evidence of a reaction phase. Figure 4.31 shows an SEM micrograph of a P100Gr/Cu-0.7Cr fracture. Separation of the P100 fibers from the matrix is shown, with little damage

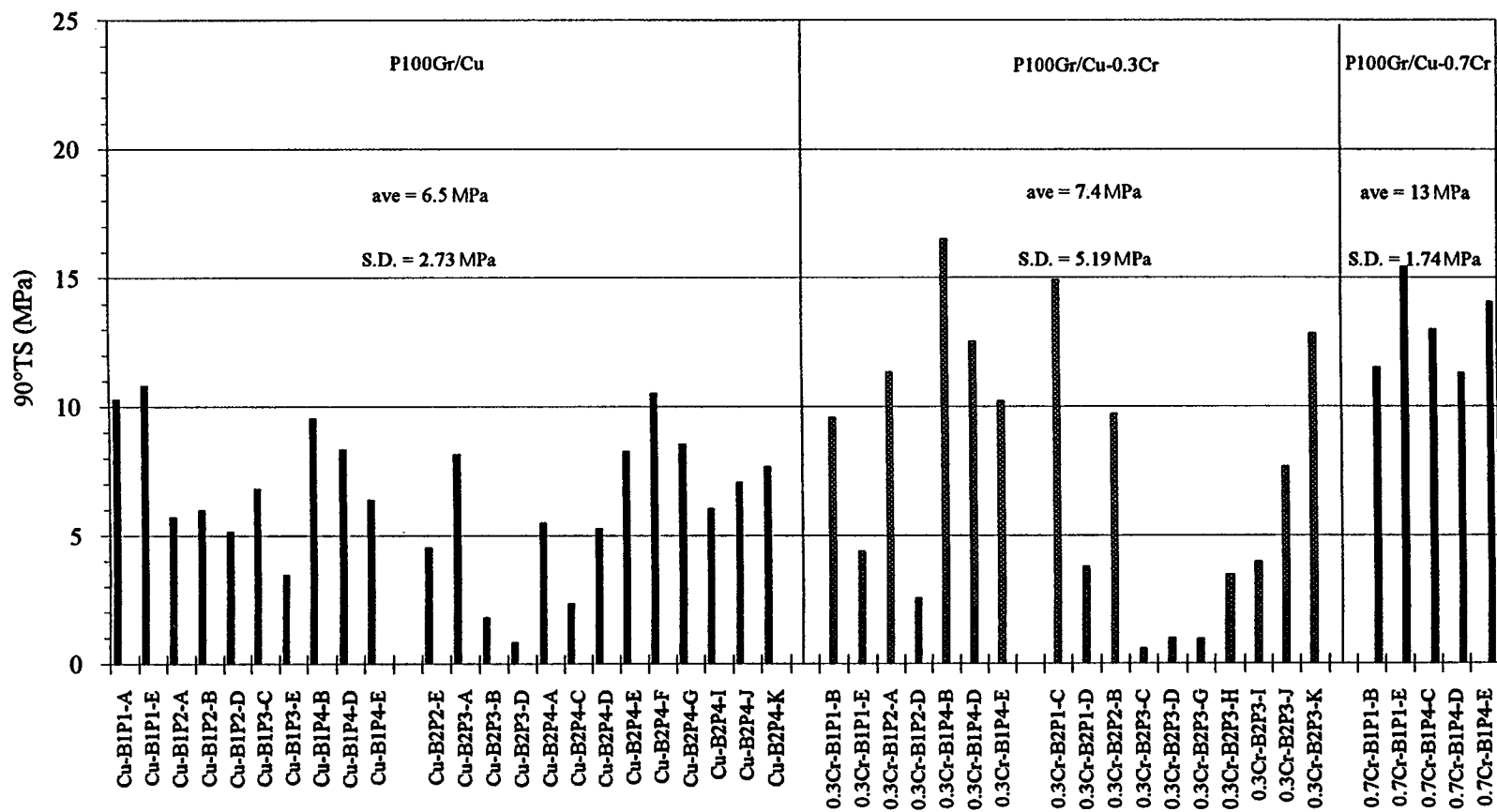


Figure 4.30. As-cast P100Gr/Cu-xCr long transverse tensile strength:90°TS (MPa).

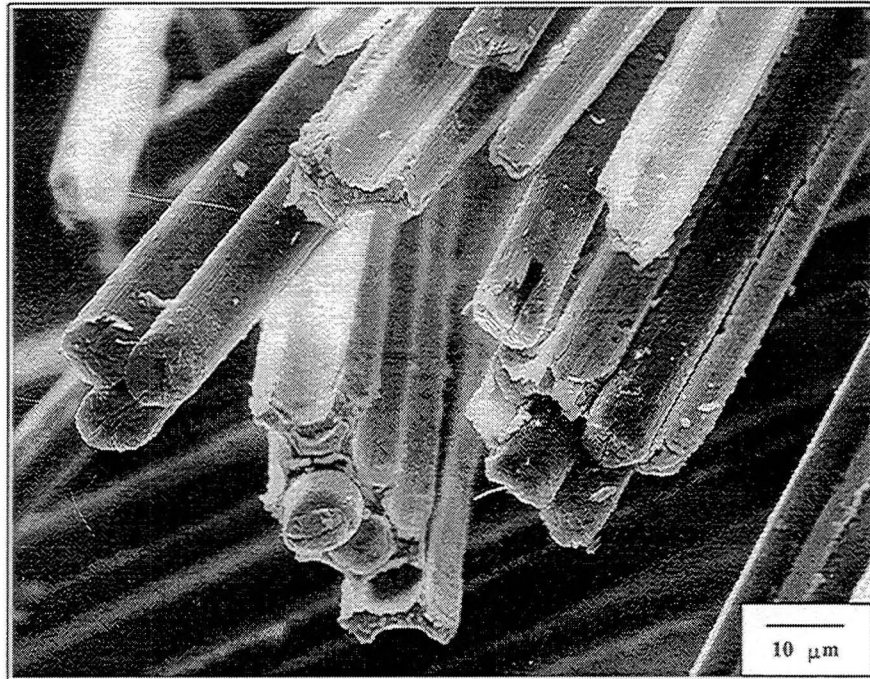


Figure 4.31. SEM micrograph of P100Gr/Cu-0.7Cr long transverse tensile fracture (0.7Cr-B1P1-E) showing separation of P100 fibers from matrix (complete debonding).

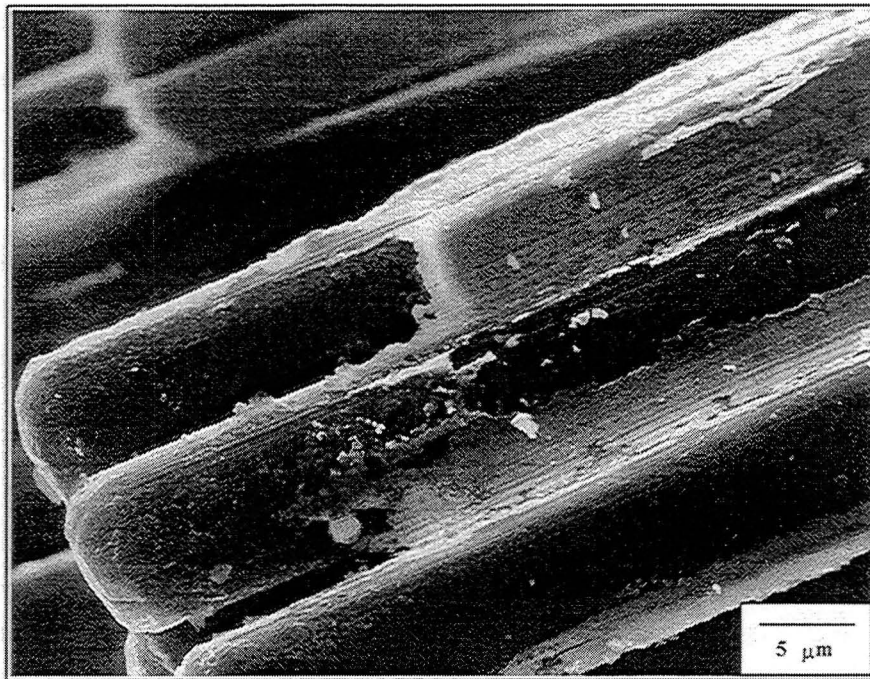


Figure 4.32. SEM micrograph of P100Gr/Cu-0.7Cr long transverse tensile fracture (0.7Cr-B1P1-E) showing small particles of reaction phase.



to most of the fiber surfaces.. Evidence of a reaction phase present is shown in Figure 4.32. This reaction phase is present in particle form on a small percentage of the fiber surfaces. Much of the reaction phase appears to be more adherent to the Cu matrix than the P100 fibers.

#### 4.7 Three-Point Bend Properties

The load-displacement data obtained during three-point bending of the P100Gr/Cu-xCr composites are linear as shown in Figure 4.33. Slopes were calculated for the composite specimens tested at each of the four span lengths. These slopes are plotted against the span length for three specimens, one from each matrix composition, in Figures 4.34 through 4.36. The curves shown represent the results of a regression analysis and yield equations in the form of  $y = mL^3 + nL$ . The elastic and shear moduli are obtained from the coefficients  $m$  and  $n$ , respectively. The elastic moduli of the composites range from 366-416 GPa. The shear moduli were found to be higher for the alloyed matrix composites than the pure Cu matrix composite. A shear modulus of 9.2 GPa was obtained for the P100Gr/Cu-0.3Cr specimen shown in Figure 4.35. For this sampling of specimens, this was highest shear modulus value.

#### 4.8 Thermal Expansion

##### 4.8.1 Long Transverse Behavior

The long transverse thermal expansion behavior of the P100Gr/Cu composites was assessed by comparing the heating portion of the cycle for each composite, as shown in Figure 4.37. The thermal expansion behaviors of copper and pyrolytic graphite are included for comparative purposes. The thermal expansion responses of the three composites are linear and vary only slightly with alloying addition. The thermal expansion behavior of the three composites falls between that of the pyrolytic graphite and pure copper.

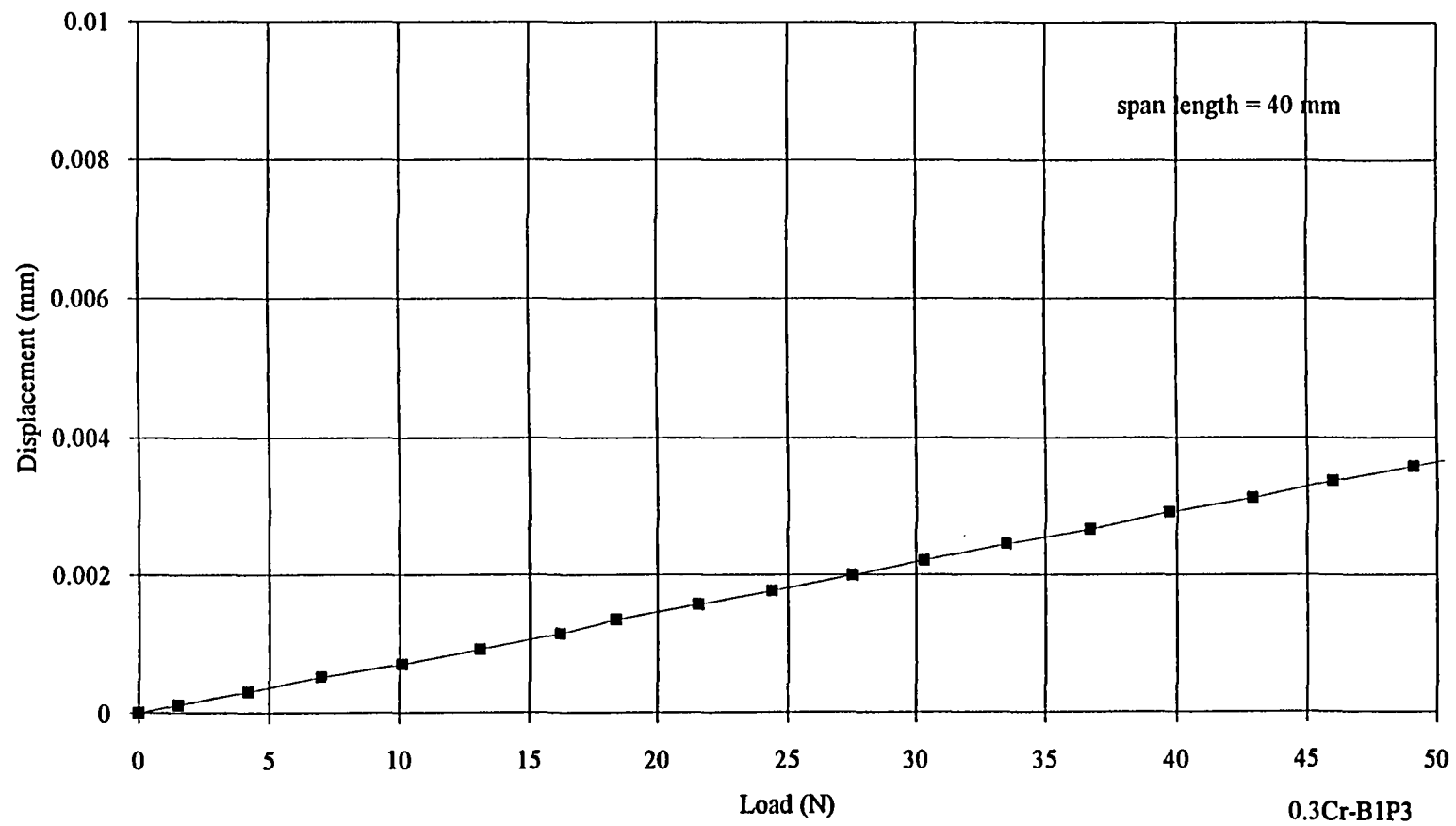


Figure 4.33. Load vs. displacement in three-point bending for P100Gr/Cu-0.3Cr composite.

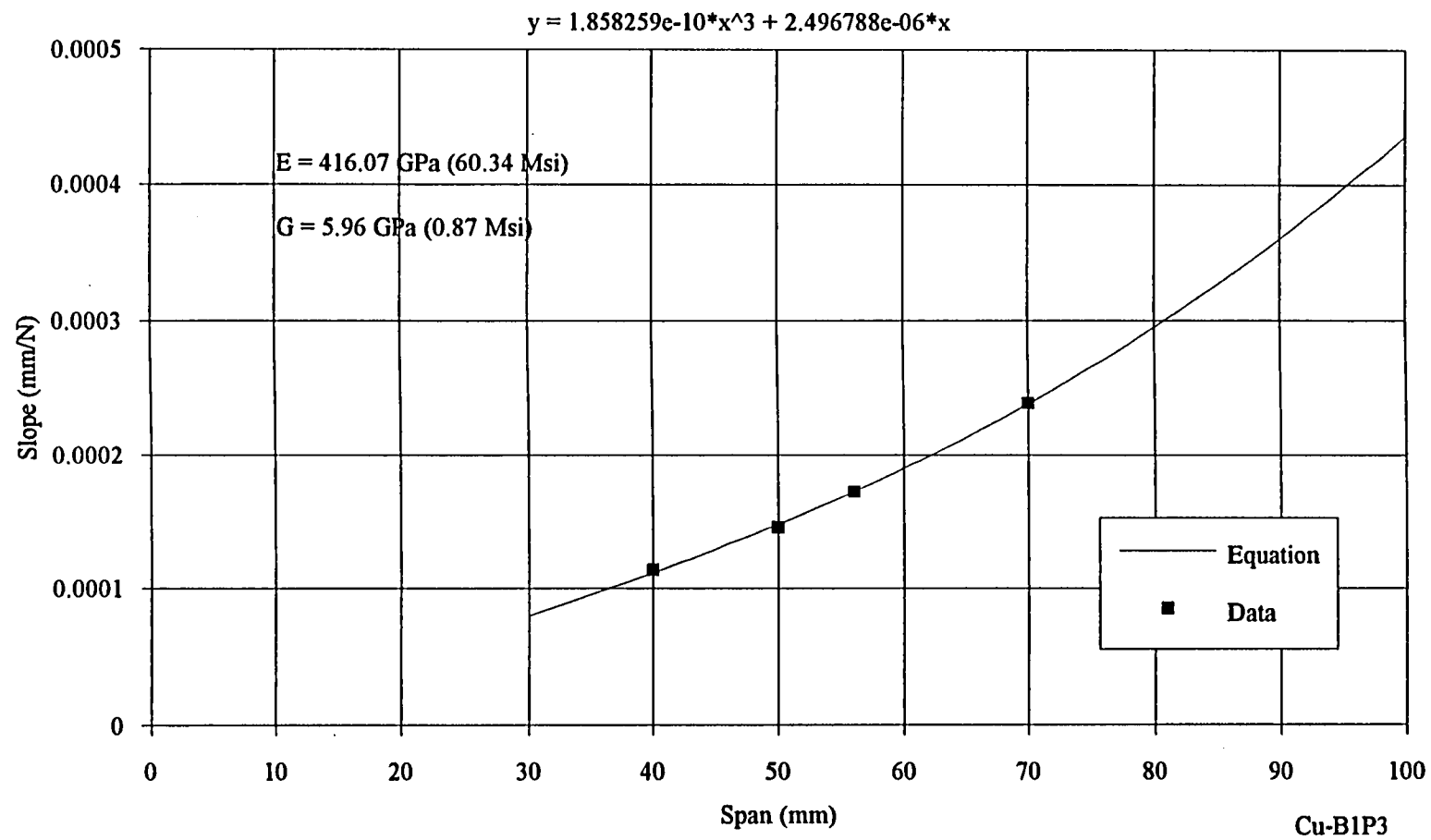


Figure 4.34. Slope vs. span length for three-point bending of P100Gr/Cu composite.

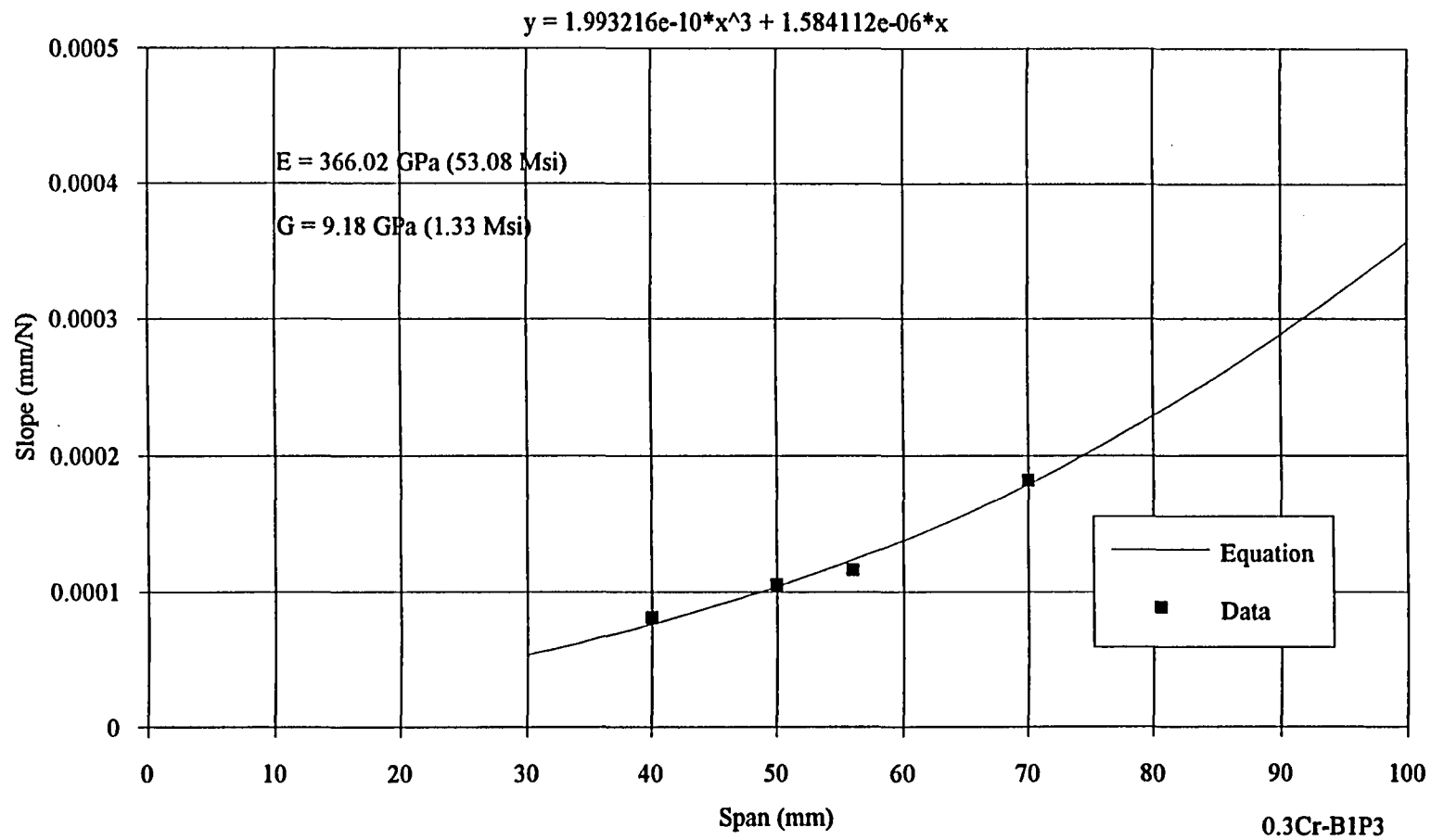


Figure 4.35. Slope vs. span length for three-point bending of P100Gr/Cu-0.3Cr composite.

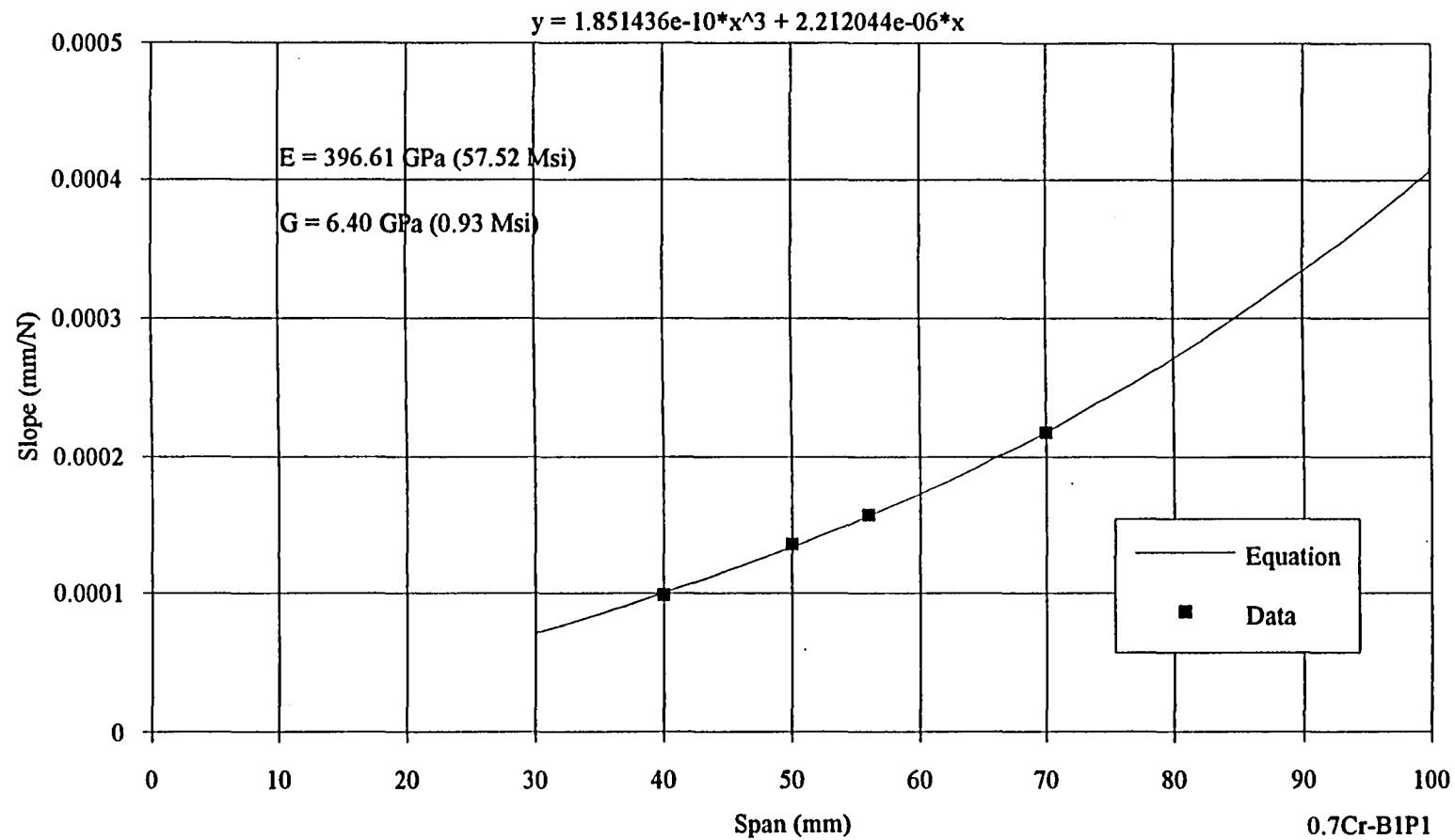


Figure 4.36. Slope vs. span length for three-point bending of P100Gr/Cu-0.7Cr composite.

#### 4.8.2 Longitudinal Behavior

The longitudinal thermal cycling behavior of a P100Gr/Cu composite is compared to that of pure copper and experimental data obtained for a P100 graphite fiber in Figure 4.38. As indicated, there is a large difference in the longitudinal thermal expansion behavior of the copper compared to the graphite fiber. The P100Gr/Cu composite exhibits a behavior that incorporates the individual responses of both the copper and the graphite. When tested to 10 cycles, a "runaway" condition is observed, in which case the composite does not return to its original length after cooling and subsequent cycling induces further change in the measured length of the specimen.

Figures 4.39 and 4.40 contain the longitudinal thermal cycling responses of the P100Gr/Cu-0.3Cr and P100Gr/Cu-0.7Cr composite systems. As shown, the alloyed matrix composites do not exhibit a "runaway" condition and the specimens undergo little to no permanent changes in length. Figure 4.41 further illustrates the effect of matrix alloying on the longitudinal thermal expansion behavior of the P100Gr/Cu composites. The figure contains the results from the first thermal cycle of three specimens, one from each matrix composition.

#### 4.8.3 Cycling Response Variability

The thermal expansion responses of the remaining specimens tested were found to be fairly reproducible. Figures 4.42 and 4.43 contain the first thermal cycles for all long transverse and longitudinal specimens from P100Gr/Cu (B1). Figures 4.44 through 4.51 compare the same sets of results for the remaining batches of plates studied. Only in cases of visible damage to the specimen, did the cycling curves vary, as shown in Figures 4.46, 4.48, 4.50. One specimen from each figure exhibits behavior that deviates from that of the others. In each case, cracks were in the longitudinal specimens and apparent after thermal cycling. Of the long transverse specimens tested, one composite buckled during cycling, and another appeared to have some surface damage which did not affect the cycling response. Table 4.2 contains an information summary of the thermal expansion specimens.

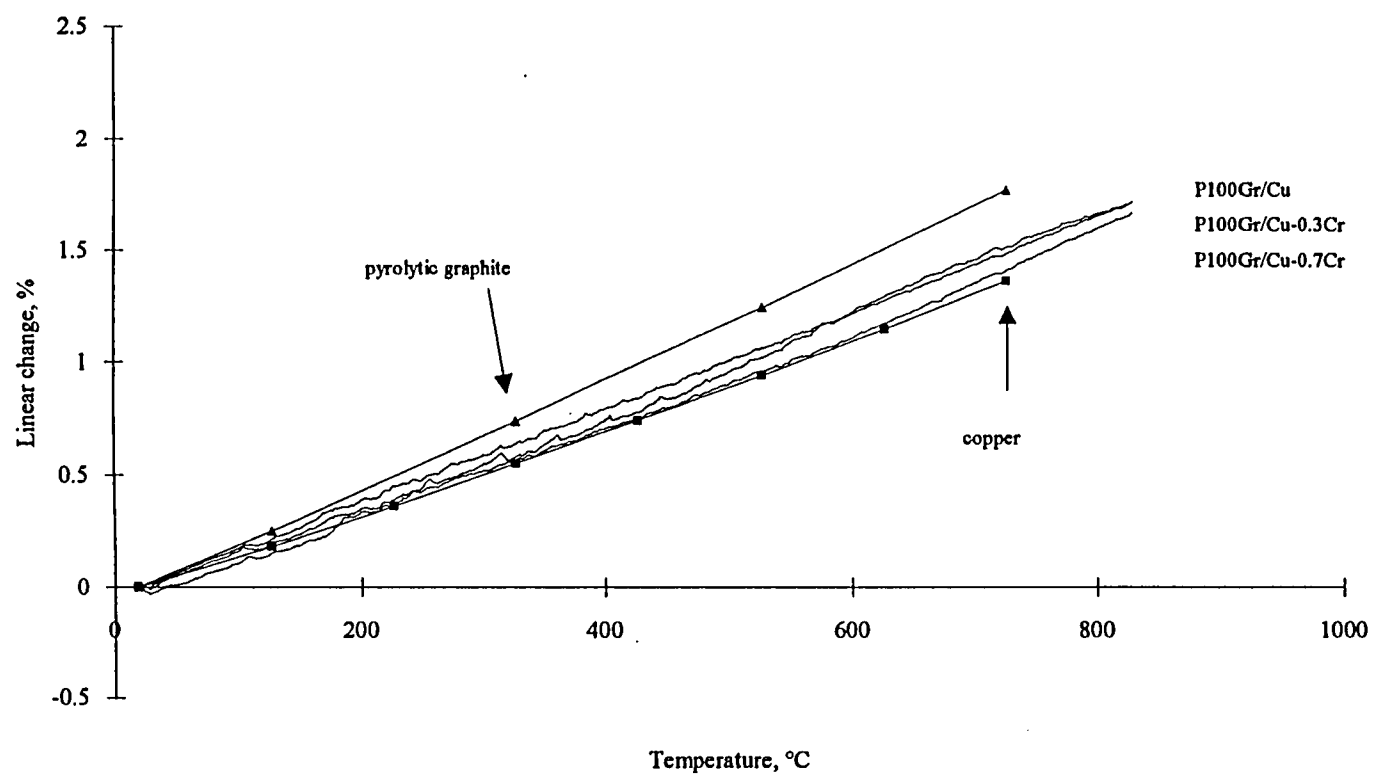


Figure 4.37. Long transverse thermal expansion behaviors of P100Gr/Cu-xCr composites as compared to those of Cu and pyrolytic Gr.

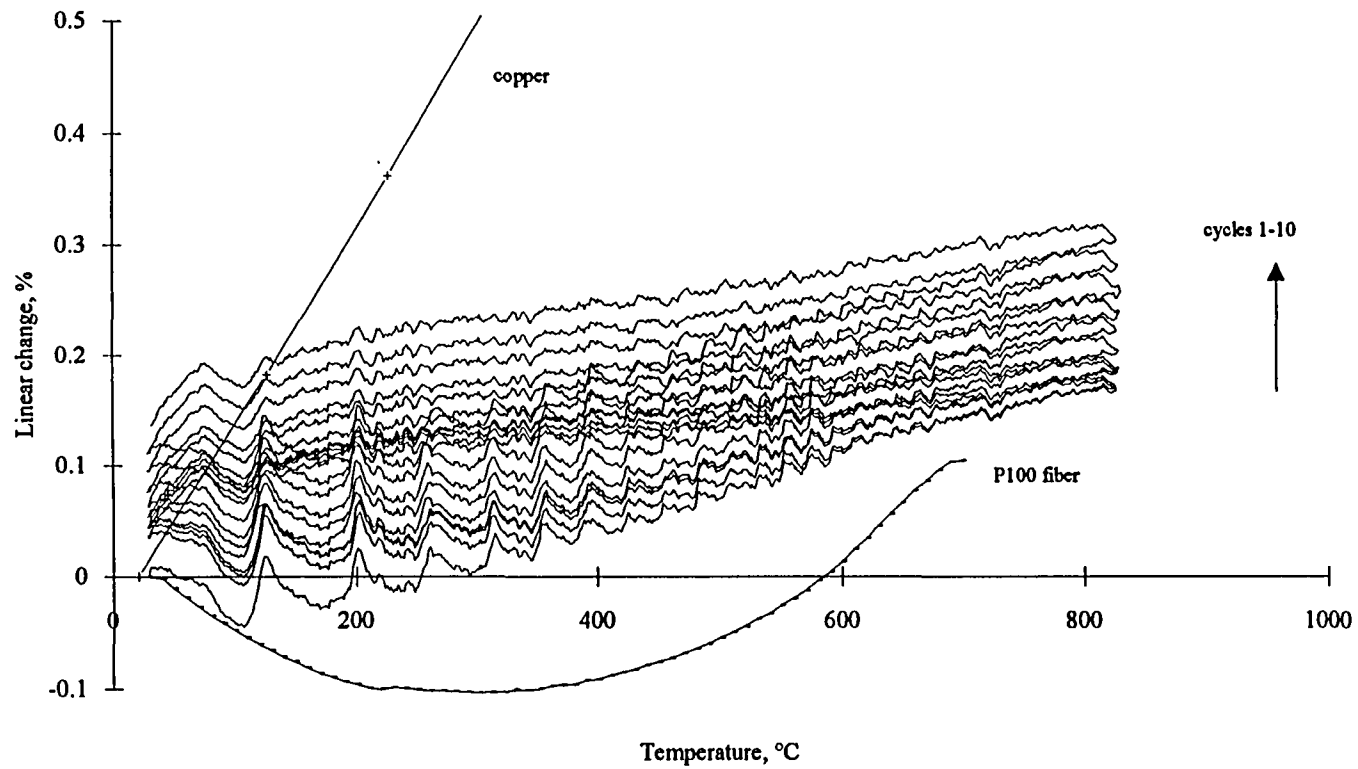


Figure 4.38. Longitudinal thermal expansion behavior of P100Gr/Cu composite as compared to those of Cu and P100 Gr fiber.



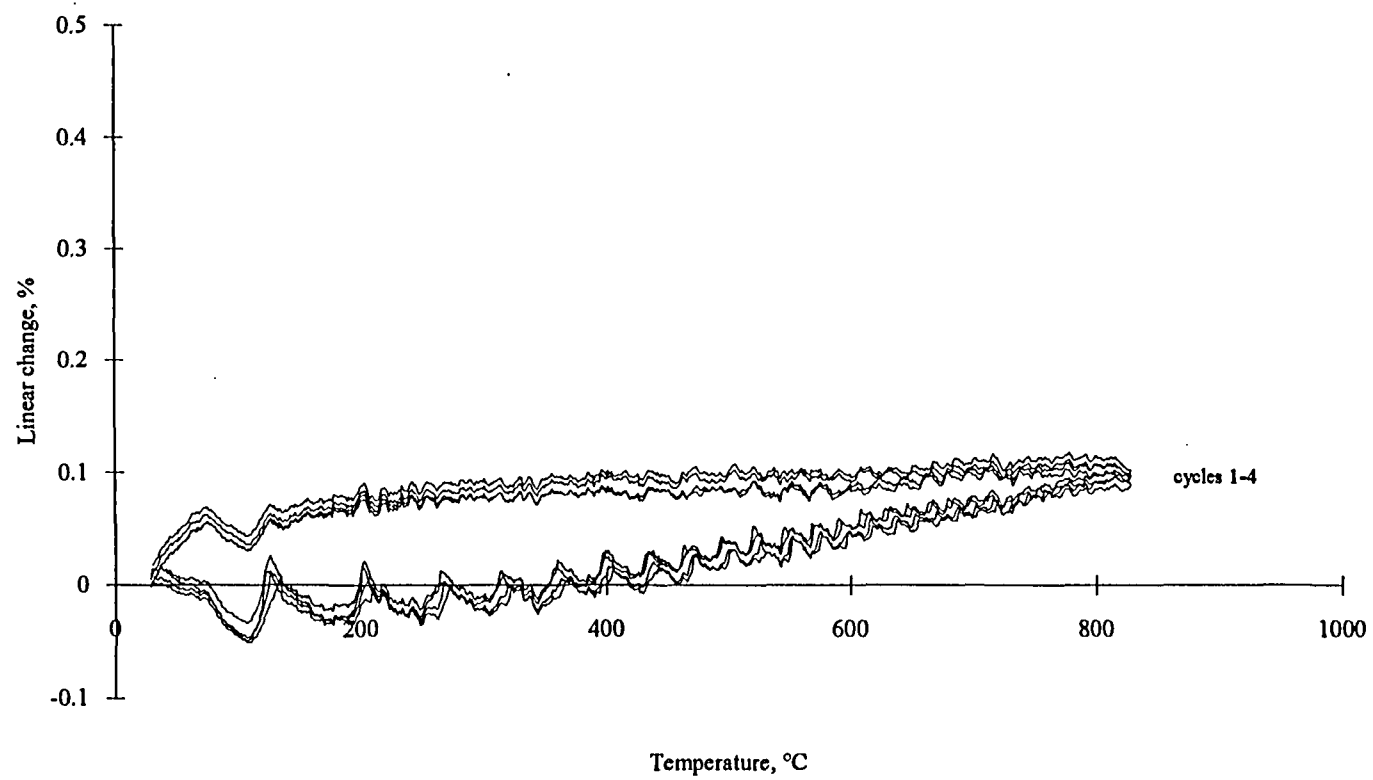


Figure 4.39. Longitudinal thermal expansion behavior of P100Gr/Cu-0.3Cr.

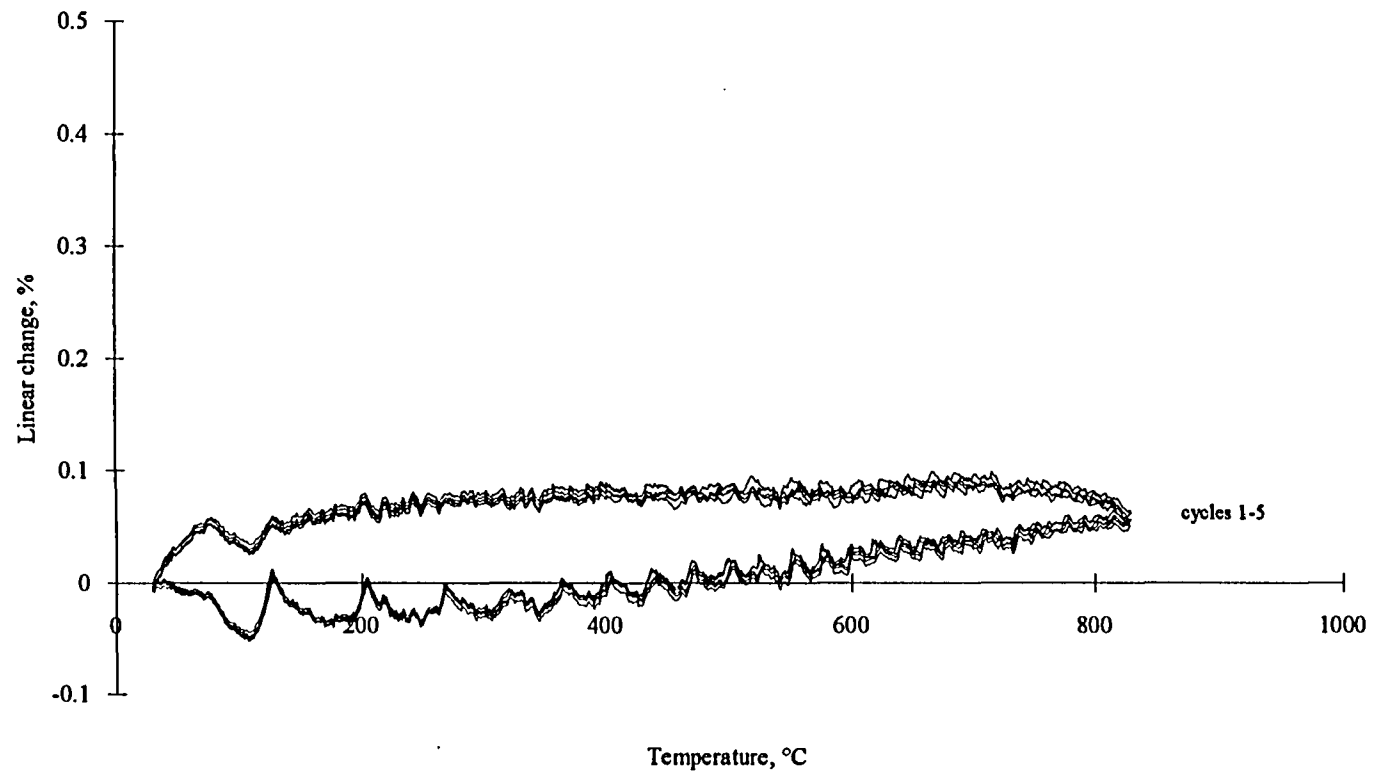


Figure 4.40. Longitudinal thermal expansion behavior of P100Gr/Cu-0.7Cr.

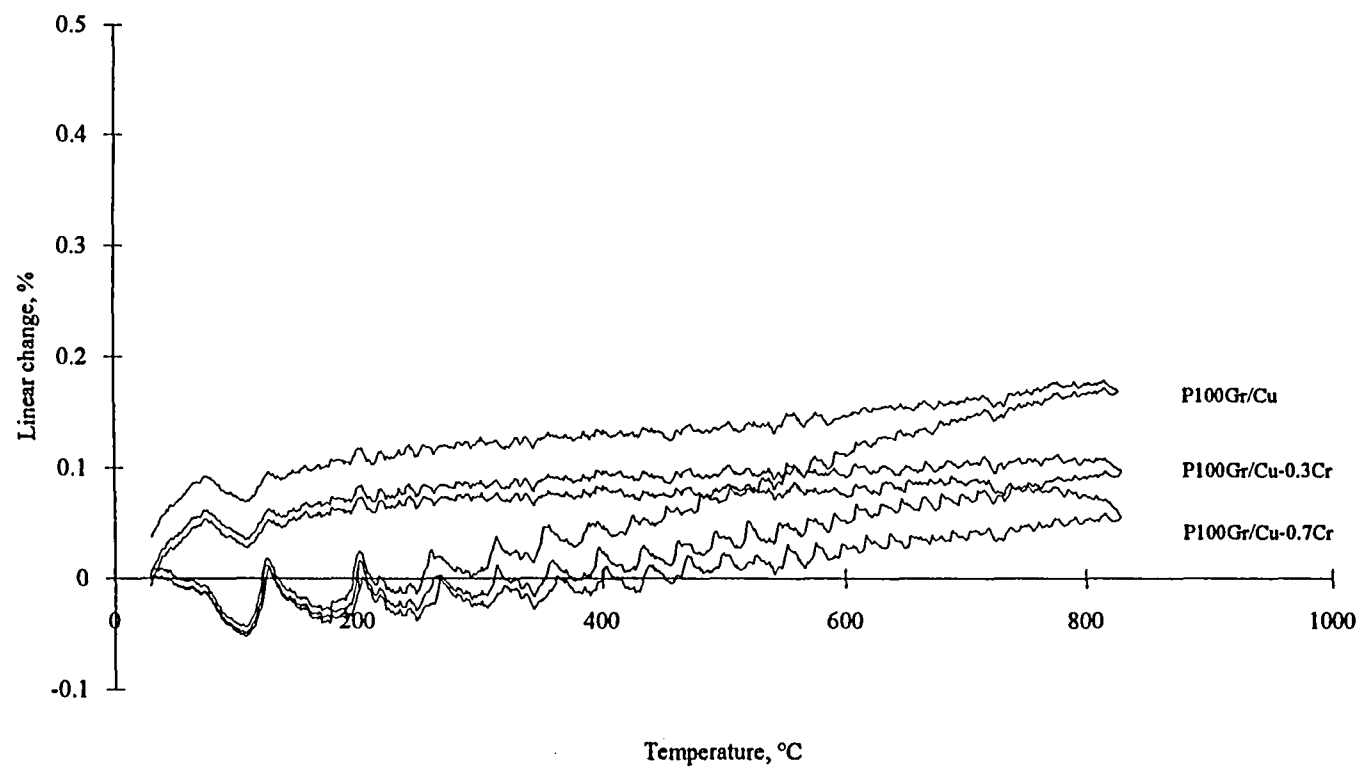


Figure 4.41. Comparison of the initial longitudinal thermal cycle of the P100Gr/Cu-xCr composites with varying matrix compositions.

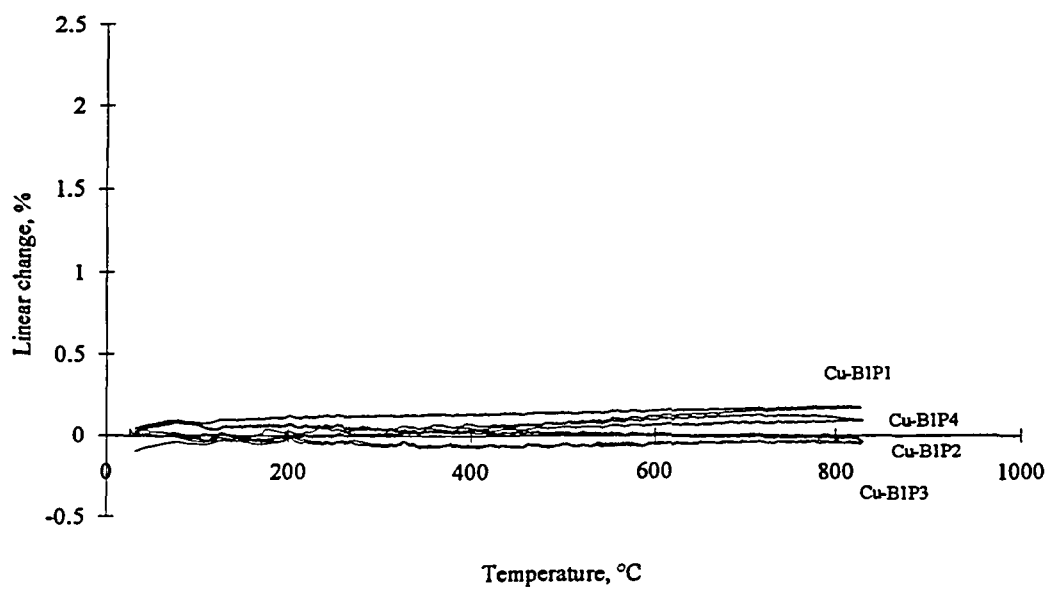


Figure 4.42. P100Gr/Cu (B1) longitudinal thermal expansion.

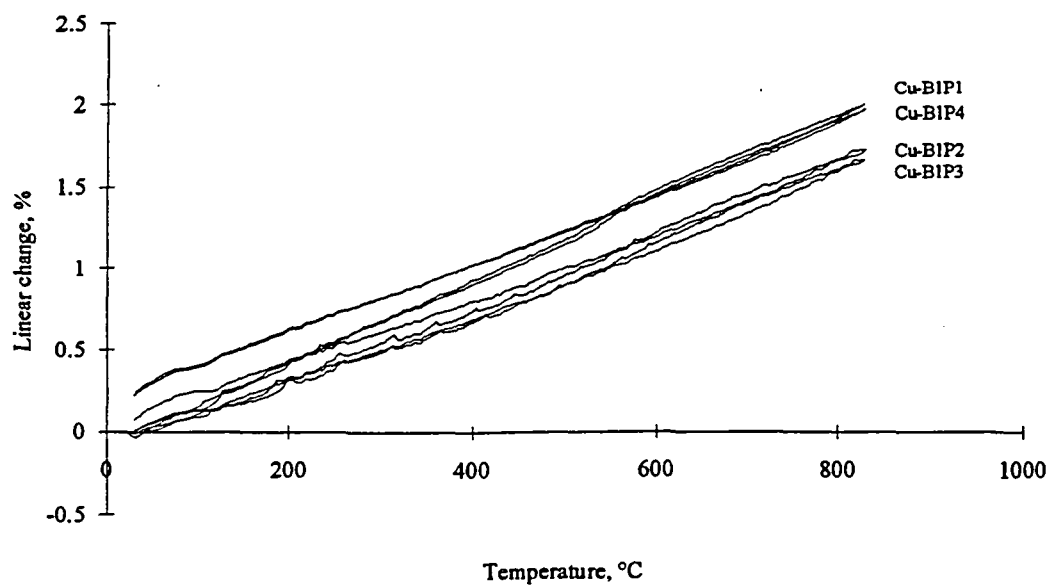


Figure 4.43. P100Gr/Cu (B1) long transverse thermal expansion.

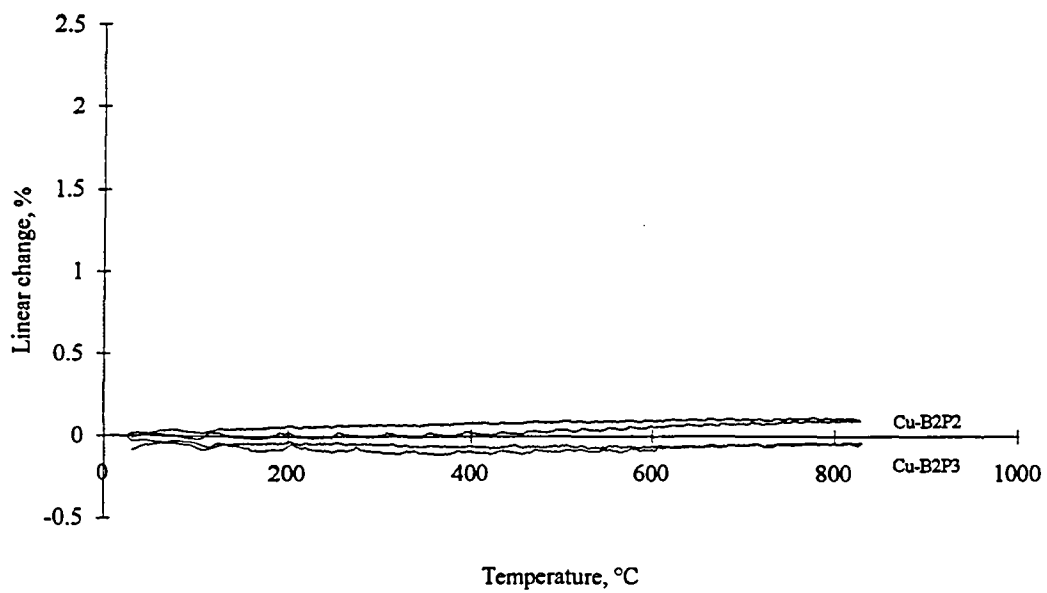


Figure 4.44. P100Gr/Cu (B2) longitudinal thermal expansion.

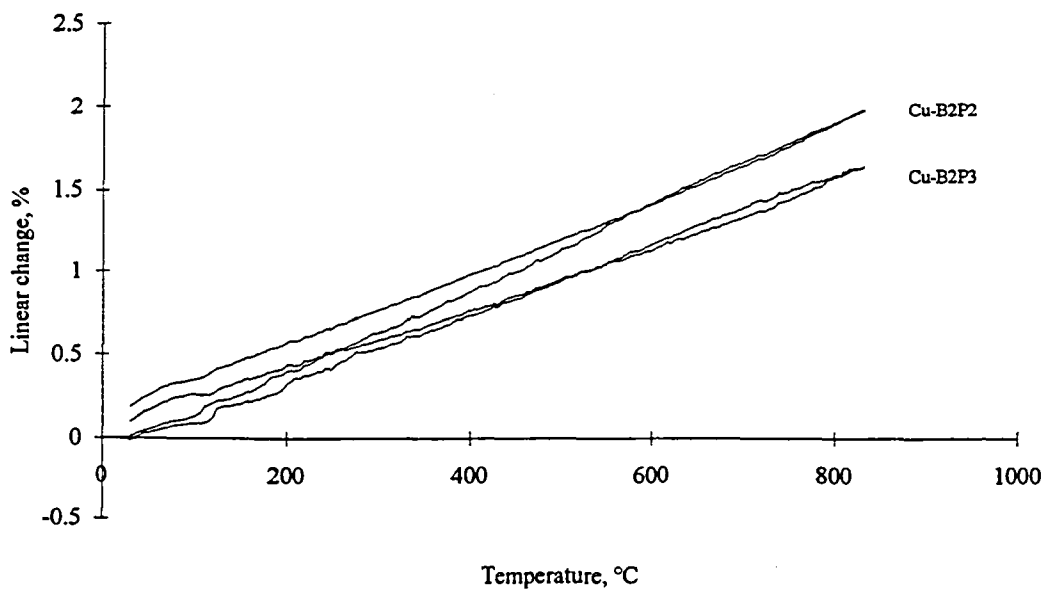


Figure 4.45. P100Gr/Cu (B2) long transverse thermal expansion.

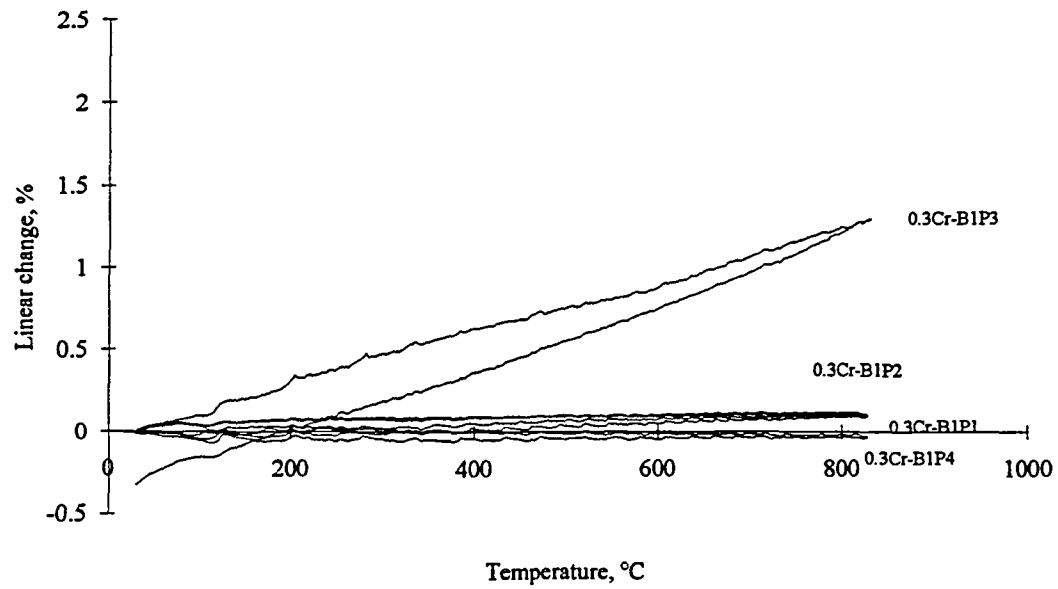


Figure 4.46. P100Gr/Cu-0.3Cr (B1) longitudinal thermal expansion.

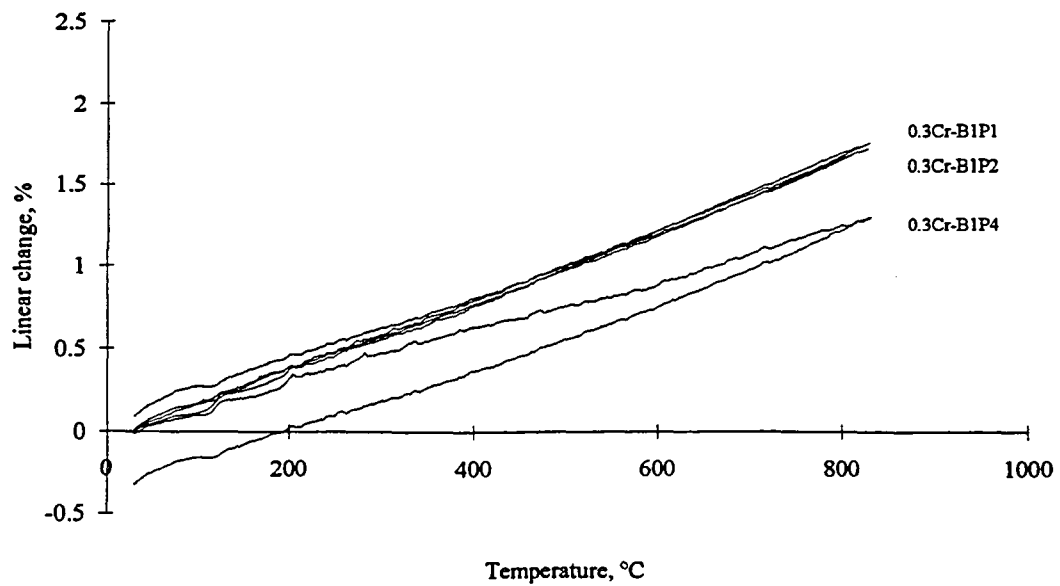


Figure 4.47. P100Gr/Cu-0.3Cr (B1) long transverse thermal expansion.

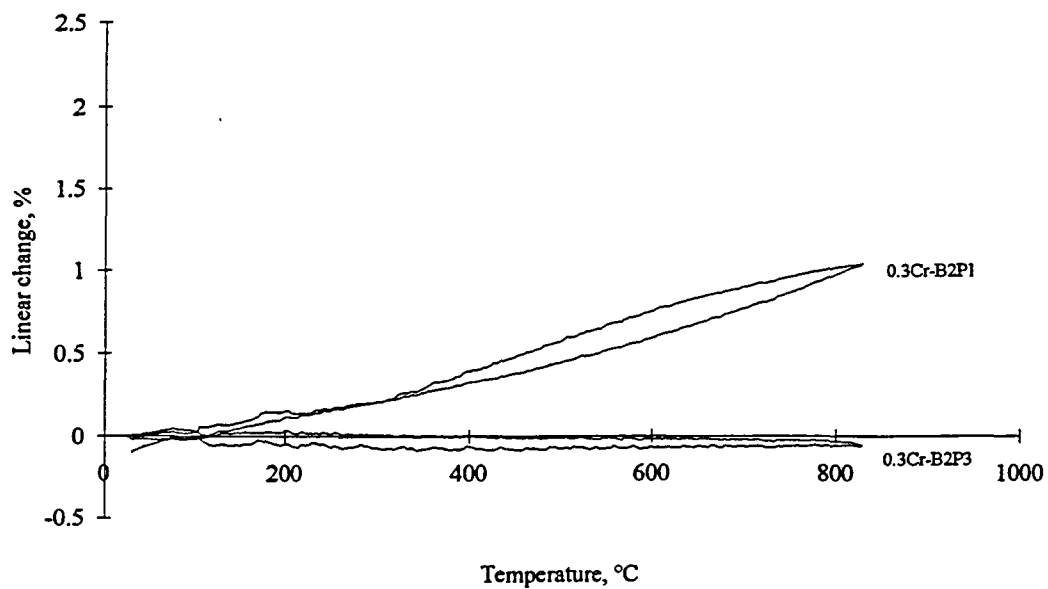


Figure 4.48. P100Gr/Cu-0.3Cr (B2) longitudinal thermal expansion.

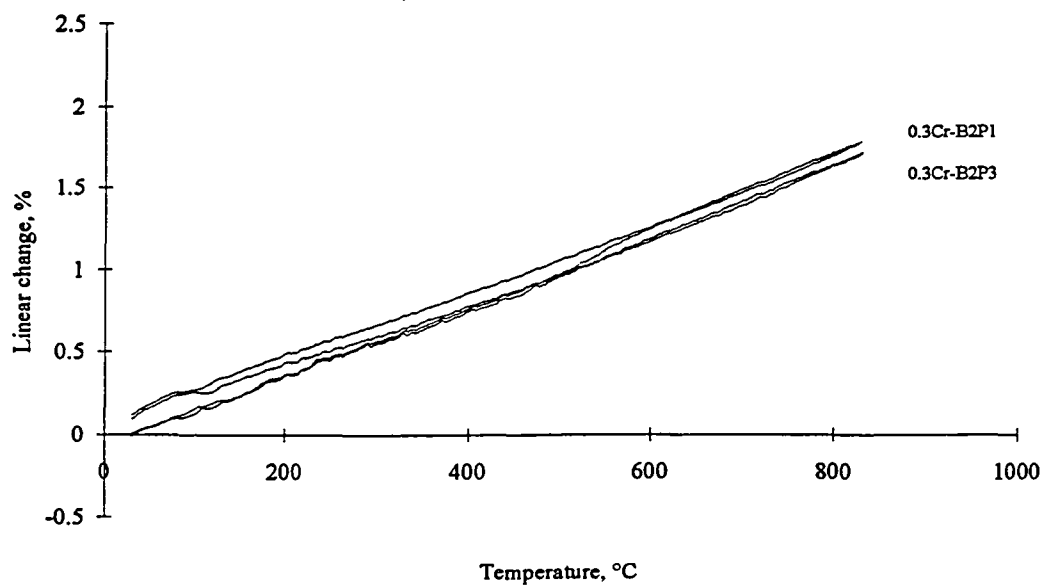


Figure 4.49. P100Gr/Cu-0.3Cr (B2) long transverse thermal expansion.

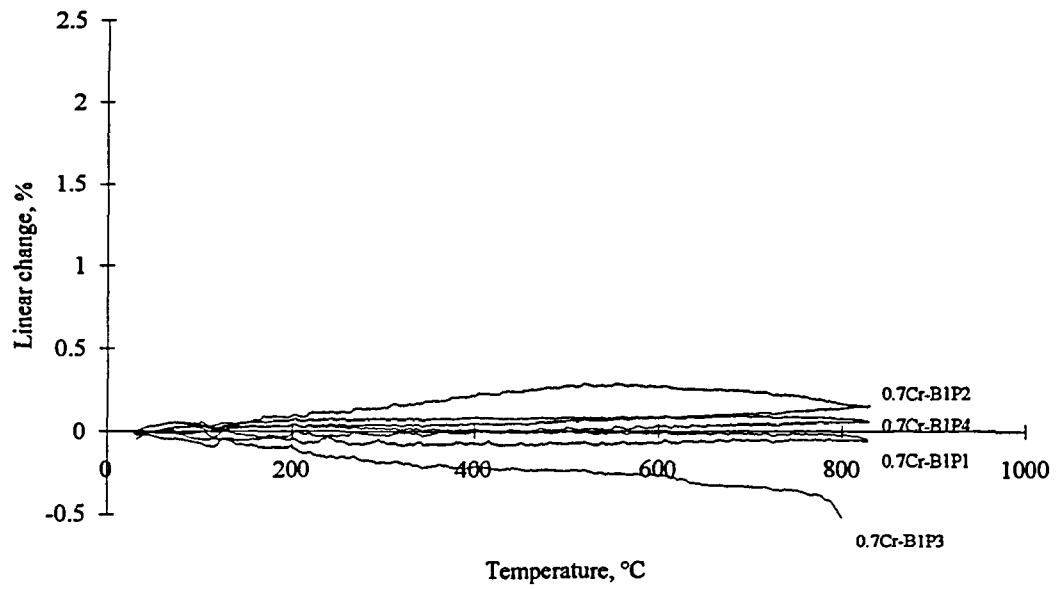


Figure 4.50. P100Gr/Cu-0.7Cr (B1) longitudinal thermal expansion.

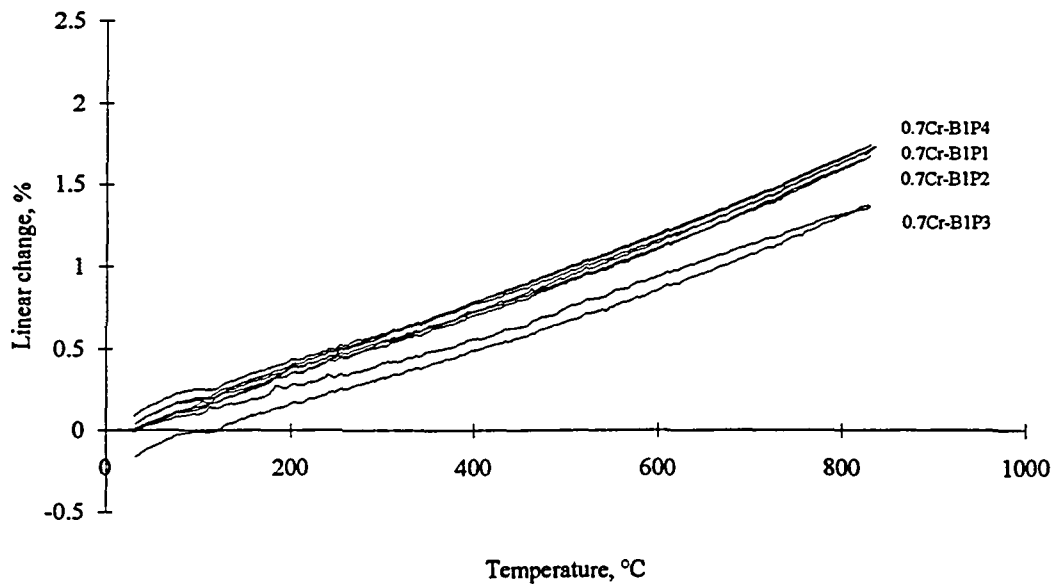


Figure 4.51. P100Gr/Cu-0.7Cr (B1) long transverse thermal expansion.



indicating density, volume percent P100 fiber and comments regarding the condition of the specimens after thermal cycling.

Table 4.2. Thermal expansion test specimen summary.

Plate	L-thermal expansion			LT-thermal expansion		
	density (g/cm <sup>3</sup> )	% P100	condition *	density (g/cm <sup>3</sup> )	% P100	condition *
Cu-B1P1	5.57	49		5.17	55	
Cu-B1P2	4.92	59		4.99	58	
Cu-B1P3	5.00	58		4.94	59	
Cu-B1P4	5.38	52		5.06	57	
Cu-B2P1	N/A	N/A		N/A	N/A	
Cu-B2P2	5.23	54	small L-cracks	5.03	58	surface damage
Cu-B2P3	4.88	60		4.71	62	
Cu-B2P4	N/A	N/A		N/A	N/A	
0.3Cr-B1P1	4.46	66		4.41	67	
0.3Cr-B1P2	5.42	52	thru L-crack	5.11	56	T-buckle
0.3Cr-B1P3	4.94	59		4.99	58	
0.3Cr-B1P4	5.63	49		5.17	55	
0.3Cr-B2P1	5.25	54	thru L-crack	4.84	60	
0.3Cr-B2P2	4.57	64		4.86	60	
0.3Cr-B2P3	N/A	N/A		N/A	N/A	
0.3Cr-B2P4	N/A	N/A		N/A	N/A	
0.7Cr-B1P1	4.86	60		5.13	56	
0.7Cr-B1P2	5.02	58	small L-cracks	4.76	62	
0.7Cr-B1P3	4.91	59	small L-cracks	4.73	62	
0.7Cr-B1P4	4.64	63		5.14	56	

\* Specimen was found to be in its original condition unless listed otherwise.

#### 4.9 Thermal Conductivity

Samples for five P100Gr/Cu-xCr composites were submitted for thermophysical property testing to 800°C in the short transverse direction. The bulk density ( $\rho$ ) was computed by measuring sample dimensions and mass. Specific heat ( $c_p$ ) was determined using a differential scanning calorimeter and thermal diffusivity ( $\alpha$ ) was measured using the laser flash technique. Thermal

conductivity ( $k$ ) was calculated as a product of those quantities, i.e.  $k = \rho c_p \alpha$ . All data are included in Table 4.3.

Table 4.3. Data used for thermal conductivity calculations.

Sample	Density (g/cm <sup>3</sup> )	Volume % P100	Temp. (°C)	c <sub>p</sub> (W-s/g-K)	α (cm <sup>2</sup> /s)	k (W/cm-K)
Cu-B1P1	5.013	56	23	0.4520	0.1320	0.29912
			50	0.4720	0.1230	0.29105
			100	0.5090	0.1100	0.28070
			200	0.5620	0.0783	0.22061
			300	0.6010	0.0602	0.18138
			400	0.6360	0.0516	0.16453
			500	0.6690	0.0489	0.16401
			600	0.7010	0.0501	0.17607
			700	0.7280	0.0739	0.26971
			800	0.7500	0.0781	0.29366
Cu-B2P3	4.712	59	23	0.4810	0.1720	0.38984
			50	0.5050	0.1650	0.39264
			100	0.5600	0.1550	0.40901
			200	0.6370	0.1030	0.30917
			300	0.6800	0.0691	0.22141
			400	0.7190	0.0546	0.18498
			500	0.7630	0.0514	0.18480
			600	0.7980	0.0550	0.20681
			700	0.8320	0.0710	0.27835
			800	0.8590	0.0764	0.30924
0.3Cr-B1P4	5.119	57	23	0.4660	0.1710	0.40793
			50	0.4780	0.1670	0.40864
			100	0.5180	0.1580	0.41898
			200	0.5780	0.1310	0.38761
			300	0.6230	0.0999	0.31861
			400	0.6520	0.0848	0.28304
			500	0.6870	0.0845	0.29718
			600	0.7230	0.1050	0.38862
			700	0.7550	0.1090	0.42128
			800	0.7780	0.1030	0.41022
0.3Cr-B1P4	5.119	57	200	0.5780	0.1540	0.45567

Sample	Density (g/cm <sup>3</sup> )	Volume % P100	Temp. (°C)	C <sub>p</sub> (W-s/g-K)	α (cm <sup>2</sup> /s)	λ (W/cm-K)
0.3Cr-B2P2	4.866	61	23	0.4720	0.1980	0.45477
			50	0.4960	0.1890	0.45617
			100	0.5440	0.1770	0.46855
			200	0.6110	0.1530	0.45490
			300	0.6690	0.1120	0.36461
			400	0.7140	0.0901	0.31304
			500	0.7540	0.0904	0.33168
			600	0.7900	0.1120	0.43055
			700	0.8230	0.1100	0.44053
			800	0.8520	0.1060	0.43947
			200	0.6110	0.1610	0.47868
0.7Cr-B1P2	4.671	63	23	0.4730	0.1400	0.30932
			50	0.4980	0.1350	0.31404
			100	0.5430	0.1340	0.33988
			200	0.6130	0.1220	0.34933
			300	0.6690	0.1120	0.35000
			400	0.7190	0.1050	0.35264
			500	0.7600	0.1020	0.36210
			600	0.7920	0.0961	0.35552
			700	0.8240	0.0850	0.32716
			800	0.8530	0.7990	0.31836
			200	0.6130	0.1350	0.38656

#### 4.9.1 Heat Capacity

Short transverse specific heat results are given in Figure 4.52. The specific heat values for the Cu-B2P3 (59% P100), 0.3Cr-B2-P2 (61% P100) and 0.7Cr-B1P2 (63% P100) samples are larger than those for the Cu-B1P1 (56% P100) and 0.3Cr-B1P4 (57% P100) samples. However, the specific heat values for the 0.3Cr-B1P4 sample are somewhat larger than those for the Cu-B1P1 sample, even though the P100 fiber content is lower.

#### 4.9.2 Thermal Diffusivity

Short transverse thermal diffusivity values are plotted in Figure 4.53. A point at 200°C was taken during cooling. The diffusivity values for all samples, with the exception of the 0.7Cr-B1P2 sample, showed decreases between room temperature and 500°C and increases between 500 and

700°C. These increases were permanent as indicated by the values at 200°C recorded during cooling that were substantially higher than the values recorded during heating.

#### 4.9.3 Thermal Conductivity

Short transverse thermal conductivity values were calculated and plotted in Figure 4.54. The curves reflect the shape of the diffusivity curves, including the permanent increases.

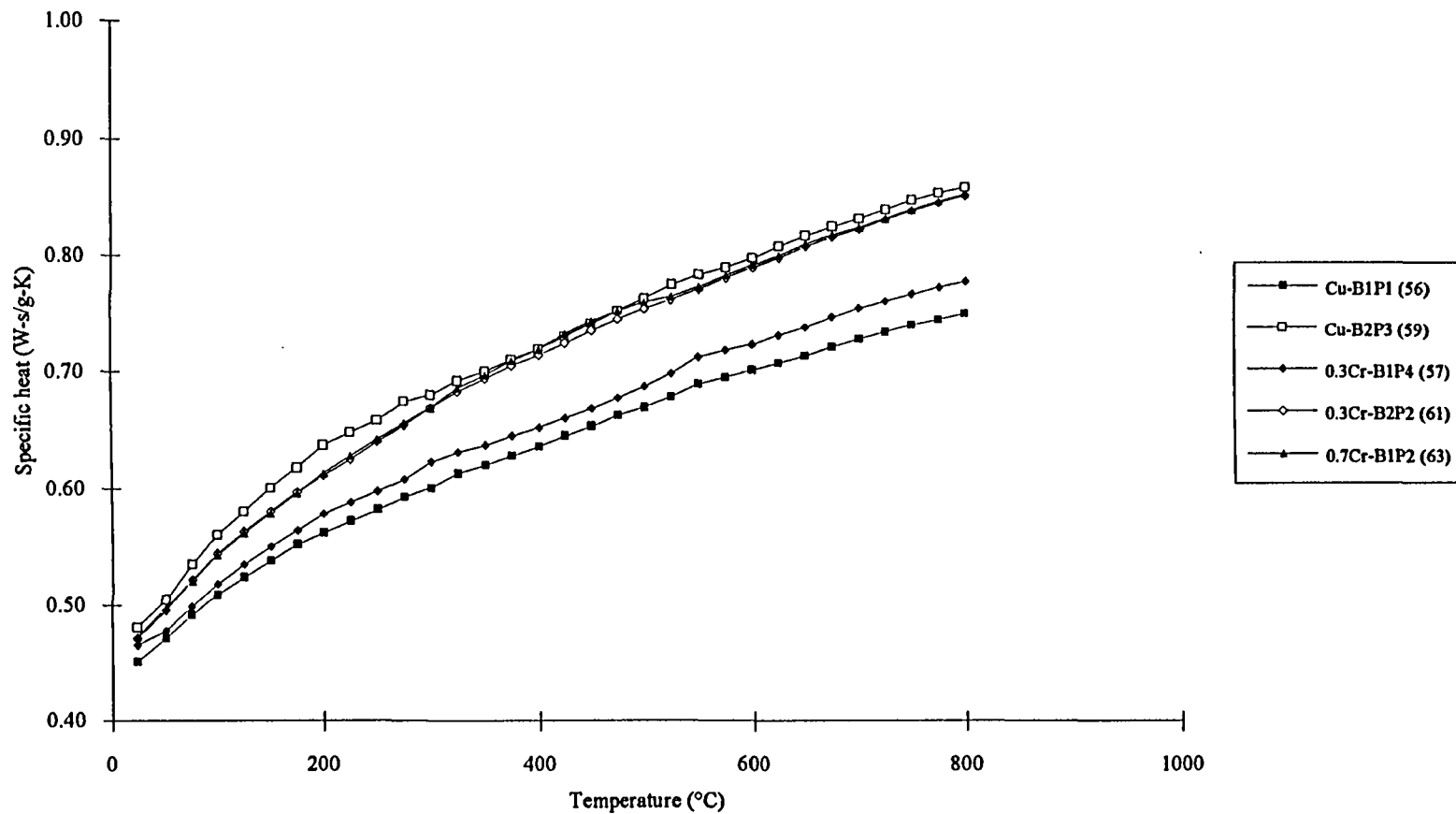


Figure 4.52. Short transverse specific heat of P100Gr/Cu-xCr composites.  
(% P100 given in parentheses)

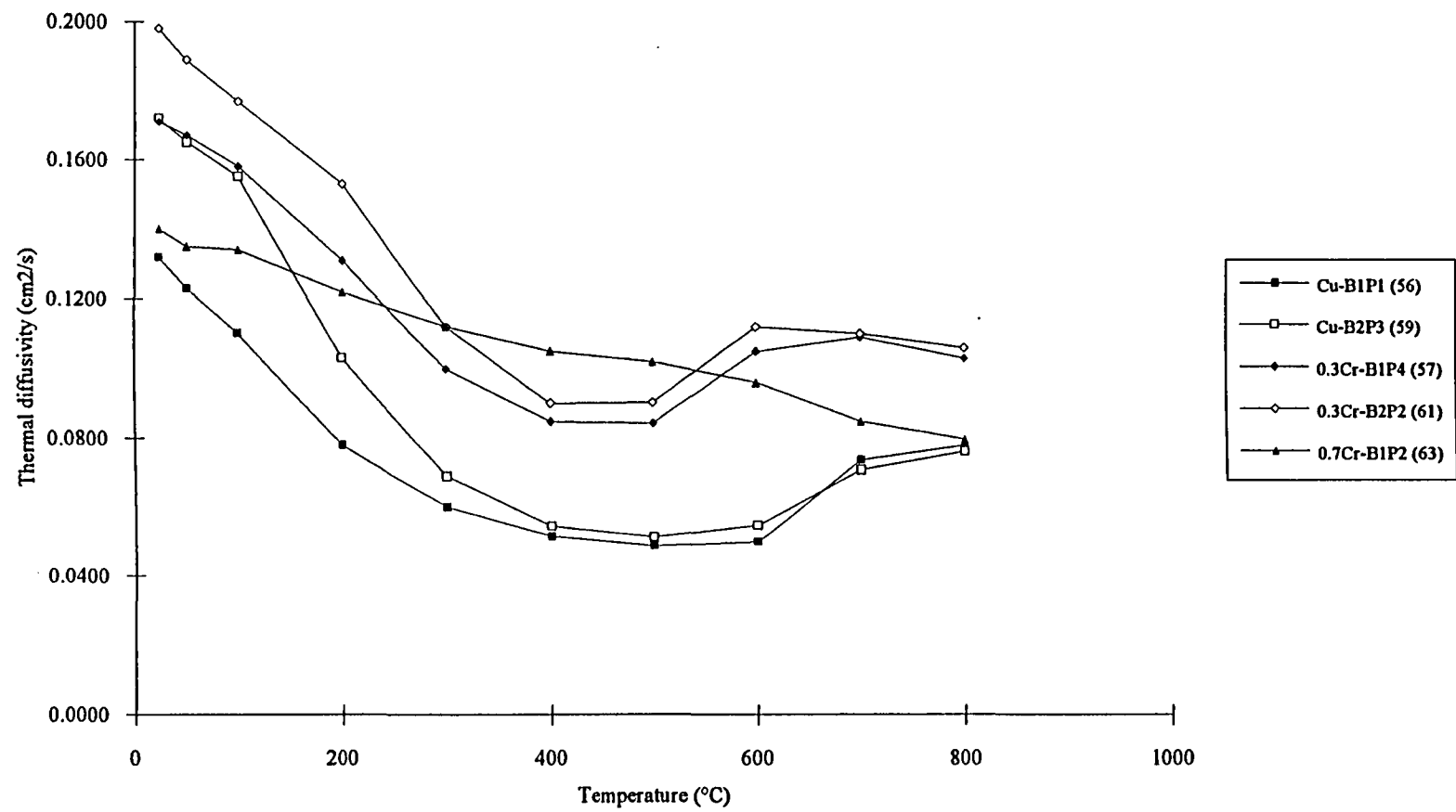


Figure 4.53. Short transverse thermal diffusivity of P100Gr/Cu-xCr composites.  
(% P100 given in parentheses)

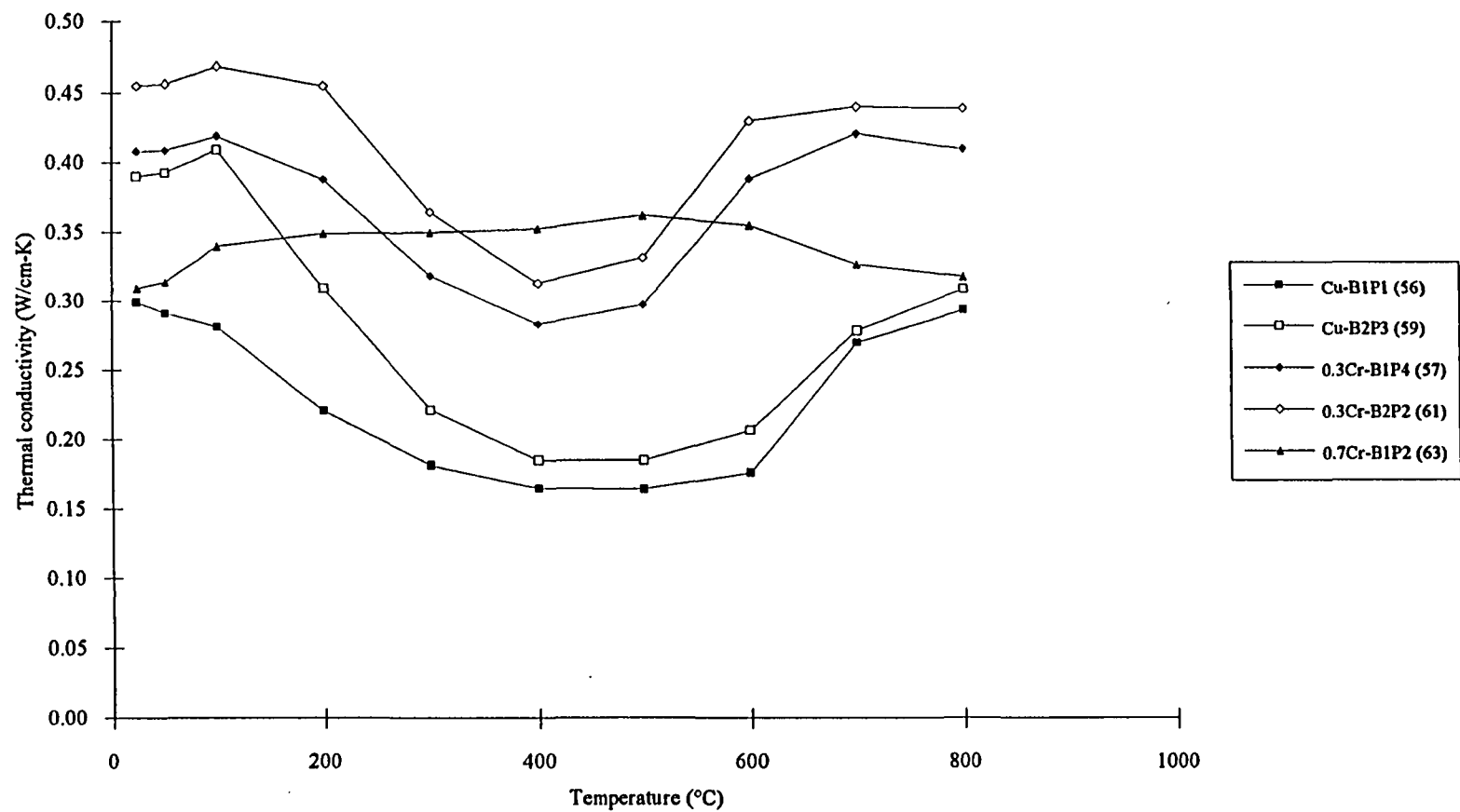


Figure 4.54. Short transverse thermal conductivity of P100Gr/Cu-xCr composites.  
(% P100 given in parentheses)

## 5 DISCUSSION

### 5.1 Casting Quality

According to the x-ray inspection and the cross sectional optical metallography, P100Gr/Cu-xCr composite plates generally are fully dense, i.e. without internal porosity. Variations in density observed using x-ray radiography are associated with isolated surface cracks. Sticking of the composite plates to the graphite molds is known to occur during the casting of the alloyed matrix systems. Sticking does not occur in the unalloyed matrix composites. The sticking is due to the formation of  $\text{Cr}_3\text{C}_2$  between the surface of the composite plate and the mold wall. Formation of such a reaction phase at the mold wall would result in a lower Cr content in the near surface region of the plate.

#### 5.1.1 Density Variations

The density is found to vary, particularly from top to bottom, in any given plate. Overall variations range from 0.1 to 0.4 g/cm<sup>3</sup>. The amount of variation in density is not consistent from plate to plate, or from batch to batch. Within a matrix composition, the determination of %P100 graphite fibers in each plate results in standard deviations of 1.12 in the volume percent fiber for seven P100Gr/Cu plates, 1.99 for seven P100Gr/Cu-0.3Cr plates and 2.86 for the four P100Gr/Cu-0.7 plates. Revisiting Equation 3.2, the volume percent fiber corresponds to composite density through the following relationship:

$$\%P100 = \frac{\rho_m - \rho_c}{\rho_m - \rho_f} \cdot 100 = \frac{8.92 - \rho_c}{6.77} \cdot 100 \quad (5.1)$$



Comparing the standard deviations in a f-test indicates that the density variations (corresponding to variations in plate thickness) are not significantly different between the compositions, with 90-95% confidence.

It is not likely that the addition of Cr to the matrix aids infiltration of the mold during pressure casting. The reaction phase can only form at the fiber surfaces once the fibers have been exposed to the molten Cu. Only then will the reaction phase form, and the molten Cu wet the reaction phase on the fiber surfaces.

#### 5.1.2 Fiber Distribution

Surveying down through the thickness while investigating the width of the plate (the long transverse direction) reveals only small variations in density, as shown by the x-ray radiographs. The short transverse optical micrographs, however, indicate that Cu channelling is occurring during the casting process. These Cu channels are intertow regions during the casting process. Difficulties in spreading the individual 2K fiber tows are evident.

The nominal %P100 in each of the cast plates is derived from the number of wraps used to fill the mold prior to infiltration. Knowing that 470 2K fiber tows were used for each casting, the actual distribution of tows can be calculated. Given a fiber of 10  $\mu\text{m}$  diameter, the cross sectional area of a 2K tow is obtained as follows:

$$A_{\text{fiber}} = \pi r^2 = 78.5 \mu\text{m}^2 \quad (5.2a)$$

$$A_{\text{tow}} = (2000) A_{\text{fiber}} = 157,079 \mu\text{m}^2 \quad (5.2b)$$

Directly backcalculating to obtain the radius of a 2K tow, would yield an underestimate of the actual radius. For an ideally close-packed bundle of fibers (identical parallel cylinders), the packing fraction is illustrated in Figure 5.1. If  $r$  is the fiber radius, the area of the "unit cell" outlined by the

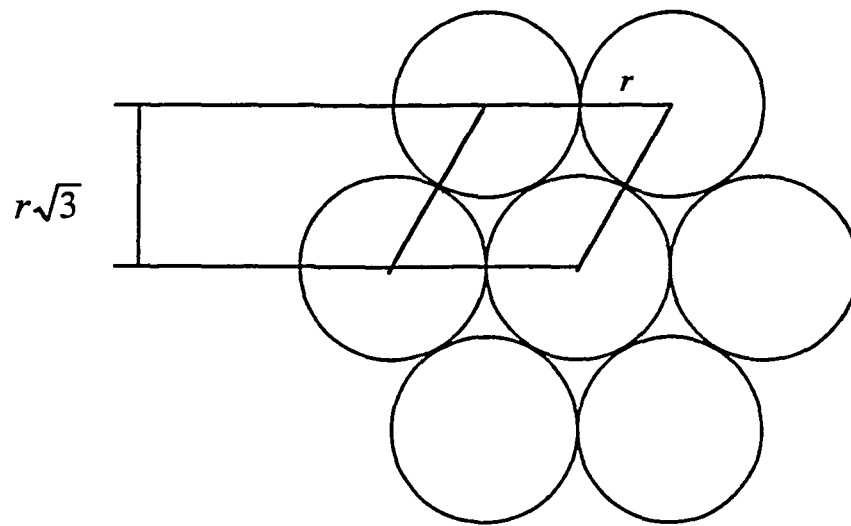


Figure 5.1. Ideally close-packed bundle of fibers of radius  $r$ .

parallelogram is  $r\sqrt{3} \cdot 2r = 2\sqrt{3}r^2$ . Since the unit cell contains one fiber, the packing fraction of a close-packed bundle (tow) of fibers is:

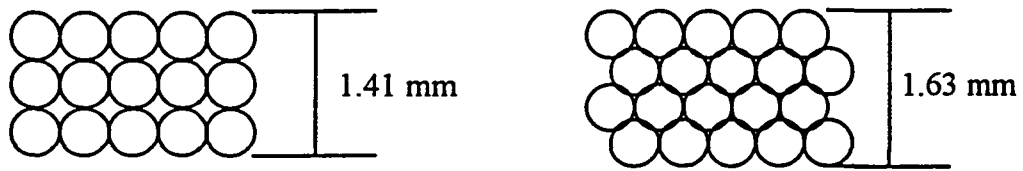
$$\eta = \frac{\pi r^2 l}{2\sqrt{3} r^2 l} = \frac{\pi}{2\sqrt{3}} = 0.9069 \quad (5.3)$$

As a result, the tow area calculated previously should be:

$$A_{tow} = (2000) A_{fiber} \cdot \frac{1}{0.9069} = 173,205 \mu m^2 \quad (5.4)$$

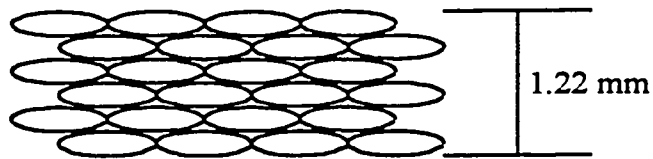
Now, backcalculating yields the correct diameter of the 2K fiber tow as 0.47 mm. Given a 76.2 mm wide plate with a thickness of 1.5-1.6 mm, it is possible to contain three rows of 157 fiber tows in a plate cross section if the fibers are arranged as shown in Figure 5.2a. A reinforcement layout of 4 rows of 117 fiber tows is possible under close-packed conditions (Figure 5.2b).

Investigation by optical metallography, however, reveals the outlines of six fiber tows in the plate cross section. The procedure by which the mold cavity is filled with fiber tows must be considered. Prior to the casting process, the molds are filled with a specified number of tows to yield a desired nominal fiber volume fraction. The fiber tows are wrapped around the mold halves from top to bottom. The fiber ends are not cut prior to infiltration in order to reduce the possibility of fiber movement in the mold. This wrapping procedure strains the fiber tows. Knowing this, it can be assumed that the resultant shape of the fiber tows is no longer circular, but somewhat elliptical. If during the wrapping process the fiber tows are strained to a "flatter" shape, it is likely that the final tow shape may be only half as wide and twice as long. This change in shape, shown in Figure 5.2c, would allow for six rows of 78 tows in the plate cross section. Consequently, this is what is observed in the optical micrographs. For a 1.52 mm thick plate, approximately 0.3 mm total thickness of Cu is



(a) parallel arrays, no strain  
3 x 157 tows in cross section

(b) close-packed, no strain  
4 x 117 tows in cross section



(c) close-packed, strain due to wrapping  
6 x 78 tows in cross section

Figure 5.2. P100 2K fiber tow packing configurations.

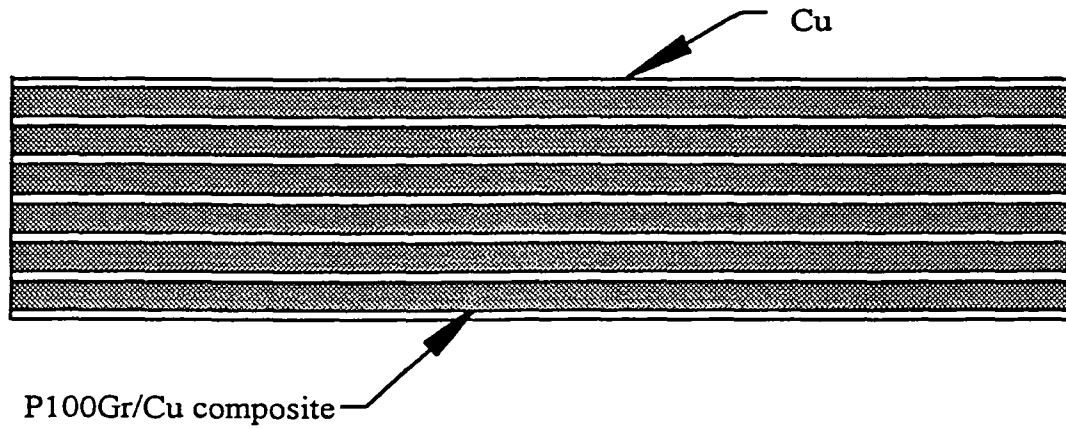


Figure 5.3. Proposed laminate construction: 20% Cu - 80% P100Gr/Cu composite.  
Plate average of 56% P100 fiber  $\Rightarrow$  P100Gr/Cu composite phase of 70% fiber.

allowed for the construction illustrated in Figure 5.2c, which is equal to 20% of the total plate thickness.

Due to the difficulty in separating the fibers within a tow, the cast plate has a cross section resembling that of a composite laminate, with the two materials being pure copper and P100Gr/Cu composite. The pure copper component comprises approximately 15-25% of the laminate, leaving 75-85% to the P100Gr/Cu composite phase. This is illustrated in Figure 5.3. Assuming that the "composite phase" of the laminate contains all of the fiber reinforcement, the volume percent of P100 fibers in composite phase is much higher than previously calculated for the entire plate, 70-74% (depending on the P100 volume fraction of the individual plate).

## 5.2 Interfacial Reaction Layer Characterization

### 5.2.1 Identification of Reaction Layer Phase

While the AES analyses assisted in locating the reaction phase through the use of elemental Cr mapping techniques, the TEM analysis led to the identification of the reaction layer as the  $\text{Cr}_3\text{C}_2$  phase. This is in agreement with thermodynamic calculations addressing the stability of the various chromium carbide phases.

### 5.2.2 Reaction Layer Continuity

The reaction phase forms in both the 0.3 and 0.7 wt% Cr matrix composites. In the P100Gr/Cu-0.7Cr system, the phase forms in a continuous layer about 200 nm thick in matrix rich regions as seen in SEM and TEM micrographs. The layer was thinner around fibers that were surrounded by lower total amounts of matrix. For the P100Gr/Cu-0.3Cr system, much of the composite contains only isolated  $\text{Cr}_3\text{C}_2$  particles at the fiber/matrix interface or unreacted fiber surface area.

In both alloyed matrix systems, many of the fiber surfaces exposed by the etching procedure revealed clean, unreacted surfaces. However, a small percentage of  $\text{Cr}_3\text{C}_2$  particles were found in the

cross sections. It is likely that a deeper etch would reveal similar trends through the length of the metallographic specimen. In any given cross section, the matrix rich regions will contain the highest percentage of Cr and therefore the largest amount of  $\text{Cr}_3\text{C}_2$  reaction phase. Fiber surfaces that appear to be free of reaction phase at one depth, may have  $\text{Cr}_3\text{C}_2$  particles present at another. This was seen in the SEM investigation of specimens with approximately 5-10  $\mu\text{m}$  of matrix removed.

### 5.2.3 Fiber/Matrix Adhesion

SEM investigation of failed long transverse tensile specimens indicated that while some  $\text{Cr}_3\text{C}_2$  particles adhere to the fibers after separation from the matrix, the majority of the reaction phase is more adherent to, and remains with, the Cu. This was seen during prior wetting studies of molten Cu-Cr alloys on Gr substrates [16]. The  $\text{Cr}_3\text{C}_2$  is less adherent to the P100 fibers due to the weak bonding to the Gr basal planes. It is also conceivable that the Gr basal planes, which are not well bonded to each other, separate and fracture. This being the case, separation of the  $\text{Cr}_3\text{C}_2$  phase from the matrix would be more difficult than separation from the fibers, as a crack would propagate parallel to the graphene sheet.

## 5.3 Tensile Properties

Absolute values for the longitudinal tensile specimens could not be determined due to premature shear failure of the Cu layer present on the surfaces prior to tensile fracture. The shear failure appears to occur between the outer Cu layer and the interior composite. The shear pull-out of the composite is characteristic of all the longitudinal specimens tested, regardless of matrix composition or heat treatment time. The highest stress achieved of all the specimens tested was 758 MPa. A way to combat this type of failure has not yet been determined. Even plates that appear to have very little Cu on the outer surface have a sufficient thickness to make shear failure favorable. Only a few hundred atomic Cu layers would be necessary. All longitudinal tensile specimens sheared at less than 13 kN. Failure of the epoxy did not occur in any of the test specimens. At this load, the

Cu in the specimen tab (grip) area only undergoes 33 MPa of stress. This is much lower than the 159 MPa shear stress of Cu. Under the pressure of the grips used during testing, the Cu/composite interface will shear.

A three-way ANOVA revealed that, on average, the longitudinal tensile strengths of the as-cast P100Gr/Cu-xCr composites are statistically significantly different with respect to matrix composition, at the 97.5% confidence level. It was found that the average P100Gr/Cu-0.3Cr composite tensile strength is lower than both the P100Gr/Cu and P100Gr/Cu-0.7Cr composite strengths. The composite strengths were not found to be statistically different at the various heat treatment times utilized. Specimen-to-specimen variation, within an individual plate, is high. Plate-to-plate and batch-to-batch variations are not significant over and above specimen-to-specimen variation. Differences in heat treated strengths with respect to matrix composition could not be discerned due to the low number of tests conducted at each heat treatment and the high specimen-to-specimen variation. The variations in the raw data do not increase or decrease with heat treatment time; the standard deviations in strength corresponding to each heat treatment are not significantly different.

The average moduli of the composites was approximately 393 GPa and was maintained after thermal exposure at 760°C for 100 hr. The moduli did not vary with matrix composition. Calculation according to the rule of mixtures (ROM) Young's modulus for uniaxial composites [63] can be determined as follows:

$$\begin{aligned}
 E_c &= E_f V_f + E_m V_m \\
 E_c &= 758\text{GPa}(.57) + 117\text{GPa}(.43) \\
 E_c &= 482\text{GPa}
 \end{aligned}
 \tag{5.5}$$

While the average moduli reached was 81% ROM, many of the specimens reached an elastic modulus equivalent to 88% ROM.



The long transverse tensile strength values are quite low. While the number of specimens tested from each composition is not consistent, the P100Gr/Cu-0.7Cr specimens have an average 90° tensile strength twice that of P100Gr/Cu and P100Gr/Cu-0.3Cr. The long transverse tensile behavior of continuous fiber reinforced composites is limited primarily by the distribution of fibers in the composite cross section. A path of adjacent fibers, under transverse loading, can act as a weak link in the specimen. The illustrations in Figure 5.4. represent (a) rows or chains of close-packed fibers with little to no Cu matrix, between fibers, due to fiber touching and (b) well-distributed fibers in the Cu matrix. Given the loading configuration shown, greater energy is required to propagate a crack and separate the well-distributed fibers than the touching fibers. As explained earlier, the cross sections of the P100Gr/Cu-xCr composites resemble a laminate structure. In the areas of "composite phase", most of the fibers are closely packed and touching. This allows for quick specimen separation to occur at fiber junctions rather than slower crack propagation through the matrix which is possible in lower volume fraction composites with evenly distributed fiber reinforcement..

#### 5.4 Bend Properties

The elastic moduli obtained in three-point bending are in the range of the values for the moduli determined through longitudinal tensile testing. Knowing this, and the accuracy of displacement measurements under the bend testing conditions, the shear moduli calculated using this test method are of the correct order of magnitude. According to the actual values, the P100Gr/Cu-0.3Cr composite has a shear modulus of 9.18 GPa, which is higher than either of the P100Gr/Cu and P100Gr/Cu-0.7Cr systems (values of 5.96 and 6.40 GPa, respectively). However, given the variability in fiber distribution from specimen-to-specimen and plate-to-plate, a different sampling of specimens could have resulted in the P100Gr/Cu-0.7Cr having the highest shear modulus, as has been observed earlier in this study. Under either circumstance, the alloyed matrix enhances the stiffness of the P100Gr/Cu composite. This is due to the presence of  $\text{Cr}_3\text{C}_2$  which increases interfacial bond strength.

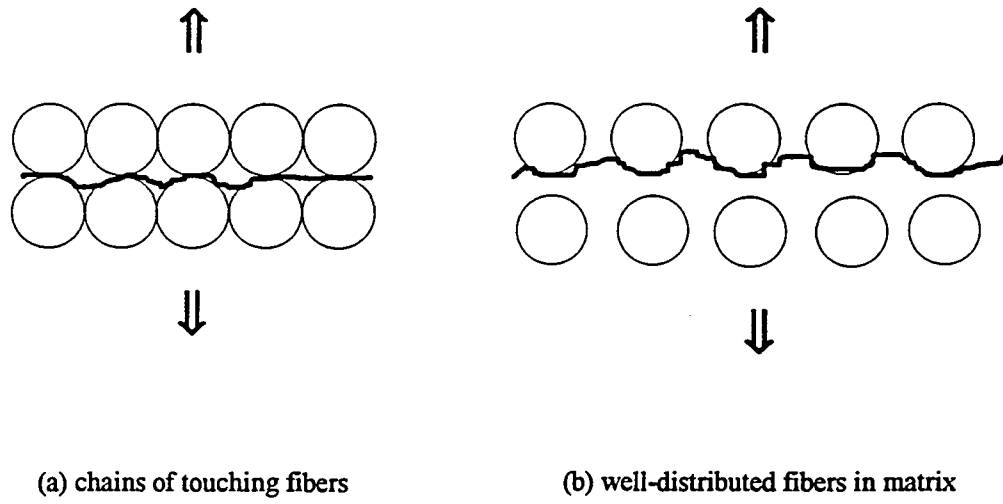


Figure 5.4. P100Gr/Cu-xCr transverse (90°) loading configurations showing path of crack propagation.

During bending, fiber/matrix sliding will occur where fibers are not well bonded to the matrix. The presence of an interfacial reaction phase inhibits this sliding and increases the stiffness of the composite. It is not necessary for this reaction phase to be in layer form. The particle nature of much of the interfacial carbide phase in the P100Gr/Cu-Cr composites is sufficient to reduce fiber/matrix sliding and increase the shear modulus.

### 5.5 Thermal Expansion Behavior

The long transverse thermal expansion behavior of the P100Gr/Cu-xCr composites falls between that of pyrolytic graphite and pure copper. It is seen in Figure 4.37, that both copper and graphite expand in the transverse or radial direction. As a result, the long transverse thermal responses of the composites exhibit expansion also.

The longitudinal thermal cycling behavior of the P100Gr/Cu-xCr composites incorporates the individual responses of both the copper and the graphite fibers. As shown in Figure 4.38 (runaway cycling), upon heating, the composite expands in a relatively linear manner, resulting in a 0.176% increase in length at 827°C. Because of the mechanical bonds created during the casting process, the negative thermal expansion behavior of the graphite limits the overall increase in length of the composite and prevents behavior which would resemble that of copper. Also occurring during heating is the expansion of both the P100 fibers and the copper in the radial or transverse direction. This creates additional mechanical bonds which "lock" the fibers and the matrix together to favor the longitudinal behavior of the graphite fibers. As a result of this mechanical locking, when the composite is cooled from 827°C to room temperature, it displays behavior similar to that of graphite.

Some hysteresis is observed during thermal cycling of Gr/Cu composites. During heating, some degradation of the mechanical bonds formed during the pressure casting process occurs. This causes the cooling behavior of the composite to deviate from the heating behavior. Upon further cycling, the transverse expansion of both the graphite fibers and the copper matrix creates a

mechanical locking effect. Although these new bonds eventually separate during cooling, the behavior is followed for subsequent cycles.

In the case of the unalloyed copper matrix composites, as shown in Figure 4.38, the composite does not return to its original length during longitudinal thermal cycling. Approximately a 0.04% change in length results from the first thermal cycle. During each subsequent cycle, while the behavior is identical, the composite undergoes a small increase in length. After ten cycles, the P100Gr/Cu composite has experienced a 0.135% increase in length.

This "runaway" condition is only characteristic of the unalloyed matrix composites. Figures 4.39 and 4.40 show stable thermal cycling behaviors for both the P100Gr/Cu-0.3Cr and P100Gr/Cu-0.7Cr composites. Both composites show little to no overall change in length after numerous cycles. The P100Gr/Cu-0.3Cr specimen experienced essentially zero linear change after four cycles; the P100Gr/Cu-0.7Cr specimen showed zero linear change after five cycles.

The thermal expansion behavior of the P100Gr/Cu composites has been found to vary with matrix composition. As shown in Figure 4.41, the addition of 0.3 wt% chromium to the copper matrix not only lowers the amount of expansion upon heating to 827°C, but also stabilizes the runaway condition seen in the unalloyed composite. There is sufficient chromium available at that composition to allow for the formation of chromium carbide at the fiber/matrix interface to create a chemical bonding effect. The improved bonding at the interface restricts the extensive expansion of the copper matrix and contraction of the P100 graphite fibers. Essentially no overall change in dimension is observed. The same is true for the P100Gr/Cu-0.7Cr composite. The higher chromium content results in a higher percentage of interfacial reaction phase, which in turn lowers the amount of expansion upon heating. At this alloying level, the thermal expansion behavior of the composite is dictated by that of the P100 graphite fibers.

## 5.6 Thermal Conductivity

The thermal conductivity of the P100Gr/Cu-xCr composites in the short transverse direction is approximately 10% of that observed in the longitudinal direction. This is in agreement with results obtained in earlier studies on P100Gr/Cu composites [1, 5]. The P100Gr/Cu and P100Gr/Cu-0.3Cr composites exhibit similar variations in thermal conductivity over the temperature range investigated. The P100Gr/Cu-0.3Cr specimens, however, have a higher thermal conductivity. This may be the result of the small amounts of chemical bonding present at the Gr/Cu interface, due to the  $\text{Cr}_3\text{C}_2$  formation, which would allow heat conduction across the interface more easily than mechanical bonding. A dip in the curve is observed between approximately 200 and 600°C. It is speculated that this is a result of the negative thermal expansion of the P100 fibers in this temperature range. Without the presence of chemical bonds, at elevated temperatures the fibers may debond from the matrix and hinder heat transport in the transverse direction.

The P100Gr/Cu-0.7Cr composites display a different behavior than the P100Gr/Cu and P100Gr/Cu-0.3Cr composites. The short transverse thermal conductivity is fairly constant with temperature. This may be due to the increased chemical bonding at the fiber/matrix interface, which not only promotes better heat transfer but also restricts the expansion of the composite, and therefore limits fiber/matrix debonding.

The short transverse thermal conductivity, like the long transverse tensile strength, is sensitive to the presence of continuous paths or channels of the Cu matrix in the composite structure. Because of the resistance of heat transfer across the fiber/matrix interface, continuous paths of Cu matrix are needed for efficient heat conduction to occur through the thickness of the composite plates.

To estimate the effective transverse thermal conductivity of the Gr/Cu interface, the parallel slab construction (see Figure 2.27), similar to the laminate described earlier in this section, can be used. Using Equation 2.29, first to eliminate the thermal conductivity of the copper matrix, and then to remove the transverse or radial conductivity of the P100 fibers, yields the effective thermal

conductivity of the interface. From the data for the short transverse thermal conductivity of the P100Gr/Cu-xCr composites shown in Figure 5.5, the thermal conductivity of the copper matrix can be removed as follows:

$$\frac{1}{k_c} = \frac{V_{Cu}}{k_{Cu}} + \frac{V_{Gr}}{k_{Gr}} \quad (5.6)$$

Inserting  $k_c$ ,  $V_{Cu}$ ,  $k_{Cu}$  and  $V_{Gr}$  into the above equation gives  $k_{Gr}$ , where  $k_{Gr}$  is the combined conductivity of P100 in the radial direction and the interface. This results in a conductivity for the P100 fibers and the interface which is approximately 40% lower than those of the composites, as shown in Figure 5.6. The transverse conductivity of the P100 fibers can be estimated by considering the morphology of the fibers in both the a-direction and the c-direction. In highly oriented pyrolytic graphite (HOPG), the ratio of the conductivities in the two directions has been reported as  $k_a/k_c = 10^5$  [73]. Taking  $k_a$  to be 5.2 W/cm-K,  $k_c$  would equal  $5.2 \times 10^{-5}$  W/cm-K. Having observed the morphology of the P100 fibers to be an oriented core filament structure (see Figure 2.5), an estimate of the transverse conductivity of the fibers is obtained by considering their radial orientation within the composite material. Figure 5.7 illustrates a few of the possible fiber orientations with respect to the direction of the heat flow. Taking this into consideration, transverse conductivities of  $k_T = 0.5k_a = 2.6$  W/cm-K and  $k_T = 0.25k_a = 1.3$  W/cm-K were used in the calculations. Using the following equation, the effective thermal conductivity of the interface for each composite was obtained and is plotted in Figure 5.8 for  $k_T = 0.5k_a = 2.6$  W/cm-K and Figure 5.9 for  $k_T = 0.25k_a = 1.3$  W/cm-K. It was assumed that the interface comprises 1% of the volume under consideration:

$$\frac{1}{k_{Gr+in}} = \frac{V_{Gr}}{k_{Gr}} + \frac{V_{in}}{k_{in}} \quad (5.7)$$

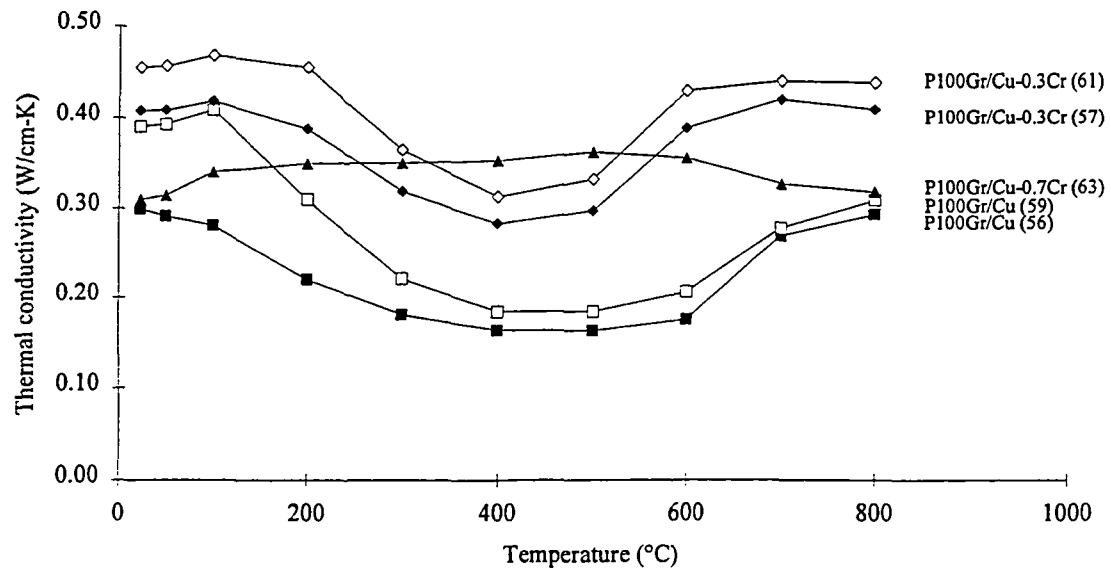


Figure 5.5. Short transverse thermal conductivity of P100Gr/Cu-xCr composites.

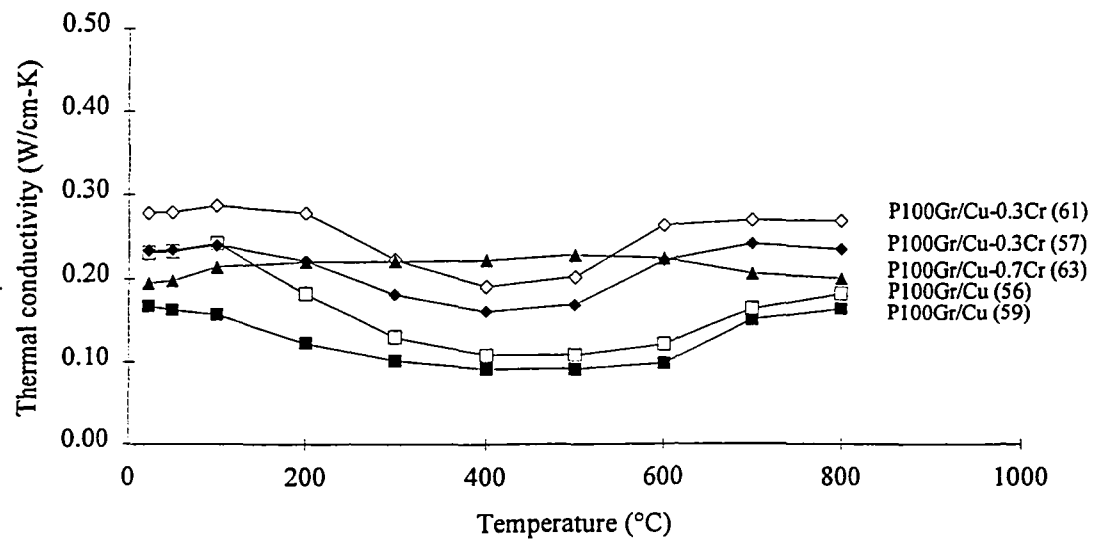


Figure 5.6. Calculated effective transverse thermal conductivity of the P100 fibers + "interface".

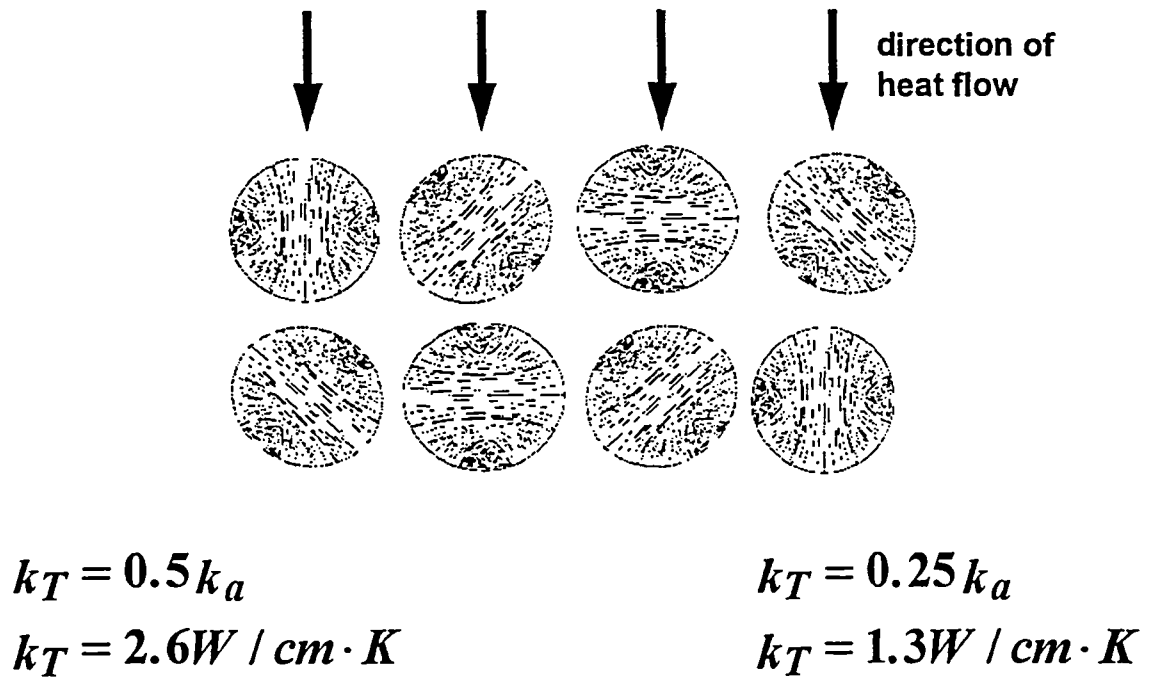


Figure 5.7. Orientation of P100 fibers in P100Gr/Cu-xCr composite with respect to direction of heat flow.



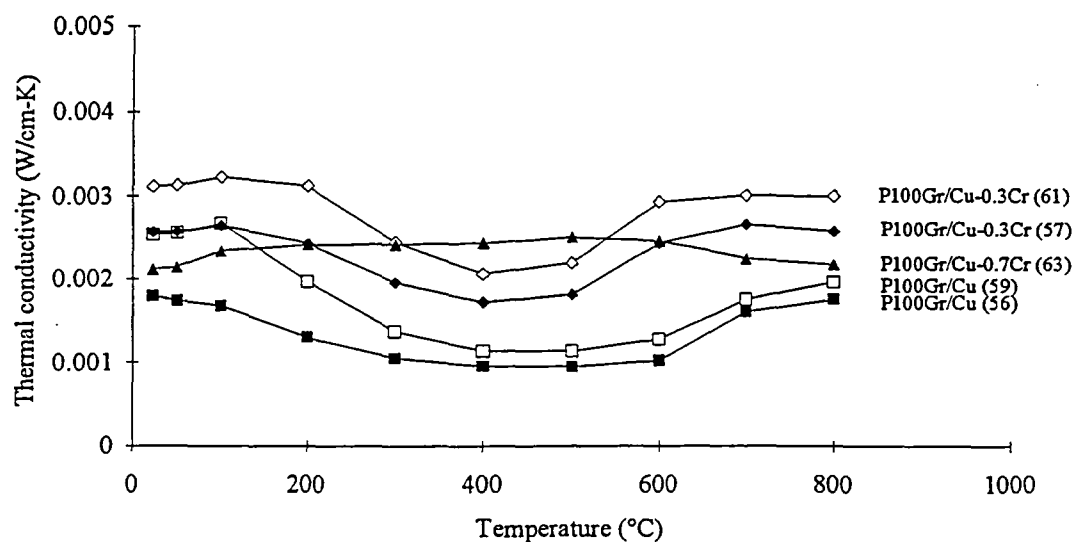


Figure 5.8. Calculated transverse thermal conductivity of the "interface".  
( $k_{Gr} = 2.6 \text{ W/cm-K}$ )

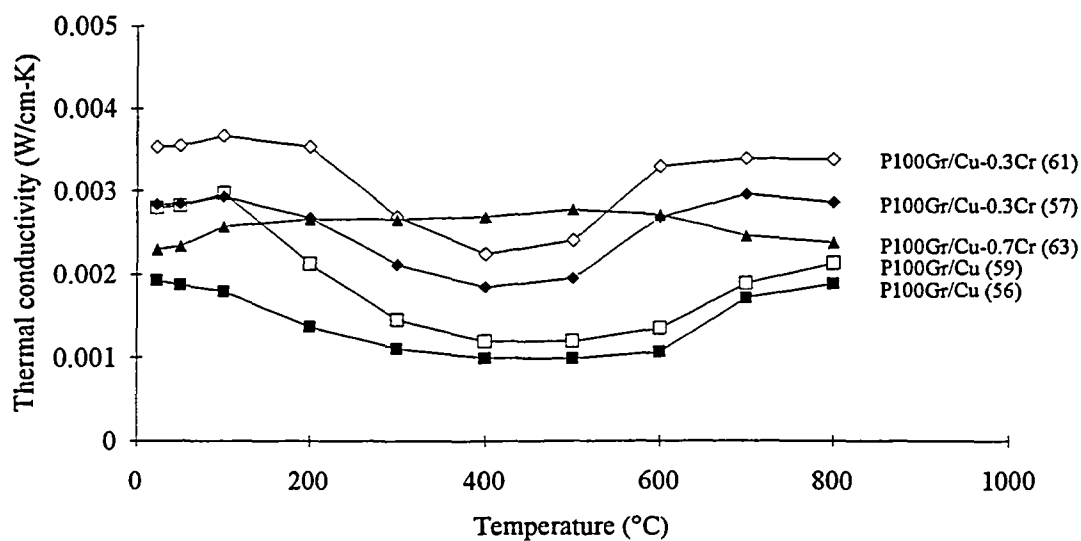


Figure 5.9. Calculated transverse thermal conductivity of the "interface".  
( $k_{Gr} = 1.3 \text{ W/cm-K}$ )

The effective thermal conductivity of the interface is two orders of magnitude lower than the combined conductivity of the P100 fibers and the interface, and is not greatly affected by the estimation of the transverse conductivity of the fibers. It is evident that the nature of the bond at the Gr/Cu interface is not favorable for heat conduction and is the controlling mechanism for short transverse thermal conductivity in P100Gr/Cu composites, as shown in Figure 5.10. This is further illustrated in the schematic of the composite components shown in Figure 5.11. The distribution of fibers in the composite is such that there are essentially no direct paths for heat conduction through the plate, via the Cu matrix, which leads to the need for conduction across the Gr/Cu interface.

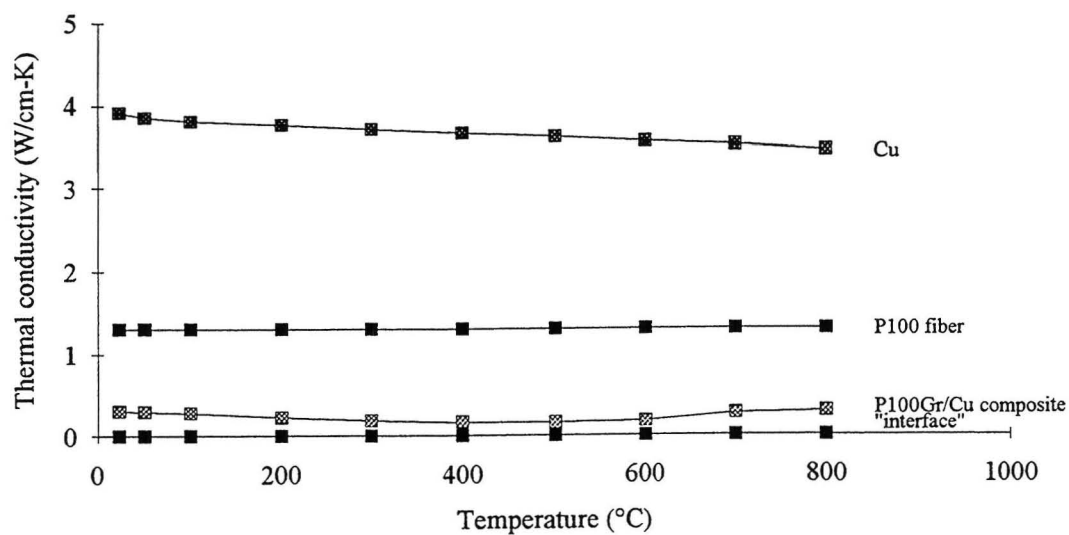


Figure 5.10. Comparison of short transverse thermal conductivity of individual components.

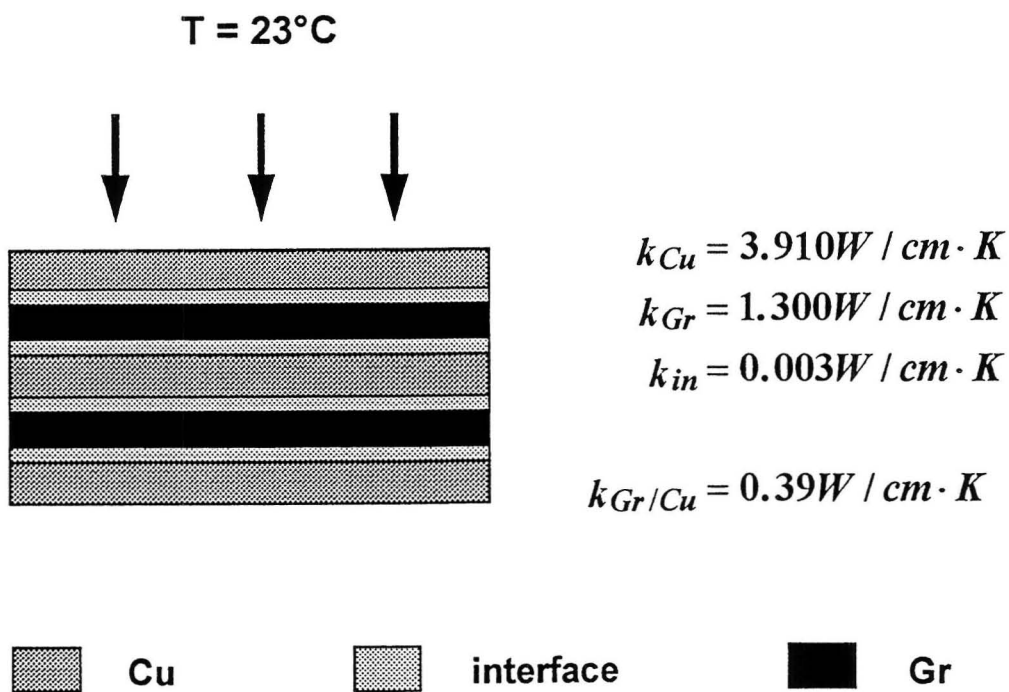


Figure 5.11. Parallel slab illustration of P100Gr/Cu-xCr composite components.

## 6 CONCLUSIONS

Pressure infiltration casting has been shown to be a viable method for producing P100Gr/Cu composites. Although the castings evaluated in this study were fully infiltrated, problems with spreading of the fiber tows and hence fiber distribution exist. Thickness variations in the plates were also identified. Due to the difficulty in spreading the fiber tows, the composite macrostructure is like that of a laminate composite. Consequently, the long transverse tensile properties and the short transverse thermal conductivity suffer.

Extensive SEM analyses, in combination with the optical microscopy and AES investigations, have qualified the distribution and continuity of the  $\text{Cr}_3\text{C}_2$  reaction phase. The  $\text{Cr}_3\text{C}_2$  forms primarily in matrix rich regions at the fiber surfaces. In these matrix rich areas, the  $\text{Cr}_3\text{C}_2$  is approximately 0.2-0.3  $\mu\text{m}$  thick and fairly continuous. Some isolated particle formation of  $\text{Cr}_3\text{C}_2$  also occurs in areas where the fibers are closely spaced. This reaction phase has been found to be more adherent to the Cu than to the P100 fibers. This is due to the weak bonding at the graphite surface in the plane of the fiber axis.

The longitudinal tensile strength of the P100Gr/Cu composites is quite high, in excess of 700 MPa. Shear failure at the Cu layer/composite interface has prevented the determination of an absolute value of the ultimate tensile strength. The elastic moduli of the composites are approximately 393 GPa. They were found to be insensitive to matrix chemistry and to thermal exposure. After 100 hr at 760°C, 84% of the as-cast strength is retained in the alloyed matrix composites; 75% in the unalloyed composites. The long transverse tensile strength is on the order of 7-13 MPa, and is higher for the alloyed matrix composites. The laminate nature of the composites controls the fracture behavior by causing separation at contact points of touching fibers in the dense areas of P100 reinforcement.

The elastic moduli obtained by three-point bend testing are in the same range as those reported for the longitudinal tensile testing. The shear moduli are low, approximately 6-10 GPa, but

are higher for the alloyed matrix composites, due to increased interfacial bonding which decreases fiber/matrix sliding in bending.

The thermal expansion responses of the P100Gr/Cu-xCr composites are very sensitive to interfacial bonding. The P100Gr/Cu composite specimens reveal a "runaway" phenomenon which is a result of the addition of small increments of permanent strain in the composite with each additional thermal cycle. The addition of Cr to the Cu matrix eliminates this behavior due to stable chemical bonding at the fiber/matrix interface. The percent linear change in specimen dimension is essentially zero in the P100Gr/Cu-Cr composites. This cycling response is constant when tested to five cycles.

The thermal conductivity of the P100Gr/Cu composites is high in the longitudinal direction, parallel to the axis of the fibers, but is quite low in the short transverse direction. The values of the short transverse thermal conductivity were determined to be 0.3-0.5 W/cm-K, as compared to almost 4 for pure Cu. The conductivities of the alloyed matrix composites are slightly higher than those of the pure Cu matrix composites. The P100Gr/Cu-0.7Cr system displays constant thermal conductivity from room temperature to 800°C while the P100Gr/Cu and P100Gr/Cu-0.3Cr systems exhibit a dip in their behavior corresponding to the temperature range in which the thermal expansion of the P100 fibers is negative. It is believed that a higher degree of bonding in the P100Gr/Cu-0.7Cr composites is responsible for this effect.

The thermal conductivity of the interface is extremely low and has been calculated to be approximately two orders of magnitude lower than that of the composite. Because the distribution of fibers in the short transverse direction is such that there are no continuous paths of Cu matrix, it is necessary to conduct heat across the Gr/Cu interface. Because the percentage of chemical bonding in the composites is so low, inefficient heat conduction across the Gr/Cu interface is limiting the overall composite conductivity in the short transverse direction.

In summary, P100Gr/Cu-Cr composites have been developed that possess high strength and stiffness, low thermal expansion, and high longitudinal thermal conductivity with low, but not zero,

short transverse thermal conductivity. These properties have been found to be stable after thermal exposure and thermal cycling due to enhanced bonding at the fiber/matrix interface. This combination of mechanical integrity and thermal stability makes P100Gr/Cu-Cr composites highly competitive materials for high heat flux applications, particularly for space power radiator panels.

## REFERENCES

- 1 McDanel, D.L. and J.O. Diaz. "Exploratory Feasibility Studies of Graphite Fiber Reinforced Copper Matrix Composites for Space Power Radiator Panels," NASA TM 102328 (1989).
- 2 Ellis, D.L. "Graphite Fiber/Copper Matrix Composites Improve Space Power Radiator Fins," 1990 Research and Technology, NASA Lewis Research Center, NASA TM 103759, pp. 30-31 (1990).
- 3 "Gr/Cu Composites Excel at Thermal Management," AM&P, vol. 139, no. 1, p. 24 (1991).
- 4 Rodini, B.T., Jr., C.L. Thaw and C.H. Zweben. "Preliminary Assessment of Composite Materials for Space Structures," NASA CR 174692 (1984).
- 5 Titran, R.H., D.L. McDanel and T.L. Grobstein. "Metal Matrix Composites for Space Power Applications," NASA TM 102114 (1989).
- 6 Huybrechts, F. and F. Delannay. "Processing of Carbon Fibre Reinforced Copper Based Composites with Chromium Additions for Control of Interface Adhesion," Powder. Met., vol. 34, no. 4, pp. 281-284 (1991).
- 7 Cook, A.J. and P.S. Werner. "Pressure Infiltration Casting of Metal Matrix Composites," Mat. Sci. Eng., vol. A144, pp. 189-206 (1991).
- 8 DeVincent, S.M. and G.M. Michal. "Improvement of Thermal and Mechanical Properties of Graphite/Copper Composites through Interfacial Modification," JMEPEG, vol. 2, no. 3, pp. 323-332 (1993).
- 9 Technical Survey - OFHC Brand Copper, American Metal Company (1957).
- 10 Mortimer, D. and M. Nicholas. "The Wetting of Carbon by Copper and Copper Alloys," J. Mat. Sci., vol. 5, no. 2, pp. 149-155 (1970).
- 11 Nicholas, M. and D. Mortimer. "The Wetting of Carbon by Liquid Metals and Alloys," Proc. of Int. Conf. on Carbon Fibers, Their Composites and Applications, London, February 2-4, pp. 1-3 (1971).
- 12 Mortimer, D. and M. Nicholas. "The Wetting of Carbon and Carbides by Copper Alloys," J. Mat. Sci., vol. 8, pp. 640-648 (1973).
- 13 Murr, L. Interfacial Phenomena in Metals and Alloys. Addison-Wesley Publ. Co., Reading, MA, p. 102 (1974).
- 14 Ramqvist, L. "Wetting of Metallic Carbides by Liquid Copper, Nickel, Cobalt and Iron," Int. J. Powder Met., vol. 1, no. 4, pp. 2-21 (1965).

- 15 Nogi, K., Y. Osugi and K. Ogino. "A New Method of Wettability Measurement Utilizing a Small Sample and Its Application to Graphite or  $\alpha$ -SiC and Liquid Cu-Cr Alloy Systems", ISIJ, vol. 30, no. 1, pp. 64-69 (1990).
- 16 DeVincent, S.M. "Development of Graphite/Copper Composites Utilizing Engineered Interfaces," M.S. Thesis, Case Western Reserve University (1991).
- 17 Mochida, I., S-H. Yoon and Y. Korai. "Control of Transversal Texture in Circular Mesophase Pitch-Based Carbon Fibre using Non-circular Spinning Nozzles," J. Mat. Sci., vol. 28, pp. 2331-2336 (1993).
- 18 Ohmae, N., M. Tagawa, M. Umeno and K. Gumi. "Atomic Configuration of Carbon Fibers Studied by Field Ion Microscopy," Tribology Trans., vol. 31, no. 4, pp. 481-488 (1987).
- 19 Bacon, R. and C.T. Moses. "Carbon Fibers, from Light Bulbs to Outer Space," Union Carbide Corporation, SPC-PP-86-01 (1986).
- 20 Edie, D.D. and M.G. Dunham. "Melt Spinning Pitch-Based Carbon Fibers," Carbon, vol. 27, no. 5, pp. 647-655 (1989).
- 21 Edie, D.D. and E.G. Stoner. "The Effect of Microstructure and Shape on Carbon Fiber Properties; in Carbon-Carbon Materials and Composites," J.D. Buckley, ed., Noyces Publications, pp. 1-20.
- 22 Thrower, P.A. "Carbon Fibers--Threads of the Future," Earth and Mineral Sci., vol. 48, no. 9, pp. 65-69 (1979).
- 23 Hughes, J.D.H. "The Evaluation of Current Carbon Fibers," J. Phys. D: Appl. Phys., vol., 20, pp. 276-285 (1987).
- 24 Donnet, J.B. and R.Y. Qin. "Study of Carbon Fiber Surfaces by Scanning Tunnelling Microscopy, Part I. Carbon Fibers from Different Precursors and after Various Heat Treatment Temperatures," Carbon, vol. 30, no. 5, pp. 787-796 (1992).
- 25 Knott, T.W. and C.T. Herakovich. "Effect of Fiber Orthotropy on Effective Composite Properties," J. Comp. Mat., vol. 25, pp. 733-759 (1991).
- 26 Johnson, D.J. "Structure-Property Relationships in Carbon Fibers," J. Phys. D: Appl. Phys., vol. 20, pp. 286-291 (1987).
- 27 Johnson, D.J. "Structure and Physical Properties of Carbon Fibres," Chemistry and Industry, pp. 692-698 (1982).
- 28 Macmillan, N.H. J. Mat. Sci., vol. 7, p. 239 (1972).
- 29 Endo, M. "Structure of Mesophase Pitch-Based Carbon Fibres," J. Mat. Sci., vol. 23, pp. 598-605 (1988).
- 30 Farmer, S. and P. Book. unpublished research, NASA Lewis Research Center (1991).



- 31 THORNEL Graphite Fiber P-100 2K. Product Information. Amoco Performance Products, Inc.
- 32 Tanabe, Y., E. Yasuda, A.R. Bunsell, Y. Favry, M. Inagaki and M. Sakai. "The Strength of Pitch-Based Carbon Fibre at High Temperature," J. Mat. Sci., vol. 26, pp. 1601-1604 (1991).
- 33 OFHC Brand Copper - A Survey of Properties and Applications. AMAX Inc. (1974).
- 34 Technical Survey - OFHC Brand Copper. The American Metal Company, Ltd. (1957).
- 35 Hunt, M. "Consider Copper for Diverse Applications," Mat. Eng., pp. 21-25 (1989).
- 36 Rajainmäki, H., A. Helenius and M. Kolehmainen. "The Production and Application of Oxygen-Free Copper," JOM, pp. 68-70 (1993).
- 37 Benson, N.D. and J. McKeown. "The Creep and Softening Properties of Copper for Alternator Windings," J. Inst. Metals, vol. 90, p. 131 (1951).
- 38 Touloukian, Y.S., R.K. Kirby, R.E. Taylor and P.D. Desai. Thermal Expansion - Metallic Elements and Alloys; in Thermophysical Properties of Matter, Vol. 12, IFI/Plenum, New York: p. 77 (1975).
- 39 Richards, J.W. "The Overall Linear Expansion of of Three Face Centered Cubic Crystals (Al, Cu, Pb) from -190°C to Near the Melting Points," ASM Trans., vol. 30, p. 326 (1942).
- 40 OFHC Brand Copper Technical Survey. American Metal Climax, Inc. (1961).
- 41 Stokes, H.J. "Apparatus for the Measurement of Young's Modulus between -200 and 700°C by Transverse Vibration in a Vacuum," Sci. Instr., vol. 37, p. 117 (1960).
- 42 Crosby, R.C. and D.H. Desy. "Dispersion Strengthening in Copper-Alumina and Copper and Boron Deoxidized Copper," NASA Tech Brief 66-10273 (North American Aviation, Inc.) (1969).
- 43 Wilkins, R.A. and E.S. Bunn. Copper and Copper Base Alloys. McGraw Hill, New York, NY (1943).
- 44 Pawlek, F. and K. Reichel. "Der Einfluss von Beimengungen auf die Elektrische Leitfähigkeit von Kupfer. Zhur. Fiz. Khim, vol. 42, no. 2, pp. 463-465 (1956).
- 45 Maxwell, P.B., G.P. Martins, D.L. Olson and G.R. Edwards. "The Infiltration of Aluminum into Silicon Carbide Compacts," Met. Trans. B., vol. 21B, pp. 475-485 (1990).
- 46 Young, R.M.K. "Infiltration Mechanics in Conventional and Hybridised Fibre Reinforced Metal-Matrix Composites," Mat. Sci. Tech., vol. 6, pp. 548-553 (1990).
- 47 Mortensen, A. and J. Cornie. "On the Infiltration of Metal Matrix Composites," Met. Trans. A, vol. 18App. 1160-1163 (1987).
- 48 Delannay, F., L. Froyen and A. Deruyetere. "Review: The Wetting of Solids by Molten Metals and Its Relation to the Preparation of Metal-Matrix Composites," J. Mat. Sci., vol. 22, pp. 1-16 (1987).

- 49 Young, T. Phil. Trans. R. Soc., vol. 95, p. 65 (1805).
- 50 Warriar, S.G. and R.Y. Lin. "TiC Growth in C Fiber/Ti Alloy Composites during Liquid Infiltration," Scripta Met. Mat., vol. 29, pp. 147-152 (1993).
- 51 DeVincent, S.M. and G.M. Michal. "Reaction Layer Formation at the Graphite/Copper-Chromium Alloy Interface," Met. Trans. A, vol. 24A, pp. 53-60 (1993).
- 52 Chakrabarti, D.J. and D.E. Laughlin. Bull. Alloy Phase Diagrams, vol. 5., no.1 (1984).
- 53 Elliot, J.F. and M. Gleiser. Thermochemistry for Steelmaking. Addison-Wesley Publ. Co., Reading, MA, pp. 135-136 (1960).
- 54 Storms, E.K. The Refractory Carbides. Academic Press, New York, NY, pp. 102-121 (1967).
- 55 Carslaw, H.S. and J.C. Jaeger. Conduction of Heat in Solids. Oxford University Press, New York, NY, pp. 119-120 (1959).
- 56 Shurygin, P.M. and V.D. Shantarin. "Compensation Effects in the Diffusion of Metals in Molten Copper," Zhur. Fiz. Khim., vol. 42, pp. 463-465 (1968).
- 57 Shewmon, P.G. Diffusion in Solids. McGraw Hill, New York, NY, p. 360 (1969).
- 58 Fries, R.J., J.E. Cummings, C.G. Hoffman and S.A. Daily. "Chemical Diffusion of C in the Group VI-B Metal Carbides," U.S. Atomic Energy Comm. Report LA-3795 (1967).
- 59 Barrett, C.S. and T.B. Massalski. Structure of Metals. McGraw Hill, New York, NY, p. 627 (1966).
- 60 Gent, A.N. and C. Wang. "What Happens after a Fibre Breaks - Pull-out or Resin Cracking?" J. Mat. Sci., vol. 28, pp. 2494-2500 (1993).
- 61 Gent, A.N. and C. Wang. "Matrix Cracking Initiated by Fibre Breaks in Model Composites," J. Mat. Sci., vol. 27, pp. 2539-2548 (1992).
- 62 Wood Handbook: Wood as an Engineering Material. U.S. Forest Products Laboratory, Agriculture Handbook No. 72 p. 8-2 (1974).
- 63 Ashbee, K. Fundamental Principles of Fiber Reinforced Composites. Technomic Publishing Co., Inc., Lancaster, PA, pp. 113-127 (1989).
- 64 Kingery, W.D. Introduction to Ceramics. Wiley and Sons, Inc., New York, pp. 583-645 (1976).
- 65 Kelly, B.T. "The Thermal Expansion Coefficients of Graphite Crystals--the Theoretical Model and Comparison with 1990 Data," Carbon, vol. 29, no. 6, pp. 721-724 (1991).
- 66 Kittel, C. Introduction to Solid State Physics. Wiley and Sons, Inc., New York, pp. 81-153 (1986).

- 67 Pollock, D.D. *Electrical Conduction in Solids*. American Society for Metals, Metals Park, OH (1985).
- 68 Bird, R.B., W.E. Stewart and E.N. Lightfoot. *Transport Phenomena*. Wiley and Sons, New York, NY (1960).
- 69 Kalnin, I.L. "Thermal Conductivity of High-Modulus Carbon Fibers," *Composite Reliability*, ASTM STP 580, American Society for Testing and Materials, pp. 560-573 (1975).
- 70 Cook, A.J. and P.S. Werner. "Pressure Infiltration Casting of Metal Matrix Composites," *Mater. Sci. Eng.*, vol. A144, pp. 189-206 (1991).
- 71 ASTM D 2344. *Standard Test Method for Apparent Interlaminar Shear Strength of Parallel Fiber Composites by Short-Beam Method*. Annual Book of ASTM Standards, American Society for Testing and Materials, vol. 15:03, p. 43 (1991).
- 72 Taylor, R.E. "A Description of the Thermophysical Properties Research Laboratory," TPRL 181-B (1990).
- 73 Kastelein, B., R.D. van Bergen, H. Postma, H.C. Meijer and F. Mathu. "Thermal Conductance of Highly Oriented Pyrolytic Graphite along the c-Direction at Very Low Temperatures including Magnetic Field Effects," *Carbon*, vol. 30, no. 6, pp. 845-850 (1992).

## Appendix I Statistical Analyses

### Simple Summary Statistics

Ref: Keller, D. J. 1992. Introduction to Statistics. RealWorld Quality Systems, Inc., Ohio: 1-45.

Variance:

$$S^2 = \frac{\sum_{i=1}^N (Y_i - \bar{Y})^2}{N-1} = \frac{(Y_1 - \bar{Y})^2 + (Y_2 - \bar{Y})^2 + \dots + (Y_N - \bar{Y})^2}{N-1}$$

where  $Y_i$  = data point,  $\bar{Y}$  = mean,  $N$  = number of data points,  $N-1$  = degrees of freedom.

Standard Deviation:

$$S = \sqrt{S^2} = \sqrt{\frac{\sum_{i=1}^N (Y_i - \bar{Y})^2}{N-1}}$$

## Appendix II Mechanical Properties

### Longitudinal Tensile Data

Longitudinal tensile data (as-cast)							
P100Gr/Cu-xCr specimen	% P100	0°TS (MPa)	E (GPa)		ave %P100	ave 0°TS (MPa)	ave E (GPa)
Cu-B1P1-N	57	713	389		57	685	382
Cu-B1P1-P	56	717	382				
Cu-B1P2-O	56	615	371				
Cu-B1P2-Q	56	713	372				
Cu-B1P3-N	56	725	390				
Cu-B1P3-P	56	672	330				
Cu-B1P4-M	58	760	389				
Cu-B1P4-O	57	676	420				
Cu-B2P2-M	60	693	383				
Cu-B2P3-O	61	556	376				
Cu-B2P3-Q	60	691	404				
0.3Cr-B1P1-M	50	682	371		57	593	372
0.3Cr-B1P1-P	52	440	385				
0.3Cr-B1P2-O	59	601	382				
0.3Cr-B1P2-Q	58	607	364				
0.3Cr-B1P3-N	57	568	405				
0.3Cr-B1P3-P	56	643	418				
0.3Cr-B1P4-M	57	585	325				
0.3Cr-B1P4-O	54	627	272				
0.3Cr-B2P1-M	60	629	371				
0.3Cr-B2P1-N	59	685	425				
0.3Cr-B2P3-O	58	560	433				
0.3Cr-B2P3-Q	63	483	316				
0.7Cr-B1P1-O	56	708	343		59	679	397
0.7Cr-B1P1-P	55	676	427				
0.7Cr-B1P2-M	66	745	477				
0.7Cr-B1P2-Q	59	742	399				
0.7Cr-B1P3-N	60	714	380				
0.7Cr-B1P3-O	59	633	376				
0.7Cr-B1P4-N	57	534	378				

Longitudinal tensile data (heat treated at 760°C)			1 HR	3 HR	10 HR	30 HR	100 HR
P100Gr/Cu-xCr	% P100		0°TS (MPa)	0°TS (MPa)	0°TS (MPa)	0°TS (MPa)	0°TS (MPa)
specimen							
Cu-B1P1-M	57		579				
Cu-B1P2-N	56		532				
Cu-B2P2-O	59		588				
Cu-B1P2-M	52			530			
Cu-B1P4-N	57			666			
Cu-B2P2-P	60			440			
Cu-B1P4-Q	57				533		
Cu-B2P3-N	61				488		
Cu-B1P3-Q	56					537	
Cu-B1P4-P	57					579	
Cu-B2P2-Q	61					533	
Cu-B1P1-Q	56						577
Cu-B1P2-P	56						485
Cu-B2P3-M	60						471
0.3Cr-B1P1-N	52		592				
0.3Cr-B1P2-N	59		610				
0.3Cr-B2P1-O	58		427				
0.3Cr-B1P2-M	59			562			
0.3Cr-B1P4-N	55			498			
0.3Cr-B2P1-P	58			562			
0.3Cr-B1P3-O	56				632		
0.3Cr-B1P4-Q	55				543		
0.3Cr-B2P3-N	62				524		
0.3Cr-B1P3-Q	56					633	
0.3Cr-B1P4-P	55					609	
0.3Cr-B2P1-Q	59					409	
0.3Cr-B1P1-Q	52						349
0.3Cr-B1P2-P	58						462
0.3Cr-B2P3-M	58						460
0.7Cr-B1P1-M	54		325				
0.7Cr-B1P2-O	58		403				
0.7Cr-B1P3-M	62			541			
0.7Cr-B1P4-P	56			387			
0.7Cr-B1P2-N	58				614		
0.7Cr-B1P4-Q	58				387		
0.7Cr-B1P1-Q	56					364	
0.7Cr-B1P3-P	60					607	
0.7Cr-B1P3-Q	59						574
0.7Cr-B1P4-O	56						558



REPORT DOCUMENTATION PAGE			Form Approved OMB No. 0704-0188	
Public reporting burden for this collection of information is estimated to average 1 hour per response, including the time for reviewing instructions, searching existing data sources, gathering and maintaining the data needed, and completing and reviewing the collection of information. Send comments regarding this burden estimate or any other aspect of this collection of information, including suggestions for reducing this burden, to Washington Headquarters Services, Directorate for Information Operations and Reports, 1215 Jefferson Davis Highway, Suite 1204, Arlington, VA 22202-4302, and to the Office of Management and Budget, Paperwork Reduction Project (0704-0188), Washington, DC 20503.				
1. AGENCY USE ONLY (Leave blank)		2. REPORT DATE August 1995		3. REPORT TYPE AND DATES COVERED Final Contractor Report
4. TITLE AND SUBTITLE Interfacial Effects on the Thermal and Mechanical Properties of Graphite/Copper Composites			5. FUNDING NUMBERS  WU-466-02-01 NCC3-94	
6. AUTHOR(S)  Sandra Marie DeVincent				
7. PERFORMING ORGANIZATION NAME(S) AND ADDRESS(ES)  Case Western Reserve University Cleveland, Ohio 44106			8. PERFORMING ORGANIZATION REPORT NUMBER  E-9817	
9. SPONSORING/MONITORING AGENCY NAME(S) AND ADDRESS(ES)  National Aeronautics and Space Administration Lewis Research Center Cleveland, Ohio 44135-3191			10. SPONSORING/MONITORING AGENCY REPORT NUMBER  NASA CR-198370	
11. SUPPLEMENTARY NOTES This report was submitted as a dissertation in partial fulfillment of the requirements for the degree Doctor of Philosophy to Case Western Reserve University, Cleveland, Ohio. Sandra Marie DeVincent, Case Western Reserve University, Cleveland, Ohio 44106 and NASA Resident Research Associate at Lewis Research Center. Project Manager, Robert Miner, Materials Division, NASA Lewis Research Center, organization code 5120, (216) 433-9515.				
12a. DISTRIBUTION/AVAILABILITY STATEMENT Unclassified - Unlimited Subject Category 26 This publication is available from the NASA Center for Aerospace Information, (301) 621-0390.			12b. DISTRIBUTION CODE	
13. ABSTRACT (Maximum 200 words)  Graphite surfaces are not wet by pure copper. This lack of wetting has been responsible for a debonding phenomenon that has been found in continuous graphite fiber reinforced copper matrix composites subjected to elevated temperatures. By suitably alloying copper, its ability to wet graphite surfaces can be enhanced. Information obtained during sessile drop testing has led to the development of a copper-chromium alloy that suitably wets graphite. Unidirectionally reinforced graphite/copper composites have been fabricated using a pressure infiltration casting procedure. P100 pitch-based fibers have been used to reinforce copper and copper-chromium alloys. X-ray radiography and optical microscopy have been used to assess the fiber distribution in the cast composites. Scanning electron microscopy and Auger electron spectroscopy analyses were conducted to study the distribution and continuity of the chromium carbide reaction phase that forms at the fiber/matrix interface in the alloyed matrix composites. The effects of the chromium in the copper matrix on the mechanical and thermal properties of P100Gr/Cu composites have been evaluated through tensile testing, three-point bend testing, thermal cycling and thermal conductivity calculations. The addition of chromium has resulted in an increased shear modulus and essentially zero thermal expansion in the P100Gr/Cu-xCr composites through enhanced fiber/matrix bonding. The composites have longitudinal tensile strengths in excess of 700 MPa with elastic moduli of 393 GPa. After 100 hr at 760°C, 84% of the as-cast strength is retained in the alloyed matrix composites. The elastic moduli are unchanged by the thermal exposure. It has been found that problems with spreading of the fiber tows strongly affect the long transverse tensile properties and the short transverse thermal conductivity of the P100Gr/Cu-xCr composites. The long transverse tensile strength is limited by rows of touching fibers which are paths of easy crack propagation under low tensile loads. The short transverse thermal conductivity is dictated by the fiber/matrix interface. Conduction across this interface has been estimated to be two orders of magnitude lower than that across the composite. This is due to the mechanical, and not chemical, nature of Gr/Cu bond.				
14. SUBJECT TERMS  Composites; Interface; Thermal expansion; Thermal conductivity; Casting; Infiltration			15. NUMBER OF PAGES 184	
			16. PRICE CODE A09	
17. SECURITY CLASSIFICATION OF REPORT Unclassified	18. SECURITY CLASSIFICATION OF THIS PAGE Unclassified	19. SECURITY CLASSIFICATION OF ABSTRACT Unclassified	20. LIMITATION OF ABSTRACT	





National Aeronautics and  
Space Administration  
**Lewis Research Center**  
21000 Brookpark Rd.  
Cleveland, OH 44135-3191

Official Business  
Penalty for Private Use \$300

POSTMASTER: If Undeliverable — Do Not Return

